UNIVERSITY OF SOUTHAMPTON

An Investigation into the Aerodynamics of Wings in Ground Effect

Jonathan David Chaim Zerihan

Submitted for the Degree of Doctor of Philosophy

School of Engineering Sciences

April 2001

Abstract

The aerodynamics of wings in ground effect has been studied using experimental and computational methods. Wind tunnel tests were used to quantify the effect of the ground on the aerodynamic performance of a wing, with the suction surface nearest to the ground. Features of the flowfield around the wing were investigated using Laser Doppler Anemometry and Particle Image Velocimetry to map the wake at the centre of the wing, and the state of the tip vortex. Initially, a single element configuration was used, both under transition free and transition fixed conditions. The application of Gurney flaps was then examined. The experimental study was completed using a double element configuration. The performance is discussed together with the flowfield results. Wind tunnel testing was performed at a Reynolds number of approximately 0.75×10^6 based on the chord of the double element wing. The application of a computational technique has been examined using a Reynolds averaged Navier-Stokes solver. Trends in the aerodynamic performance of a single element aerofoil in ground effect were predicted well using a Spalart-Allmaras turbulence model.

Acknowledgements

Although this thesis describes the studies completed throughout the research, it is not representative of all the work that was performed, especially by members of the university staff and other organisations whose support I am very much grateful for. These acknowledgements are directed to everyone who has helped me in any way, including those who I have not been able to list.

It is without doubt that I owe most of my thanks to Xin Zhang, for having faith in my abilities, supervising me throughout the research, keeping me encouraged, and constantly suggesting areas to investigate. The research programme was created by Xin and Mike Gascoine, then of the Tyrrell Racing Organisation, who acted as my initial industrial supervisor. For all their technical assistance, including the manufacture of the wind tunnel models, especially in such a difficult time, I am indebted to all the aerodynamicists and model makers at Tyrrell.

Further technical assistance was given by British American Racing with the wind tunnel models, when Willem Toet took over the supervision of the project. I am grateful for Willem's time discussing results and guidance throughout the testing. In addition to this, David Jeffrey also deserves huge amounts of thanks for his help, both as an aerodynamicist at BAR, and with the design of the models whilst writing up his thesis at Southampton.

The majority of this thesis describes experimental work performed in the wind tunnels. None of this would have been possible without the efforts of the technicians, which always go understated. Thanks to Geoff Thomas, Geoff Baldwin, Mike Tudorpole, and Mike Thomas, running the wind tunnels, maintaining the systems, and also acting as model makers, throughout the 26 weeks of testing, including those many late nights whilst LDA testing, all of which was a once in a while effort for me, but normal work for them.

Others in the university who I should thank include everyone in the department including all my office mates, for help regarding work and as friends; Andrea, Andreas, Graham, Kenji, and specifically Ed Rayner for help with the computers.

I do not think that I would have been able to complete the work without other friends, mainly from the Wessex Motor Club, including Paul Swindells for being the eternal optimist, Dick for his astounding ability to remain sensible at all times, Muppet for his superb sense of hearing, Azzo for driving us both into a tree, Henry for grinning all the time, James for not liking doughnuts, and Paul Marwood for just being a top bloke, all of whom were unfortunate enough to live with me. Also, Jerry especially for all those dinners, Takashi for all the rallies we did together, but not for driving my car into a tree, and the others; Steve, Tom, Jonah, Sion, and everyone else. And to Kaos.

A final thanks to my family, my parents David and Sheila Zerihan, who have supported me and encouraged me throughout everything that I have done.

Contents

1 Introduction and Literature Review **1**

1.1 Introduction to Topic 1
1.2 Motivation for Research 2
1.3 Applicability of Research 2
1.4 Literature Review 3
1.4.1 Relevant Research 3
1.4.2 Experimental Representation of Ground Plane 3
1.4.3 Lift Producing Wings in Ground Effect 4
1.4.4 Downforce Producing Wings in Ground Effect 5
1.4.5 Finite Trailing Edge Wings 7
1.4.6 Gurney Flaps 8
1.4.7 Multi-element Flows 8
1.4.8 Three-dimensional Vortical Flows 9
1.5 Aims of Research Programme 10
1.6 Summary 11

2 Research Programme **13**

2.1 Methodology 13
2.2 Wind Tunnel Models 14
2.2.1 Single Element Wing 14
2.2.2 Double Element Wing 14
2.2.3 Construction 15
2.2.4 Gurney Flaps 15
2.3 Pressure Tappings 15
2.4 Model Installation in Wind Tunnel 16
2.5 Wind Tunnel Setup 17
2.6 Reynolds Numbers 18
2.7 Wing Height and Incidence Variation 18
2.8 Laser Doppler Anemometry Technique 19

2.9 Particle Image Velocimetry Technique 19
2.10 Summary 21

3 Single Element Wing in Freestream **31**
3.1 Introduction to Chapter 31
3.2 Forces 31
3.3 Surface Pressures 31
3.3.1 Chordwise Pressures; Centre 31
3.3.2 Chordwise Pressures; Tip 32
3.3.3 Spanwise Pressures 32
3.4 Summary 32

4 Single Element Wing in Ground Effect at the Reference Incidence **37**
4.1 Introduction to Chapter 37
4.2 Forces 37
4.3 Surface Pressures 38
4.3.1 Chordwise Pressures at Wing Centre 38
4.3.2 Suction Surface Canonicals 38
4.3.3 Spanwise Pressures 39
4.3.4 Chordwise Pressures near to Wing Tip 40
4.3.5 Integrated Pressures 40
4.4 Oil Flow Visualisation 41
4.5 Laser Doppler Anemometry Surveys 41
4.6 Particle Image Velocimetry Surveys near to Wing Tip 42
4.7 Discussion 44
4.8 Summary 45

5 Single Element Wing in Ground Effect at Various Incidences **57**
5.1 Introduction to Chapter 57
5.2 Forces 57
5.2.1 Variation of Downforce with Height 57
5.2.2 Liftcurves at Varying Heights 58
5.3 Surface Pressures 58
5.3.1 Chordwise Pressures 58
5.3.2 Canonicals 59
5.4 Discussion 59
5.5 Summary 59

6 Single Element Wing with Fixed Transition **63**
6.1 Introduction to Chapter . . . 63
6.2 Forces in Freestream . . . 64
6.3 Forces in Ground Effect . . . 64
6.4 Surface Pressures . . . 64
6.5 Laser Doppler Anemometry Surveys . . . 65
6.6 Particle Image Velocimetry Surveys at Wing Centre . . . 66
6.7 Discussion . . . 67
6.8 Summary . . . 68

7 Single Element Wing with Gurney Flaps **78**
7.1 Introduction to Chapter . . . 78
7.2 Forces in Freestream . . . 78
7.3 Forces in Ground Effect . . . 79
7.4 Surface Pressures . . . 79
7.5 Laser Doppler Anemometry Surveys . . . 80
7.6 Particle Image Velocimetry Surveys at Wing Centre . . . 82
7.7 Discussion . . . 83
7.8 Summary . . . 85

8 Double Element Wing **94**
8.1 Introduction to Chapter . . . 94
8.2 Forces . . . 94
8.3 Surface Pressures . . . 96
8.3.1 Chordwise Pressures at Wing Centre . . . 96
8.3.2 Spanwise Pressures . . . 98
8.3.3 Chordwise Pressures near to Wing Tip . . . 100
8.3.4 Integrated Pressures . . . 101
8.4 Particle Image Velocimetry Surveys near to Wing Tip . . . 102
8.4.1 Mean Flow Results . . . 102
8.4.2 Instantaneous Results . . . 104
8.5 Oil Flow visualisation . . . 106
8.5.1 Transition . . . 107
8.5.2 Flow Three-dimensionality . . . 108
8.6 Laser Doppler Anemometry . . . 108
8.7 Discussion . . . 111
8.7.1 Downforce Generation . . . 111
8.7.2 Tip Effects . . . 112
8.7.3 Transition . . . 114

8.7.4 Wake . . . 115
8.8 Summary . . . 116

9 A Computational Fluid Dynamics Model of an Aerofoil in Ground Effect 155
9.1 Introduction . . . 155
9.2 Computational Model . . . 155
9.2.1 Governing Equations . . . 155
9.2.2 Turbulence Modelling . . . 157
9.2.3 Numerical Algorithm . . . 157
9.2.4 Boundary Conditions . . . 157
9.2.5 Grid Strategy . . . 158
9.2.6 Solution Process . . . 159
9.3 Results . . . 159
9.3.1 Aerodynamic Performance . . . 159
9.3.2 Flowfield . . . 161
9.4 Discussion . . . 164
9.5 Summary . . . 165

10 Further Discussions 182
10.1 Introduction . . . 182
10.2 Single Element, Transition Free . . . 182
10.2.1 Freestream . . . 182
10.2.2 Ground Effect . . . 183
10.2.3 Comparisons . . . 183
10.3 Transition Fixing . . . 184

11 Conclusions and Recommendations for Future Work 186
11.1 Conclusions . . . 186
11.2 Recommendations for Future Work . . . 187
11.2.1 Computational Modelling . . . 187
11.2.2 Aeronautical Field . . . 188
11.2.3 Practical Applications . . . 188

A Fixed Ground Case 198
A.1 Introduction . . . 198
A.2 Results . . . 198
A.2.1 Forces . . . 198
A.2.2 Surface Pressures . . . 199
A.2.3 Canonical Pressures . . . 199
A.2.4 Discussion . . . 199

B Vortex Generators **203**
B.1 Introduction 203
B.2 Description of Tests 203
B.3 Results 204
B.4 Conclusion 205

C Uncertainty and Repeatability **207**
C.1 Introduction 207
C.2 Uncertainty of Force Measurements 207
C.3 Repeatability of Force Measurements 208
C.4 Uncertainty of Surface Pressures 209
C.5 Repeatability of Surface Pressures 210
C.6 Uncertainty of PIV Results 211
C.7 Repeatability of PIV Results 212
C.8 Uncertainty of LDA Results 212

D Miscellaneous **217**
D.1 Effect of Pressure Tappings 217

List of Figures

1 (a) Single element wing with endplate. (b) Single element wing profiles; Tyrrell 026 wing and derived NASA GA(W)-2 LS(1)-0413 MOD profiles. (c) Double element wing with endplate. (d) Double element wing profile with datum and low flap angle. 22

2 Model installation in wind tunnel. (a) Close up of single element wing in 3.5m×2.5m wind tunnel (b) Double element wing in 2.1m×1.7m wind tunnel. 23

3 Schematic of the moving ground rig in the 2.1m×1.7m wind tunnel. 24

4 Aerodynamic performance of single element wing in freestream (a) Liftcurve. (b) Drag polar. 34

5 Surface pressures in freestream (a) Chordwise at wing centre. (b) Spanwise. 35

6 Chordwise surface pressures in freestream at wing centre and wing tip (a) $\alpha = 1°$. (b) $\alpha = 13°$. 36

7 Aerodynamic performance of single element wing in ground effect at $\alpha = 1°$ (a) Downforce with height. (b) Drag with height. 46

8 Chordwise surface pressures at wing centre in ground effect at $\alpha = 1°$ (a) Moderate and large ground heights. (b) Small ground heights. 47

9 Surface pressures (a) Suction surface canonicals at wing centre in ground effect at $\alpha = 1°$. (b) Integrated surface pressures in ground effect at $\alpha = 1°$. 48

10 Spanwise surface pressures in ground effect at $\alpha = 1°$ (a) Raw results. (b) Normalised. 49

11 Spanwise surface pressures at wing centre and wing tip in ground effect at $\alpha = 1°$ (a) h/c=0.313. (b) h/c=0.134. 50

12 Oil flow visualisation on suction surface, leading edge lowermost (a) $h/c = 0.134$ (b) $h/c = 0.090$ (c) $h/c = 0.067$ 51

13 LDA u/U_∞ velocity contours at heights of $h/c = 0.448, 0.224, 0.134, 0.090$ 52

14 LDA u/U_∞ velocity profiles (a) Wake profiles at $x/c = 1.2$. (b) Wake profiles for $h/c = 0.134$. 53

15 Wing tip vortex at heights of $h/c = 0.448, 0.224, 0.134, 0.090$; contours of planar vorticity 54

16 The ground effect for an aerofoil (a) Image model. (b) Diffuser effect. 55

17 Downforce in ground effect; (a) Downforce with height for various incidences. (b) Liftcurves at different heights. 60
18 (a) Liftslope in ground effect. (b) Suction surface canonicals at $\alpha = 5°$. 61
19 Chordwise surface pressures at wing centre in ground effect at $\alpha = 5°$ (a) Moderate and large ground heights. (b) Small ground heights. 62

20 Forces in freestream, transition fixed; (a) Liftcurve. (b) Drag polar. 69
21 Forces in ground effect; (a) Downforce. (b) Drag. 70
22 Surface pressures at wing centre (a) Effect of transition fixing. (b) Pressure distributions at different heights. 71
23 LDA u/U_∞ velocity contours at heights of $h/c = 0.448, 0.224, 0.134, 0.067$ 72
24 LDA u/U_∞ velocities; (a) Boundary layer profiles at $x/c = 1.0$, suction surface (b) Wake surveys at $h/c = 0.448$ 73
25 LDA u/U_∞ wake surveys; (a) $h/c = 0.224$. (b) $h/c = 0.067$. 74
26 LDA results; (a) u/U_∞ velocities at $x/c = 1.5$. (b) $u'u'/U_\infty^2$ perturbation velocities at $x/c = 1.2$ 75
27 Instantaneous PIV vorticity contours at heights of $h/c = 0.448, 0.179, 0.134, 0.067$. 76
28 Schematic of wake profile 77

29 Forces in freestream; (a) Liftcurve. (b) Drag polar, transition free. 86
30 (a) Downforce in ground effect. (b) Increment in downforce over clean wing, transition free. 87
31 Surface pressure distributions at wing centre (a) Effect of adding Gurney flap at $h/c = 0.448$. (b) Distributions with Gurney flap for different heights, transition free. 88
32 Surface pressure distributions at wing centre (a) Pressure difference at trailing edge. (b) Suction surface canonical pressures, transition free. 89
33 LDA u/U_∞ velocity contours at heights of $h/c = 0.448, 0.224, 0.134$ with 2.90% Gurney flap and at $h/c = 0.224$ for the clean wing, transition fixed. 90
34 LDA u/U_∞ velocity wake surveys for clean wing and 2.90% Gurney flap at $h/c = 0.134$ (a) $x/c = 1.5$. (b) $x/c = 2.0$, transition fixed. 91
35 Instantaneous PIV vorticity contours at heights of $h/c = 0.448, 0.224, 0.134, 0.067$, transition fixed. 92

36 Forces in ground effect; (a) Effect of varying flap overlap and gap at a height of $h/c = 0.263$ at the datum flap angle. (b) Downforce with ground height. 117
37 Downforce with ground height, including flow regions and features, (a) Low flap angle. (b) High flap angle. 118
38 (a) Drag with ground height. (b) Chordwise surface pressures at wing centre in freestream, for double and single element wings 119

39 Chordwise surface pressures at wing centre in ground effect for $-8.5°$ flap deflection (a) Large heights. (b) Small heights. 120
40 Chordwise surface pressures at wing centre in ground effect for datum flap deflection (a) Large heights. (b) Small heights. 121
41 Spanwise surface pressures on main element at quarter-chord position for $-8.5°$ flap deflection (a) Large heights. (b) Small heights. 122
42 Spanwise surface pressures on main element at quarter-chord position for datum flap deflection (a) Large heights. (b) Small heights. 123
43 Normalised spanwise surface pressures on main element (a) Low flap deflection. (b) High flap deflection. 124
44 Spanwise surface pressures on flap at quarter-chord position for $-8.5°$ flap deflection (a) Large heights. (b) Small heights. 125
45 Spanwise surface pressures on flap at quarter-chord position for datum flap deflection (a) Large heights. (b) Small heights. 126
46 Chordwise surface pressures at centre and near to wing tip at $h/c = 0.395$, a typical type a height (a) Low flap angle. (b) High flap angle. 127
47 Chordwise surface pressures at centre and near to wing tip at a height on type a/b boundary (a) Low flap angle at $h/c = 0.184$. (b) High flap angle at $h/c = 0.263$. . 128
48 Chordwise surface pressures at centre and near to wing tip at $h/c = 0.105$, a typical type b height (a) Low flap angle. (b) High flap angle. 129
49 Integrated surface pressures on main element and flap with ground height (a) Low flap angle. (b) High flap angle. 130
50 Vorticity contours showing mean flow results for wing tip vortex at low flap angle. (a) $h/c = 0.263$ at $x/c = 0.672$, (b) $h/c = 0.263$ at $x/c = 1.092$, (c) $h/c = 0.211$ at $x/c = 0.672$, (d) $h/c = 0.211$ at $x/c = 1.092$ 131
51 Vorticity contours showing mean flow results for wing tip vortex at low flap angle. (a) $h/c = 0.158$ at $x/c = 0.672$, (b) $h/c = 0.158$ at $x/c = 1.092$, (c) $h/c = 0.105$ at $x/c = 0.672$, (d) $h/c = 0.105$ at $x/c = 1.092$ 132
52 Vorticity contours showing mean flow results for wing tip vortex at high flap angle. (a) $h/c = 0.263$ at $x/c = 0.672$, (b) $h/c = 0.263$ at $x/c = 1.092$, (c) $h/c = 0.211$ at $x/c = 0.672$, (d) $h/c = 0.211$ at $x/c = 1.092$ 133
53 Vorticity contours showing mean flow results for wing tip vortex at high flap angle. (a) $h/c = 0.158$ at $x/c = 0.672$, (b) $h/c = 0.158$ at $x/c = 1.092$, (c) $h/c = 0.105$ at $x/c = 0.672$, (d) $h/c = 0.105$ at $x/c = 1.092$ 134
54 Wing tip vortex at a height of $h/c = 0.263$, at quarter-chord position on flap, low flap angle, a type *a* flow. Vorticity contours showing (a) mean flow results and (b,c,d) three instantaneous snapshots representative of the flow. 135

55 Wing tip vortex at a height of $h/c = 0.211$, at quarter-chord position on flap, low flap angle, a type *a* flow. Vorticity contours showing (a) mean flow results and (b,c,d) three instantaneous snapshots representative of the flow. 136
56 Wing tip vortex at a height of $h/c = 0.158$, at quarter-chord position on flap, low flap angle, a type *b* flow. Vorticity contours showing (a) mean flow results and (b,c,d) three instantaneous snapshots representative of the flow. 137
57 Wing tip vortex at a height of $h/c = 0.105$, at quarter-chord position on flap, low flap angle, a type *b* flow. Vorticity contours showing (a) mean flow results and (b,c,d) three instantaneous snapshots representative of the flow. 138
58 Wing tip vortex at a height of $h/c = 0.263$, at quarter-chord position on flap, high flap angle, a type *a* flow. Vorticity contours showing (a) mean flow results and (b,c,d) three instantaneous snapshots representative of the flow. 139
59 Wing tip vortex at a height of $h/c = 0.211$, at quarter-chord position on flap, high flap angle, a type *b* flow. Vorticity contours showing (a) mean flow results and (b,c,d) three instantaneous snapshots representative of the flow. 140
60 Wing tip vortex at a height of $h/c = 0.158$, at quarter-chord position on flap, high flap angle, a type *b* flow. Vorticity contours showing (a) mean flow results and (b,c,d) three instantaneous snapshots representative of the flow. 141
61 Wing tip vortex at a height of $h/c = 0.105$, at quarter-chord position on flap, high flap angle, a type *b* flow. Vorticity contours showing (a) mean flow results and (b,c,d) three instantaneous snapshots representative of the flow. 142
62 Wing tip vortex at a height of $h/c = 0.263$, at $x/c = 1.092$, high flap angle, a type *a* flow. Vorticity contours showing (a) mean flow results and (b,c,d) three instantaneous snapshots representative of the flow. 143
63 Wing tip vortex at a height of $h/c = 0.211$, at $x/c = 1.092$, high flap angle, a type *b* flow. Vorticity contours showing (a) mean flow results and (b,c,d) three instantaneous snapshots representative of the flow. 144
64 Oil flow visualisation on suction surface showing leading edge lowermost; transition location for low flap angle, (a) $h/c = 0.395$ (b) $h/c = 0.158$. 145
65 Oil flow visualisation on suction surface showing leading edge lowermost; transition location for high flap angle at $h/c = 0.211$, (a) entire wing (b) close up near to wing centre. 146
66 Oil flow visualisation on suction surface showing leading edge lowermost; tip flow for low flap angle, (a) $h/c = 0.395$ (b) $h/c = 0.211$ (c) $h/c = 105$. 147
67 Oil flow visualisation on suction surface showing leading edge lowermost; tip flow for high flap angle, (a) $h/c = 0.211$ (b) $h/c = 0.105$. 148
68 LDA u/U_∞ velocity contours at heights of $h/c = 0.395, 0.211, 0.105$ for low flap angle 149
69 LDA u/U_∞ velocity contours at heights of $h/c = 0.395, 0.211, 0.105$ for high flap angle 150

70 LDA u/U_∞ wake surveys for low flap angle; (a) Streamwise surveys at $h/c = 0.211$. (b) Surveys at $x/c = 1.066$ for different heights. 151
71 LDA u/U_∞ results; (a) Wake surveys at $x/c = 1.066$ for low and high flap angles. (b) Boundary layer surveys at flap trailing edge. 152
72 LDA $u'u'/U_\infty^2$ perturbation velocities; (a) Boundary layer surveys at flap trailing edge. (b) Streamwise surveys at $h/c = 0.211$ for low flap angle. 153

73 Schematic of computational grid including boundary conditions 166
74 Computational mesh; (a) $h/c = 0.179$. (b) Leading edge region. (c) Trailing edge region. (d) $h/c = 0.313$. 167
75 Forces in ground effect; (a) Downforce. (b) Drag. 168
76 Comparison of computational and experimental surface pressures; (a) freestream. (b) $h/c = 0.671$. 169
77 Comparison of computational and experimental surface pressures; (a) $h/c = 0.448$. (b) $h/c = 0.313$. 170
78 Comparison of computational and experimental surface pressures; (a) $h/c = 0.224$. (b) $h/c = 0.179$. 171
79 Comparison of computational and experimental surface pressures; (a) $h/c = 0.134$. (b) $h/c = 0.090$. 172
80 Comparison of computational and experimental boundary layer surveys at suction surface trailing edge; (a) $h/c = 0.224$. (b) $h/c = 0.134$. 173
81 Comparison of computational and experimental wake surveys at $h/c = 0.448$; (a) $x/c = 1.2$. (b) $x/c = 1.5$. 174
82 Comparison of computational and experimental wake surveys at $h/c = 0.224$; (a) $x/c = 1.2$. (b) $x/c = 1.5$. 175
83 Comparison of computational and experimental wake surveys at $h/c = 0.134$; (a) $x/c = 1.2$. (b) $x/c = 1.5$. 176
84 u/U_∞ velocity contours within wake and ground boundary layer; (a) $h/c = 0.448$, S-A. (b) $h/c = 0.224$, S-A. (c) $h/c = 0.134$, S-A. (d) $h/c = 0.134$, $k-\omega$. (e) $h/c = 0.134$ LDA results 177
85 u/U_∞ velocity contours within wake and ground boundary layer; (a) $h/c = 0.448$, S-A. (b) $h/c = 0.224$, S-A. (c) $h/c = 0.134$, S-A. (d) $h/c = 0.134$, $k-\omega$. 178

86 (a) Pressure distributions (b) Integrated pressures and overall forces, in freestream and ground effect, for single element wing, transition free. 185

87 (a) Downforce in ground effect for fixed ground and moving ground, (b) Canonical pressure distributions for fixed ground, for single element wing, transition free, at $\alpha = 1°$. 201

88 Chordwise pressure distributions at wing centre for fixed ground (a) large and moderate heights (b) small heights, for single element wing, transition free, at $\alpha = 1°$. . 202

89 (a) Schematic showing vortex generator (b) Oil flow visualisation on suction surface with leading edge lowermost showing effect of vortex generators. 206

90 (a) Uncertainty, (b) Long term repeatability, for single element wing, transition free, at $\alpha = 1°$. 214

91 (a) Uncertainty and long term repeatability at $h/c = 0.224$, (b) Short term repeatability at $h/c = 1.343$, for single element wing, transition free, at $\alpha = 1°$. 215

92 (a) Comparison of wake profiles at $x/c = 1.5$ extracted from PIV results with LDA survey for single element wing, transition fixed, $h/c = 0.313$ at $\alpha = 1°$. (b) Estimation of 95% confidence level of $u'u'/U_\infty^2$ for single element wing, transition fixed, $h/c = 0.448$ at $x/c = 1.5$. 216

93 Oil flow visualisation on suction surface showing leading edge lowermost; (a) Pressure tapped wing (b) Untapped wing. 218

List of Tables

1 Previous studies of downforce producing wings in ground effect 12

2 Single element wing coordinates at reference incidence of 1°. 25
3 Main element coordinates at reference incidence of $\alpha = 14.1°$. 26
4 Flap coordinates at reference incidence of $\alpha = 14.1°$. 27
5 Location of chordwise tappings of single element wing (S), or main element of double element wing,(D). Quarter-chord suction surface tappings at $\eta = 0.182, 0.909$, pressure surface at $\eta = 0.136, 0.818$ 28
6 Location of spanwise tappings at quarter-chord position, for single element wing and main element of double element wing 29
7 Location of chordwise tappings on flap. The x/c columns represent the location of the tappings for the double element wing, the x/c_f columns are for a flap based coordinate system. Quarter-chord suction surface tappings are at $\eta = 0.182, 0.909$, pressure surface at $\eta = 0.136, 0.818$ 29
8 Location of spanwise tappings at quarter-chord position, flap. 30

9 Boundary layer detachment location at small ground heights. 56
10 Maximum vorticity in wing tip vortex at $x/c = 1.2$. 56

11 Wake information including maximum velocity deficit and 99% wake thickness; clean wing 77

12 Wake information including maximum velocity deficit and 99% wake thickness; 2.90% Gurney flap 93

13 Maximum vorticity in wing tip vortex; double element wing. $\omega_{1/4}$ for results at flap quarter-chord position, i.e. $x/c = 0.672$. $\omega_{t/e}$ behind trailing edge, at $x/c = 1.092$. 154

14 Grid dimensions and total number of cells 179
15 Computational and experimental C_l 179

16 Wake information including minimum velocity and 99% wake thickness for experimental and computational results at $x/c = 1.5$. 180
17 Ground boundary layer information including minimum velocity, edge velocity, and 99% boundary layer thickness for experimental and computational results at $x/c = 1.5$.181

Nomenclature

b = Wing span; 1100mm

c = Wing chord; 223.4mm for single element wing, 380.0mm for double element wing

c_f = Flap chord; 165.7mm

C_D = Drag coefficient, $D/q_\infty c$

C_d = Sectional drag coefficient

C_L = Lift coefficient, $L/q_\infty c$. Positive lift implies a downforce; force directed to ground

C_{Lmax} = Maximum lift coefficient

C_{Lclean} = Lift coefficient for clean wing

C_l = Sectional lift coefficient

C_{lcent} = Sectional lift coefficient at wing centre

C_{ltip} = Sectional lift coefficient near to wing tip

C_P = Pressure coefficient, p/q_∞

$\overline{C_P}$ = Canonical pressure coefficient, $1 - \frac{C_P - 1}{C_{P_{MAX}} - 1}$

C_{Pnorm} = Normalised spanwise pressure coefficient for lower surface pressures, $C_P / \int C_P d\eta$

C_{Pmax} = Pressure coefficient at maximum suction

h = Height above ground; distance between lowest point on suction surface and ground plane at incidence zero

Re = Reynolds number based on wing chord, $\rho U_\infty c/\mu$

s = Distance from start of pressure recovery

$s_{T/E}$ = s at trailing edge

U_∞ = Freestream velocity

u, v, w = Velocity components in x, y, z axes system

$u'u', v'v', w'w'$ = Turbulent stresses in x, y, z axes system

u_{min} = Minimum u velocity component in wake

x, y, z = Cartesian coordinates, x positive downstream, y positive up, z positive to starboard

x_{sep} = Separation point on suction surface

Greek Symbols

α = Incidence

δ = Increase in sectional lift at wing centre from wing tip, C_{lcent}- C_{ltip}

δ_{99} = Wake thickness, as measured by 99% displacement thickness

δ_{bottom} = Bottom of wake thickness

δ_{clean} = Wake thickness for clean wing

δ_{gurney} = Wake thickness for wing with 2.90% Gurney flap

δ_{top} = Top of wake thickness

$\Delta C_L|_{GF}$ = Percentage increase in downforce with Gurney flap over a clean wing

ΔC_{Pte} = Difference in pressure coefficient at trailing edge

μ = Viscosity
ρ = Density
η = Non-dimensionalised span from wing tip, $2z/b$
ω = Planar vorticity; $\frac{\partial v}{\partial z} - \frac{\partial w}{\partial y}$ for tip vortex
Ω = Non-dimensionalised vorticity, $\omega c/U_\infty$
ζ = Distance from surface measured along a line from trailing edge of suction surface perpendicular to surface

Glossary

CFD = Computational fluid dynamics
f/s = Freestream
g/e = Ground effect
GF = Gurney flap
LDA = Laser Doppler anemometry
PIV = Particle image velocimetry
RANS = Reynolds-averaged Navier-Stokes
S-A = Spalart-Allmaras (turbulence model)
ZOC = Zero operate calibrate

Chapter 1

Introduction and Literature Review

This chapter describes the background to the subject and the previous studies performed into wings in ground effect. The intentions of the research programme are described. The relevant literature is reviewed that is applicable to the current research, including aspects related to wings in general with finite trailing edges, multiple elements, and wing tip vortices.

1.1 Introduction to Topic

The use of wings on racing cars was first seen in 1966, on the Chaparral Can-Am car, and then in Formula 1 two years later. The wings were mounted on tall struts, far from interactions with the body of the car and the ground, with one wing at the front, and one at the rear. Safety issues caused the high wings to be banned after a short time, and by 1970, the wings were placed at the rear of the car, behind and above the rear wheels, the rear wing, and in front of the front wheels near to the ground, the front wing. Since then, the basic configuration of the wings has remained the same.

The front wing of a contemporary year 2000 racing car operates in very strong ground effect, at typical heights of 70-100mm from the ground [1], and produces about 25-30% of the total downforce of the car [2]. Putting this into context, at its top speed, the car as a whole can produce about three times the weight of the car in downforce, from the front wing, the rear wing, and the underside (undertray) which feeds the diffuser. In fundamental terms, the downforce, or aerodynamic grip, works in conjunction with the mechanical grip, to improve the acceleration, braking, and cornering speed of the car. However, it is not only the overall level of downforce that is the important factor. As the car accelerates or brakes, the front wing changes height from the ground, due to the suspension movements on the car. This severely affects the level of downforce produced by the

front wing. In terms of drivability, the best performing car is a well-balanced one. If there is too little grip at the front of the car compared to the rear of the car, the car will not turn in to the corner as it understeers. Oversteer occurs if there is too little grip at the rear of the car compared to the front. It is not only important to have a car that handles well for performance reasons, it is also a significant safety issue.

In addition to the aerodynamic performance of the front wing, another significant issue is the wake that it generates. The flow to the undertray and diffuser in particular, but also the radiators and rear wing, is severely affected by the front wing because they all operate in the wake from the wing.

1.2 Motivation for Research

Only a single study [3] has been performed experimentally investigating a wing with the suction surface near to a moving ground. The study only considered a single element wing, and no three-dimensional effects nor off-surface flowfield data are presented.

Because of the severe effect of the ground, fixed ground tests are not believed to be of significantly more use than tests in freestream. It is believed that, because the surface producing the majority of the normal force (i.e. suction surface) is nearest to the ground, fixed ground tests effect the results to a higher degree than aircraft type wing tests, where the pressure surface is nearer to the ground. Ranzenbach and Barlow [4, 5, 6] only performed two-dimensional experimental tests in proximity to a fixed ground, only presenting forces at different heights. Jasinski and Selig [7] also only performed tests using a fixed ground. However, they do present a small selection of surface pressures and flowfield results.

Due to the lack of a suitable experimental database, previous computational studies investigating such wings in ground effect [3, 4, 8, 5, 6] are deemed to be of little value with respect to outright quantitative results of the configuration.

Clearly, there exists a large gap in studies performed on wings in ground effect that are supposed to simulate the flow around a racing car front wing.

1.3 Applicability of Research

Similarities are drawn in this thesis illustrating the comparisons between increasing the incidence of a wing in freestream, and reducing the height of a wing in ground effect, on the performance of a wing including the stall. The experimental data which includes both unsteady and time-averaged results of both the wake flow at the centre of the wing and the tip vortex, for configurations of current interest including a multi-element wing, should be useful to the general aeronautical industry. Complex flow phenomena such as vortex breakdown (of a wing tip vortex) and vortex shedding (behind a Gurney flap and a finite trailing edge) are presented which are contemporary

general aerodynamic problems.

1.4 Literature Review

1.4.1 Relevant Research

Although the current work concerns the ground effect, specifically for a wing with the suction surface nearest to the ground, other factors are relevant. The wing in question features a finite trailing edge, and Gurney flaps are also under investigation. The application of other flow control techniques such as vortex generators are included, in light of early experimental results. Also, the effect of a double element configuration has been studied, in addition to the single element wing. For both wings, three-dimensional effects were examined, and hence they are also described in the literature review.

1.4.2 Experimental Representation of Ground Plane

The effect of ground proximity on aerodynamic devices has been investigated experimentally since the early days of powered flight. Different experimental methods have been used from the beginning, the most basic of which is a fixed ground simulation, whereby the ground plane is represented by a ground that is fixed, for example the wind tunnel floor, or a dedicated ground plate [9, 10, 11, 12]. One disadvantage of this is that a boundary layer inevitably grows along the ground. This can be reduced by using a dedicated ground plane board starting a short distance upstream of the model, for example, suspended in the tunnel. The boundary layer can also be sucked away, through the ground, but this is an expensive mechanism. The major flaw using a fixed ground, however, is that the boundary conditions are physically incorrect, for the real case, this simulation would represent an aircraft flying over a moving ground. Tangential blowing can be used [13] to inject flow close to the ground at the freestream velocity. In practice, this method is not widely used, due to the complexities of the system.

Another popular method is known as the image or reflection method [14, 15, 16, 17]. In this example, two identical wind tunnel models are used, the second inverted and placed at a finite distance below the first. In theory, the flow generated is symmetrical about the imaginary ground plane. This, however, is difficult to implement due to the fact that both models have to be perfectly symmetrical. The problem of vortex interaction between the two models can be eliminated through the use of a splitter plate, separating the two wakes. However, a boundary layer will grow along the splitter plate, similar to the fixed ground method. In addition to this, the reflection method only really represents an inviscid ground effect, as the velocity of the ground plane will be dictated by the velocity of the dividing streamline between the models, not necessarily freestream.

The only physically correct method to model the ground effect is by using a moving belt, travelling at the required velocity, i.e. freestream. The first successful tests using this method were

performed by Klemin in the 1930's [18], although Eiffel had tried it unsuccessfully two decades earlier. Achieving the rotation of the ground belt is difficult in practice, due to vibrations generated by the rollers, and also the lateral motion of the belt. In addition to this, it is required to keep the belt flat, usually performed by sucking the belt from underneath onto a flat surface, and if the ground is mounted in the floor of the tunnel, the wind tunnel wall boundary layer has to be removed before the start of the belt. Studies with moving belts have become more popular over the last 20 years [19, 20, 21, 3], from tests in wind tunnels used predominantly for ground vehicles.

Work by Werlè in the 1960's [22, 23] compares water tunnel results taken for a variety of wing and ground vehicle type models, for the three methods used for representing the ground plane, as described above. Significant differences are found for two-dimensional aeronautical type wings. For the fixed ground case, the flow is shown to separate from the ground aft of the trailing edge, and the region of flow separation at a high angle of attack is different to the moving ground case. For the method of images, the ground plane is seen to move at a different speed to freestream, depending on the angle of attack of the wing. Three-dimensional effects are also considered, and it is shown that behind a delta wing configuration, the vortex interacts with the ground plane for the fixed ground tests, resulting in significantly different flow features when compared to the image method tests.

1.4.3 Lift Producing Wings in Ground Effect

Although the current study concerns a wing with the suction surface near to a ground plane, a short account of a selection of studies performed on wings with the pressure surface near to the ground is given below.

Experimental Studies

Early tests [9] using a fixed ground on an RAF6 aerofoil, were the first to substantiate claims by pilots that in proximity to the ground, a cushioning effect was observed, whereby the lift increases and the drag reduces for a given angle of attack. Other early tests, using a reflection method [24], showed that liftslope increases can also be expected. Pressure distributions show that in proximity to the ground, the pressure surface pressures increase, due to the image beneath the ground plane inducing a lower velocity in that region [16].

Although it is a common result for the lift at a given angle of attack to increase, this does not necessarily correspond to an increase in the maximum lift coefficient, because a reduction in the stalling angle is generally observed. In fact, for a single element wing, some reports show a slight increase in the maximum lift coefficient [14, 15], some a decrease [10], and some little change [25]. For multi-element wings, a reduction in the maximum lift coefficient has generally been found [16, 10]. The results seem to be dependent on the exact wing configuration and the representation of the ground plane, in addition to the aspect ratio of the wing [26].

In addition to the beneficial ground effect for an aircraft type wing, whereby the image aerofoil induces greater pressures on the pressure surface of the real aerofoil, there is also a detrimental effect whereby the diffuser effect may cause a reduction in pressure on the pressure surface, and hence reduce the overall loading [26].

The improvement in the aerodynamic efficiency of wings close to the ground can be seen in the practical application of wing in ground effect aircraft (WIG), such as the Ekranoplan, of which a wide range of literature is available.

Computational Studies

Numerous computational studies have been performed using both inviscid panel type methods, and also RANS solvers more recently. Panel methods simply use the image system to represent the ground plane [27, 28, 29, 30]. The main effect of ground proximity is again showed to be a reduction in the lower surface velocities, giving rise to the increase in lift [27], but the adverse pressure gradient on the suction surface is also seen to increase. Three-dimensional tests by the same author reveal increases in flow three-dimensionality as the ground is approached, in addition to liftslope increases nearer to the ground. Using RANS solvers, two-dimensional tests have been performed [31, 32, 33, 34]. The effect of modelling a ground plane at freestream velocity compared with other boundary conditions (e.g. symmetrical and fixed ground type) is shown to be significant [32, 33] with particular reference to the pressure distributions on the pressure surface, as would be expected.

1.4.4 Downforce Producing Wings in Ground Effect

It is perhaps ironic, that the first comment on the aerodynamics of a wing in ground effect with the suction surface near to the ground was made by Zahm in 1921 [9], in a paper reporting experiments he performed on the ground effect for an aircraft wing:

> A complete set of readings also were taken with the ground plane "above" the aerofoil, that is opposite to the chambered surface. The most striking features of these readings are the great increase of lift with increasing incidences up to 12°, and the considerable increase of drag with proximity of the ground-plane at all the incidences used, i.e., from 0° to 14°. The data were taken rather for completeness than for their practical importance, and hence are not given here.

Until very recently, however, studies of downforce producing wings in ground effect were very limited. Dominy [35] presented a short description of the aerodynamics of such a wing. He described the ground effect as effectively constraining the flow over the suction surface, hence generating an increase in suction. The downforce generated by the wing was reported to vary in relation to the ground height. Dominy postulated that in close proximity to the ground, the wing

would stall due to the boundary layer separating because of the large suction and the associated adverse pressure gradient.

Table 1 lists fundamental research performed on downforce producing wings in ground effect, together with a summary of the work and methods used.

Experimental Studies

The only work published performed in a wind tunnel with a moving ground facility on the subject is published by Knowles *et al* [3]. A single element GA(W)-1 wing was tested at a variety of incidences for a range of heights from out of ground effect down to 0.12c from the ground. Force results show that the downforce generated increases as the ground is approached, for all incidences tested at. The liftslope was also seen to increase in ground effect. Surface pressures for a selection of incidences are presented. It was observed that the lower surface suctions increase in ground effect, and that very close to the ground, stalled flow occurs over the rear portion of the wing.

A series of studies by Ranzenbach and Barlow demonstrate the ground effect for a single element and a double element aerofoil configuration. Their work begins to address the topic, using two-dimensional experimental work in a *fixed ground* wind tunnel on a NACA 0015 [4] and NACA 4412 [5] sections for the single element studies, and a NACA $63_2 - 215$ Mod B section with a 30% slotted flap [6] for the double element studies. The effect of changing the height from the ground was investigated for a single incidence. Although computational studies were performed in greater detail (see below), experimental results only present the overall force generated at different heights from the ground. As in previous research, it was found that the downforce increased as the height from the ground reduced. However, at a ground clearance of about 0.1c, the downforce was found to reach a maximum, below which the downforce dropped sharply. They called this the *force reduction phenomenon*, the cause of which was explained from computations (below).

Jasinski and Selig [7] present an experimental study of a three-dimensional multi-element wing in ground effect, using a *fixed ground* facility. The aerodynamic performance of the wing is presented in terms of liftcurves at a single height of 0.3c from the ground, including the effect of varying the flap deflection angle. In addition to this, flowfield measurements taken 1c downstream of the trailing edge of the wing are presented for two flap deflection angles. Two trailing vortices were observed rolling up from the endplate, the size of which increased for the larger flap deflection.

Computational Studies

Katz's work on computational modelling of entire racing cars using panel methods [36], and RANS solvers [37], and solely front wing aerodynamics with a panel method program [38, 39, 40] introduces the topic. The earliest results [38] used a mirror image technique to model the ground for a thin wing. The downforce was found to increase asymptotically with increasing ground proximity. Katz comments that the large downforce obtained close to the ground would be limited due to viscous effects. The effect of the aspect ratio of the wing is also considered, and, using the lifting line model,

Katz proposes that the ground effect is less severe for lower aspect ratio wings. In later work [39, 40] Katz illustrated the effect of the ground on the pressure distribution around a wing at a clearance of 0.3c between the ground and the suction surface, as significantly increasing the suction surface suctions, when compared with the wing in freestream. More recently [37] results are presented from a RANS analysis of the entire car. At a single height, chordwise pressure distributions are presented near to the centre and near to the tip of the front wing. Flow separation was observed near to the trailing edge of the flap. It can be seen that the the loading on the flap is lower nearer to the tip of the wing compared to the wing centre.

In addition to their experimental results, Knowles *et al* [3] present a selection of two-dimensional panel method results for comparison. Results compare reasonably at large heights or low incidences, but are poor closer to the ground.

Ranzenbach and Barlow have performed the only dedicated simulations of a two-dimensional wing in ground effect using a RANS solver, for a single element NACA 0015 [4] and NACA 4412 wings [8, 5], and a double element NACA $63_2 - 215$ Mod B section with a 30% slotted flap [6]. Single element computations compare well with the experimental study [4, 5] in terms of downforce produced with the fixed ground conditions. The force reduction phenomenon is modelled reasonably well in the computational results close to the ground. Using vorticity plots, it is put forward that the force reduction phenomenon is due to a merging of the wing and ground boundary layers. The boundary layers are shown to merge upstream of the trailing edge of the aerofoil for a small ground height, below the force reduction phenomenon. The presence of the boundary layers reduces the flow velocity between the suction surface and the ground, leading to an increase in pressure, and hence a reduction in downforce. Extending the study to the correct ground conditions with a moving ground yields the result that the downforce produced at different ground heights is qualitatively similar to the fixed ground case, although the magnitude of the downforce and also the height at which the force reduction phenomenon occurs is greater for the moving ground case. For the double element study, similar results are presented [6]. The authors again state that the wing and ground boundary layers merge, the cause of the force reduction phenomenon. Although this cannot be seen in the computational vorticity plots, the authors comment that the process of the merging of the boundary layers occurs downstream of the aerofoil.

1.4.5 Finite Trailing Edge Wings

Although the use of wings with a finite trailing edge, including the divergent trailing edge (DTE), was originally intended for transonic cruise aircraft, the effect of a finite trailing edge has been investigated at low speeds [41, 42, 43]. Experiments by Allison [44] found the trailing edge to improve the aerodynamic performance at these conditions. Using the LDA technique, Pailhas *et al* [41] have investigated a thick trailing edge aerofoil and found the mean flowfield to be characterized by two counter rotating vortices downstream of the trailing edge. In a similar study, Koss *et al* [45] found high levels of fluctuating $u'u'$ velocity, in two distinct peaks, in the near-field

wake region, from their experiments.

1.4.6 Gurney Flaps

The Gurney flap was first used by the American racing car driver, Dan Gurney. It is a simple device, consisting of a short strip, fitted perpendicular to the pressure surface along the trailing edge of a wing. With a typical size of $1 - 5\%$ of airfoil chord, it can exert a significant effect on the lift or downforce of a wing, with a small change in the stalling incidence, leading to a higher maximum lift coefficient, as described by Liebeck [46]. Gurney flaps are commonly used on racing car wings due to their ease of application.

There has been a substantial body of research on Gurney flaps over the past twenty years. Many studies are concerned with aeronautical applications. The effects of Gurney flaps on aerodynamic forces and pressures were reviewed and studied in model tests by, among others, Liebeck [46], Giguère *et al* [47], and Myose *et al* [48]. On the lift enhancement mechanism, there exists a variety of explanations. Liebeck was the first to propose a short region of separated flow directly upstream of the Gurney flap, with two counter-rotating vortices downstream, which he described as having a *turning effect* on the local flowfield. He was referring to a mean flowfield.

Recently, Jeffrey [49] and Jeffrey *et al* [50] conducted a Laser Doppler Anemometry (LDA) study of flow around wings fitted with Gurney flaps of various sizes. It was found that the time-averaged flow downstream of a Gurney flap consists of two counter-rotating vortices. Smoke-flow visualisation showed the instantaneous flow structure to consist of a wake of alternately shedding vortices. The presence of regular vortex shedding was substantiated through post-processing of LDA results. The vortex shedding sustains an increase in the base suction, which is nearly constant across the downstream face of the Gurney flap, and is loosely related to the formation length of the recirculation region. The upstream face decelerates the flow, in a manner similar to a flat plate immersed in a turbulent boundary layer. The Gurney flap therefore introduces a pressure difference at the trailing edge, leading to an increase in the total circulation. The flowfield behind the Gurney is similar to that behind a blunt trailing edge.

Although the recent studies of Jeffrey present an explanation of the instantaneous in addition to the mean flowfield, and the resulting aerodynamic performance of the Gurney, there is a lack of studies of Gurney flap aerodynamics in ground effect, with the only exception of Katz and his co-workers (e.g. Katz and Langman [51]), where only very basic surface pressures are presented.

1.4.7 Multi-element Flows

The study of multi-element flows is an area that has challenged researchers for a long time. Fundamental studies on multi-element aerofoils e.g. [52, 53, 54, 55] have been used as an experimental basis, detailing the flow physics for two-dimensional computational studies, e.g. [56, 57, 58, 59] using RANS solvers.

In his review paper, Smith [60] described the five beneficial effects of the gaps between the elements in multi-element flows:

- Slat effect. The circulation on a forward element induces a flow in an opposite direction to the natural circulation near to the leading edge of a downstream element. This reduces the leading edge pressure peak on the downstream element, resulting in lower pressure recovery demands and a delayed separation.

- Circulation effect. The flap causes a circulation effect on the upstream element, effectively inducing a considerably greater circulation on the upstream element.

- Dumping effect. The trailing edge of the upstream element is in a high velocity region. The boundary layer leaves, or is *dumped* from the upstream element at a higher velocity than freestream. The pressure recovery demand of the forward element is therefore reduced.

- Off-the-surface pressure recovery. The boundary layer dumped from the upstream element decelerates to freestream velocity in the wake out of contact with a wall. This is more efficient than deceleration in contact with a wall.

- Fresh-boundary-layer effect. The leading edge of each element starts off with a fresh, thin, boundary layer that is less likely to separate than a thick one.

The process of geometry optimisation whereby the location of the individual elements with respect to each other is optimized for the aerodynamic performance can be seen in many publications, for example experimentally [61, 62, 63], and more recently computationally [59, 63]. Boundary layer merging has been investigated in detail [64, 65, 66]. For an optimized aerofoil, some researchers have found the slat boundary layer to merge along the main element [67], whereas Smith [60] theorized that the phenomenon occurs at the trailing edge of the downstream element.

1.4.8 Three-dimensional Vortical Flows

Numerous studies of the trailing tip vortex from a wing have been performed, both using experimental methods [68, 69, 70, 71] and computational RANS studies [72, 73] examining the rollup in the near-field region, and the behaviour in the far-field region. Briefly, the vortex rollup for a blunt wing tip as described by Khorrami [72] involves a separated shear layer from the tip at the pressure surface which is a constant source of vorticity. Within the vortex, the centrifugal force generates a strong radial pressure gradient, with the core having the minimum pressure. This causes the shear layer to get wrapped around the vortex, resulting in a stronger vorticity. The vortex core has a high axial speed, and in Khorrami's results was found to have a speed up to twice freestream. Ramaprian *et al* [71] found that the rollup was nearly completed and the vortex was axisymmetric within a distance of about two chords from the trailing edge.

At a high angle of attack, the aerodynamics of vortices over a delta wing breaking down appears in a wide range of documentation, and is discussed by Payne *et al* [74] and Delery [75]. In basic terms, the adverse pressure gradient induces a rapid deceleration in the axial speed of the vortex. The location of the breakdown moves upstream along the wing for increasing angle of attack. Vortex breakdown is also commonly observed in rectangular wings [72, 75].

In addition to breaking down, vortex unsteadiness resulting in vortex wandering is a phenomenon observed in much work [68, 69, 70, 76]. Although earlier studies [68, 70] cite the freestream turbulence as the reason for the vortex wandering, Gursul [76] proposed that vortex wandering is due to Kelvin-Helmholtz instabilities in the shear layer being ingested into the vortex, for example higher levels of turbulence in the shear layer compared to freestream, or separated flow. Green and Acosta [69] observed more severe fluctuations for the higher angle of attack case.

The motion of a trailing vortex near to the ground has been investigated by Harvey and Perry [77] using experiments in a moving ground wind tunnel. For a lift-producing wing, the vortex moves closer to the ground as it travels downstream. It was observed that after the descent, the vortex then rises away from the ground. The vortex was seen to induce a cross flow on the floor, with the suction peak below the vortex. This results in a cross flow boundary layer under an adverse pressure gradient. For the vortex sufficiently close to the ground, a bubble of separated flow occurs, with a vorticity opposite to the main vortex. This forms a secondary vortex that leaves the ground, interacts with the main vortex, and causes it to rise away from the ground.

No studies have been found commenting on the interaction of a vortex from an upstream element on the downstream element of a wing, an area relevant to the current research. Storms *et al* [78] were the first to perform an experimental study into the flowfield about a part span flap. In essence, the wing, with a half-span Fowler flap, was tested as a two-dimensional aerofoil, i.e. with tip losses only from the inboard edge of the flap. Chordwise pressures near to the (inboard) tip show a small reduction in pressure, and a more significant increase in suction over the rear portion of the flap, when compared to results far from the tip. The suction peak, over the fore portion of the flap, however reduces. The effect of the (flap) tip vortex rolling up on the flap tip is to induce a higher velocity region. Sectional lift coefficients show that overall, there is a loss in lift on the flap as the tip is approached. More recent studies over similar part span flap configurations [79, 80, 81, 72] all show the *saddle* type pressure distributions near to the flap tip, some acknowledging that this is due to the direct influence of the tip vortex.

1.5 Aims of Research Programme

The aims of the research programme are to:

- Quantify the aerodynamic performance of generic wings in ground effect.
- Identify the flowfield physics pertaining to the wings, including the wake.

- Investigate the effect of Gurney flaps on a wing in ground effect.
- Examine the application of a computational technique to model the ground effect.

1.6 Summary

It has been shown that large gaps exist in the current understanding of the flow relating to a racing car wing in ground effect. Although previous research into wings in ground effect has been performed, the overall study needs to consider all of the different aspects described above.

Reference	Expt.	Computation	No. elements	2D/3D	Ground	Result types
Knowles *et al* [3]	✓	panel method	single	2D	moving	forces, surface pressures
Ranzenbach and Barlow [4]	✓		single	2D	fixed	forces, some surface pressures
" (computation)		RANS	single	2D	fixed, moving	forces, some surface pressures
Ranzenbach and Barlow [8]		RANS	single	2D	fixed, moving	forces, some surface pressures
Ranzenbach and Barlow [5]	✓		single	2D	fixed	forces, some surface pressures
" (computation)		RANS	single	2D	fixed, moving	forces, some surface pressures
Ranzenbach *et al* [6]	✓		double	2D	fixed	forces, some surface pressures
" (computation)		RANS	double	2D	fixed, moving	forces, some surface pressures
Jasinski and Selig [7]	✓		double	3D	fixed	forces, surf. pressures, hotwire
Katz [38, 36]		panel method	single	2D	moving	forces, surface pressures
Katz [39, 40]		panel method	double	2D	moving	forces, surface pressures
Katz *et al* [37]		RANS	double	3D	moving	surface pressures

Table 1: Previous studies of downforce producing wings in ground effect

Chapter 2

Research Programme

This chapter outlines the methods and procedures used in the research. The test models, their installation in the wind tunnels, and the equipment used for model testing is described in detail.

2.1 Methodology

In order to investigate the flow around a modern Formula 1 car front wing, it was decided to perform initial tests on a generic single element wing, with a cambered profile. Having isolated the effect of running close to the ground for a single element wing, tests were performed on a generic double element wing. The double element wing uses the single element wing as the main element in addition to a large flap, and is more representative of a modern Formula 1 car front wing.

The forces and surface pressures acting on the wing have been measured for the single and double element models at a wide range of ground heights. For the single element wing, tests were performed for several incidences at each height. The effect of changing the flap deflection angle was investigated for the double element wing at the different heights. The effect of ground height for the wings at a single reference incidence was examined, using on-surface oil flow visualisation. Off-surface results were also taken over a chordwise slice at the semispan of the wing with a three-component Laser Doppler Anemometry system (LDA) to extract mean flow and turbulence data, and a two-component Particle Image Velocimetry system (PIV) to compare the mean flow results and to examine the instantaneous flowfield. In addition to this, the PIV system was used to investigate the tip vortex from the wings, using cross flow surveys. On the single element wing, tests were also performed with Gurney flaps, and with fixed transition, in addition to free transition. Double element tests were only performed transition free. Short investigations for which only a limited amount of data was taken were also performed for a single element wing in proximity of a fixed ground, and for the application of vortex generators on the single element wing, both detailed in the appendices.

Computations have been performed using a RANS solver on a single element aerofoil at various ground heights, with turbulence modelled using both the Menter $k-\omega$ and Spalart-Allmaras one equation turbulence models [82]. The numerical model has been validated using the experimental surface pressure and off-surface flow visualisations performed at the wing centre.

Using the experimental database, a detailed analysis has been performed, and the flow physics is described for the performance of the wings in ground effect.

2.2 Wind Tunnel Models

The use of wing profiles designed for aeronautical flow regimes has previously proved problematic when applied to racing car front wings. Modern F1 racing cars use wings that have been designed for their specific application. Since the intention of the research is to investigate the flow around the front wing of a racing car using a generic wing, it was decided that the wing profiles developed by the industrial partners should be used for the research, to avoid encountering problems identified when using aeronautical wings.

2.2.1 Single Element Wing

The single element model was designed as a direct scale model of the main element of the 1998 Tyrrell 026 F1 car front wing. A span of 1100mm was used, which corresponds to less than 75% of the width of the moving belt in the smaller wind tunnel, to minimize effects at the edge of the belt [83]. In order to maintain a similar three-dimensionality for the flow, the wing was designed with the same aspect ratio as the wing on the car. This gives a wing chord of 223.4mm for the aspect ratio of 4.92, a scale of exactly 80% of the racing car main element. The chord of the wing is constant across the entire span. The wing features a finite trailing edge, of thickness 1.65mm, corresponding to 0.007c, due to manufacturing reasons. Generic endplates were used throughout testing, the geometry of which were chosen to allow the wing to be tested at very low ground heights, of dimensions 250×100×4mm. The configuration can be seen in Figure 1a. The wing coordinates are listed in Table 2.

The wing profile has been developed from a NASA GA(W) profile, type LS(1)-0413 MOD, as can be seen in Figure 1b. Modifications have been applied to both surfaces [84]. The camber of the suction surface is reduced, and the lowest point on the suction surface is moved forwards. This has the effect of reducing pressure recovery demands. The pressure surface is flattened, increasing the pressure, and a modification is made to the leading edge.

2.2.2 Double Element Wing

As described above, the single element wing was used as the main element for the double element wing. The flap on the racing car wing is designed for high lift applications, and features a thin

profile over the aft portion of the wing. The flap on the car does not have a constant chord over the whole span of the wing; near to the wing tip the thin portion of the profile is extended, and the chord is greater compared to the profile over the central portion of the wing. To isolate the ground effect for a wing of constant profile, the flap profile chosen was that at the centre of the racing car wing, scaled to 80% of full size, and used for the whole span of the wing. The chord of the flap is 165.7mm, the aft 35mm approximately of which is the thin region; 1mm thick. With the flap gap and overlap optimized for the datum flap angle, the chord from the leading edge of the main element to the trailing edge of the flap is 378.9mm. For the lower flap angle, the chord is 381.5mm. For simplicity, a chord of 380.0mm was used for the non-dimensionalisation of all double element results. The combined chord corresponds to an aspect ratio of 2.89. The wing profile for the datum and the low flap deflection can be seen in Figure 1d. The endplates used were based on the endplates used on the racing car wing, and are rectangular with dimensions 400×170×4mm, Figure 1c. The main element and flap coordinates are listed in Tables 3 and 4.

2.2.3 Construction

The models were manufactured using Carbon Fibre Composites (CFC), by the industrial partner, using the same methods as for their real car wings. A resin male is made for each surface, from which a CFC mold is made, enabling duplicate items to be made for each surface, for the tapped and untapped models. Each surface is laid up using bonded sheets of CFC, together with a stiffening Aluminium honeycomb core. Pressure tubing is added where appropriate, and the lower and upper surfaces are then bonded together. The surface of the model is smooth, equivalent in quality to a polished wooden model.

2.2.4 Gurney Flaps

Gurney flaps were tested on the single element wing, using pre-formed brass angle section. Two sizes were used, 3mm and 6mm. Having set the incidence of the wing, aluminium foil, then glue, was applied to the pressure surface at the trailing edge, to attach the Gurney. The Gurneys were applied normal to the local curvature of the surface, with the aft face at the trailing edge. Including the thickness of the tape and glue, the Gurney heights correspond to 1.5% and 3.0% chord.

2.3 Pressure Tappings

Two models for each element have been manufactured; a clean wing used for forces, oil flow visualisation, PIV and LDA, and identical models, with the addition of pressure tappings for surface pressure results. The tappings are made using hypodermic tubing of 0.85mm internal diameter mounted flush to the surface, approximately 20mm long internal to the wing. To the hypodermic tubing is connected a flexible PVC tube, the other end of which is attached to the

pressure transducer. To avoid passing the tubes from the wing to a transducer outside the tunnel and unnecessarily disturbing the flow, the wing was designed with a hollow on the right hand side, to accommodate the small ZOC pressure transducer. The transducer can then be connected to the desired PVC tubes that connect to the hypodermic tube, with all tubes fully contained within the wing. For the double element wing, the endplate on the opposite side of the wing to the pressure tappings features cut-outs at the main element and flap tip. The PVC tubes from the tappings in the flap are passed out of the flap tip, and into the main element at the tip, and are then connected to the transducer. This arrangement causes minimal disturbance to the flow region of interest.

The single element wing contains 125 tappings in total, the exact locations of which are given in Tables 5 and 6. The tappings are arranged into two chordwise groups, and one spanwise group. The chordwise groups are located near to the semispan and near to the tip. For ease of manufacture, and to accommodate more tappings, each group of chordwise tappings is orientated at 22.5° to the streamwise direction, with the pressure surface tappings slightly outboard of the suction surface tappings. Each chordwise group comprises 25 tappings on the suction surface and 23 on the pressure surface. There are 27 additional spanwise tappings at the quarter-chord position, 14 on the suction surface and 13 on the pressure surface.

A similar configuration was used for the 77 pressure tappings on the flap. The chordwise group at both the centre and the tip contains 13 tappings on the suction surface and 12 tappings on the pressure surface. It was not possible to tap the thin portion near to the trailing edge of the flap. At the quarter-chord position for the flap only, 27 additional spanwise tappings were installed.

The pressure transducer can acquire results from up to 64 tappings at once. Hence, for a full set of readings on the single element wing, two runs were performed. For the double element wing, four runs were required. During testing, it was found that it was necessary to block the internal end of any tubes not connected to the pressure transducer, from runs investigating the repeatability with different tubes disconnected from the transducer.

2.4 Model Installation in Wind Tunnel

The installation of the wings in the wind tunnels can be seen in Figure 2. Two large telescopic struts support the wing at the front from the overhead balance, at 350mm from the centreline. The struts attach to brackets internal to the wing at the quarter chord position, about which the wing is pivoted. At the rear, a third strut is used, of variable length, to alter the incidence of the wing, the pitch strut. The main struts are located above the mid-length position of the rolling road, equidistant from the centreline of the tunnel. The struts are slotted where they connect to bracketry attaching to the overhead balance. Testing at different heights is performed by moving the main struts up or down.

Most testing of wings using this tricycle arrangement use a horizontal arm attaching the wing to the rear pitch strut. However, this would disturb the wake flow at the wing trailing edge for

LDA surveys, and would also constrain the incidence range in close proximity to the ground. Using a previously tested method [49], angled trailing arms extend from the pressure surface of the wing, behind the main struts, upward and rearward, to a horizontal circular bar. The pitch strut is attached to the circular bar.

Double element testing is performed by changing the endplates and adding the flap and associated brackets. The same trailing arms and circular bar are used. Brackets, extending from the pressure surface of the flap, located at the centreline and 350mm either side of the centreline are used to hold the flap rigidly in place at the required gap, overlap, and deflection. Locating holes in the endplates also secure the flap to the main element at the tips. Different brackets and endplates were used for the geometry optimisation.

2.5 Wind Tunnel Setup

The models were designed for testing in the University of Southampton low speed 3.5m×2.5m R.J.Mitchell tunnel for the LDA surveys and the smaller 2.1m×1.7m wind tunnel for the other results. Both of the tunnels are of a conventional closed jet, closed circuit design. At 30m/s, the streamwise component of turbulence intensity is 0.2% in the 2.1m×1.7m tunnel.

For correct modelling of the ground plane, the tunnels are equipped with a large, moving belt rig, as can be seen in Figure 3, for the 2.1m×1.7m wind tunnel. The driven roller is at the rear end of the belt, powered by a hydraulic motor. The belt is kept taught by applying weights to a tension roller. A tracking roller is located near to the rear of the rig, the vertical location of which is controlled throughout the run to ensure that the belt remains at the centre of the main rollers. The large suctions generated between the model and the ground have a tendency to lift the belt from the large flat platen over which the belt travels. Using holes in the platen, suction is applied to the belt to keep it flat over the platen. Nine suction chambers are used to distribute the suction applied to the model, arranged in a three by three layout. The six side chambers are connected to three suction pumps which supply S1, S2, and S3 suctions. Three more pumps are used for the three central chambers C1, C2, and C3. The belt suction is monitored constantly throughout the run. Cooling water is passed through the platen to counter the large amount of heat generated due to the friction between the belt and the platen. A system is located upstream of the belt for removal of the boundary layer that grows along the floor of the wind tunnel. The boundary layer is scooped away using a large slot through which suction is applied, together with a small perforated plate. With the boundary layer suction applied, the velocity is within ±0.2% of the freestream value from 2mm from the ground [85]. The belt and boundary layer suction can also be seen in Figure 2b. The large tunnel has a similar layout for the rolling road, approximate dimensions of the moving belt are 1.9m×4.2m. The belts for both the tunnels are manufactured by Amarral, and have a smooth surface finish. These products are used by other wind tunnels in research and industry, for moving ground applications.

2.6 Reynolds Numbers

The speed of the wind tunnel is limited by the rolling road at 40m/s. However, at this top speed, it was not possible to apply enough belt suction to keep the belt flat over the platen. Acceptable results were found at 30m/s, and this was used for all tests.

All force, surface pressure and oil flow visualisation tests were performed at a constant dynamic pressure. The LDA and PIV tests were performed at constant speed. At the constant dynamic pressure of 56.25mm water, corresponding to $U_\infty \approx 30m/s$, the Reynolds number based on the wing chord for the single element wing falls in the range of $0.430 - 0.462 \times 10^6$ due to variations in the wind tunnel temperature and the ambient pressure. The double element tests were performed at Reynolds numbers in the range $0.735 - 0.765 \times 10^6$ based on the total chord.

The wind tunnel model corresponds to 80% of the scale of the wing on the car. Current wind tunnel testing of entire racing cars is performed using models not greater than 50% scale, at speeds of not more than 40m/s. The reference speed and model size correspond to Reynolds numbers in the range approximately 20% to 50% higher than current racing car model testing.

2.7 Wing Height and Incidence Variation

The wing was tested at several ground heights, from freestream to less than 0.05c above the ground. The height was defined by the distance from the ground to the lowest point on the wing, with the wing incidence set to zero degrees. Aluminium spacers and shims were used to set the height between runs. The length of the telescopic struts were altered such that the required height of shims could be slid gently between the suction surface and the ground at each wing tip. Freestream tests were performed at a height of 750mm, i.e. at a height very close to the centre of the 2.1m×1.7m tunnel. This corresponds to a non-dimensionalized height of 3.36c for the single element wing, and 1.97c for the double element wing.

Having set the height, the incidence of the wing was then varied using a rotation about the quarter chord position. For the single element wing, forces and surface pressures were taken for a range of incidences. Flow visualisations were performed at a single reference incidence. All quoted incidences are measured relative to a line at 2.45° to the chordline. The incidence was measured by placing the inclinometer on a bed resting on the pressure surface of the wing, on a line from the trailing edge to the second most proud part of the pressure surface, resulting in a true incidence which is equal to the quoted incidence plus 2.45°. The reference incidence of 1° at which most tests were performed is the incidence corresponding to endplates parallel to the ground, with the wing in its datum position as on the car, i.e. a true incidence of 3.45°. For the double element wing, the same inclinometer bed was used, on the pressure surface of the main element. The reference incidence of 1° was used for all tests again, with the endplates parallel to the ground. The true incidence for the double element wing at the datum flap deflection is 14.1°.

2.8 Laser Doppler Anemometry Technique

Laser Doppler anemometry (LDA) enables measurement of flow velocities and turbulence statistics at a single location, using a seeded flow. A 5W Ar-ion laser is used, in conjunction with a Bragg cell and a colour splitter. The purpose of the Bragg cell is to divide the laser beam into two parts, and to introduce a fixed frequency difference to one of the beams, creating a shifted and an unshifted beam. A colour splitter is then used to create three pairs of beams, which are used to measure velocity components in the three directions. The pairs of beams are of different wavelengths; blue, green, and violet in colour. These are focussed into optical fibres, bringing them to a probe containing the transmitting and receiving optics.

Two probes are used in the system for the transmitting optics. The first probe emits the blue and the green beams. A second probe is used to emit the violet beams. Each probe contains a lense, which is used to focus the individual beams to a single point; the measurement volume. This is an ellipsoid, of approximate width on the minor axis of 0.3mm, and contains a gaussian intensity distribution. The second probe is aligned such that all six beams converge to the measurement volume.

Within the measurement volume, the fringes from the individual beams combine to form an overall interference pattern of parallel bright and dark planes. The distance between the fringes is a function of the wavelength. A seeding particle which is within the measurement volume scatters light back to a photodetector, in a manner described below. When the seeding particle moves through the measurement volume, this causes changes in the optical path lengths of the beams, causing a pulsating light intensity at the photodetector.

In addition to containing transmitting optics, each probe also contains receiving optics, which consists of lenses used to focus the light to a photomultiplier with an interference filter, via optical fibres. The two component probes were used in a backscatter configuration, whereby the probe used to transmit the blue and the green beams is used to receive the light which has been scattered back from the violet beams. Similarly, the light from the blue and the green beams scattered by the particle is received by the probe used to transmit the violet beams.

The light patterns are processed into signals by the photomultiplier at the Doppler frequency, with one photomultiplier system for each beam. Then, three spectrum analysers are used to filter and amplify the signal. The frequency data is extracted using a fast Fourier transform algorithm. Using the frequency, and the distance between the fringes, which is known, each component of the velocity can be calculated.

2.9 Particle Image Velocimetry Technique

Particle image velocimetry (PIV) is a non-intrusive method of flow visualisation, where instantaneous images are taken of a seeded flow, which is illuminated by laser. The system used is

two-dimensional.

Seeding was introduced to the flowfield by the use of a Smoke Processor SP2, located downstream of the working section. A water based smoke fluid was used (DJ fluid, type DJ mix, manufactured by Jem, Martin Professional). The typical particle size produced is approximately 1 micron. During testing, it was observed that the quality of the results was highly dependent on the seeding quality, and the data were adversely affected if either too little or too much seeding was present. The seeding input was controlled manually throughout the run, the density constantly monitored to retain the optimum level.

A laser source is used to illuminate a sheet over which results are acquired. It is common to acquire PIV results for a streamwise region of interest, and many studies of wing configurations have been performed in this way. In the current study, this configuration was used to obtain results in the wake region. A few studies have also used PIV to obtain cross flow results, for example [86]. This type of configuration was also used, in order to map the wing tip vortex. The laser system specification is a Gemini PIV 15 laser, using Tempest Nd:YAG lasers, producing 120mJ at 532nm. The laser was located outside the wind tunnel for the vortex investigations, and downstream of the moving ground for the streamwise investigations.

A Dantec HiSense camera (type 13 gain 4) was mounted perpendicular to the light sheet, and is used to record the results. The camera has a resolution of 1280 $\times$ 1024 pixels, and a Nikkor 24mm f/2.8D lens was used. For streamwise measurements, the camera was mounted outside the wind tunnel, and a small cut made in the tunnel wall, with the camera approximately 1.5m from the light sheet. The streamwise extent over which the flow was mapped is approximately 220mm. For the vortex flow investigations, the camera was mounted behind the rear of the moving belt, about 2m from the light sheet. A spanwise region of about 300mm was modelled.

Having located the camera and the laser, it is necessary to focus the camera onto the light sheet. During testing, this was found to be critical in order to achieve good results. With the camera very slightly off focus, the quality of the results deteriorated rapidly. Frequently, it was not possible to tell whether the camera focus was perfect until data had been taken.

To capture a single instantaneous image of the flow, the laser is operated to give two pulses, a short time interval apart, which is user defined. The time interval required depends on the flow characteristics, e.g. flow velocity within and through the light sheet, and the post-processing methods applied. Typically, time intervals of 10-40 microseconds were used, to obtain the optimum results. The rate at which instantaneous sample pairs were taken was varied from 1-2Hz. For each run, 50 datasets were taken, over which time it was possible to monitor the seeding quality. For later studies, more than one run was performed, and 100-200 datasets were taken.

Having acquired the raw images, each pair of images is processed to give flowfield data. The camera image is divided into interrogation regions. The displacement of groups of particles in each interrogation region is measured using a correlation technique, for the two images in each pair. Because there is travel of the interrogation area from the first image to the second, an overlap

related to this must be specified. This is known as the cross-correlation, and generates velocity vectors for each dataset. The number of vectors generated is a function of the interrogation area used, and the degree of overlap, which is dependent on the quality of the results. Typically, an interrogation area of 32 × 32 pixels was used, with a 50% overlap. This produces 77 × 61 vectors. The cross-correlation was performed in conjunction with a FlowMap 1100 Processor. The FlowManager software program was used [87].

Inevitably, not all vectors that are generated are true to the flow. These outliers will generally have velocities significantly larger than the others, and may account for approximately 1% of all vectors. These were eliminated through a range validation, whereby vectors with velocities that exceeded carefully chosen values in each direction were removed. The normal procedure is then to have two more levels of post-processing; a moving average and a filter. These were not used, as they were found to blur the results too much in regions of high velocity gradients. The mean flow results are obtained by taking a statistical average of the instantaneous results. The effect of the processing level on the results is discussed in the appendix.

When performing the tests, attempts were made to eliminate all residual light from the wind tunnel. This was not always possible, and small amounts of light contaminated the tunnel, for example from the suction box area. Residual light has the effect of making the second image in the pair significantly brighter than the first, and reducing the general quality of the results. Another problem encountered whilst testing is that of reflections occurring. Because of the nature of the reflection being a light region, or conversely a dark region for a shadow, this will yield an incorrect cross-correlation. As an example, when studying the tip vortex, reflections were sometimes observed between the endplate and the ground, originating from the lower edge of the endplate. Reflections were also seen on the moving belt. Often, the reflections were due to the wind tunnel walls, or wing support structure. It was inevitable that some reflections remained, however.

2.10 Summary

Wind tunnel tests have been used to quantify the effect of the ground for an isolated single element wing. The generic double element tests are used to further the study for a configuration that is more similar to a racing car front wing. The single element tests are performed at a wide range of heights and incidences for the aerodynamic performance, and at a single incidence for the flowfield investigations. Double element testing is at a single incidence, but for more than one flap angle at a range of heights.

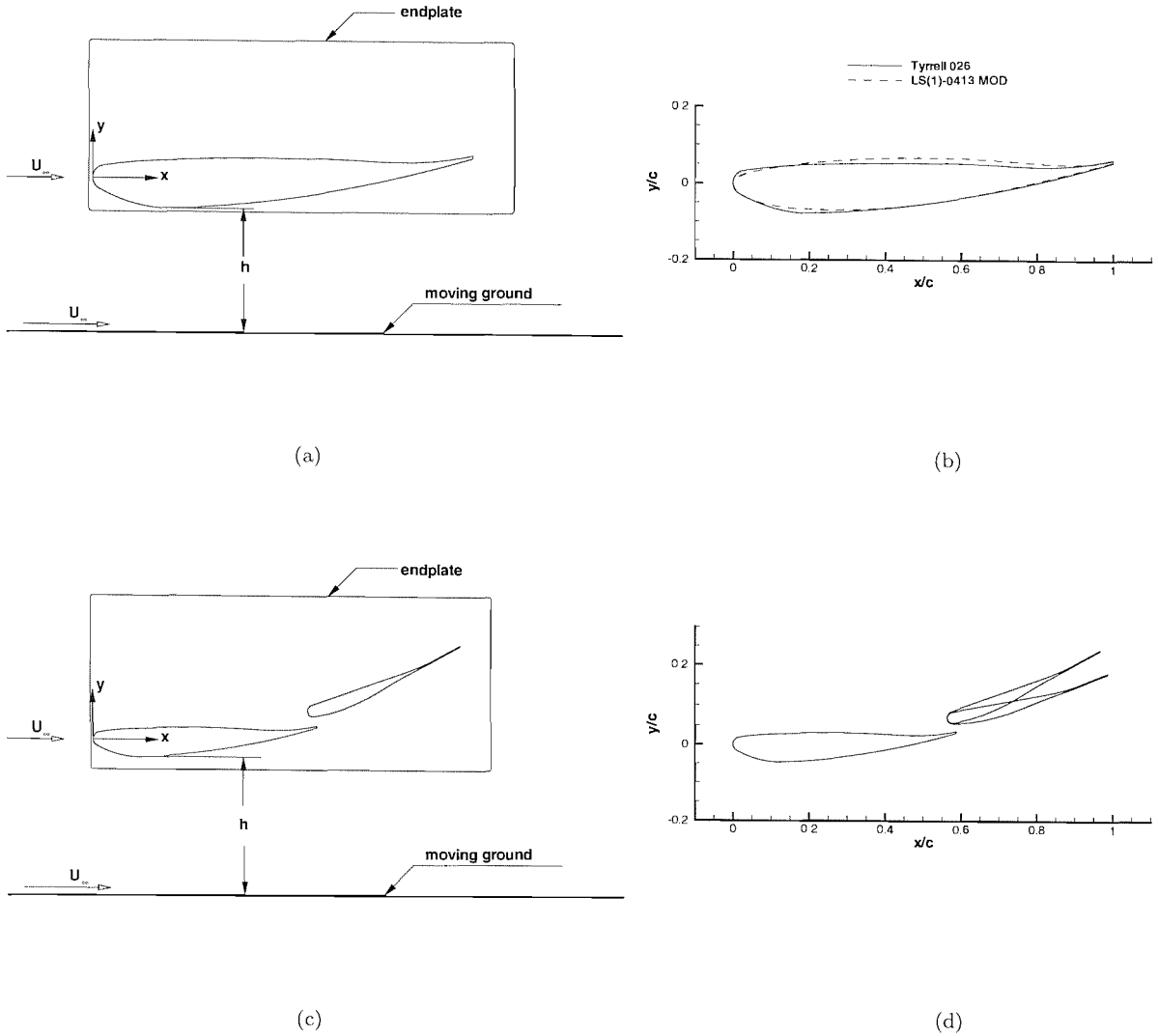

Figure 1: (a) Single element wing with endplate. (b) Single element wing profiles; Tyrrell 026 wing and derived NASA GA(W)-2 LS(1)-0413 MOD profiles. (c) Double element wing with endplate. (d) Double element wing profile with datum and low flap angle.

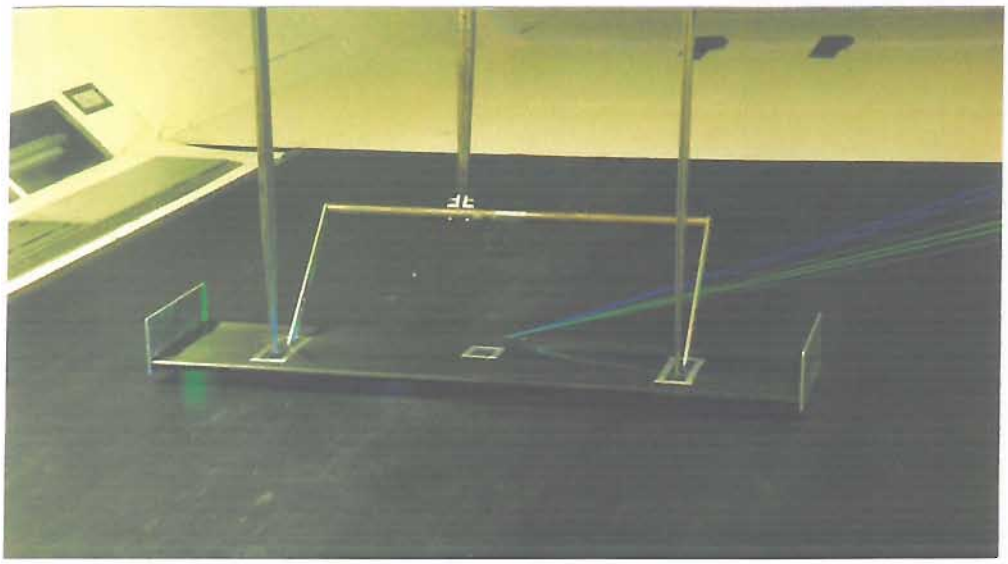

(a)

(b)

Figure 2: Model installation in wind tunnel. (a) Close up of single element wing in 3.5m×2.5m wind tunnel (b) Double element wing in 2.1m×1.7m wind tunnel.

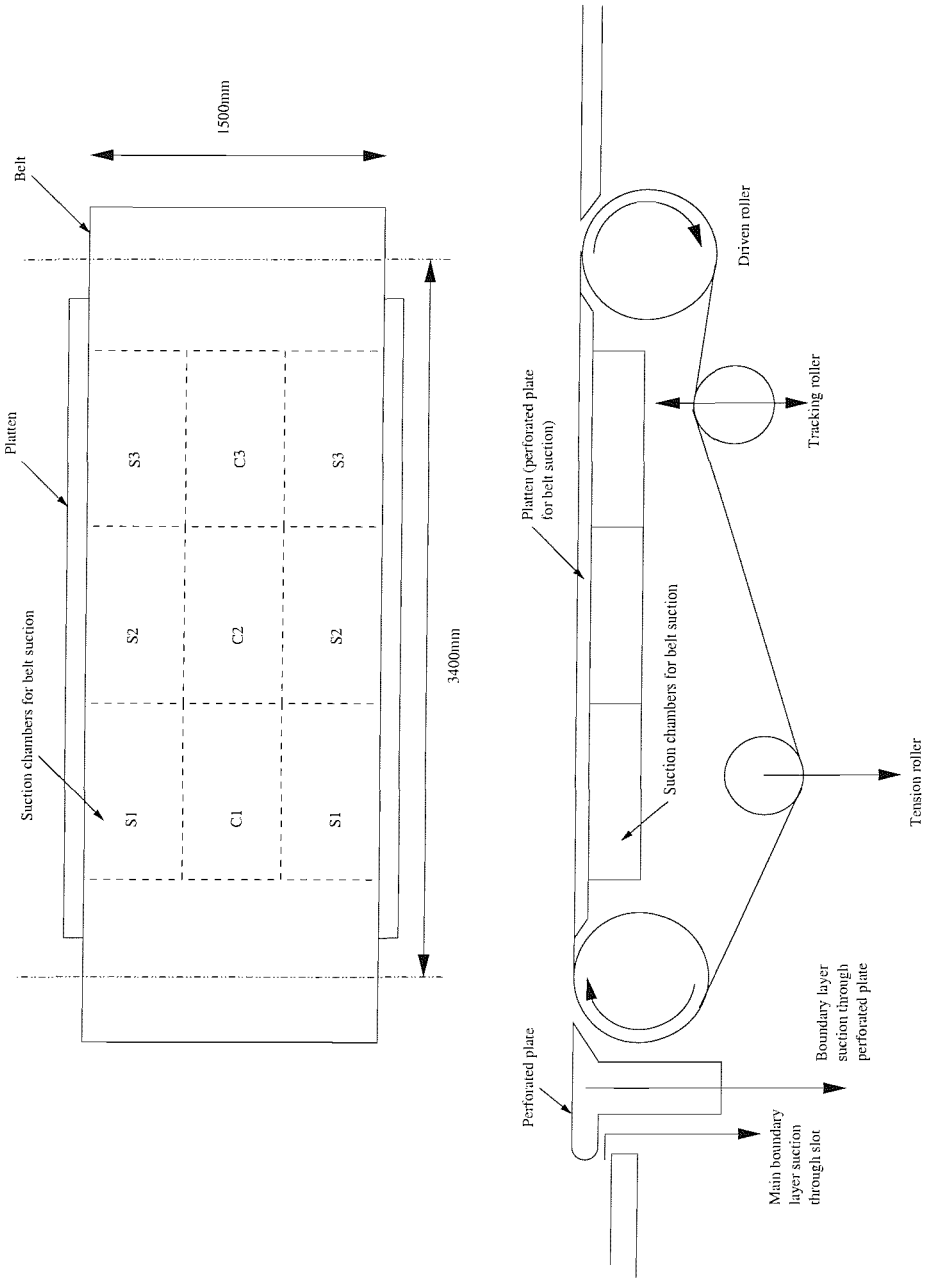

Figure 3: Schematic of the moving ground rig in the 2.1m×1.7m wind tunnel.

Suction surface		Pressure surface	
x/c	y/c	x/c	y/c
0.0000	0.0000	0.0000	0.0000
0.0010	-0.0076	0.0010	0.0079
0.0020	-0.0107	0.0020	0.0109
0.0049	-0.0168	0.0051	0.0173
0.0099	-0.0228	0.0101	0.0232
0.0149	-0.0266	0.0151	0.0271
0.0199	-0.0294	0.0201	0.0300
0.0249	-0.0320	0.0251	0.0313
0.0298	-0.0345	0.0301	0.0322
0.0348	-0.0369	0.0351	0.0330
0.0398	-0.0393	0.0401	0.0338
0.0448	-0.0416	0.0451	0.0346
0.0498	-0.0438	0.0501	0.0354
0.0548	-0.0460	0.0551	0.0361
0.0598	-0.0481	0.0601	0.0369
0.0698	-0.0520	0.0701	0.0382
0.0797	-0.0557	0.0801	0.0395
0.0897	-0.0591	0.0902	0.0407
0.0997	-0.0622	0.1002	0.0417
0.1197	-0.0676	0.1202	0.0436
0.1396	-0.0718	0.1402	0.0451
0.1596	-0.0750	0.1602	0.0463
0.1796	-0.0769	0.1802	0.0472
0.1996	-0.0778	0.2002	0.0480
0.2496	-0.0762	0.2501	0.0498
0.2996	-0.0732	0.3001	0.0515
0.3496	-0.0692	0.3501	0.0527
0.3996	-0.0645	0.4001	0.0534
0.4496	-0.0590	0.4501	0.0537
0.4996	-0.0526	0.5001	0.0535
0.5497	-0.0454	0.5501	0.0529
0.5997	-0.0373	0.6001	0.0518
0.6497	-0.0285	0.6500	0.0503
0.6997	-0.0188	0.7000	0.0482
0.7498	-0.0083	0.7500	0.0456
0.7998	0.0031	0.8000	0.0438
0.8498	0.0152	0.8500	0.0443
0.8999	0.0282	0.9000	0.0479
0.9199	0.0336	0.9200	0.0502
0.9399	0.0392	0.9400	0.0530
0.9599	0.0449	0.9600	0.0562
0.9799	0.0507	0.9800	0.0599
0.9900	0.0537	0.9900	0.0619
1.0000	0.0567	1.0000	0.0640

Table 2: Single element wing coordinates at reference incidence of 1°.

Suction surface		Pressure surface	
x/c	y/c	x/c	y/c
0.0000	0.0000	0.0000	0.0000
0.0006	-0.0044	0.0006	0.0047
0.0011	-0.0063	0.0012	0.0064
0.0029	-0.0098	0.0030	0.0102
0.0058	-0.0134	0.0059	0.0136
0.0087	-0.0156	0.0089	0.0159
0.0117	-0.0173	0.0118	0.0176
0.0146	-0.0188	0.0148	0.0184
0.0175	-0.0203	0.0177	0.0189
0.0205	-0.0217	0.0207	0.0194
0.0234	-0.0231	0.0236	0.0199
0.0263	-0.0245	0.0265	0.0204
0.0293	-0.0258	0.0295	0.0208
0.0322	-0.0270	0.0324	0.0212
0.0351	-0.0283	0.0354	0.0217
0.0410	-0.0306	0.0412	0.0225
0.0469	-0.0328	0.0471	0.0232
0.0528	-0.0348	0.0530	0.0239
0.0586	-0.0366	0.0589	0.0245
0.0704	-0.0398	0.0707	0.0256
0.0821	-0.0422	0.0824	0.0265
0.0939	-0.0441	0.0942	0.0272
0.1056	-0.0452	0.1059	0.0278
0.1174	-0.0457	0.1177	0.0282
0.1468	-0.0448	0.1471	0.0293
0.1762	-0.0430	0.1765	0.0303
0.2056	-0.0407	0.2059	0.0310
0.2350	-0.0379	0.2353	0.0314
0.2644	-0.0347	0.2647	0.0316
0.2938	-0.0309	0.2941	0.0315
0.3232	-0.0267	0.3234	0.0311
0.3526	-0.0219	0.3528	0.0305
0.3820	-0.0167	0.3822	0.0295
0.4114	-0.0110	0.4116	0.0283
0.4409	-0.0049	0.4410	0.0268
0.4703	0.0018	0.4704	0.0257
0.4997	0.0090	0.4998	0.0261
0.5291	0.0166	0.5292	0.0282
0.5409	0.0198	0.5409	0.0295
0.5527	0.0230	0.5527	0.0311
0.5644	0.0264	0.5645	0.0330
0.5762	0.0298	0.5762	0.0352
0.5821	0.0316	0.5821	0.0364
0.5880	0.0333	0.5880	0.0377

Table 3: Main element coordinates at reference incidence of $\alpha = 14.1°$.

Suction surface		Pressure surface	
x/c	y/c	x/c	y/c
0.5643	0.0757	0.5643	0.0757
0.5687	0.0633	0.5720	0.0863
0.5744	0.0601	0.5785	0.0886
0.5805	0.0597	0.5849	0.0908
0.5868	0.0605	0.5914	0.0929
0.5931	0.0614	0.5979	0.0951
0.6248	0.0678	0.6302	0.1059
0.6570	0.0779	0.6625	0.1167
0.6896	0.0908	0.6948	0.1275
0.7240	0.1065	0.7271	0.1383
0.7573	0.1249	0.7594	0.1491
0.7895	0.1434	0.7918	0.1600
0.8229	0.1617	0.8241	0.1709
0.8566	0.1789	0.8567	0.1836
0.8895	0.1967	0.8897	0.1996
0.9230	0.2158	0.9232	0.2186
0.9564	0.2345	0.9567	0.2372
0.9669	0.2402	0.9670	0.2429

Table 4: Flap coordinates at reference incidence of $\alpha = 14.1°$.

Suction surface			Pressure surface		
x /mm	x/c (S)	x/c (D)	x /mm	x/c (S)	x/c (D)
0	0.000	0.000	0	0.000	0.000
2	0.009	0.005	2	0.009	0.005
4	0.018	0.011	4	0.018	0.011
6	0.027	0.016	6	0.027	0.016
8	0.036	0.021	8	0.036	0.021
10	0.045	0.026	10	0.045	0.026
15	0.067	0.039	15	0.067	0.039
20	0.090	0.053	20	0.090	0.053
25	0.112	0.066	25	0.112	0.066
30	0.134	0.079	30	0.134	0.079
40	0.179	0.105	40	0.179	0.105
56	0.251	0.147	56	0.251	0.147
65	0.291	0.171	70	0.313	0.184
75	0.336	0.197	90	0.403	0.237
85	0.380	0.224	110	0.492	0.290
95	0.425	0.250	125	0.559	0.329
110	0.492	0.290	140	0.627	0.369
130	0.582	0.342	150	0.671	0.395
150	0.671	0.395	160	0.716	0.421
160	0.716	0.421	170	0.761	0.448
170	0.761	0.448	185	0.828	0.487
180	0.806	0.474	200	0.895	0.527
190	0.850	0.500	222	0.994	0.584
200	0.895	0.527			
211	0.944	0.555			
222	0.994	0.584			

Table 5: Location of chordwise tappings of single element wing (S), or main element of double element wing,(D). Quarter-chord suction surface tappings at $\eta = 0.182, 0.909$, pressure surface at $\eta = 0.136, 0.818$

Suction surface		Pressure surface	
z /mm	η	z /mm	η
5	0.009	5	0.009
15	0.027	15	0.027
25	0.045	25	0.045
50	0.091	50	0.091
75	0.136	75	0.136
100	0.182	100	0.182
130	0.236	130	0.236
165	0.300	165	0.300
235	0.427	235	0.427
275	0.500	275	0.500
315	0.573	315	0.573
355	0.645	355	0.645
400	0.727	400	0.727
450	0.818	450	0.818
500	0.909	500	0.909
550	1.000		

Table 6: Location of spanwise tappings at quarter-chord position, for single element wing and main element of double element wing

Suction surface			Pressure surface		
x /mm	x/c_f	x/c	x /mm	x/c_f	x/c
0	0.000	0.564	0	0.000	0.564
2	0.012	0.570	2	0.012	0.570
5	0.030	0.577	5	0.030	0.577
10	0.060	0.591	10	0.060	0.591
15	0.091	0.604	15	0.091	0.604
20	0.121	0.617	20	0.121	0.617
30	0.181	0.643	30	0.181	0.643
41	0.247	0.672	41	0.247	0.672
50	0.302	0.696	50	0.302	0.696
60	0.362	0.722	60	0.362	0.722
80	0.483	0.775	80	0.483	0.775
100	0.604	0.827	100	0.604	0.827
120	0.724	0.880			

Table 7: Location of chordwise tappings on flap. The x/c columns represent the location of the tappings for the double element wing, the x/c_f columns are for a flap based coordinate system. Quarter-chord suction surface tappings are at $\eta = 0.182, 0.909$, pressure surface at $\eta = 0.136, 0.818$

Suction surface		Pressure surface	
z /mm	η	z /mm	η
5	0.009	5	0.009
15	0.027	15	0.027
25	0.045	25	0.045
50	0.091	50	0.091
75	0.136	75	0.136
100	0.182	100	0.182
140	0.255	140	0.255
180	0.327	180	0.327
220	0.400	220	0.400
260	0.473	260	0.473
300	0.545	300	0.545
350	0.636	350	0.636
400	0.727	400	0.727
450	0.818	450	0.818
500	0.909	500	0.909
550	1.000		

Table 8: Location of spanwise tappings at quarter-chord position, flap.

Chapter 3

Single Element Wing in Freestream

3.1 Introduction to Chapter

In this chapter experimental results are presented for the aerodynamic performance of the single element wing in freestream, as a baseline case. The downforce and drag generated by the wing, and also surface pressures are investigated. The tests were performed with free transition, in the 2.1m×1.7m wind tunnel.

3.2 Forces

Force results obtained from the overhead balance can be seen in Figure 4. The liftcurve is of a familiar shape; a straight line region is followed by a maximum downforce, which then falls off slightly to a plateau. C_{Lmax} has a value of 1.35, and occurs at an incidence of 11.3°. The liftslope has been calculated as $4.57/rad$.

3.3 Surface Pressures

3.3.1 Chordwise Pressures; Centre

Chordwise pressures for the tappings at the centre of the wing can be seen in Figure 5a. As the incidence is increased, this results in an increase in the loadings over the leading portion of the wing. The associated pressure recovery due to the increase in peak suction, from $x/c \approx 0.2$ increases. Small scale trailing edge separation over the rearmost $10\%c$ can be seen for the 9° case, as being represented by the constant pressure region. As the incidence increases, a larger constant

pressure region is seen, and the loading is lost as the boundary layer separates for the 13° case. Tests indicated that the large scale separation occurred between 11° and 13°, which corroborates with C_{Lmax} occurring at 11.3° from the force results. Near to the leading edge, at approximately 2%c, a sharp peak in the suction can be seen for the higher incidences.

3.3.2 Chordwise Pressures; Tip

An indication to the three-dimensionality to the flow can be seen in Figure 6 where the chordwise pressures are presented for the centre and tip tappings.

At the low incidence of $\alpha = 1°$ (Figure 6a), it can be seen that near to the tip, reduced suctions and pressures result on the suction surface and pressure surface respectively. This is due to a combination of two different factors. Primarily, nearer to the wing tip, there is a lower circulation due to the tip effect losses. Another effect of the wing tip vortex seems to be present. The tip vortex induces an upwash, which, when resolved with the freestream velocity, results in a lower effective incidence for the flow near to the tip. A slight bump can be seen in the suctions at $x/c \approx 0.3$. Oil flow visualation performed on the wing, not presented here, indicates transition to occur at this location, through a small transition bubble.

At the higher incidence of $\alpha = 13°$ (Figure 6b), where large scale flow separation has already occurred at the centre of the wing, the results at the tip show that the flow is still attached at this location. A lower pressure recovery is present nearer to the wing tip, due to the effect of the tip vortex.

3.3.3 Spanwise Pressures

Spanwise pressures from the quarter-chord tappings are presented in Figure 5b, for the same incidences as the chordwise centre results, further highlighting the three-dimensionality of the flow. For unstalled incidences, the pressures are reasonably constant from $\eta \approx 0.2$, increasing with incidence, indicating a significant region of quasi-two-dimensional flow. When the wing stalls, loading is lost over the central portion of the wing first, as can be seen by the reduced suctions from $\eta \approx 0.6$ for the $\alpha = 13°$ case. As the incidence is increased, a suction peak appears at the wing tip, due to the influence of the wing tip vortex.

3.4 Summary

Forces and pressures for the wing in freestream give expected results, for a generic three-dimensional wing in freestream. A large area of quasi-two-dimensional flow exists for the lower and midrange incidences. As the incidence increases and as stall occurs, three-dimensional effects dominate.

Oil flow results not presented here reveal that the the flow first separates at the trailing edge at the centre of the wing, at an incidence where maximum downforce occurs. As the incidence

is increased, through the plateau region of the liftcurve, the separation point moves forwards and outwards.

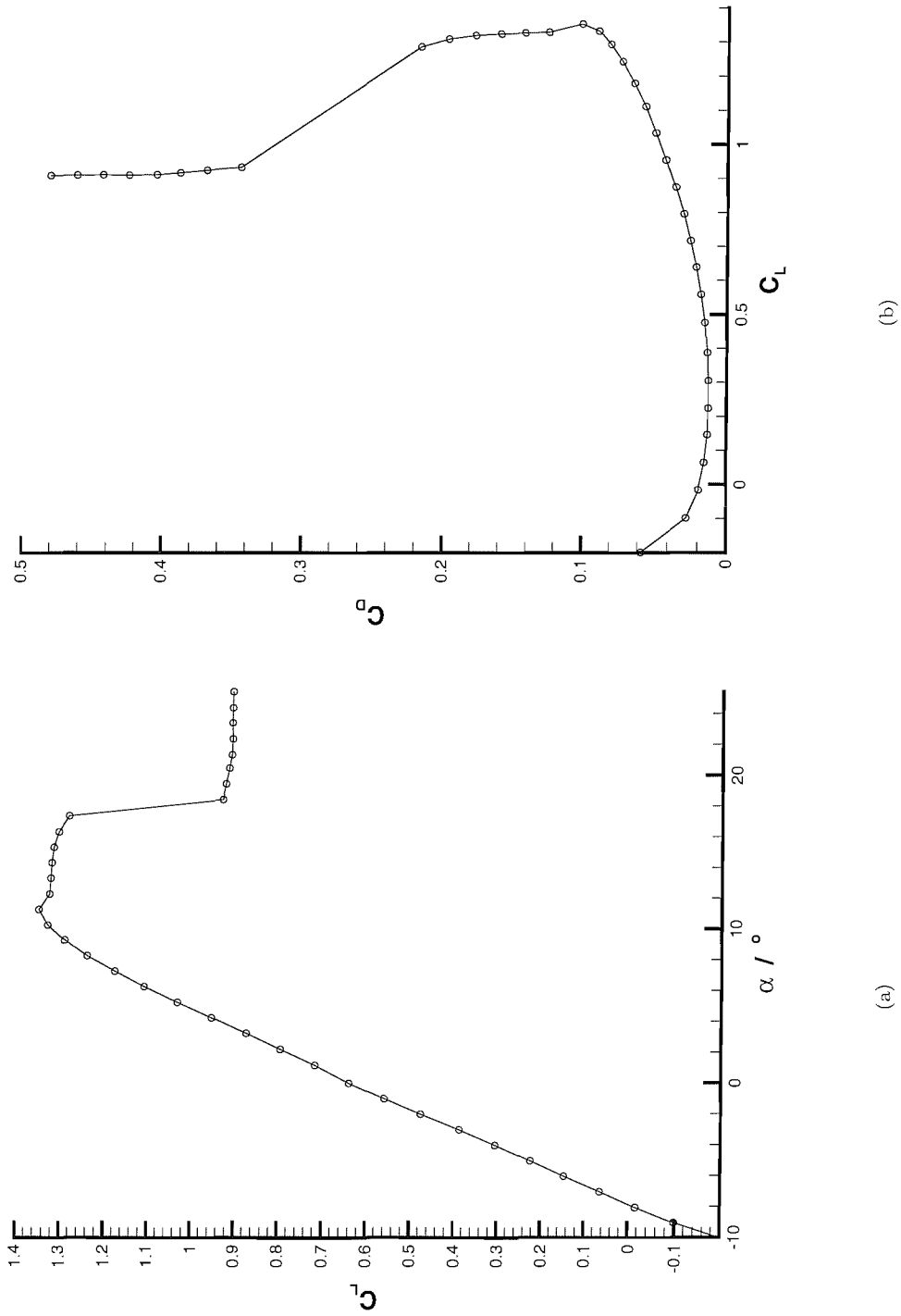

Figure 4: Aerodynamic performance of single element wing in freestream (a) Liftcurve. (b) Drag polar.

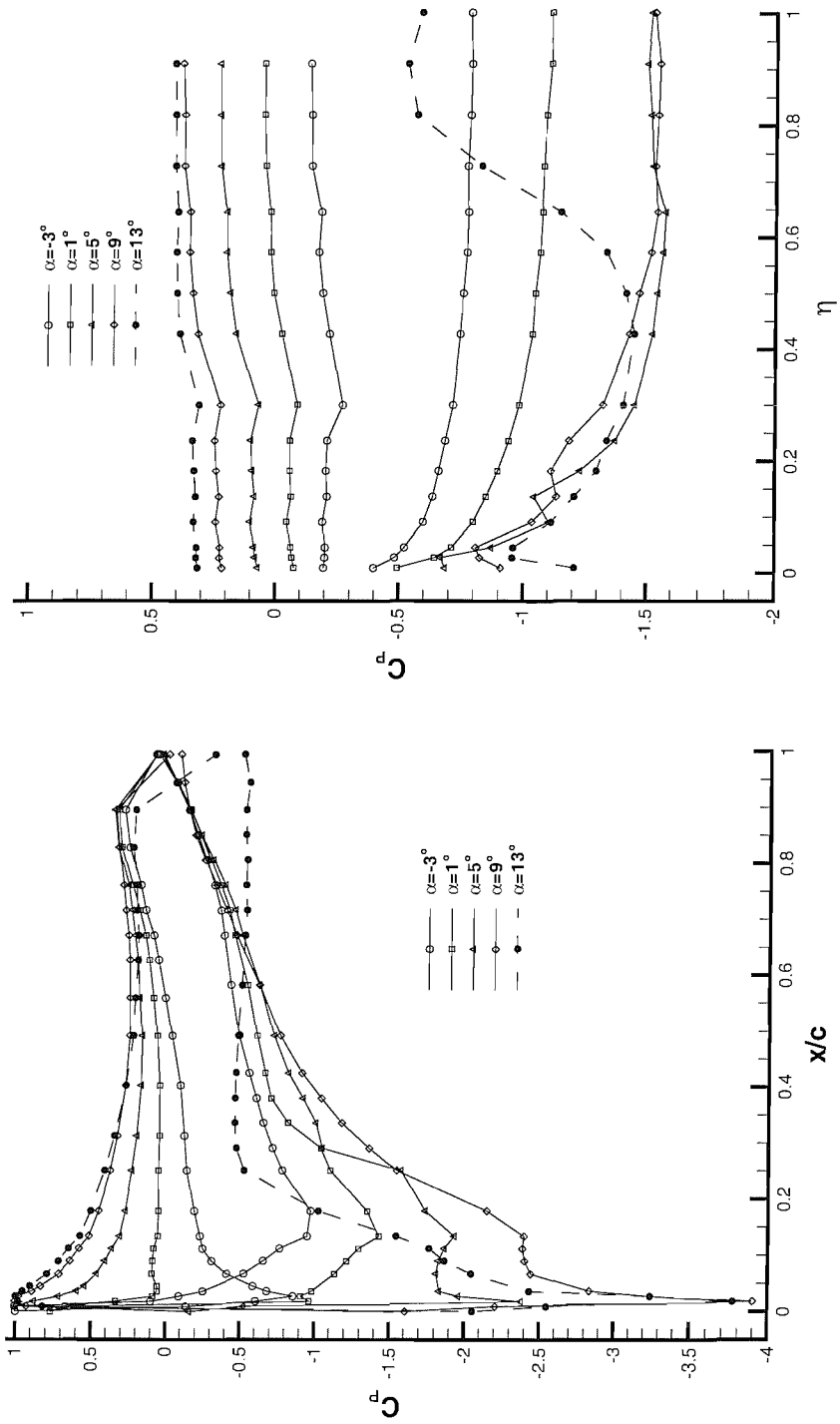

Figure 5: Surface pressures in freestream (a) Chordwise at wing centre. (b) Spanwise.

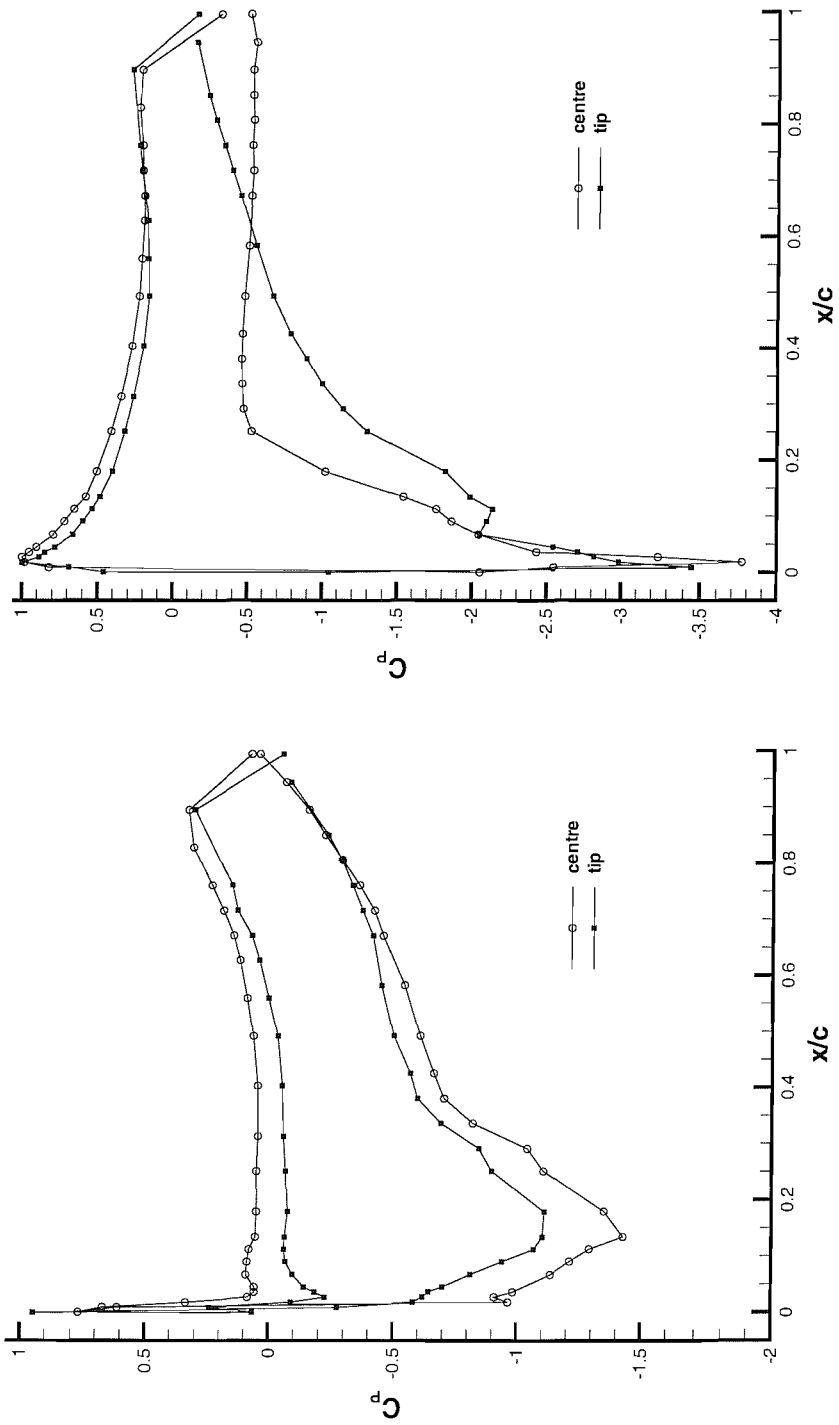

Figure 6: Chordwise surface pressures in freestream at wing centre and wing tip (a) $\alpha = 1°$. (b) $\alpha = 13°$.

Chapter 4

Single Element Wing in Ground Effect at the Reference Incidence

4.1 Introduction to Chapter

This chapter presents the experimental results found from testing the single element wing at the reference incidence of $\alpha = 1°$ at a selection of ground heights, with free transition. The aerodynamic performance is discussed, and flowfield results are used to describe the reasons for the performance at different heights from the ground.

4.2 Forces

Figure 7a presents the effect of ground height on the downforce. At a height of $h/c = 0.671$, a large ground height, the downforce generated corresponds to a coefficient of $C_L = 0.84$, compared with the freestream value of 0.69 at the reference incidence. As the wing is brought closer to the ground through large and moderate heights, the slope of the line increases as a larger increment in downforce is obtained for a given increase in ground proximity, i.e. the sensitivity of downforce to ground height increases. At a height of $h/c \approx 0.15$ from the ground, there is a gradual, and then significant deviation from this previous trend, and the downforce reaches a maximum at a height of $h/c = 0.082$, corresponding to a $C_L = 1.72$.

The results for the variation of the drag with height can be seen in Figure 7b. As the ground height is reduced, the downforce increases until it reaches a maximum. This contributes to the induced drag of the wing, and hence the drag increases with increasing ground proximity for moderate and large heights. However, the drag does not decrease in a similar manner to the downforce below the force reduction phenomenon; the drag continues to increase for all ground heights closer to the ground than the maximum downforce. Since the lift-induced drag is not increasing through these

small ground heights, and the total drag is, some other physical phenomenon must be occurring here to increase the drag.

4.3 Surface Pressures

4.3.1 Chordwise Pressures at Wing Centre

The chordwise surface pressures at the centre of the wing for a selection of heights are presented in Figure 8. For the moderate and large ground heights (Figure 8a), the effect of moving the wing closer to the ground is to increase the suctions over the entire suction surface, including the peak suction. The effect of the ground is to constrain the flow, and when combined with the suction created between the wing and the ground, the flow is accelerated. Moreover, concerning the reflection method, the image aerofoil induces a high velocity region in this between the wing and the ground. Results on the pressure surface are very similar for all the heights. For the smaller heights (Figure 8b), the peak velocity on the suction surface increases for *all* ground heights, including past the height where the maximum downforce occurs. From the leading edge to $x/c \approx 0.12$ on the suction surface, there is a negligible gain in suction, unlike the case for the greater heights. Significant gains in suction are achieved from the peak suction to $x/c \approx 0.4$. This is the part of the wing nearest to the ground, experiencing the accelerated flow most. In close proximity to the ground, less than $h/c = 0.179$, a small constant pressure region can be seen near to the trailing edge of the suction surface. As the ground is approached, the size of the constant pressure region increases in size. This shows a region of separated flow, where the boundary layer has separated from the trailing edge of the suction surface. Again, the pressure surface pressures are similar for most heights, with a tendency for reducing pressure with ground height.

4.3.2 Suction Surface Canonicals

Canonical pressures [60] are useful in separation analysis, allowing pressure recoveries to be compared directly as long as the Reynolds number based on the momentum thickness at the start of the pressure recoveries are similar. The pressures in the recovery region from the suction peak to the trailing edge are effectively normalized by the maximum suction, using the equation $\overline{C_P} = 1 - \frac{C_P - 1}{C_{P_{MAX}} - 1}$. This yields the result that a $\overline{C_P}$ of 0 corresponds to the suction peak, whilst a $\overline{C_P}$ of 1 represents a stagnation. The canonical pressures are plotted against the distance from the suction peak non-dimensionalized by the distance from the suction peak to the trailing edge.

Although this is not an ideal method when applied to experimental results, due to the discrete sampling points at each pressure tapping, the suction surface pressure recoveries for the chordwise central tappings, have been replotted in their canonical form as can be seen in Figure 9a. The locus of separation points measured from the oil flow visualisation (see below) has also been plotted in the figure. It can be seen that, for the first portion of the pressure recovery, to $s/s_{T/E} \approx 0.3$,

the canonical pressures decrease with increasing ground proximity. A more significant increase in canonical pressure with increasing ground proximity is seen for the remaining portion of the recovery. For the largest ground height, the pressure recovery is initially small, but increases as the trailing edge is approached. As the ground height is reduced to the $h/c = 0.224$ case, the pressure recovery appears broadly constant. This is the height at which a very small region ($x_{sep}/c \approx 0.99$) begins to appear. With increasing ground proximity, the initial part of the second portion of the pressure recovery increases, but then falls off near to the trailing edge as the flow separates. From the canonical pressure distributions it can further be seen that the flow separates due to it not being able to withstand the adverse pressure gradient.

4.3.3 Spanwise Pressures

Spanwise surface pressures from the quarter-chord tappings for a selection of heights are shown in Figure 10a. As seen before, the suction increases as the ground is approached, and there is little variation of the pressure surface value as the ground height changes. It is interesting to note that even as the wing stalls as large scale flow separation occurs, the effect is not as three-dimensional as the freestream results. For the stalled wing in freestream, the boundary layer separates from the whole of the suction surface. In ground effect, the suctions at the quarter-chord location seem relatively unaffected, as the separation point does not move this far forwards.

Due to the large variation in surface pressures with ground height, it is difficult to compare the spanwise variations of pressure directly, using the results taken using the pressure tappings at the quarter-chord. The pressure distributions for each height have been normalized by dividing by the integral of the pressures with respect to the spanwise position, for the suction surface results. Hence, for fully two-dimensional flow, C_{Pnorm} would correspond to -1 over the entire suction surface. The results are presented in Figure 10b. Although the results lie very close to each other, an effect of the ground height on the three-dimensional characteristics can still be observed. For the cases in freestream and at large heights, a relatively large area of quasi two-dimensional flow exists near to the centre of the wing. As the ground height is reduced, the region of two-dimensional flow reduces in size and the tip losses become greater; the wing effectively reduces aspect ratio. Although not particularly clear in the figure, careful examination of the results yields the result that in very close proximity to the ground, the distribution starts to become more two-dimensional. In fact, numerical analysis of the distribution of C_{Pnorm} at all the heights yields the result that at a height of $h/c = 0.179$ the most three-dimensionality to the flow is exhibited. At this height, the tip losses are the greatest, although since the results are very close, it is difficult to reach a definite answer.

4.3.4 Chordwise Pressures near to Wing Tip

Comparisons of the chordwise pressure at the centre of the wing and near to the tip for a moderate ground height of $h/c = 0.313$ can be seen in Figure 11a. Near to the tip, the effect can be seen to be similar to the freestream comparisons; a loss in the loading on both the pressure and suction surfaces, as has been described above. It seems that the loss in suction surface loadings at the tip for the ground effect case is more significant than for the freestream case; it can be seen that the loss in suction at the suction peak for this height for the tip tappings compared to the centre tappings is greater than the loss for the freestream case (Figure 6a). The centre tapping with the peak suction is at $x/c = 0.134$; for the tip tappings, this is at $x/c = 0.179$. Again, this may be indicative of the fact that the tip flow is at a lower effective incidence due to the vortex upwash effect.

For the case at a small ground height of $h/c = 0.134$ (Figure 11b), a similar effect can be seen. Again, a significant difference is visible in the suction surface loadings between the wing centre and wing tip. Also, the reduction in suction at the peak is greater than the results for the other height of $h/c = 0.313$, and the freestream results. At this height, the centre tappings highlight a region of flow separation. The tip tappings do not exhibit this separation, similar to the freestream case at high incidence. A significant factor is that the reduced circulation results in a smaller pressure recovery demand at the tip. The reduction in local flow incidence at the tip may also be a factor. The tapping with the peak suction is at $x/c = 0.179$ for both cases.

4.3.5 Integrated Pressures

For both the chordwise tappings at the centre of the wing, and also the chordwise tapings near to the wing tip, the pressure distributions have been integrated to estimate the two-dimensional sectional lift coefficient, C_l. The variation of the sectional lift coefficient with ground height can be seen in Figure 9b, together with the three-dimensional lift coefficient C_L as measured from the overhead balance. This is another method of presenting the three-dimensionality of the flow. As expected, C_{lcent} is greater than C_L over all heights, i.e. the wing as a whole suffers from three-dimensional effects, with a similar characteristic shape for the curve. The δ values, $C_{lcent} - C_{ltip}$ show how the difference in sectional lift coefficient between the two spanwise locations varies with ground height, i.e. it is a measure of the three-dimensionality of the flow. In freestream, $\delta = 0.21$, which increases through large and moderate heights, to reach a maximum of 0.53 at $h/c = 0.134$, and reduces to 0.44 at $h/c = 0.067$. That is to say that as the ground is approached, the downforce generated in the centre of the wing increases at a greater rate than the downforce generated near to the tip, until $h/c = 0.134$. Below this height, the downforce at the tip is more closely matched to the downforce at the centre, as the flow three-dimensionality reduces.

4.4 Oil Flow Visualisation

Oil flow visualisation was performed, at a selection of ground heights at the reference incidence. A mixture of Titanium Dioxide and paraffin was applied to both surfaces, and then allowed to dry with the tunnel running at the reference speed.

Figure 12 shows the results of a selection of oil flow visualisation tests performed on the wing at the reference incidence, at heights of $0.134c$, $0.090c$, and $0.067c$, showing the suction surface with the leading edge lowermost. Transition, through the means of the short reattachment bubble can be seen at approximately $0.3c$. At $h/c = 0.134$, a small region of separated flow can be seen over the central portion of the suction surface of the wing, commencing at $x/c \approx 0.95$. Nearer to the ground, at $h/c = 0.090$, very near to the maximum downforce, the region of separated flow at the trailing edge has increased so that separation occurs at $x/c \approx 0.8$. At a point past the maximum downforce, $h/c = 0.067$, the region of flow reversal has increased in size again; separation occurs at $x/c \approx 0.7$.

The presence of the wing tip vortices can be seen in each of the diagrams. The effect of the vortices result in trailing edge separation being avoided near to the wing tips. The two reasons have been discussed above. No other large scale three-dimensional flow effects can be seen from the flow visualisation tests.

The flow visualisation tests were found to be extremely sensitive to the mixture applied to the wing surface. Small spots of unmixed powder in the imperfect mixture, less than 0.2mm in diameter in some cases cause early transition and effect the flow downstream. Points where transition has been caused early by the non-perfect mixture cause slightly early separation, as can be seen in the figure.

The detachment point of the boundary layer from the results of the oil flow visualisation tests are presented in Table 9. The point of separation was taken as near as possible to the wing semispan, in regions not effected by premature transition. When the results are plotted in a graph, the points follow a curve with no significant discontinuities. The separation points have been included in the canonical pressures (above).

4.5 Laser Doppler Anemometry Surveys

In order to investigate the wake of the wing, and the flow very close to the ground, LDA testing was performed at the semispan, at several heights. Near-field results were taken in the region $x/c = 1.0 - 1.5$, from above the trailing edge of the wing to the ground. Points were clustered in regions of high velocity gradients, using grids in the region $x/c = 1.0 - 1.2$. Data at $x/c = 1.5$ were added from a single vertical traverse. Results in this section examine the mean flow characteristics of the wake. Any unsteady characteristics are discussed in later chapters.

In Figure 13, u/U_∞ velocity contours and streamlines are presented for heights of $h/c =$

$0.448, 0.224, 0.134$ and 0.090. In the region between the wing trailing edge and the ground, the greatest velocities are found. The flow can be seen to decelerate due to the streamwise adverse pressure gradient present, from the x/c position of 1.0 to 1.5. At $h/c = 0.224$ and $h/c = 0.134$, a small region of flow can be seen just below and to the rear of the trailing edge that has a small (or negative) velocity. This increases in size as the ground is approached, and for $h/c = 0.090$ the region is significantly larger, and negative velocities are clear. This is a region of flow reversal.

The characteristics of the wake of the wing can be seen to change as the ground height is changed. For the $h/c = 0.448$ and $h/c = 0.224$ cases the path of the wake as seen by the velocity deficit rises as it moves downstream. For the $h/c = 0.134$ case, where flow separation is present, the path of the wake is of a smaller angle and is less likely to follow the angle of the trailing edge. Closer to the ground, at $h/c = 0.090$, large scale flow separation exists, and the path of the wake has deviated more, following a horizontal path.

In addition to the path of the wake changing, the size of the wake also changes with ground height, increasing as the ground is approached, for all heights tested at. As the wing moves closer to the ground, the peak suction increases. The associated adverse pressure gradient for the recovery increases in a similar manner, and the boundary layer thickens as it comes closer to separation. The overall effect is for a thicker boundary layer, and hence wake, as the ground is approached. Eventually, when significant flow separation is present, the size of the wake increases rapidly.

An effective ground boundary layer can be seen near to the ground. The ground moves with a velocity equal to freestream. The accelerated flow near to the ground gives rise to the effective boundary layer above the ground. These can be seen in the contours in Figure 13 and also more clearly in results plotted as wake surveys, Figure 14 at an x/c position of 1.2. Within approximately 0.02c of the ground, the u/U_∞ velocity reaches a value of approximately 1.2. Very near to the ground, less than 0.01c, however, a velocity *deficit* can be seen for most cases. It is believed that this is due to fluid originally moving at freestream velocity, retarding due to the adverse pressure gradient in the streamwise direction from peak suction. The wake profiles also show the effect of the increasing wake size with ground proximity. The velocity profiles at different heights for the high speed fluid moving between the wing and the ground reach approximately the same value, increasing very slightly with increasing ground proximity. For a single height of $h/c = 0.134$, u/U_∞ wake velocities are plotted at x/c positions of 1.2 and 1.5. Again, both the effective ground boundary layer, and the velocity deficit very close to the wall can be seen. The high speed fluid is seen to retard as it advances downstream. Both the wing wake and the velocity deficit near to the ground are also seen to diffuse.

4.6 Particle Image Velocimetry Surveys near to Wing Tip

From the surface pressure results, it can be seen that the tip effects follow a trend as the ground height is reduced, until a height of $h/c \approx 0.15$, where the trend starts to reverse. It was decided

to perform PIV tests to investigate the wing tip vortex at different heights from the ground. The laser light sheet was set up to illuminate a cross-plane region at $x/c = 1.2$, i.e. behind, but close to the endplate. The camera was located downstream of the moving ground, perpendicular to the light sheet, aimed at a position slightly inboard of the endplate. The bottom edge of the image was lined up on the ground. Results were taken using 100 datasets, performing a cross-correlation with a 50% overlap on 32×32 pixels to give results on a 77×61 grid. In addition to this, the results were range validated.

The strength of the vortex, as measured by the vorticity, can be seen in Figure 15 represented by the vorticity contours, at heights of $h/c = 0.448, 0.224, 0.134$ and 0.090. Table 10 lists the strength of the vortex for all heights tested at. The vorticity is derived from the velocity gradients, hence there will be errors incurred due to the finite grid spacing.

In the figures, the black lines represent the lower and upper profiles of the wing. Note that the top line is in fact the trailing edge, at $y/c = 0.061$. The results do not extend to the ground due to the fact that in PIV processing, the results are averaged for a finite cell, the location of which corresponds to the centre of that cell.

For the $h/c = 0.448$ case, the core of the vortex can be seen by the region of high positive vorticity in red. The black lines represent the profile lines of the wing and the outline from the endplate. A region of small but positive vorticity can be seen at a height near to that of the trailing edge; the wake. Very close to the surface of the endplate, more areas of small but positive vorticity can be seen, in the light green colour. Results have to be viewed with caution very close to the surface, as reflections may have contaminated the results, giving a false value of vorticity. The shear layer from the lower outer surface of the endplate is in the process of rolling up to feed the main vortex. Another region of positive vorticity exists from the inboard upper surface of the endplate. A small area of negative vorticity (light blue) is a secondary vortex to the weak vortex from the upper surface of the endplate, and seems to originate from the outboard upper surface of the vortex. As the main vortex in the lower part of the image rolls up, the strong positive vorticity near to the endplate causes a secondary area of negative vorticity due to the induced velocities and the shear. At $h/c = 0.224$, the main vortex and the secondary vortex at the bottom of the endplate are both stronger. The vorticity distribution at the top of the endplate is similar. Close to the ground, however, a region of negative vorticity is present, but difficult to see, from $z/c = -0.1$ to 0.4 over the lowest $0.05c$ of the image, in light blue. This is due to the velocities induced from the main vortex close to the ground. At $h/c = 0.134$, the main vortex at the bottom of the endplate and both the shear layers from the inner lower surface of the endplate and near to the ground are all stronger. The $h/c = 0.090$ case features a significantly reduced strength of vortex, which also appears somewhat oval. Table 10 lists the maximum vorticity from the tip vortex for all heights; this increases steadily throughout all heights, until $h/c = 0.134$, and then falls sharply.

4.7 Discussion

The downforce and the drag in ground effect have been quantified. The downforce increases asymptotically with increasing ground proximity through large and medium ground heights. The gradient then starts to decrease, and the downforce reaches a maximum of $C_L = 1.72$ at a height of $h/c = 0.082$ from the ground. This compares with the freestream value of $C_L = 0.69$. All results follow a smooth curve. Results from Ranzenbach and Barlow's experimental study using a NACA 4412 section [5] give a maximum downforce of $C_L \approx 0.93$ at $h \approx 0.9$ using a fixed ground. This compares to a downforce far from the ground of $C_L \approx 0.41$. Their results feature a sharper curve in the region of the maximum downforce, compared to the smoother results of the current study. The computational study that they performed with the moving ground conditions gives a smoother curve more similar to the current results. The maximum downforce corresponds to a slightly greater value of $C_L \approx 1.06$. For both of their results, the maximum downforce is significantly smaller than the maximum found in the current study.

The drag increases for all heights. This is in contrast to the general result of the aerodynamics of wings in ground effect whereby the drag reduces as the ground is approached. However, this result is reported for wings with a lift coefficient moderately greater than out of ground effect. For the current study, there is a small drag increase at larger heights, and a more significant drag increase at small heights. The significant increases in downforce contribute to the induced drag at all heights. The additional increase in drag close to the ground is due to separation.

Although three-dimensional effects are present, the peak in downforce is mainly a two-dimensional result, as can be seen in Figure 9b. Considering the surface pressures at the centre of the wing at a height near to the force reduction phenomenon, a reduction in height will lead to increases in suction over some portions of the wing, and increases in pressure over some other portions. The maximum downforce will occur at a height at which all of the contributions to the force, when summed, are a maximum. For example at heights of $h/c = 0.090$ and $h/c = 0.067$, i.e. either side of the maximum downforce, as the height is reduced, the pressures are reduced over the entire pressure surface. This contributes to a reduction in downforce. Over the range $x/c = 0.1 - 0.5$ on the suction surface the pressures reduce (greater downforce), and over most of the remainder they increase (less downforce). Hence, it is not a single feature that causes the maximum downforce, it is due to a summation of the pressures. The more significant effect causing a reduction in performance is due to the boundary layer separation at small heights. The reduction in pressure over the pressure surface is also a factor.

The effect of the ground on an aerofoil is shown in Figure 16a using the image approach. In this method, an image aerofoil is placed beneath the ground plane at a height equal to that of the real aerofoil from the ground. This creates a symmetry line to the flow at the location of the ground plane. The circulation of the image aerofoil is in a direction opposite to the circulation of the real aerofoil. It is clear that the circulation due to the image aerofoil will induce a suction onto the real aerofoil, especially over the suction surface, but also over the pressure surface. The magnitude

of this is dependent on the height from the ground. As described previously, there are problems associated with the image approach due to the fact that it only considers inviscid effects, and the ground will have a velocity greater than freestream. In addition to this, the diffuser effect is also significant, which is an enhanced effect of the image model. Considering only the real aerofoil, Figure 16b, it is clear to see that the flow will be accelerated most around the lowest point on the suction surface, i.e. the region where the height is the lowest. In addition to explaining the trends for the surface pressure distributions, this also accounts for the fact that the suction peak moves forwards from the location in freestream.

As the height is reduced the flow three-dimensionality increases. The greater suctions feed a stronger tip vortex. However, at a height below $h/c = 0.134$, PIV results show a sudden reduction in vortex strength. In addition to this, higher levels of $v'v'/U_\infty^2$ and $w'w'/U_\infty^2$ turbulence quantities were found. Two reasons are proposed for the reduction in vortex strength. It is likely that the direct influence of the ground is the main factor. The distance between the wing, or endplate, and ground is not sufficient for the vortex to roll up. Another possibility is that the vortex wandering phenomenon may be occurring, due to Kelvin-Helmholz instabilities in the shear layer. At this height from the ground, significant regions of separated flow exist, which may be ingested into the vortex core. Surface pressures indicate the similar effect of flow three-dimensionality decreasing below $h/c = 0.134$, from sectional downforce values at the wing centre and near to the tip, and also from spanwise pressures on the quarter-chord. The reduction in the strength of the tip vortex does not adversely effect the maximum downforce. The tip losses reduce at heights below $h/c = 0.134$, contributing to small *increases* in overall downforce. There is, however, no visible significant effect of this in the overall downforce.

Fundamentally, the LDA results show that, at a height of $h/c = 0.067$, i.e. below the force reduction phenomenon, the wake from the wing is distinct from the boundary layer over the ground, at $x/c = 1.5$. For the current study, the force reduction phenomenon is not due to a merging of the wing and ground boundary layers. In addition to this, the wake increases size as the height is reduced. This is attributed to the portion from the suction surface boundary layer, the size of which increases due to the increasing adverse pressure gradient with ground proximity.

4.8 Summary

The aerodynamic performance of a wing in ground effect has been investigated at a single incidence. A maximum downforce was observed at a certain height close to the ground and below this the downforce decreased. Although no single factor is entirely responsible, boundary layer separation is a major contributing factor, which is first observed at a much greater height. The tip vortex was found to increase in strength, and then suddenly reduce, at a height above that for maximum downforce. The wake was seen to grow, due to the portion from the suction surface boundary layer.

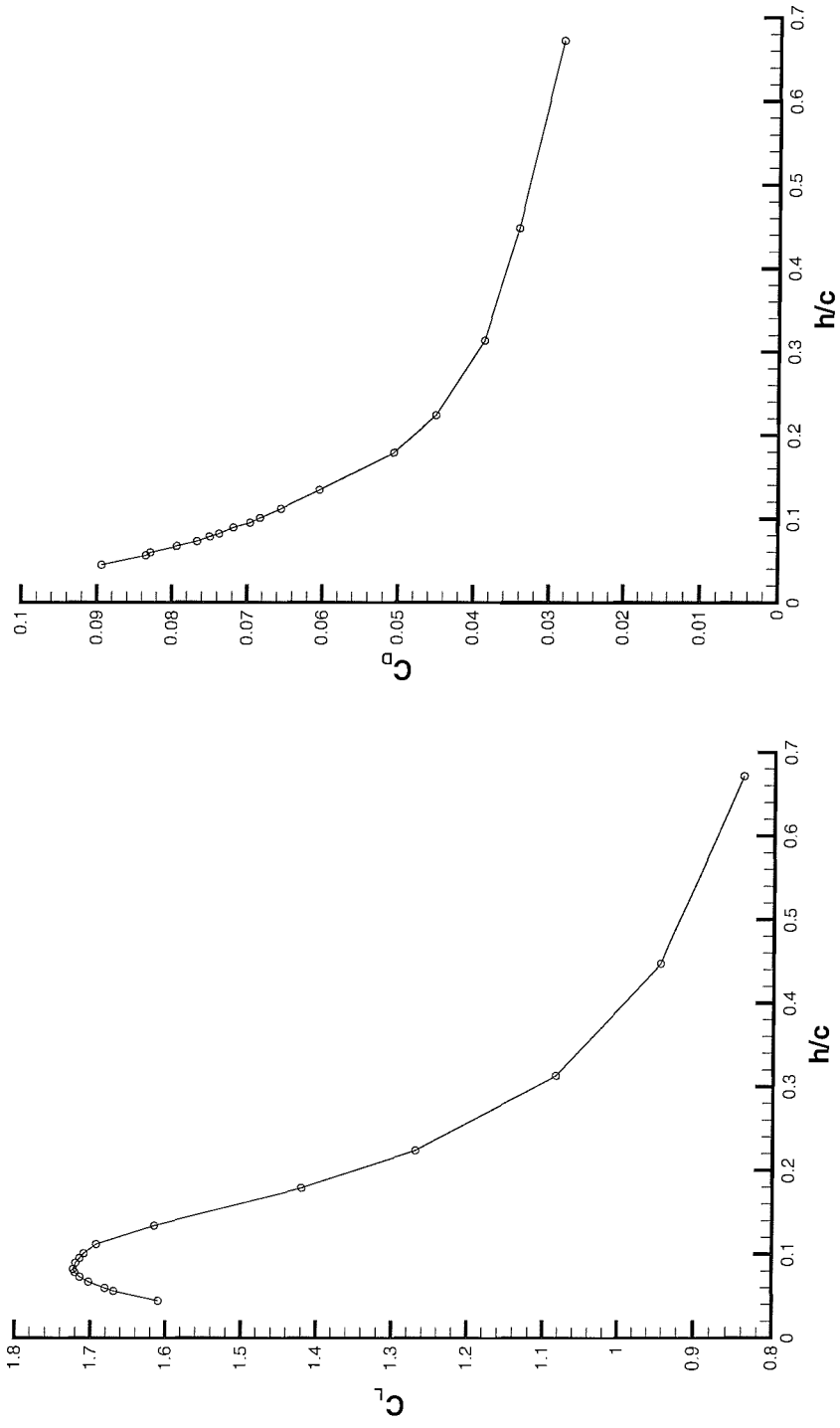

Figure 7: Aerodynamic performance of single element wing in ground effect at $\alpha = 1°$ (a) Downforce with height. (b) Drag with height.

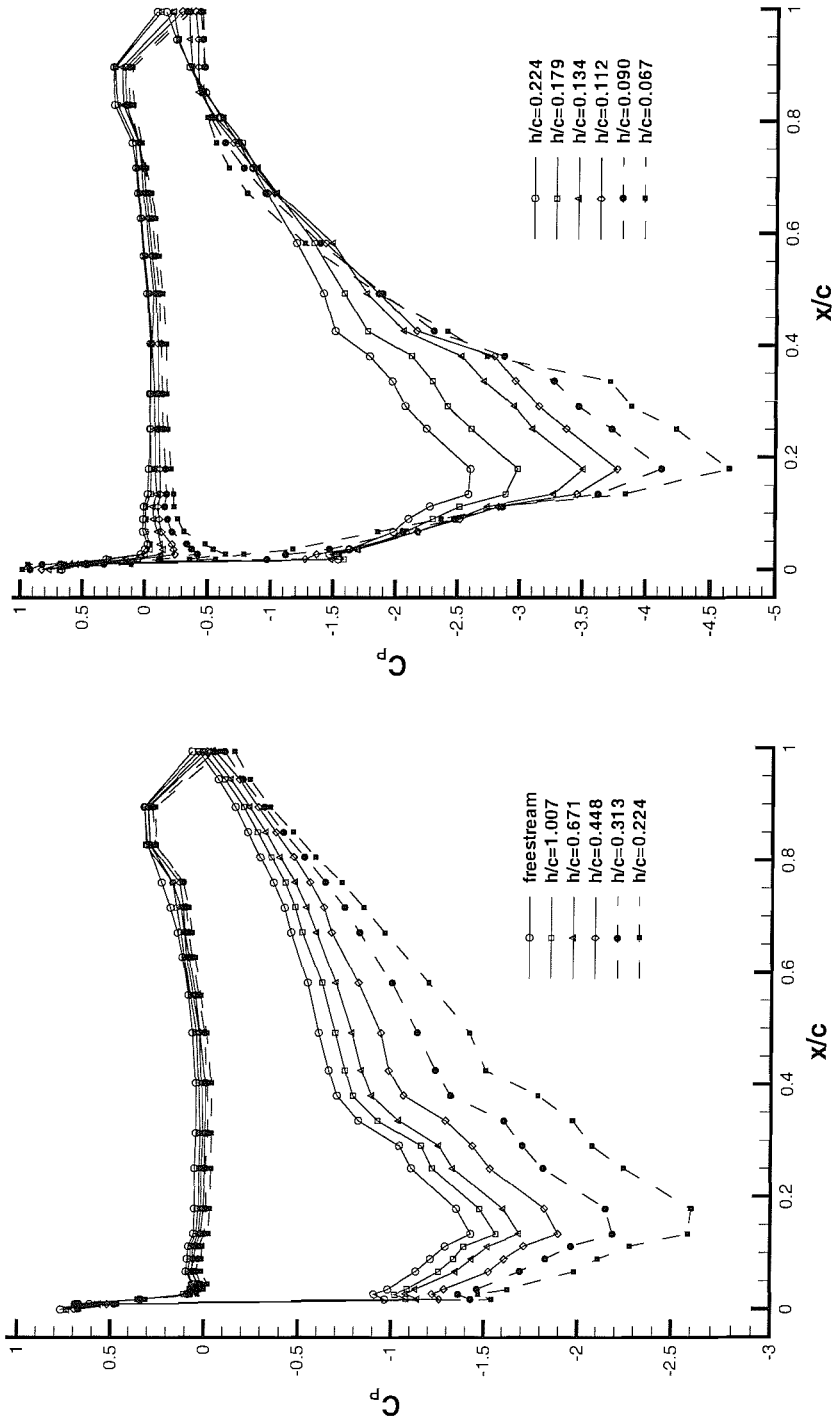

Figure 8: Chordwise surface pressures at wing centre in ground effect at $\alpha = 1°$ (a) Moderate and large ground heights. (b) Small ground heights.

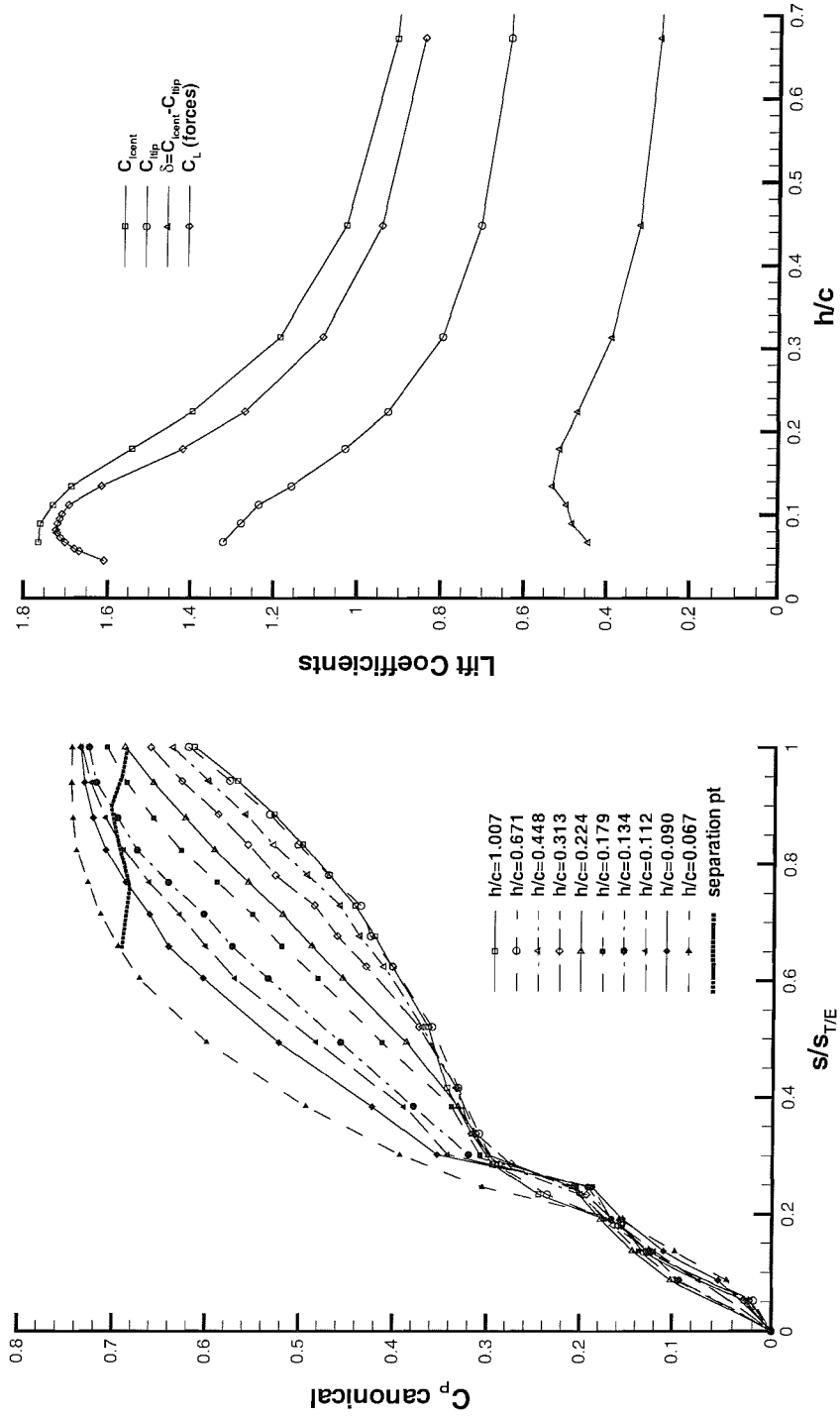

Figure 9: Surface pressures (a) Suction surface canonicals at wing centre in ground effect at $\alpha = 1°$. (b) Integrated surface pressures in ground effect at $\alpha = 1°$.

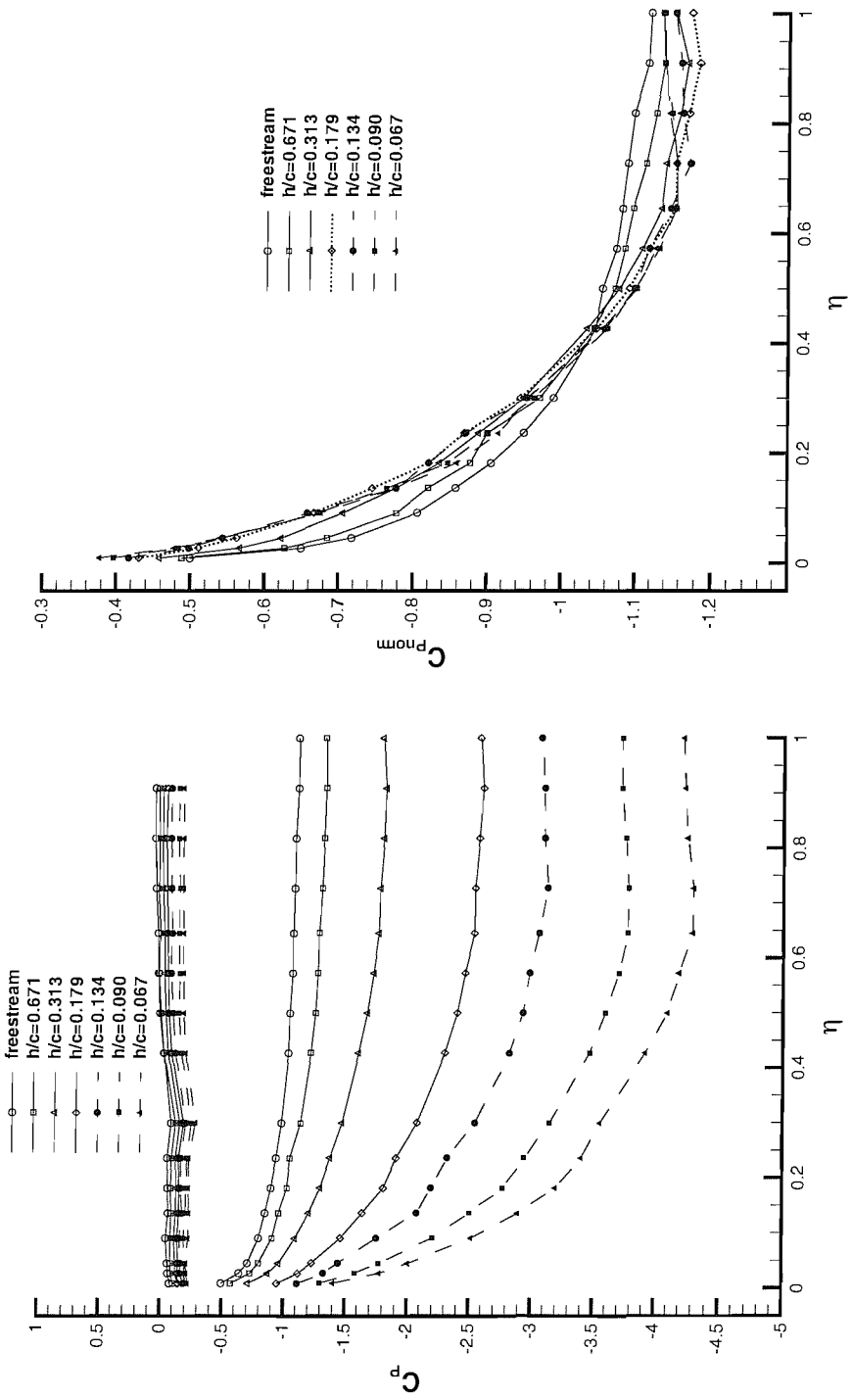

Figure 10: Spanwise surface pressures in ground effect at $\alpha = 1°$ (a) Raw results. (b) Normalised.

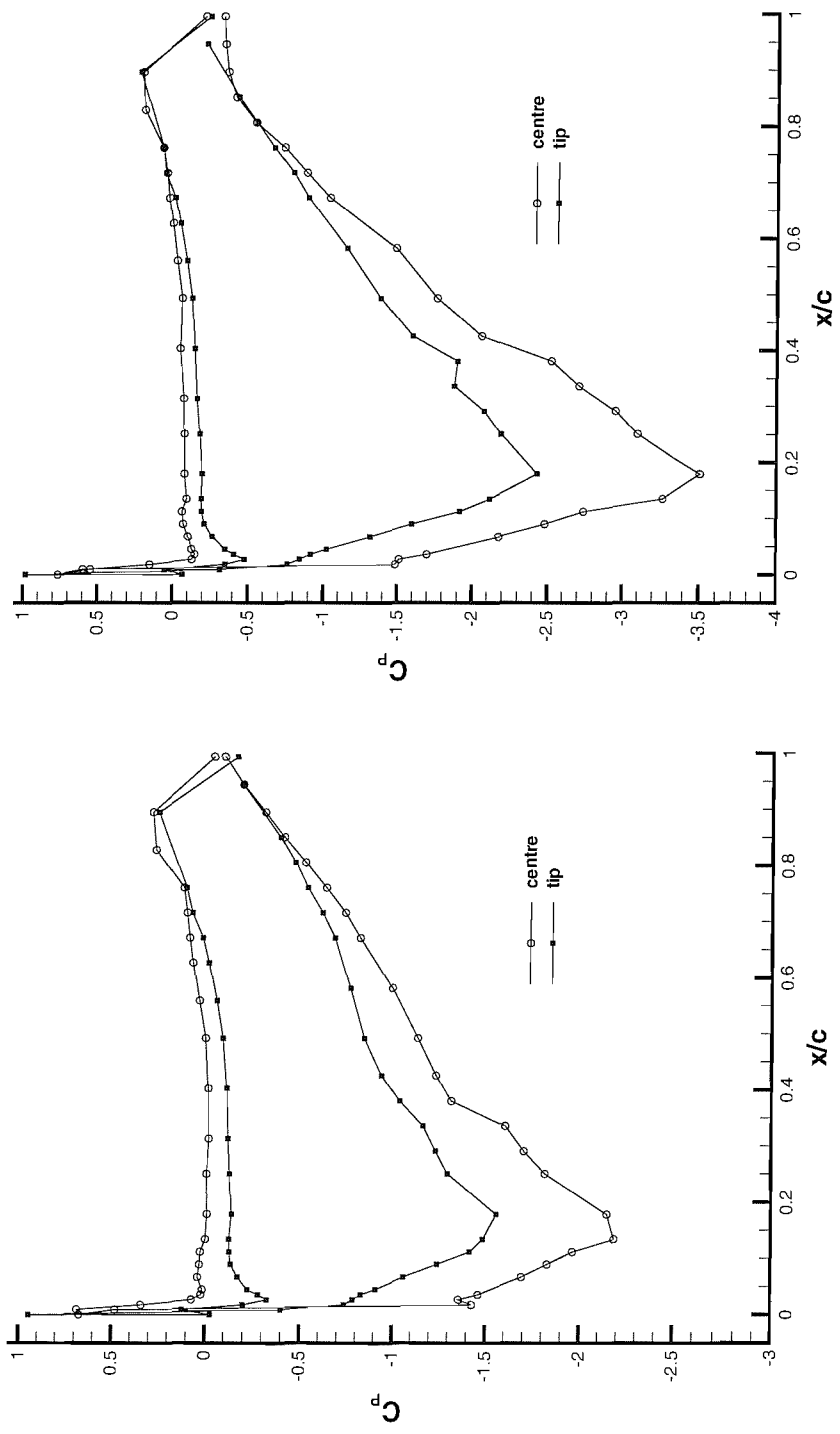

Figure 11: Spanwise surface pressures at wing centre and wing tip in ground effect at $\alpha = 1°$ (a) h/c=0.313. (b) h/c=0.134.

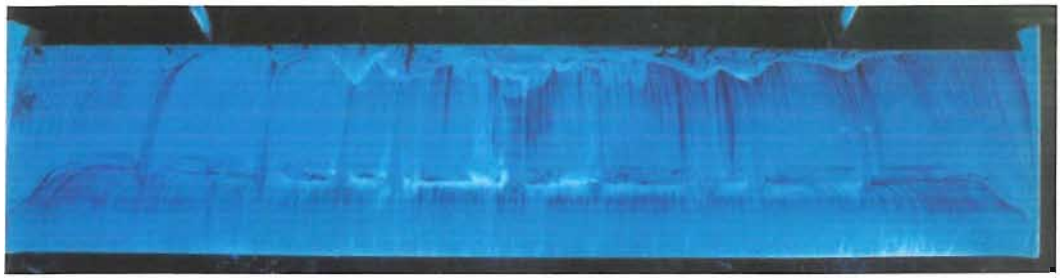

(a)

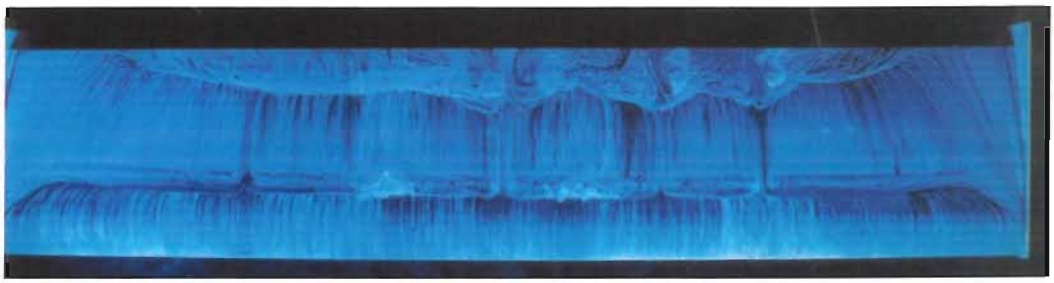

(b)

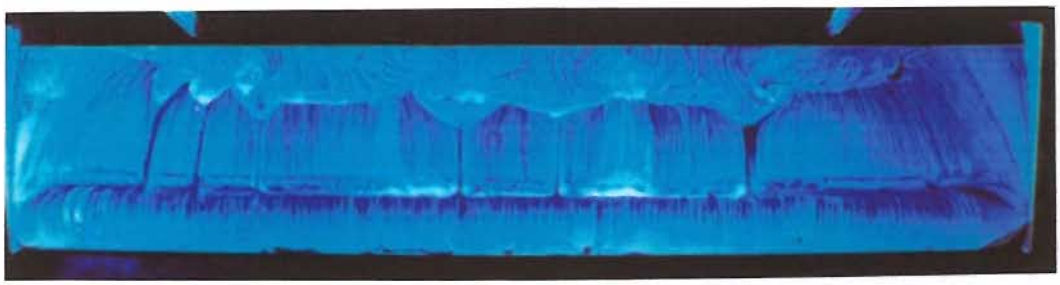

(c)

Figure 12: Oil flow visualisation on suction surface, leading edge lowermost (a) $h/c = 0.134$ (b) $h/c = 0.090$ (c) $h/c = 0.067$

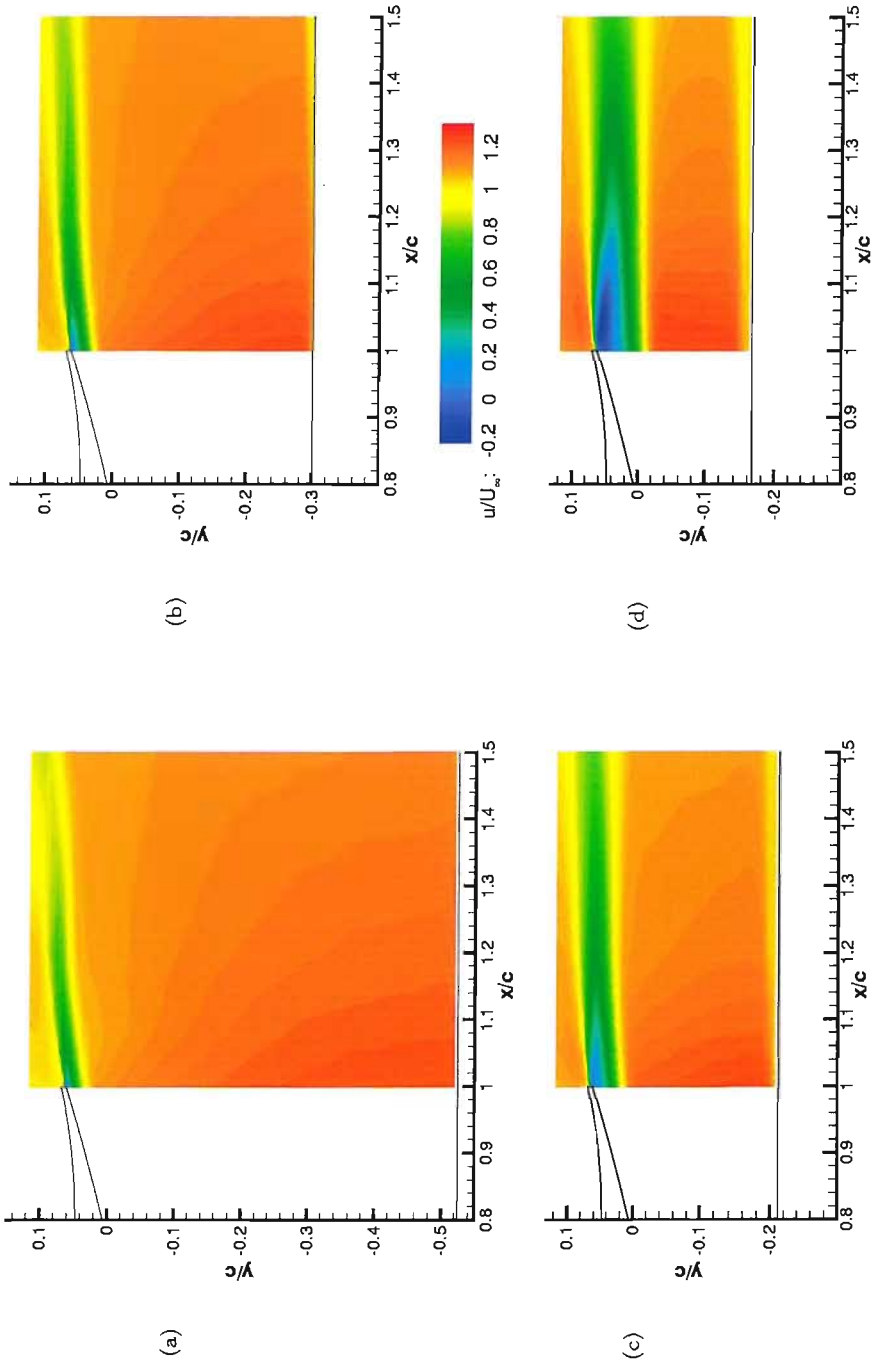

Figure 13: LDA u/U_∞ velocity contours at heights of $h/c = 0.448, 0.224, 0.134, 0.090$

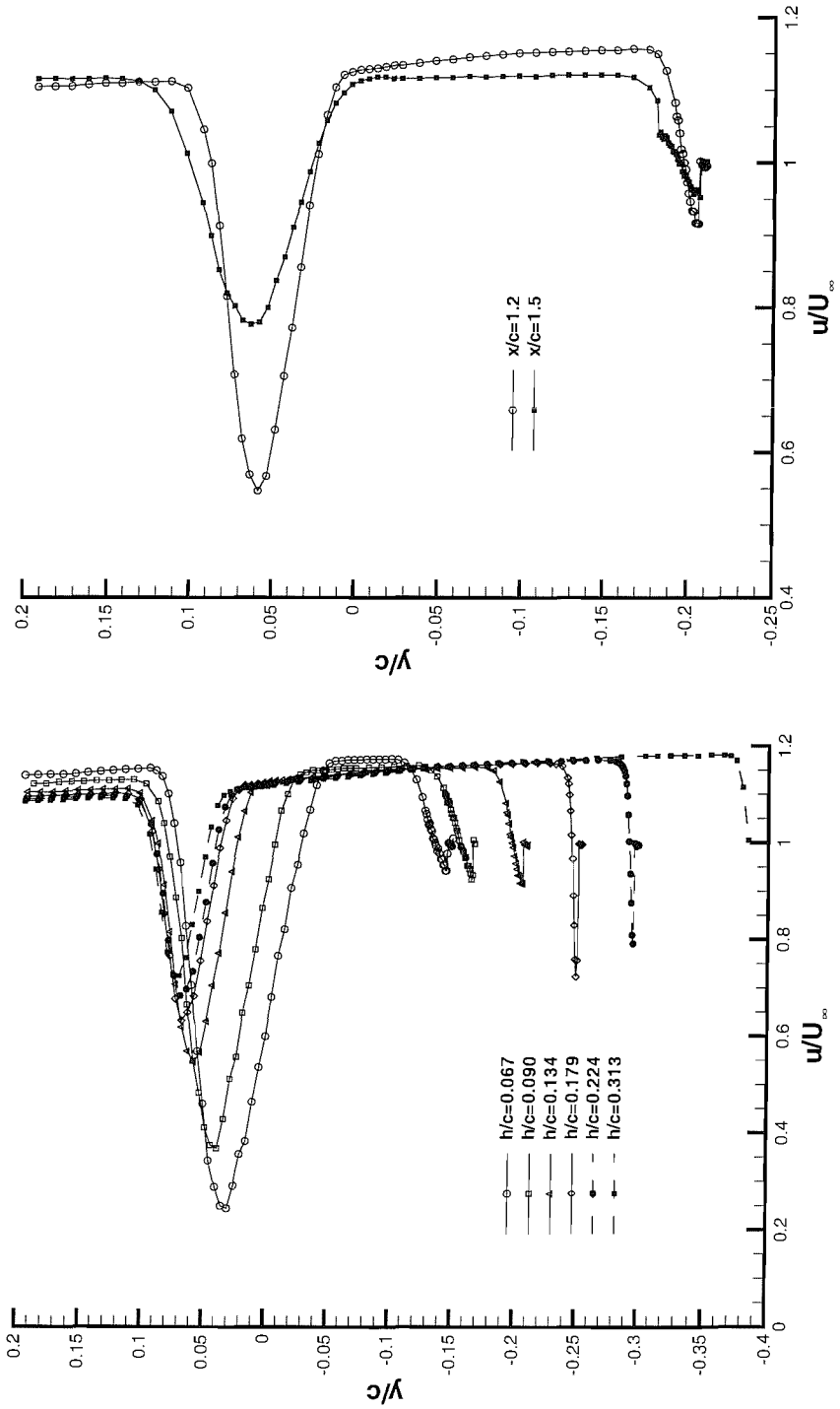

Figure 14: LDA u/U_∞ velocity profiles (a) Wake profiles at $x/c = 1.2$. (b) Wake profiles for $h/c = 0.134$.

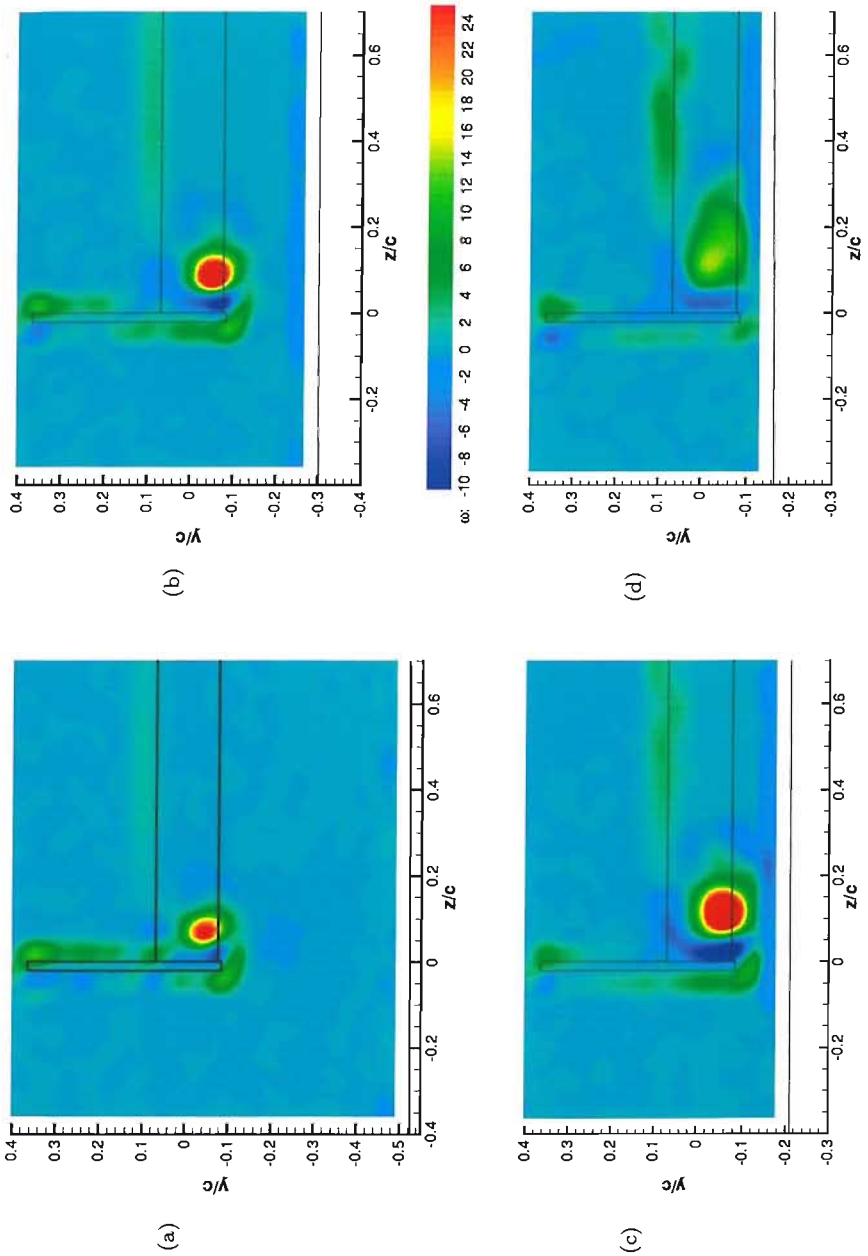

Figure 15: Wing tip vortex at heights of $h/c = 0.448, 0.224, 0.134, 0.090$; contours of planar vorticity

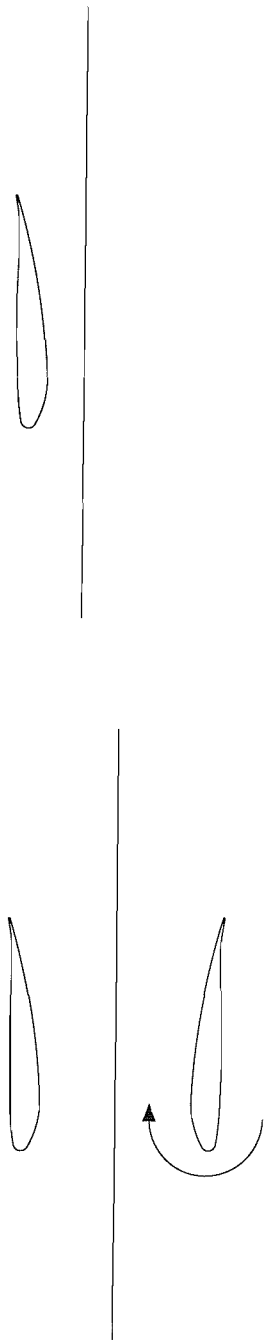

(a)

(b)

Figure 16: The ground effect for an aerofoil (a) Image model. (b) Diffuser effect.

h/c	x_{sep}/c
0.224	0.99
0.179	0.96
0.134	0.91
0.112	0.87
0.090	0.80
0.082	0.78
0.076	0.75
0.067	0.71

Table 9: Boundary layer detachment location at small ground heights.

h/c	$\omega c/U_\infty$
0.671	28.9
0.448	22.0
0.313	37.4
0.224	45.1
0.179	47.6
0.134	64.5
0.112	28.2
0.090	14.9
0.067	7.00

Table 10: Maximum vorticity in wing tip vortex at $x/c = 1.2$.

Chapter 5

Single Element Wing in Ground Effect at Various Incidences

5.1 Introduction to Chapter

This chapter presents the experimental results found from testing the single element wing at a variety of incidences at the different ground heights. All testing was performed transition free. The aerodynamic performance is discussed together with the surface pressure results. Typically, incidences in the range $-10°$ to $+25°$ were tested, although for the cases in close proximity to the ground, the endplates did not allow testing over the more extreme negative incidences.

5.2 Forces

Due to the nature of the results, results can be presented as curves of downforce with height for various incidences, and liftcurves at various heights. Both approaches are used, since the results are both of interest.

5.2.1 Variation of Downforce with Height

The variation of downforce with height for incidences from $\alpha = -3°$ to $9°$ is presented in Figure 17a. For the lowest ground heights, the geometry of the endplates prevented the lowest incidence runs to be performed. Hence at $-3°$ and $-1°$ the force reduction phenomenon cannot be seen to occur. Apart from the highest incidence, in addition to increasing the downforce, the effect of increasing the incidence is to reduce the sensitivity of the downforce to the ground height. To illustrate the general effect, the slope of the curves between heights of $h/c = 0.179$ and 0.134, a region of force enhancement typical of practical application, reduces from 4.3 at $1°$ to 2.9 at $3°$, 1.8 at $5°$, and

1.1 at 7°. The effect of reducing the sensitivity to ground height as the incidence increases is to reduce the gain in downforce at the maximum downforce compared to out of ground effect. For the same incidences, the increments in downforce from a height of $h/c = 0.671$ to the maximum downforce for each of the same incidences are 0.90, 0.82, 0.75 and 0.70 respectively. There is also a slight tendency for the force reduction phenomenon to occur at a larger ground height for higher incidences.

5.2.2 Liftcurves at Varying Heights

Replotting the results as more familiar liftcurves for the different heights, Figure 17b, shows the effect of incidence on downforce at each height. Note that the symbols represent only every other experimental data point. At the largest heights, the liftcurves are of a similar shape to the freestream case. The trailing edge stall occurs at decreasing incidence with decreasing ground height, but C_{Lmax} increases. For all ground heights applicable, the liftslope has been calculated for the straight line region, i.e. for the range of incidences where the flow is fully attached, Figure 18a. The liftcurve is seen to increase as the ground height is reduced.

For moderate heights of $h/c = 0.134 - 0.313$, the downforce consistently reduces more after the maximum, in a gentle, then sharper manner. The straight line, low incidence, region of the liftcurve begins to form two straight lines joined by a gentle curve, this being caused by the trailing edge separation, for example $h/c = 0.224$ at $\alpha \approx 0°$ The maximum downforce increases with reducing ground height to a value of C_{Lmax}=2.26 occurring at $h/c = 0.134$, $\alpha = 12.3°$, the maximum value in the study. The incidence at the position of maximum downforce also increases.

For closer ground proximities practically all cases involve separated flow, the curves generally depicting both a partly straight region, falling off once the maximum downforce has been reached, or mainly the falling off region for the most extreme of cases. The combination of separated flow, the extreme ground effect, and the diffuser effect with high ratio leading edge to trailing edge heights, causes the unfamiliar shapes. For nearly all of the midrange to higher incidences, a greater downforce could be attained at a larger ground height. The maximum downforce, together with the angle at which it occurs, decreases with decreasing height.

5.3 Surface Pressures

5.3.1 Chordwise Pressures

The chordwise pressures at the centre of the wing are presented in Figure 19 over a range of heights, for $\alpha = 5°$. The effect of varying the height on the pressure distributions at $\alpha = 5°$ is similar to the results for the reference incidence of $\alpha = 1°$, Figure 8. The loadings on the suction surface increase, until the pressure recovery is such that flow separation results, as seen by the constant pressure regions. On examination of the pressure near to the trailing edge, it is possible to conclude that

boundary layer separation occurs at a greater height for the higher incidence $\alpha = 5°$ case.

5.3.2 Canonicals

For the same incidence of $\alpha = 5°$, the suction surface canonicals have been plotted in Figure 18b. Comparing the canonical pressures with the separation point from the oil flow visualisation in the previous section gives the approximate result that separation occurs at a canonical pressure in the range $\overline{C_P} = 0.68 - 0.71$. If this is superimposed on the canonical pressures at $\alpha = 5°$, it can be concluded that flow separation is likely to occur at a height at approximately $h/c = 0.5$ for $\alpha = 5°$, significantly greater than that for $\alpha = 1°$.

Although not illustrated here, results have also been analysed at incidences of $\alpha = -3°$ and $9°$. The effect of increasing the incidence causing a greater height at which separation occurs in ground effect is supported by the analysis of these results.

5.4 Discussion

As the incidence of the wing is increased in freestream, the boundary layer comes nearer to separation, which occurs at approximately $11°$ in freestream. It has been shown that ground proximity causes greater pressure recovery from which the boundary layer is more likely to separate. Separation will occur at some ground height for a particular incidence. For a higher incidence, the ground effect compounded with the higher incidence implies that the boundary layer is closer to separation, and has the overall effect that separation will occur at a greater height for the greater incidence.

Separation results in a loss of circulation, and a loss of downforce. For the higher incidence case, separation, and the loss of downforce occurs at a greater height than for the lower incidence case. This results in a lower maximum downforce for the higher incidence case. The downforce with height curves for the greater incidences are less sensitive to the ground height, both in terms of magnitude of downforce gain from freestream to the force reduction phenomenon, and the slope of the line in the force enhancement region.

The well known ground effect of the liftcurve increasing with proximity to the ground is observed [38].

5.5 Summary

The effect of an increase in the incidence of the wing has been shown to cause a greater maximum downforce, and a lower gradient for the downforce with height curve, in the force enhancement region. If the incidence is increased, the flow is closer to separation, changing the characteristics of the downforce with height.

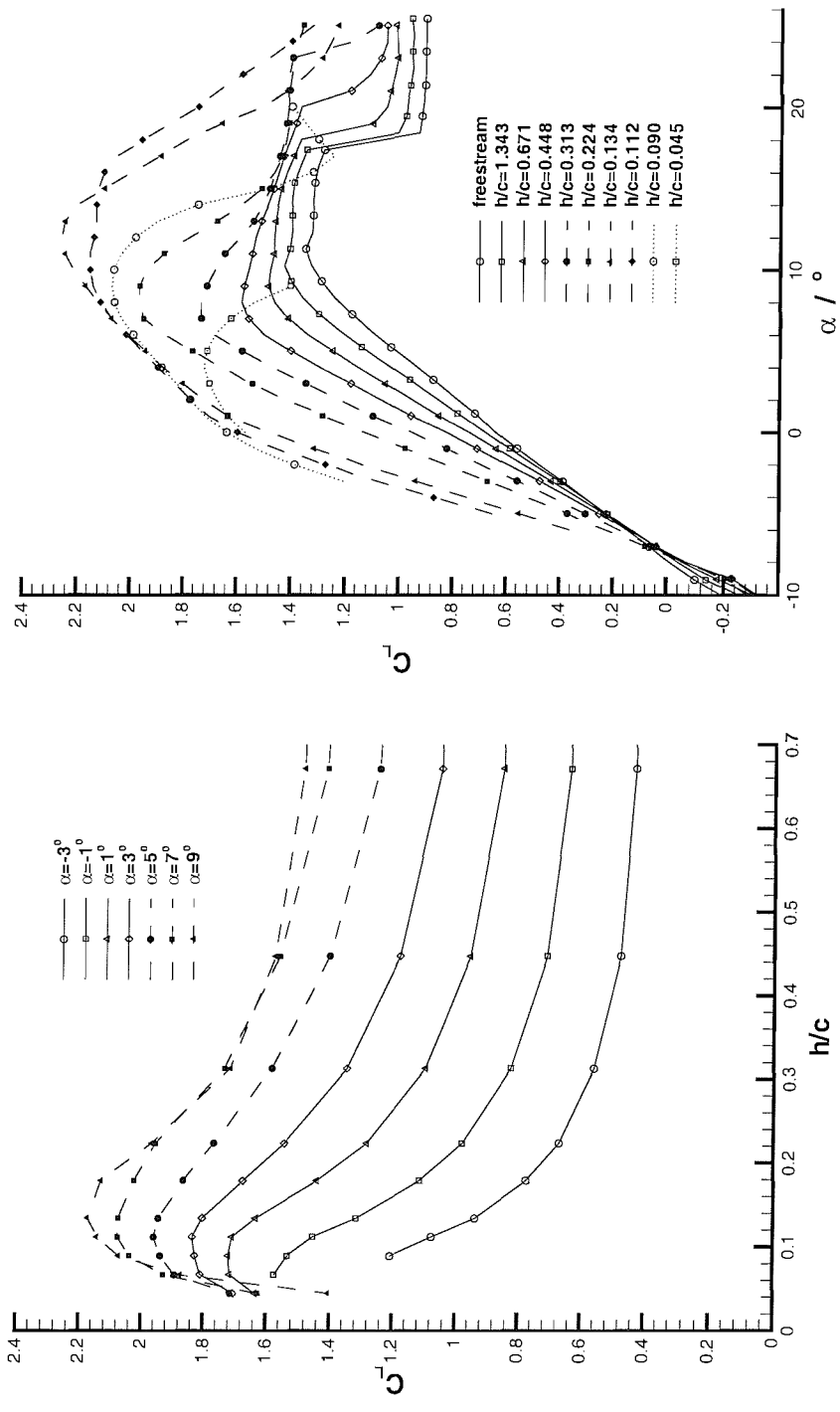

Figure 17: Downforce in ground effect; (a) Downforce with height for various incidences. (b) Liftcurves at different heights.

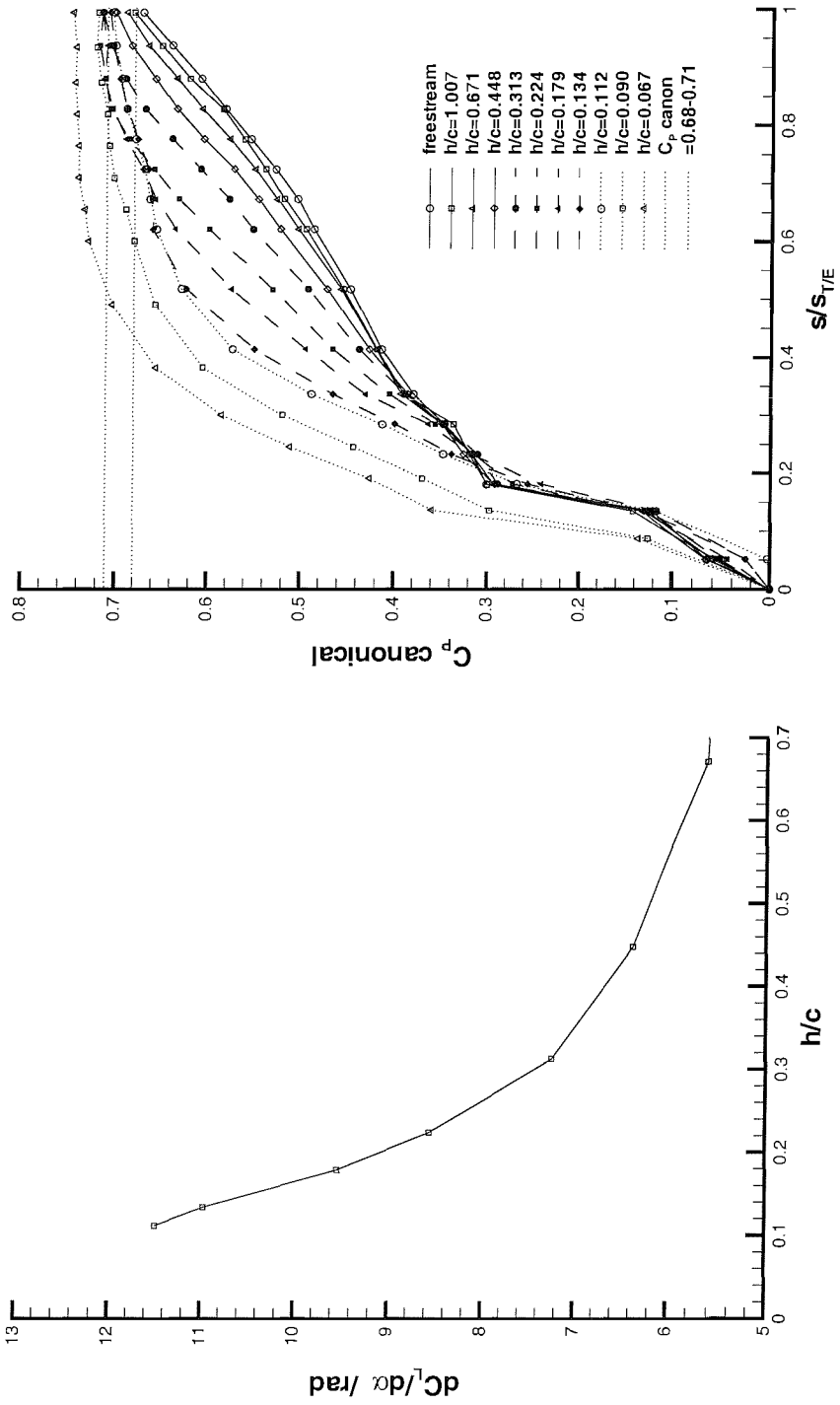

Figure 18: (a) Liftslope in ground effect. (b) Suction surface canonicals at $\alpha = 5°$.

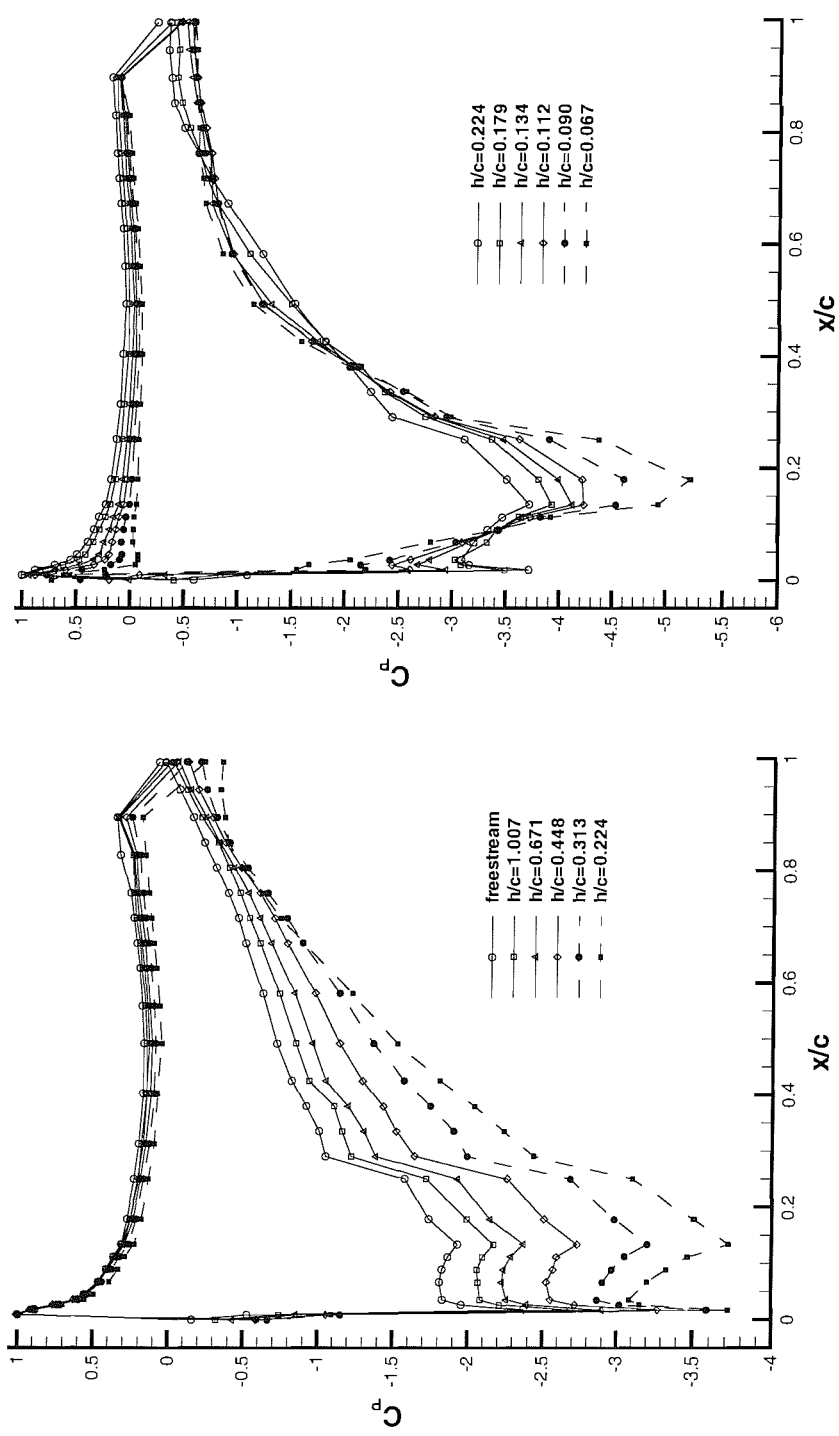

Figure 19: Chordwise surface pressures at wing centre in ground effect at $\alpha = 5°$ (a) Moderate and large ground heights. (b) Small ground heights.

Chapter 6

Single Element Wing with Fixed Transition

6.1 Introduction to Chapter

This chapter presents the results found from experimental testing of the single element wing at the reference incidence of 1° at a selection of ground heights, with fixed transition. The boundary layer was tripped using strips applied to the suction and pressure surfaces at $x/c = 0.1$, of length less than 0.015c. The primary reason for fixing transition was for CFD modelling purposes. Preliminary CFD runs using transition fixed at the location of natural transition proved problematic and produced erroneous results. Results with the boundary layer tripped are also of practical interest. It is common for the front wing to pick up dirt, dust, and debris through a race. The tests with tripped transition may give an indication of the effects to the flow state at the end of a race.

Initial tests with fixed transition were performed with 140 grit strips, using a sizing procedure detailed by Braslow and Knox [88]. However, it was found that this was an insufficient size to trip the boundary layer. It was then decided to perform transition fixed tests with 60 grit, and a range of data was obtained. However, later in the study, it was discovered that the 60 grit strip was too large, and it was adversely effecting the results. Tests were then repeated with 100 grit. This size was found to be sufficient to trip the boundary layer, with results that were not as significantly effected as the 60 grit transition fixing.

As part of this investigation, forces, surface pressures, LDA and PIV methods were used. Because the three-dimensionality effects close to the ground have already been discussed for a single element wing, these were not investigated for the transition fixed case. Instead, the features of the wake flow at the wing centre were examined in greater detail.

6.2 Forces in Freestream

As a datum, the liftcurve and the drag polars are presented in freestream, Figure 20.

The liftcurve for the transition fixed case illustrates a lower C_{Lmax} of 1.22, occurring at an incidence of $\alpha = 9°$. The boundary layer is thicker for the transition fixed case compared to the transition free case, and closer to separation, for a given incidence. Stall occurs at a lower incidence, resulting in a lower C_{Lmax}.

The drag increases at practically all values of C_L. The boundary layer is turbulent over a large portion of the chord, in addition to the direct increase in profile drag from the trip strip.

6.3 Forces in Ground Effect

Figure 21a shows the variation of downforce with height at the reference incidence for transition free and transition fixed cases. At large and moderate ground heights, above $h/c \approx 0.2$, the downforce for the transition fixed case is a little lower than that for the transition free case. The difference increases as the height is reduced. Below $h/c \approx 0.2$, the difference between the two curves becomes significant. In a similar manner to the transition free results, the gradient of the curve reduces, and the downforce eventually reaches a maximum. This occurs at a height of $h/c = 0.112$, a little greater than the transition free case, which is at $h/c = 0.082$. There is a marked difference between the magnitude of the downforce; the transition fixed case peaks at $C_L = 1.39$, compared to $C_L = 1.72$ for the transition free case. At heights below the maximum downforce, the reduction in downforce is significantly less severe than the transition free case, and the curve is more plateau shaped. Figure 21b gives the drag at different heights. The transition fixed results feature a broadly constant increase in C_D over the transition free results. Unfortunately, problems were encountered with the drag measurement component of the overhead balance, and the drag results for the transition fixed case were not as repeatable as found in other tests.

6.4 Surface Pressures

Surface pressures results at the semispan are presented here only. Three-dimensional effects have been described for the transition free results in an earlier chapter. Figure 22a shows the pressure distribution at the wing centre at a height of $h/c = 0.134$ for the transition free and fixed cases. The main effect of fixing transition is to reduce the suctions over the suction surface. The peak suction is reduced, along with the suction upstream of this, the acceleration region, and downstream of this, the pressure recovery. The pressure recovery is smoother, and there is no bump in pressure from the separation bubble, as in the transition free case. Near to the trailing edge, it can be seen that a greater portion of the flow is separated, from the plateau in the curve. For the transition free case at this height, the boundary layer separates at $x/c = 0.91$. The exact point of detachment

is not known for the transition fixed case.

The pressure distributions at different heights are given in Figure 22b. The effect of the ground on the surface pressure distribution is qualitatively similar to the transition free case. For the larger heights, the suctions increase over the entire suction surface, including the adverse pressure gradient for the recovery. The pressure surface values are similar. For very small ground heights, gains in suction occur over the lowest part of the suction surface, and also the pressure surface. Increases in suction occur over most of the remainder. Comparing the transition fixed and free results at all heights (not presented here) gives the result that the suction surface distributions are effected by a greater extent for the smaller ground heights.

6.5 Laser Doppler Anemometry Surveys

The LDA system was again used to investigate the wake at the semispan. The grid was extended vertically and further downstream, compared to the transition free tests.

Figure 23 presents time-averaged LDA results for the u/U_∞ velocity contours at heights of $h/c = 0.448, 0.224, 0.134$ and 0.067. The general flow features of interest can be seen qualitatively in the plots. The wake becomes thicker as it moves downstream, with the velocity deficit reducing due to small-scale turbulence. As the ground is approached, the wake increases size, and velocity deficits become larger. In addition to this, the path of the wake changes, such that the angle reduces with increasing ground proximity. Between the wake and the ground, the flow faces an adverse pressure gradient, especially visible in the region of $x/c = 1.0 - 1.5$. For the lowest case to the ground, $h/c = 0.067$, the wake from the wing merges with the ground plane, at $x/c \approx 1.5$.

Boundary layer profiles were taken at $x/c = 1.0$ at the suction surface, along a line ζ normal to the surface, and are presented in Figure 24a. A small spacing was used for the points close to the wing. The first points were taken on the surface. Due to the finite size of the measurement volume, and the flare from the surface, the distance ζ from the surface was calculated using the last data point with no data to be $\zeta = 0.0$. The true surface is therefore very slightly lower than this point. The thickening of the boundary layer can be seen as the height is reduced. For the $h/c = 0.224$ case, the boundary layer seems to be on the verge of separating. It is difficult to be more certain due to the limitations of the system. The results at the two lower heights clearly show that the boundary layer has separated from the surface, from the flow reversal present.

Figure 24b shows a series of wake surveys performed at a height of $h/c = 0.448$. The velocity at the maximum velocity deficit increases from $u/U_\infty = 0.81$ at $x/c = 1.5$ to 0.90 at 2.0 and 0.93 at 3.0. The height at which this occurs increases from $y/c = 0.08$ to 0.10 and 0.13, for the three locations, as the height of the wake increases, as can be seen in the contours (Figure 23). The height at the top of the wake, as defined by the 99% velocity at the edge of the wake, increases from $y/c = 0.13$ to 0.16 and 0.22 at the three locations. This compares with the height at the bottom of the wake remaining approximately constant at y/c=0.04, 0.04 and 0.06 respectively.

The thickness of the wake increases from $\delta = 0.09$ to 0.12 and 0.16. Information regarding the growth of the wake for several different heights has been tabulated in Table 11. Similar results for heights of $h/c = 0.224$, and 0.067 are presented in Figure 25, giving similar trends as the wake moves downstream.

The effect of changing the height of the wing above the ground on the wake at $x/c = 1.5$ is shown in Figure 26a. The wake grows significantly as the ground is approached, from $\delta_{99}/c = 0.09$ to 0.11, 0.17, 0.22 and 0.23. Again, these are available in Table 11. For the smallest height, $h/c = 0.067$, the wake has merged with the ground boundary layer, and the quoted size for the thickness is not strictly valid. For the next height, $h/c = 0.090$, (not illustrated here) the wake appears close to merging with the ground boundary layer. The location of the top of the wake remains constant, at $y/c \approx 0.12$ for all of the heights. However, the bottom reduces height from $y/c = 0.04$ for the greatest ride height to -0.11 for the smallest height. This has the effect of lowering the height at which the maximum velocity deficit occurs as the ground is approached. The maximum velocity deficit also increases. Again a velocity deficit can be seen very close to the ground. The effect of reducing the height of the wing is to increase the size of the region of velocity deficit, in terms of its thickness.

Figure 26b shows velocity profiles for the $u'u'/U_\infty^2$ perturbation velocity, from the results at $x/c = 1.2$. At the largest height, $h/c = 0.448$, there appear to be two distinct peaks of $u'u'/U_\infty^2$ velocity from the wake of the wing. At the next height, $h/c = 0.224$, the perturbation velocities have increased in magnitude and the twin peaks are a little more distinct, also the case for $h/c = 0.134$. For the results at $h/c = 0.067$, the peaks grow again. However, the lower peak is a significant amount larger than the first peak, both in terms of the $u'u'/U_\infty^2$ values, and the height range of the results. The results at $x/c = 1.2$ were extracted from the trailing edge grid results, not the the wake surveys. These grids do not contain the extra points very close to the ground needed to map the ground boundary layer thoroughly. However, for the lower two heights, a definite increase in $u'u'/U_\infty^2$ velocity can be seen close to the ground.

6.6 Particle Image Velocimetry Surveys at Wing Centre

The tip vortex was not investigated as the effect of the ground has been documented for the transition free configuration. The PIV system was used to investigate the wake of the wing at the semispan, in the near-field region, to elucidate any unsteady effects. Since the LDA system had been used for the mean flow results, the fundamental reason for employing the PIV system is to investigate the instantaneous flow field, not the time-averaged results. The laser light sheet was set up to illuminate a streamwise slice at the semispan of the wing, with the laser mounted downstream of the moving ground. The camera was located perpendicular to the light sheet, as to cover the rearmost portion of the wing and the near wake, including the ground. The bottom edge of the image was lined up on the ground. In order to capture results upstream of the endplate

trailing edge, a perspex endplate was used on the side between the camera and the light sheet.

Results were taken using 50 datasets, performing a cross-correlation with a 75% overlap on 32×32 pixels to give results on a 157×125 grid. In addition to this, the results were range validated. It was found to be necessary to process the results at this high grid density to pick up the flow structures as discussed below. Performing any averaging or filtering has the effect of blurring the results too much, such that the results are do not show the existence of these flow structures. Because of the high processing level and the varying quality of the data during the run, most raw images contained areas of bad quality data, especially the results through the perspex endplate; mainly due to patches with a lack of particles in the image. During the cross-correlation stage of processing, the velocities in these areas are resolved incorrectly. When the vorticity is calculated, the bad quality results will cause a high or low vorticity concentration.

In Figure 27, instantaneous vorticity contours are presented at heights of $h/c = 0.448, 0.179, 0.134$ and 0.067. The image for each height has been selected as that which best illustrates the flow structures, showing the best quality results most representative of the flow. The area in the top left portion of each image has been removed, as the results here are obscured by the wing supporting brackets. For the images at large heights, the wing tip casts a shadow over the pressure surface region. Similarly, at small heights, a shadow is cast over the suction surface region. The results are incorrect, but have not been deleted.

At a height of $h/c = 0.448$, the suction surface boundary layer is resolved well. It seems that the boundary layers from the suction surface and the pressure surface form two shear layers, which then form discrete vorticity concentrations, from $x/c \approx 1.2$. The strength of the vortices reduces rapidly as they are convected downstream. The image at $h/c = 0.179$ shows more noise in the results. However, the vortex shedding can still be seen. The vortices emanating from the pressure surface are larger and stronger, and seem more discrete. The vortices from the suction surface are again larger and stronger than for the case at the greater height. However, they seem less ordered. The separation between consecutive vortices has increased. At a height of $h/c = 0.134$, all of the vortices are stronger, less regular, and more chaotic. The effect is amplified for the results at $h/c = 0.067$.

6.7 Discussion

The general effect of transition fixing on the wing is to reduce the downforce by a small value at large ground heights, the deficit increasing significantly with reducing heights. The maximum downforce occurs at a greater height, $h/c = 0.112$, and at heights below this, the downforce falls off slightly. Fixing transition, and increasing the incidence of a wing both have the effect of increasing the boundary layer thickness. The boundary layer is closer to separation than for the transition free case. This results in boundary layer separation occurring at a greater height for the transition fixed case, effectively reducing the circulation, and causing a lower downforce to be generated.

A more thorough study of the wake again shows the growth of the wake as the ground height is reduced to be due to the portion from the suction surface, and the increase in the adverse pressure gradient encountered as the height is reduced. For the lowest case to the ground, $h/c = 0.067$, the wake from the wing merges with the ground boundary layer, at $x/c \approx 1.5$, from the mean flow results. Examination of $u'u'/U_\infty^2$ turbulent velocities in the wake at $x/c = 1.2$ shows the existence of two peaks of the fluctuating velocities. The peaks are of roughly the same size for heights greater and including $h/c = 0.134$. At $h/c = 0.067$, the lower peak is significantly larger than the upper peak.

The instantaneous wake properties investigated using the PIV system shows the existence of vortex shedding from the finite trailing edge. At $h/c = 0.448$, the vortices seem regular and discrete. As the ground height is reduced, the shedding becomes less regular and more chaotic. It is difficult to observe a discrete frequency of the vortex shedding. Of significance regarding vortex shedding is the thickness of the separating shear layers with respect to the distance between the shear layers. From LDA results, the time-averaged thickness of the boundary layer at the trailing edge of the suction surface was found to be $\delta_{99}/c = 0.05$ for a moderate ground height. The thickness of the finite trailing edge is 0.007c. The thickness of the boundary layer at the trailing edge (of the suction surface) will vary with time because of its turbulent nature. The range of the ratios of the boundary layer thickness to the distance between the shear layers increases as the height is reduced, from LDA results, implying that the vortex shedding will be less regular as the height is reduced, in terms of the frequency and size of the vortices that are shed. Vassilopoulos and Gai [42], found that a turbulent boundary layer which increased the shear layer instability at a blunt trailing edge had the effect of increasing the number of discrete shedding frequencies.

6.8 Summary

The effect of fixing transition of the single element wing has been quantified. A small difference in downforce exists between this and the free transition case at larger heights. The difference increases, and at small heights a greatly reduced downforce is generated. The flow features are similar to those for the transition free wing, but separation is induced earlier. The wake study has shown the existence of vortices to be shed from the finite trailing edge. As the height is reduced, the shedding becomes less regular and more chaotic, due to the increased turbulence and boundary layer thickness from the suction surface.

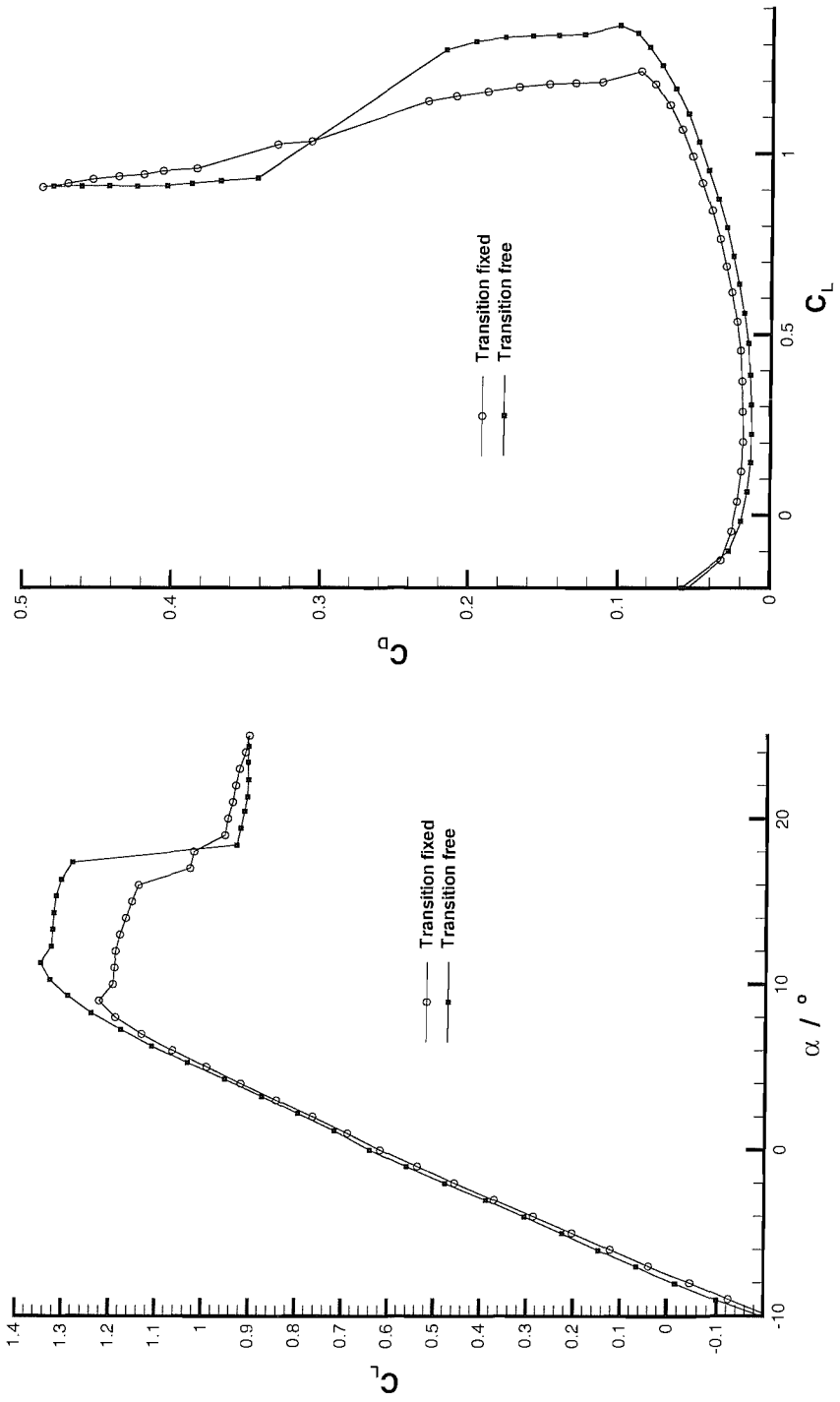

(b) (a)

Figure 20: Forces in freestream, transition fixed; (a) Liftcurve. (b) Drag polar.

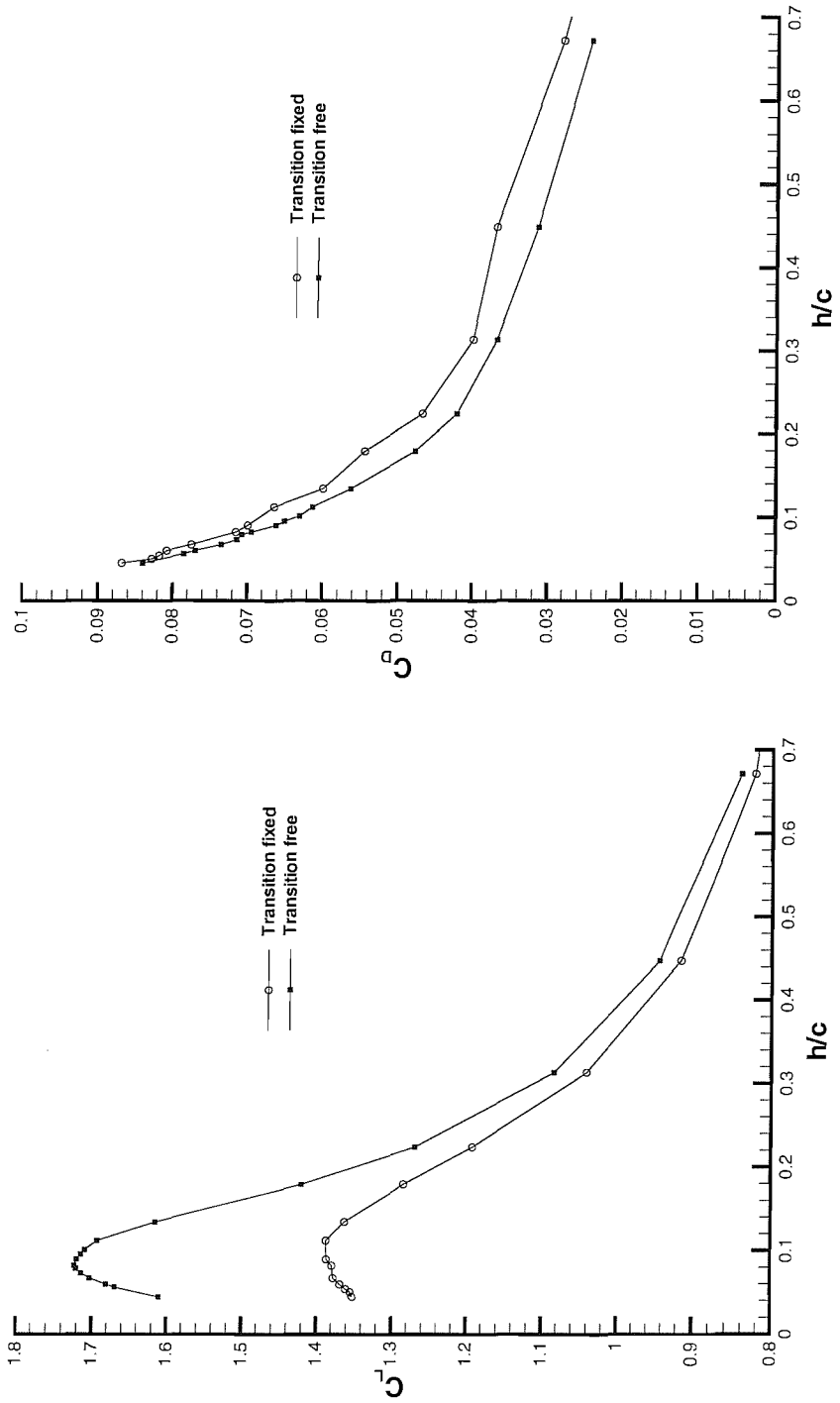

(b) (a)

Figure 21: Forces in ground effect; (a) Downforce. (b) Drag.

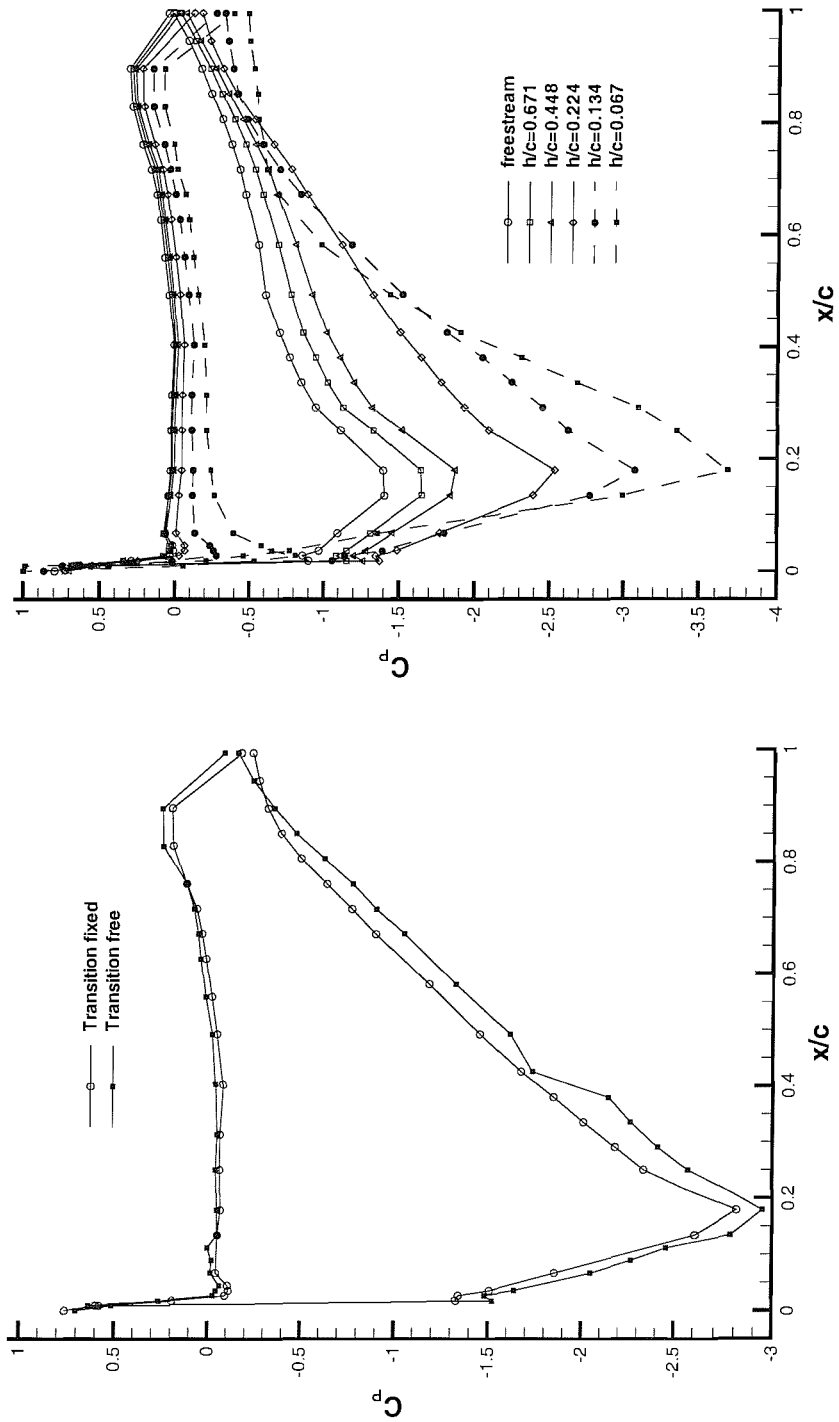

Figure 22: Surface pressures at wing centre (a) Effect of transition fixing. (b) Pressure distributions at different heights.

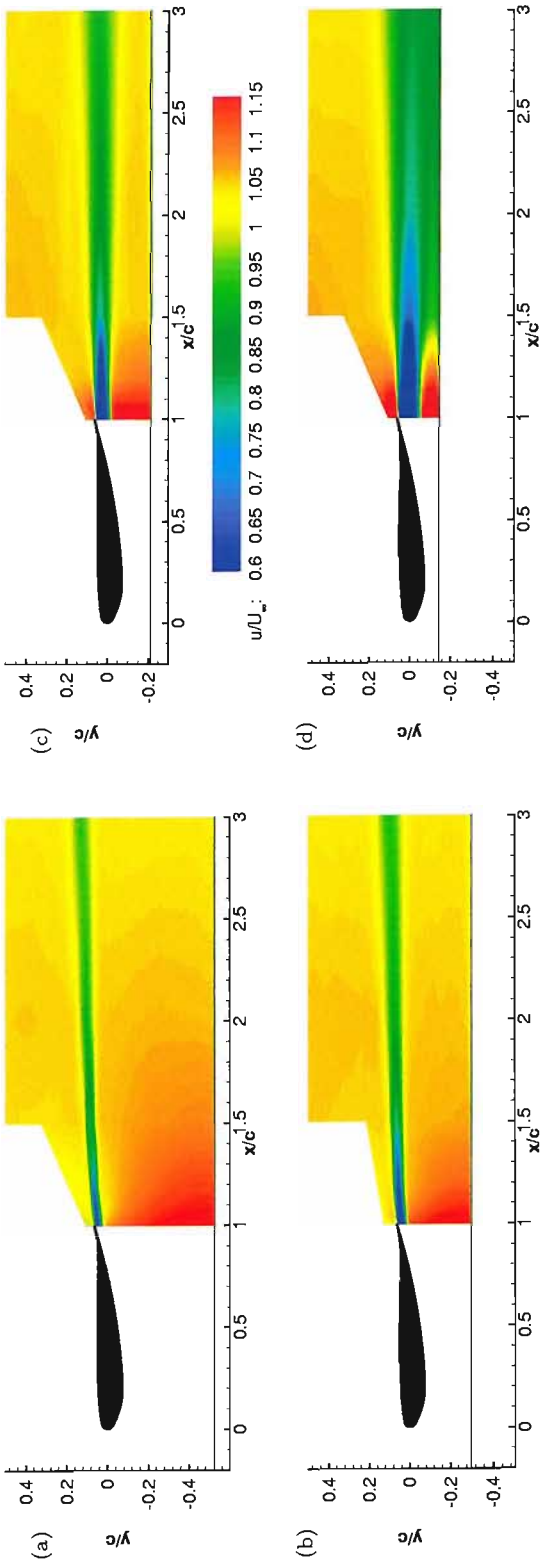

Figure 23: LDA u/U_∞ velocity contours at heights of $h/c = 0.448, 0.224, 0.134, 0.067$

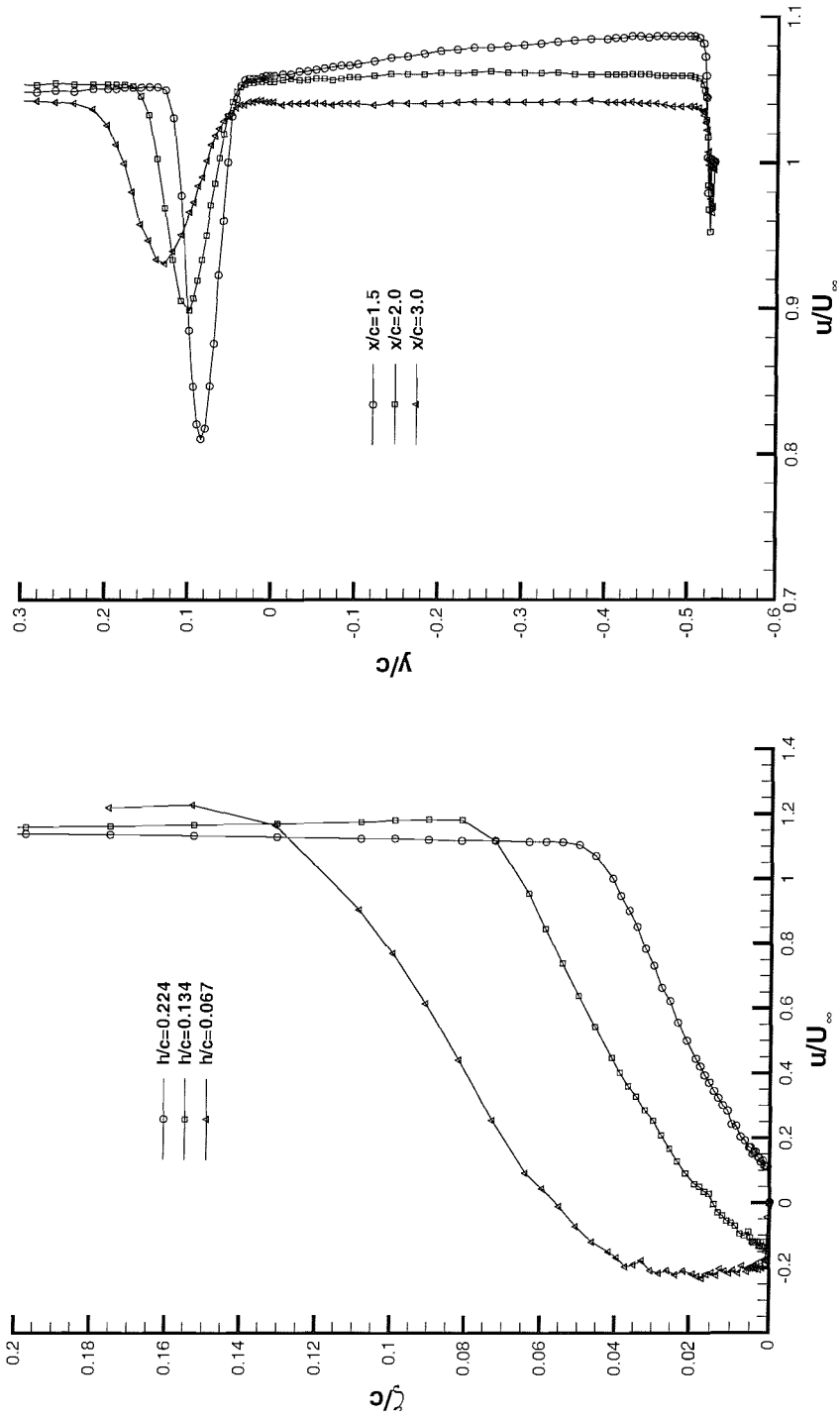

Figure 24: LDA u/U_∞ velocities; (a) Boundary layer profiles at $x/c = 1.0$, suction surface (b) Wake surveys at $h/c = 0.448$

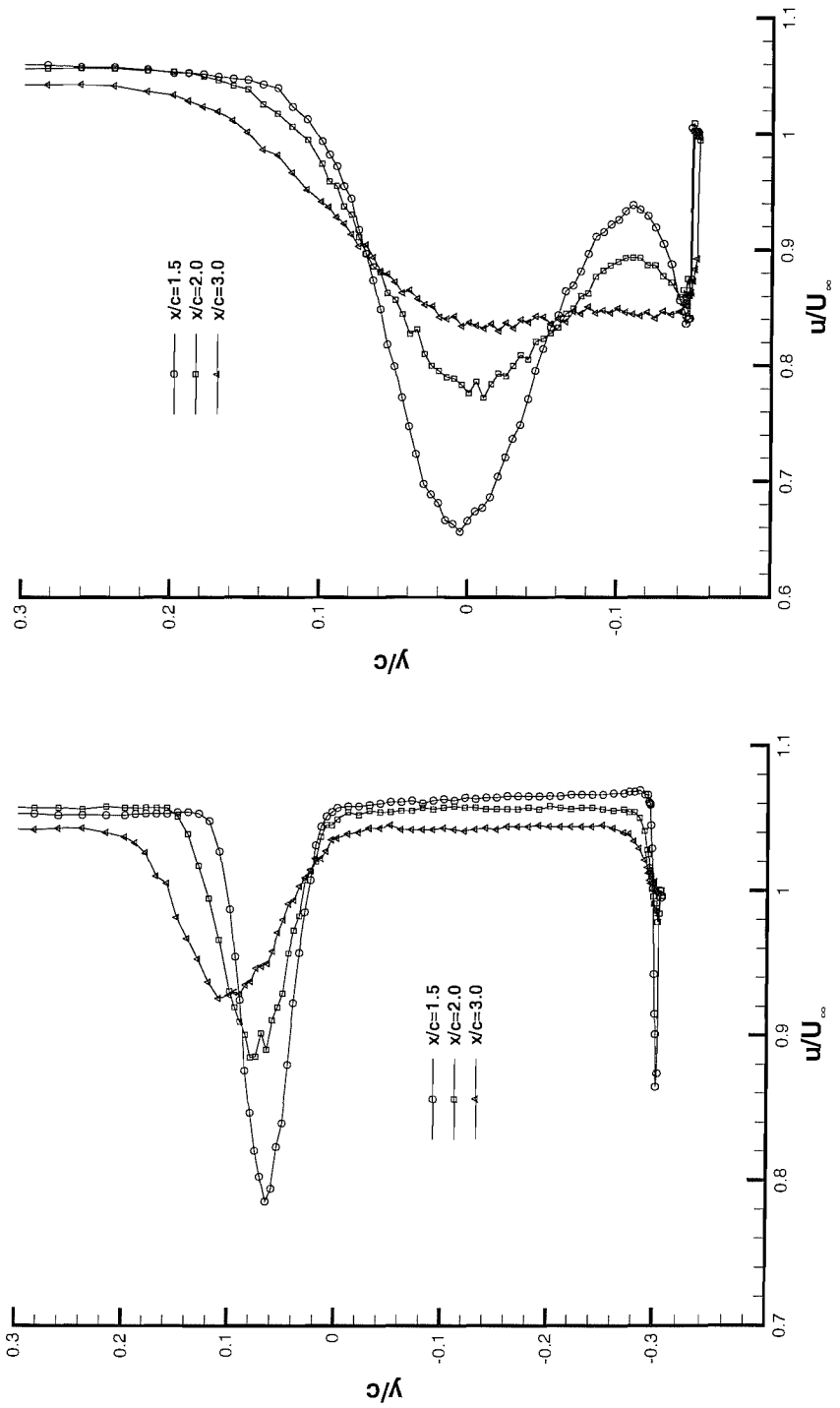

(a) (b)

Figure 25: LDA u/U_∞ wake surveys; (a) $h/c = 0.224$. (b) $h/c = 0.067$.

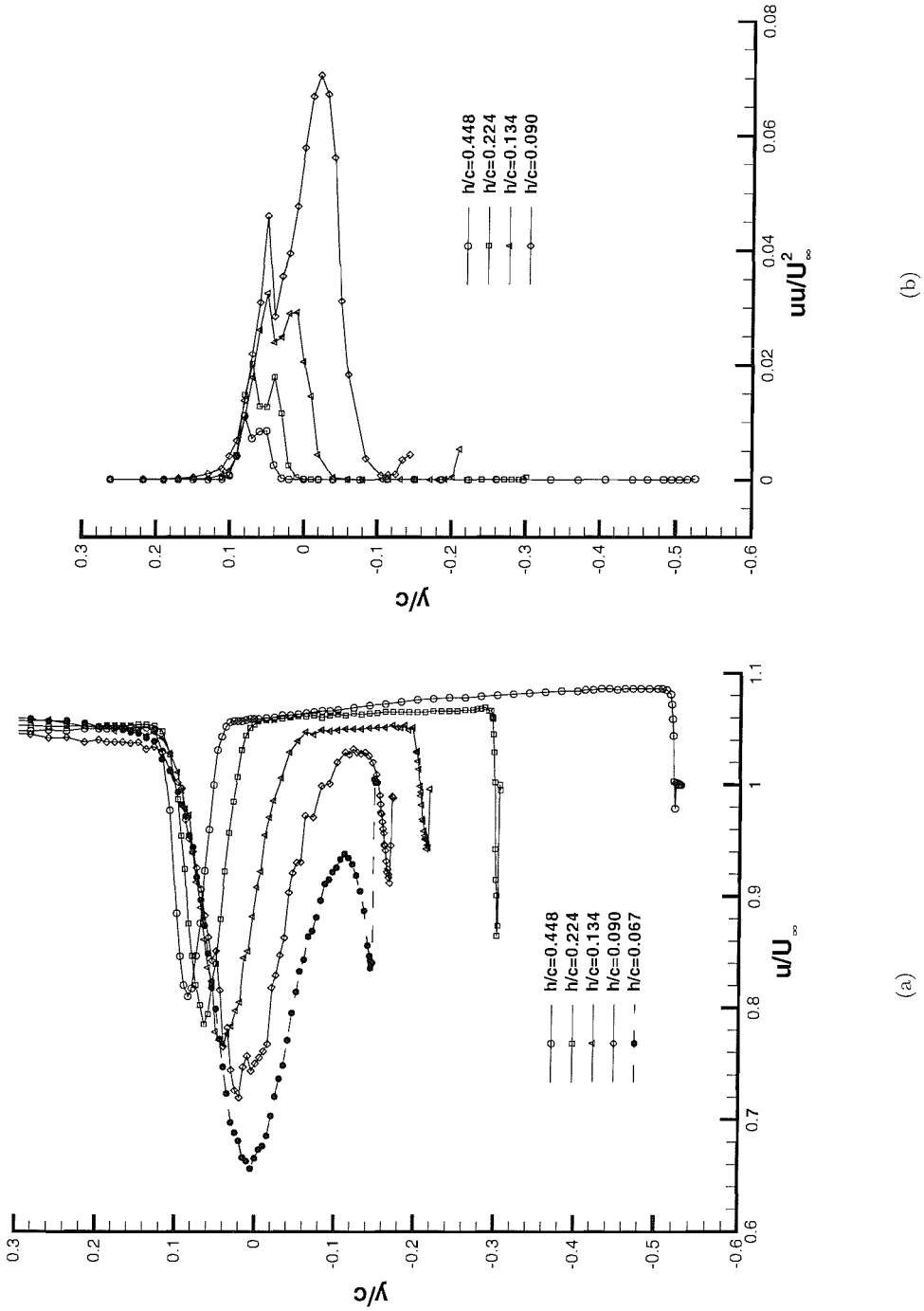

Figure 26: LDA results; (a) u/U_∞ velocities at $x/c = 1.5$. (b) $u'u'/U_\infty^2$ perturbation velocities at $x/c = 1.2$

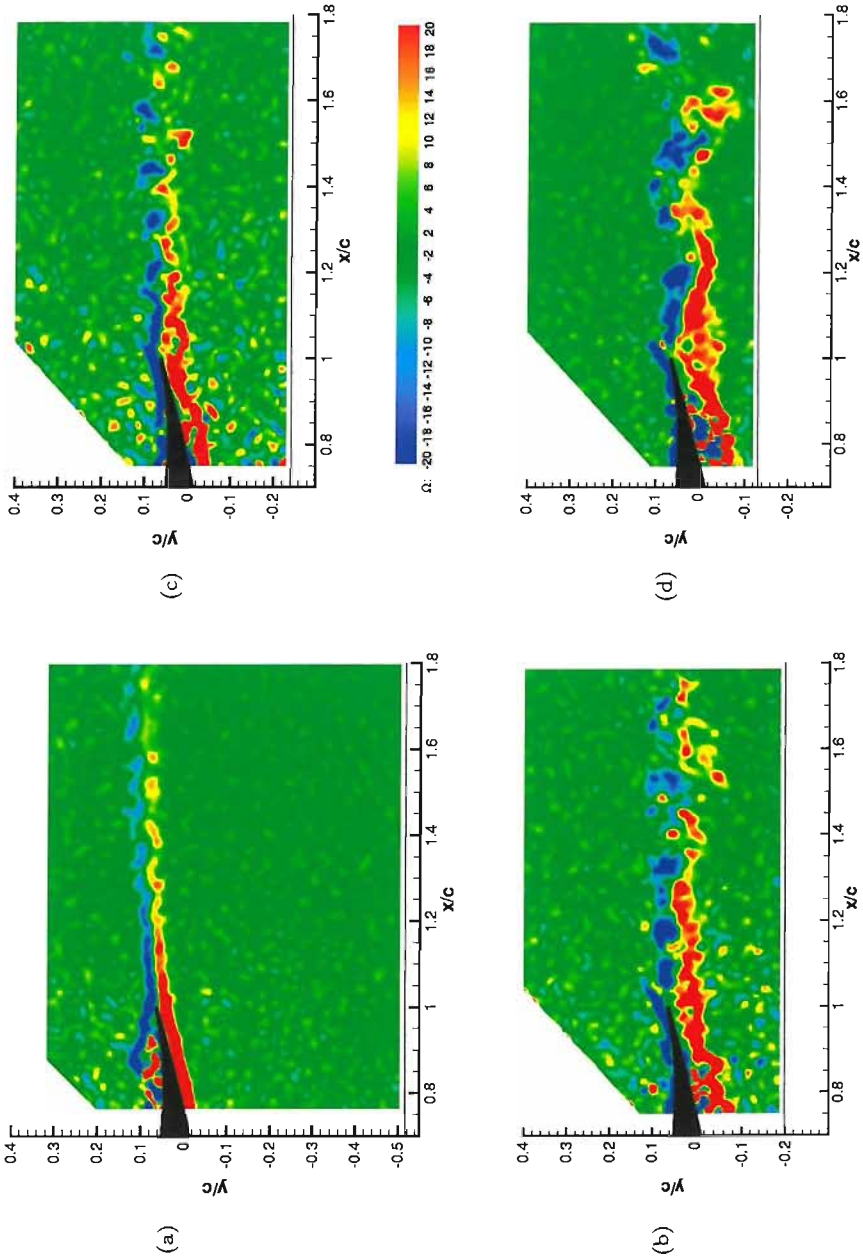

Figure 27: Instantaneous PIV vorticity contours at heights of $h/c = 0.448, 0.179, 0.134, 0.067$

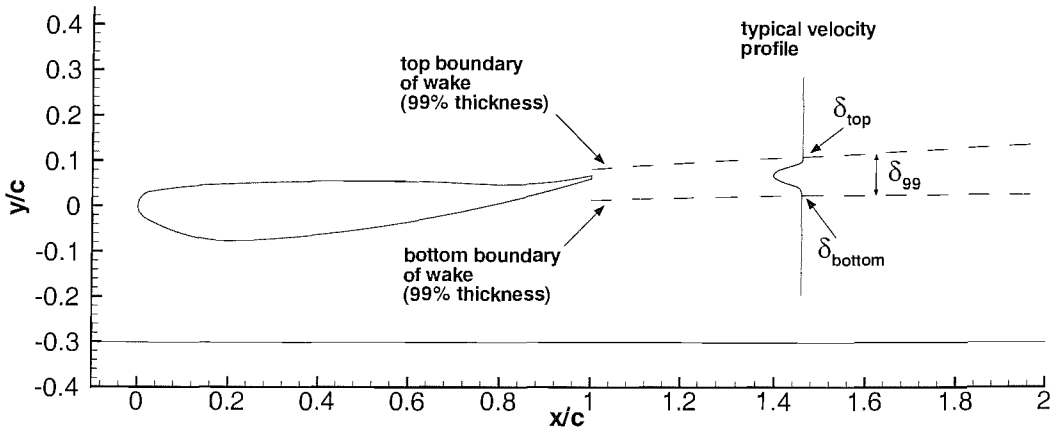

Figure 28: Schematic of wake profile

h/c	x/c	u_{min}/U_∞	y/c at u_{min}	y at δ_{top}	y at δ_{bottom}	δ_{99}/c
0.448	1.5	0.81	0.08	0.13	0.04	0.09
	2.0	0.90	0.10	0.16	0.04	0.12
	3.0	0.93	0.13	0.22	0.06	0.16
0.313	1.5	0.81	0.08	0.13	0.04	0.09
	2.0	0.89	0.09	0.16	0.04	0.13
	3.0	0.93	0.14	0.22	0.04	0.18
0.224	1.5	0.79	0.07	0.13	0.01	0.11
	2.0	0.88	0.08	0.16	0.01	0.15
	3.0	0.93	0.12	0.20	0.01	0.19
0.179	1.5	0.78	0.05	0.12	-0.02	0.14
	2.0	0.88	0.06	0.15	-0.03	0.18
	3.0	0.91	0.07	0.19	-0.03	0.22
0.134	1.5	0.77	0.04	0.12	-0.05	0.17
	2.0	0.85	0.04	0.14	-0.07	0.21
	3.0	0.91	0.05	0.19	-0.08	0.27
0.112	1.5	0.73	0.04	0.13	-0.07	0.20
	2.0	0.85	0.04	0.16	-0.08	0.24
	3.0	0.91	0.06	0.20	-0.10	0.30
0.090	1.5	0.72	0.02	0.12	-0.10	0.22
	2.0	0.84	0.02	0.16	-0.11	0.27
	3.0	0.90	0.01	0.19	-0.12	0.31
0.067	1.5	0.66	0.00	0.13	-0.11	0.23
	2.0	0.77	-0.01	0.17	-0.10	0.27

Table 11: Wake information including maximum velocity deficit and 99% wake thickness; clean wing

Chapter 7

Single Element Wing with Gurney Flaps

7.1 Introduction to Chapter

This chapter presents the experimental results found from testing the single element wing with two different Gurney sizes at a selection of ground heights. Forces and surface pressures were initially performed in the same tests as transition fixing was being investigated, using the 60 grit. On reflection of the significant effect of transition fixing (using the 60 grit), the forces and surface pressures were repeated with the Gurney flaps for the free transition case. The LDA and PIV tests at the wing centre were done during the same tests as for the clean wing, as an extra investigation, when the wakes were investigated for the transition fixed (100 grit) configuration. To remove the trip strips thoroughly would have taken too much time, and it was decided to investigate the wake for the transition fixed (100 grit) configuration. Due to time constraints, forces and pressures were not taken with the Gurney flaps for the transition fixed (100 grit) configuration.

Forces and surfaces pressures are presented for the transition free case. The effect of the Gurney flap on the streamwise flow is presented using chordwise surface pressures, and PIV and LDA tests at the centre of the wing. The LDA and PIV results are for fixed transition.

7.2 Forces in Freestream

As a baseline case, forces in freestream were measured. The liftcurves can be seen in Figure 29a. The results suggest that fitting a Gurney increases C_L at zero incidence, and has a small effect on the stalling angle, leading to an increase in C_{Lmax}.

Adding a Gurney reduces slightly the incidence at which stall occurs, from 11° to 10°, but it should be noted that the spacing between the measurement points was typically 1°, which gives an

indication of uncertainties in the results. The smaller Gurney has a disproportionately large effect on the force increment. It can also be seen that the stall of the wing becomes sharper with the addition of the Gurney flaps, with a sharper stall for the larger Gurney compared to the smaller Gurney.

The gain in C_L with the addition of the Gurney from the clean wing increases with incidence. This causes a non-linear liftslope, decreasing with incidence. The mean value for the liftslope, however, increases with the Gurney added. The smaller Gurney is seen to have a disproportionately large effect on the liftslope increase. Values of the liftslope are 4.57, 5.38, and $5.73°/rad$ for the clean wing, the 1.45% and the 2.90% Gurney flap respectively.

Drag polars are plotted in Figure 29b as well. For most practical values of C_L (up to a critical value) the Gurney flaps increase the drag.

7.3 Forces in Ground Effect

The downforce at $\alpha = 1°$ is presented for a variety of heights in Figure 30a. The effect of adding the Gurney is to increase the downforce produced, by a seemingly constant amount at all heights. The maximum downforce attained by the wing with the small Gurney corresponds to $C_L = 2.27$ at $h/c = 0.112$, and the large Gurney $C_L = 2.52$ at $h/c = 0.112$. These compare with the results for the clean wing of $C_L = 1.72$ at $h/c = 0.082$. The height at which the maximum downforce occurs increases when the Gurney flaps are added, despite the fact that there were few heights tested at near to the maximum downforce for the wing with the Gurneys. It can also be seen that the reduction in downforce below the maximum is sharper than for the clean wing. Results at other incidences and for fixed transition not included here show similar effects.

Figure 30b presents the gain in downforce with the Gurney compared to the clean wing, $\Delta C_L|_{GF}$, with the downforce of the clean wing. These plots have been used by Jeffrey [49] to show that the lift gain with the Gurney is a function of the lift for the clean wing, not the wing profile, for a wing in freestream as the incidence is varied. Jeffrey's results show that the points collapse onto the same line for a particular size Gurney, for different wings; a NACA0012 and a high lift e423. The current results are presented for freestream, where the wing incidence has been varied, and for ground effect, where the ride height has been varied at $\alpha = 1°$. It is clear that the results for freestream and ground effect are significantly different. In ground effect, adding a Gurney flap increases the downforce more significantly than in freestream.

7.4 Surface Pressures

Figure 31a shows the pressure distributions from the chordwise tappings at the wing centre, for the clean wing and the 1.45% Gurney flap at a height of $h/c = 0.448$. The final point on the pressure surface has not been included, due to it being covered by the Gurney. However, it can be seen that

a finite pressure difference at the trailing edge exists. Adding the Gurney increases the pressure on the pressure surface. Over the last 30%c of the pressure surface however, the increase in pressure is greater than for further upstream of this. In addition to this, greater suctions are found over the entire suction surface. The increment in suction is also seen to increase over the final 30%c, from 0.29 at $x/c = 0.72$, to 0.32 at $x/c = 0.85$ and 0.36 at $x/c = 0.99$. In addition to this, the separation bubble at the transition location has been brought forwards with the Gurney flap, and a suction spike near to the leading edge has been highlighted, both features on the suction surface.

Results in Figure 31b show the pressure distributions as the ground height is varied. The effect of changing the height from the ground on the pressure distribution is similar to earlier results for the clean wing as can be seen in earlier chapters. At larger ground heights, the suctions increase over the entire suction surface, and the pressures reduce slightly on the pressure surface. At very small heights, separation occurs on the suction surface.

The variation of pressure difference at the trailing edge with ground height is shown in Figure 32a. The pressure difference has been calculated using the final pressure tappings on each surface; at $x/c = 0.99$ for the suction surface and $x/c = 0.90$ on the pressure surface. Due to the Gurney covering the final tapping on the pressure surface, the results can only be compared qualitatively. It can be seen that as the ground height is reduced, the pressure difference increases steadily from 0.89 at $h/c = 0.671$ to 0.95 at $h/c = 0.179$, then increases more rapidly to a maximum of 1.06 at $h/c = 0.112$. Closer to the ground than this, the pressure difference drops sharply.

The canonical pressures are presented in Figure 32b for the 1.45% Gurney flap, and for the clean wing. The range of canonical pressures at which separated flow was first observed from the oil flow visualisation tests, $\overline{C_P} = 0.68 - 0.71$, is also included. For each height, the results for the clean wing are shown with the dashed line and the hollow symbols, for the Gurney the pressures are represented by the solid line with filled symbols. For each of the five heights, the canonical pressures are reduced when the Gurney is added, with a more significant reduction at the larger heights. For the clean wing, the boundary layer is just separating at $h/c = 0.224$. When the Gurney is added, the flow seems to be still attached at the trailing edge. At $h/c = 0.134$ a significant region of flow separation exists on the clean wing; the boundary layer has probably just started to separate for the wing with the Gurney.

7.5 Laser Doppler Anemometry Surveys

Figure 33 presents time-averaged LDA results for the u/U_∞ velocity contours for the wing in ground effect with the large Gurney at heights of $h/c = 0.448, 0.224$, and 0.134, showing the wake of the wing in the far-field, including results on the ground plane. In addition to this, a sample plot is shown for the clean wing, at $h/c = 0.224$.

The general flow features of interest can be seen qualitatively in the plots, and are similar to the results for the clean wing in the previous chapters. The wake becomes thicker as it moves

downstream, with the velocity deficit reducing due to small-scale turbulence. As the ground is approached, the wake increases size, and velocity deficits become larger. In addition to this, the path of the wake changes, such that the angle reduces with increasing ground proximity. Between the wake and the ground, the flow faces an adverse pressure gradient, especially visible in the region of $x/c = 1.5 - 2$ in the first two plots. Very close to the ground, the velocity deficit can be seen. As flow very near to the ground is retarded, due to the adverse pressure gradient from the point of maximum suction, the velocity deficit near to the ground is formed. This increases in size with increasing ground proximity, and appears to be larger than for the clean wing.

Comparisons of the results for the clean wing and the wing with the Gurney at $h/c = 0.224$ show that the flowfield is significantly effected. The size of the wake with the Gurney is much greater than for the clean wing. Also, the wake is deflected more due to the Gurney increasing the circulation.

Wake surveys, highlighting the effect of the Gurney on the u/U_∞ mean velocities are shown in Figure 34, for stations at $x/c = 1.5$ and 2.0 at a height of $h/c = 0.134$. Detailed information from the wake surveys at three heights, with and without the Gurney flap is presented in Table 12.

Adding the Gurney flap to the wing causes a larger wake in terms of the thickness of the wake, and the maximum velocity deficit. At $x/c = 1.5$ for $h/c = 0.134$ in Figure 34a, the thickness of the wake has been measured as $\delta_{99}/c = 0.015$ for the clean wing, compared to $\delta_{99}/c = 0.024$ for the wing with the Gurney. The maximum velocity deficit is $u/U_\infty = 0.77$, compared to 0.72 for the clean wing and wing with Gurney respectively. The height of this minimum velocity increases from $y/c = 0.04$ to 0.07 with the Gurney flap compared to the clean wing, as the Gurney flap has deflected the path of the wake. Although the location of the top of the wake thickness increases from $y/c = 0.12$ to 0.20, the location of the bottom remains roughly constant at -0.05 to -0.04.

Further downstream, at the $x/c = 2.0$ and 3.0 locations for $h/c = 0.134$, as can be seen in Figure 34b and Table 12, the effect of the Gurney is similar. Small-scale turbulence has diffused the wake of the wing such that the wakes are thicker and the maximum velocity deficits are reduced. The Gurney still has the effect of reducing the minimum velocity, and increasing the height of the location thereof. This changes from $y/c = 0.04$ to 0.09 at $x/c = 2.0$, to 0.05 and 0.13 at $x/c = 3.0$. The velocities reduce from $u/U_\infty = 0.85$ to 0.77, and from 0.91 to 0.82 at the two positions. This shows that the wake is deflected through a higher angle with the Gurney. The location of the top of the wake thickness increases significantly with the Gurney; 0.14 to 0.22 at $x/c = 2.0$, and 0.19 to 0.33 at $x/c = 3.0$. The bottom of the wake grows less significantly; from -0.07 to -0.10, and from -0.08 to -0.10 at the two x/c positions.

Results for the clean wing show that the wake thickness increases from $\delta_{99}/c = 0.17$ to 0.21 and 0.27 at the three positions at this height. This compares to thicknesses of $\delta_{99}/c = 0.24, 0.32$ and 0.43 for the wing with the Gurney. The increases in wake thickness when the Gurney is added are 0.09, 0.13, and 0.18 respectively. A significant result on the overall flowfield is that, when the Gurney is added, in addition to increasing the size of the wake, the wake grows at a greater

rate. This trend can also be seen in the results for the other heights, at $h/c = 0.448$ and 0.224, in Table 12.

The other trends of the path of the wake being deflected though a higher angle can be seen examining the locations of the maximum velocity deficit with and without the Gurney, for the other heights tested. For example, at $h/c = 0.448$, this increases height from $y/c = 0.08, 0.10, 0.13$ for the clean wing, to 0.13, 0.17, and 0.22 for the wing with the Gurney.

7.6 Particle Image Velocimetry Surveys at Wing Centre

The purpose of the PIV testing was to provide an understanding of the vortex shedding behind the Gurney flap in the near wake region in ground effect. The laser light sheet was set up to illuminate a streamwise slice at the semispan of the wing, with the laser mounted downstream of the moving ground. The camera was located perpendicular to the light sheet, as to cover the rearmost portion of the wing and the near wake, including the ground. The bottom edge of the image was lined up on the ground. In order to capture results upstream of the endplate trailing edge, a perspex endplate was used on the side between the camera and the light sheet.

Results were taken using 50 datasets, performing a cross-correlation with a 75% overlap on 64×64 pixels to give results on a 77×61 grid. In addition to this, the results were range validated. The tests were performed during the same session as the investigations on the clean wing. It was not possible to process the results at the same grid density as for the clean wing as too much noise existed in the results. Simply adding the Gurney flap caused too much disturbance to the flow, and reduced the quality of cross-correlated data.

Snapshots of the flow showing instantaneous vorticity contours are shown in Figure 35 at heights of $h/c = 0.448, 0.224, 0.134$ and 0.067. Descriptions given here are for the typical snapshot, as can be seen in the Figure, and also with reference to other results showing additional trends not presented here. Again, for the large ground heights, the setup was such that a shadow was cast over the pressure surface, and for the small heights, a shadow was cast over the suction surface. This gives incorrect readings in these regions, but they have not been blanked out. The top left corner of the image has been removed as this area was obscured by the support arrangement.

At a height of $h/c = 0.448$, the boundary layer on the suction surface is resolved well and appears regular and attached to the surface. Results above the pressure surface are erroneous. Discrete regular vortices can be seen to be shed behind the Gurney flap. Although not overly clear due to the contour levels used, the vortices reduce in strength as they move downstream. At $h/c = 0.224$, the vortices are not as regular as the $h/c = 0.448$ case in terms of size. It appears that the first vortex forms a little further downstream. When different contour levels are used, it can be seen that the shear layer from the pressure surface to $x/c \approx 1.2$ contains a concentration of negative vorticity that is attached to the shear layer upstream by a region of vorticity of smaller magnitude at $x/c \approx 1.12$, i.e. the vortex is about to be shed. The vortices are also of greater

strength than for the $h/c = 0.448$ case. At $h/c = 0.134$, the vortices are less regular in terms of shape, and also the frequency at which they are shed, and they are stronger than at the greater heights. The distribution of vorticity is also more uneven, e.g. two concentrations of negative vorticity can be seen at $x/c \approx 1.55$. For $h/c = 0.067$, the flow is highly chaotic. The shedding is less regular in terms of frequency, distribution of vorticity, and magnitude of vorticity. For example, at $x/c = 1.55, y/c = 0.2$, a small concentration of positive vorticity exists of magnitude $\omega c/U_\infty \approx 20$, near to a larger region of negative vorticity of maximum strength $\omega c/U_\infty \approx 40$. Observation of several images shows the shedding to have a direct interaction with the ground.

7.7 Discussion

The general qualitative effect of the Gurney flaps on the performance of the wing in freestream compares with previous studies; the downforce for a given angle of attack in the linear region is increased, and a sharper stall is found when the Gurney flap is added. A small Gurney flap produces a disproportionately large increase in downforce. It is difficult to compare results directly due to different test Reynolds numbers, Gurney flap sizes, and baseline aerofoil sections being used in the current tests compared to other research.

As described by Jeffrey [49, 50], the upstream face of the Gurney flap retards the flow, as can be seen in the current surface pressure distributions. The vortex shedding increases the trailing edge suction, causing a finite pressure difference at the trailing edge, resulting in an increase in downforce. Although this has been discussed previously, the instantaneous PIV results enable the flowfield to be visualised to a higher degree, and the vortex shedding procedure will be discussed with reference to Figure 35 at the height of $h/c = 0.448$. The shear layer from the suction surface is rolling up to form a vortex at the instant shown in time. The vortex centre is at $x/c = 1.1$, $y/c = 0.09$, but the vortex has not been shed from the shear layer. A region of positive vorticity of a lower magnitude joins the vortex to the rest of the shear layer. The shear layer from the top of the Gurney flap is being drawn in, at $x/c = 1.04$, $y/c = 0.12$, and is just cutting off the vorticity from the shear layer from the suction surface that is feeding the vortex at $x/c = 1.1$, $y/c = 0.09$. When it is shed downstream, a similar procedure will then cause a vortex to be shed from the pressure surface shear layer.

The ground does *not* have a benign effect on the performance of the wing with the Gurney flap added. The increase in downforce over the clean wing is significantly greater than that for a wing in freestream. This increase with the Gurney increases steadily in ground effect, is greatest at $h/c = 0.179$, then starts to reduce slightly, then more significantly. Surface pressures using the two tappings nearest to the trailing edge show how the pressure difference at the trailing edge varies in ground effect. This increases steadily to $h/c = 0.179$, then increases sharply to $h/c = 0.112$, then falls sharply. Adding the Gurney reduces the pressure recovery demands, as shown in the canonical plots. It can be deduced that, from the plots, boundary layer separation is present for

heights less than $h/c = 0.179$. The sharp increase in the pressure difference at the tappings nearest to the trailing edge at heights less than $h/c = 0.179$ is believed due to the flow separating. The reduction in performance of the wing with the Gurney flap relative to the clean wing, at heights less than $h/c = 0.179$ is believed to be due to the boundary layer separating near to the trailing edge of the suction surface, preventing regular vortex shedding behind the Gurney flap.

Adding a Gurney flap to an aerofoil in freestream has the effect of a point circulation at the trailing edge, inducing an increase in circulation about the section. As described in previous chapters for the clean wing, using the reflection technique of modelling the ground, the image aerofoil is represented by a circulation equal and opposite to the real aerofoil. The image induces a higher velocity to the real aerofoil, especially in the suction surface region. Hence, if the circulation is increased around an aerofoil by adding a Gurney flap, this will result in a greater strength of the image circulation, and greater velocities induced on the real aerofoil, i.e. there is a secondary effect of the ground with the Gurney flap.

For the PIV results, obtained with fixed transition, the boundary layer is believed to have separated from the suction surface for the three lowest heights for which results are presented here. The vortex shedding becomes successively less regular and more chaotic as the ground is approached, as the boundary layer separation point moves forwards.

Although the instantaneous PIV results for the clean wing, Figure 27, and the wing with the Gurney flap, Figure 35 were processed using different grid densities, making direct comparisons difficult, qualitative features can be compared. Examining the effect of the Gurney flap on the flowfield at the largest height, $h/c = 0.448$, where the effect of the ground is not extreme, it can be seen that the vortex shedding behind the Gurney flap appears more regular than behind the finite trailing edge of the clean wing. Some of this can be attributed to the processing methods employed. However, it can be seen that the spacing between successive vortices is regular behind the Gurney flap, but appears more irregular behind the clean wing, i.e. there is a regular frequency of vortex shedding behind the Gurney flap. Figure 24a shows that the boundary layer thickness at the trailing edge in the suction surface for a typical height is $\delta_{99}/c \approx 0.05$ for the clean wing. The finite trailing edge has a thickness of 0.007c, and the large Gurney for which all off-surface flow visualisation performed 0.029c. Of significance regarding vortex shedding is the thickness of the separating shear layers with respect to the distance between the shear layers. The thickness of the boundary layer at the trailing edge (of the suction surface) will vary with time because of its turbulent nature. The range of the ratios of the boundary layer thickness to the distance between the shear layers will be larger for the clean wing, than for the wing with the Gurney flap. Hence, the vortex shedding for the clean wing will be less regular than for the wing with the Gurney flap.

Adding a Gurney flap is seen to increase the size of the mean flow wake, measured by the 99% displacement thickness, and also deflects the centre line of the wake through a larger angle. The maximum velocity deficit also increases when the Gurney is added. In addition to the wake thickness increasing, it also grows at a larger rate, compared to the wake from the clean wing.

7.8 Summary

The effect of Gurney flaps has been investigated on the single element wing in ground effect. In terms of the downforce produced, the effect of adding a Gurney flap is qualitatively similar to that for a wing in freestream. The downforce is increased, with larger gains as the incidence is increased, or as the height is reduced. A small Gurney has a disproportionately large effect compared to a large Gurney. The stall is sharper with the Gurney flap, due to the onset of flow separation. Adding a Gurney to a wing is more significant in ground effect than in freestream, where up to twice the gain compared to that in freestream can be obtained. The ground effect as modelled using the image technique and the high velocities induced by the image circulation, is coupled with the circulation effect when a Gurney flap is added. In addition the pressure recovery demands are reduced with the Gurney flap.

The instantaneous flow behind a Gurney flap is characterized by a street of alternately shedding, discrete vortices when the flow is fully attached. At heights associated with separated flow, the shedding becomes less regular and more chaotic. The aerodynamic performance of the Gurney flaps then deteriorates. With a Gurney flap, the mean-flow wake is deflected through a greater angle, is thicker, and grows at a greater rate, than for the clean wing.

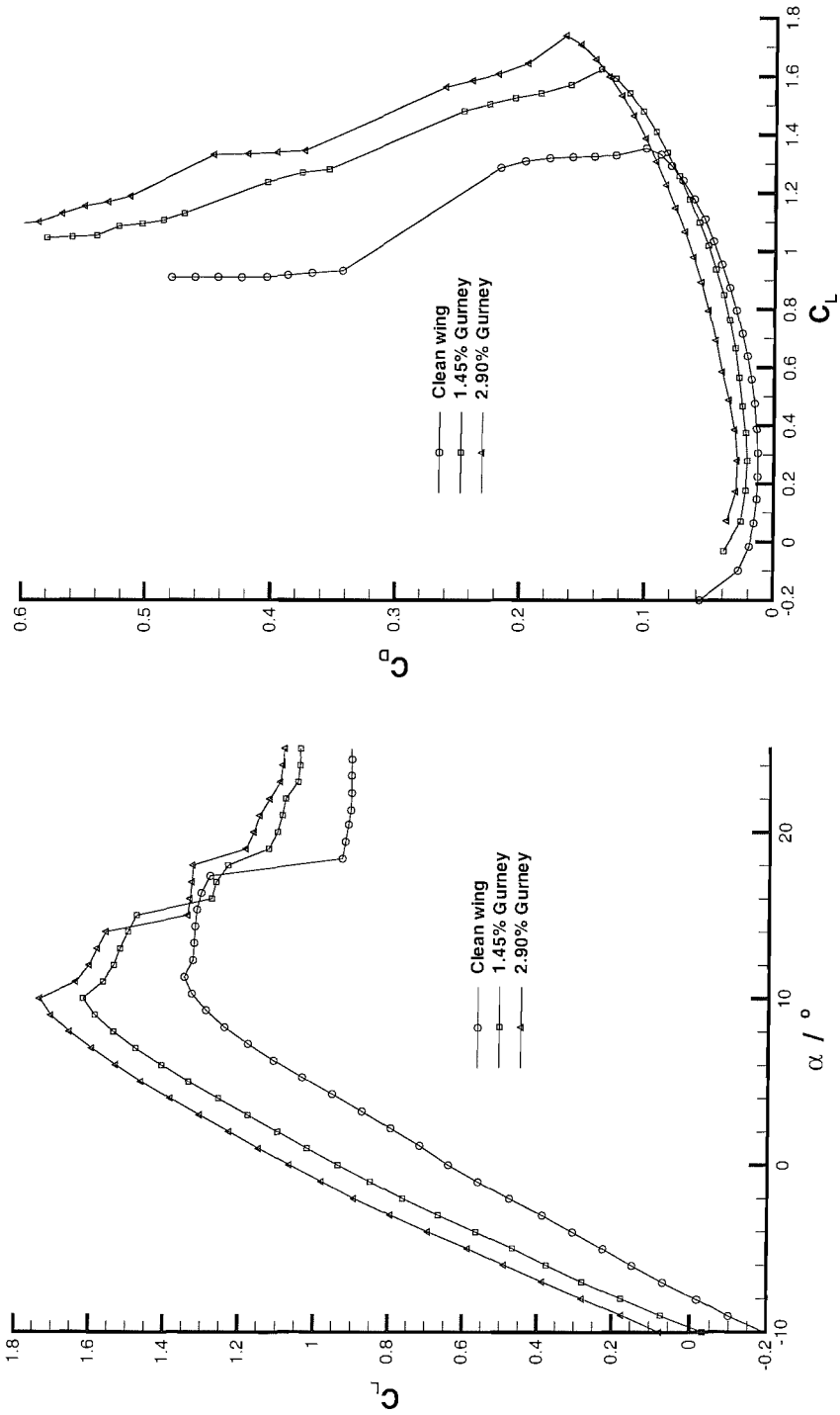

Figure 29: Forces in freestream; (a) Liftcurve. (b) Drag polar, transition free.

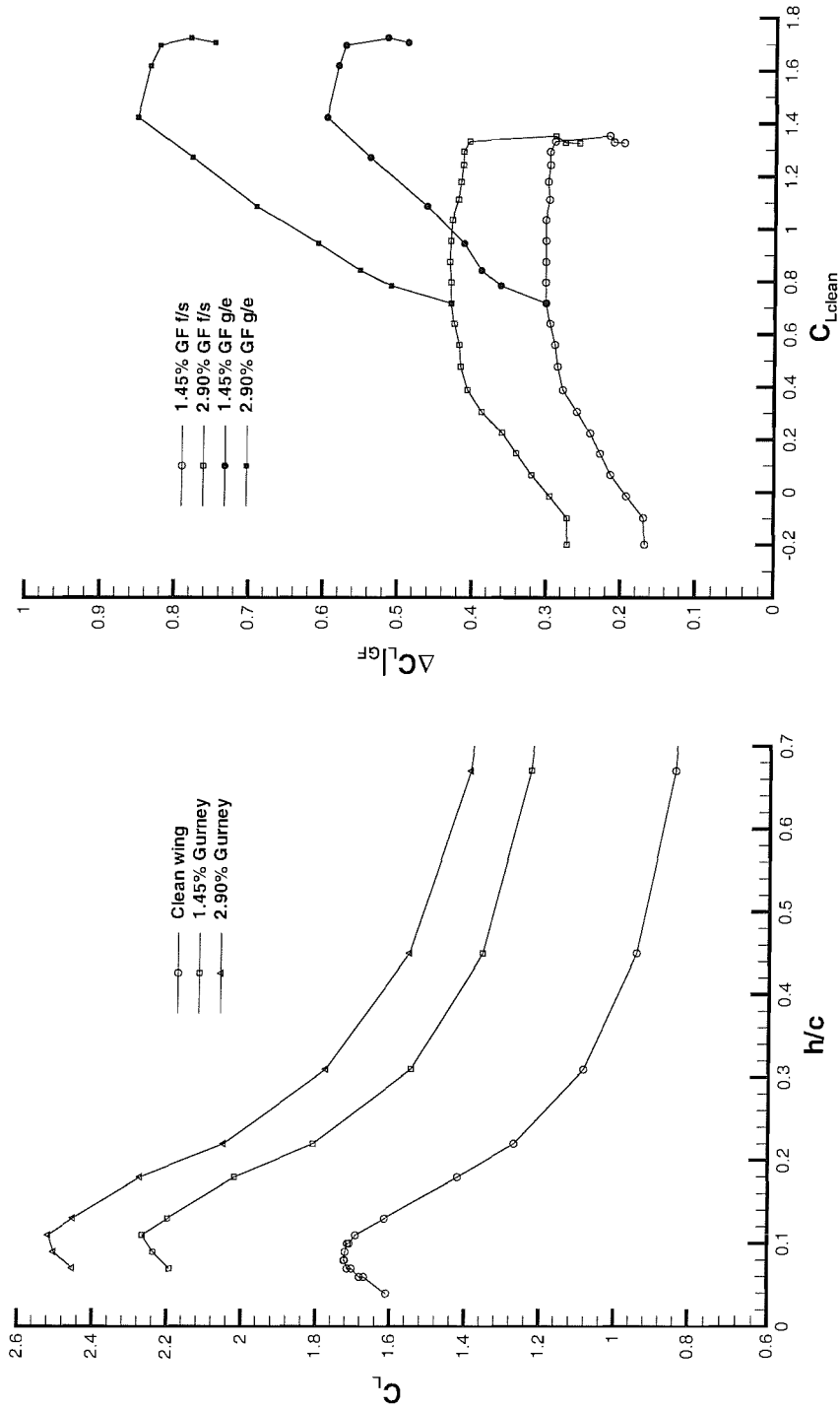

Figure 30: (a) Downforce in ground effect. (b) Increment in downforce over clean wing, transition free.

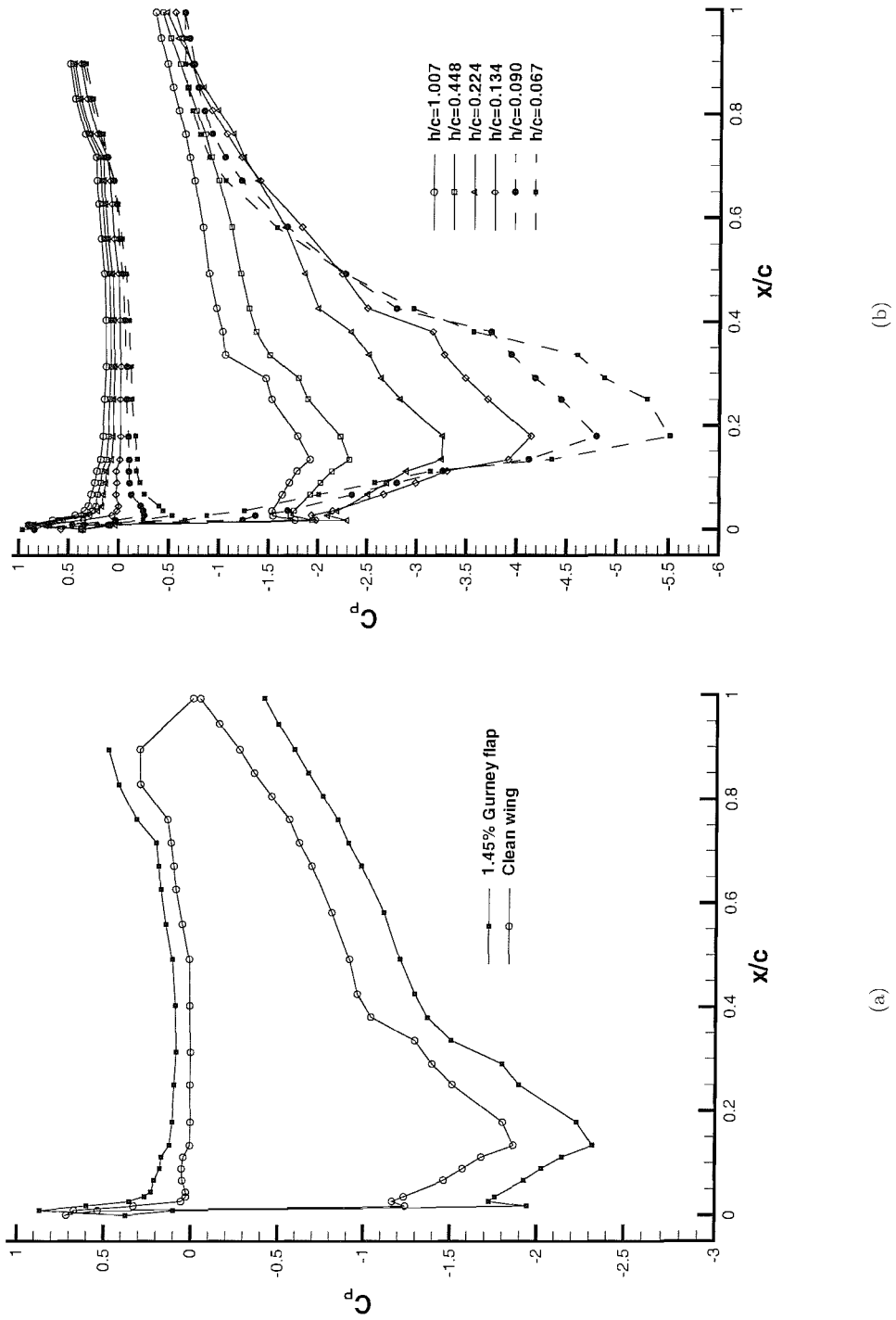

Figure 31: Surface pressure distributions at wing centre (a) Effect of adding Gurney flap at $h/c = 0.448$. (b) Distributions with Gurney flap for different heights, transition free.

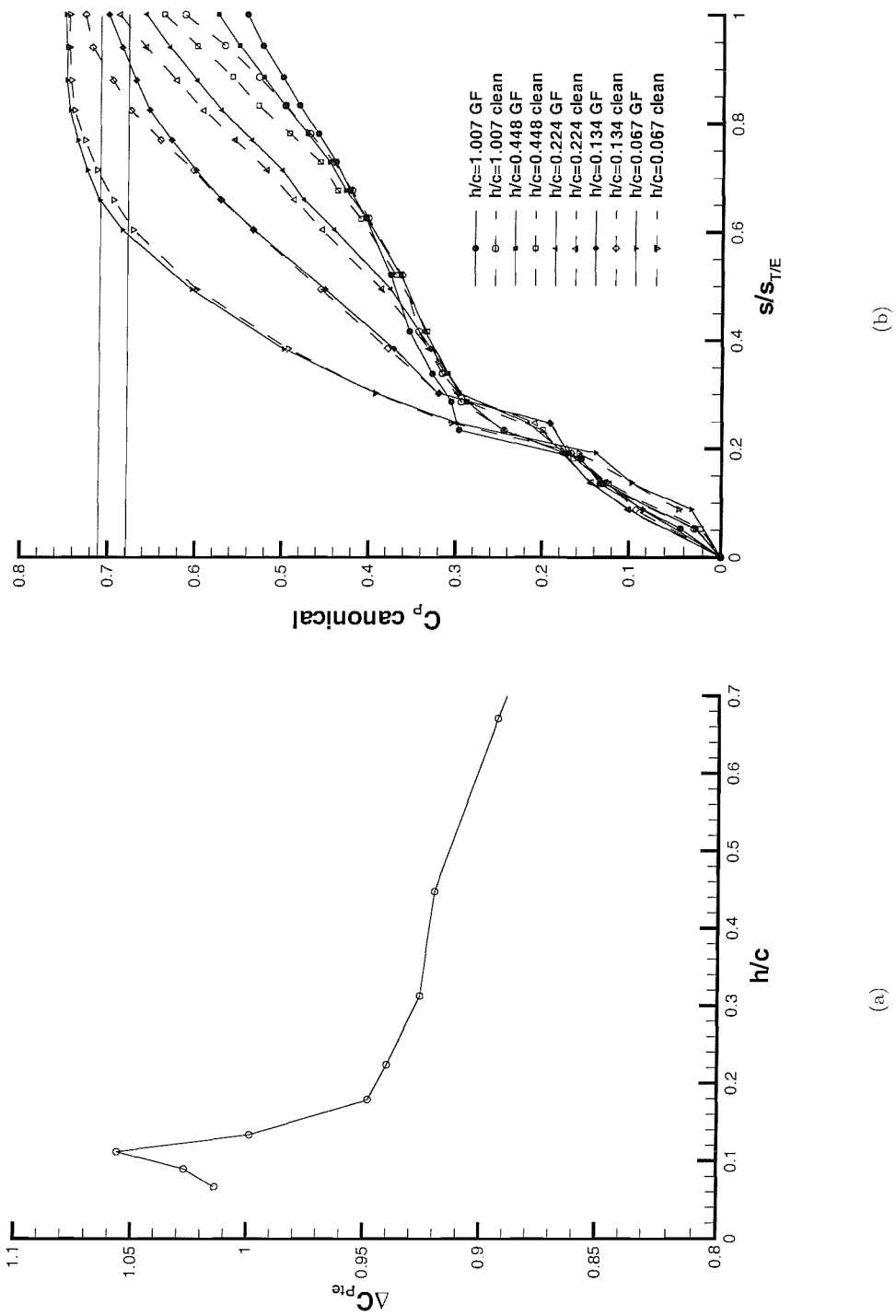

Figure 32: Surface pressure distributions at wing centre (a) Pressure difference at trailing edge. (b) Suction surface canonical pressures, transition free.

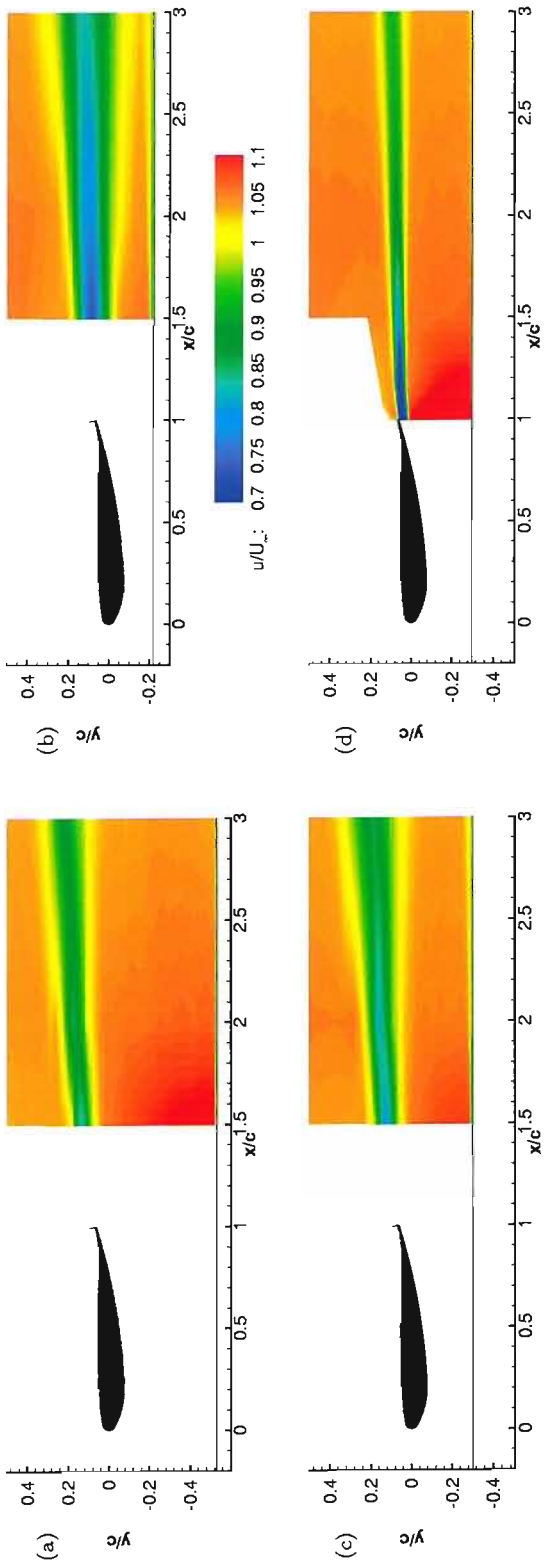

Figure 33: LDA u/U_∞ velocity contours at heights of $h/c = 0.448, 0.224, 0.134$ with 2.90% Gurney flap and at $h/c = 0.224$ for the clean wing, transition fixed.

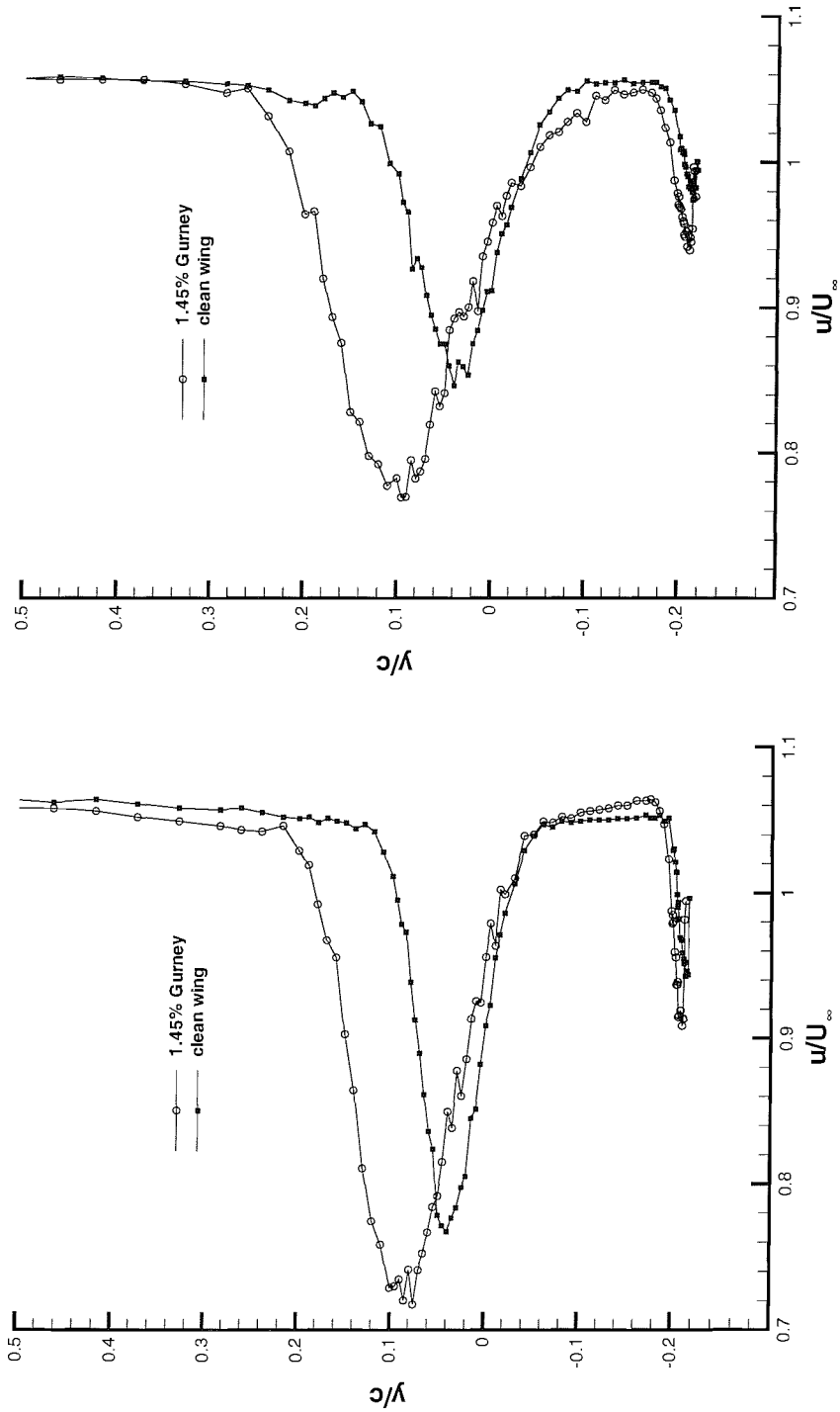

Figure 34: LDA u/U_∞ velocity wake surveys for clean wing and 2.90% Gurney flap at $h/c = 0.134$ (a) $x/c = 1.5$. (b) $x/c = 2.0$, transition fixed.

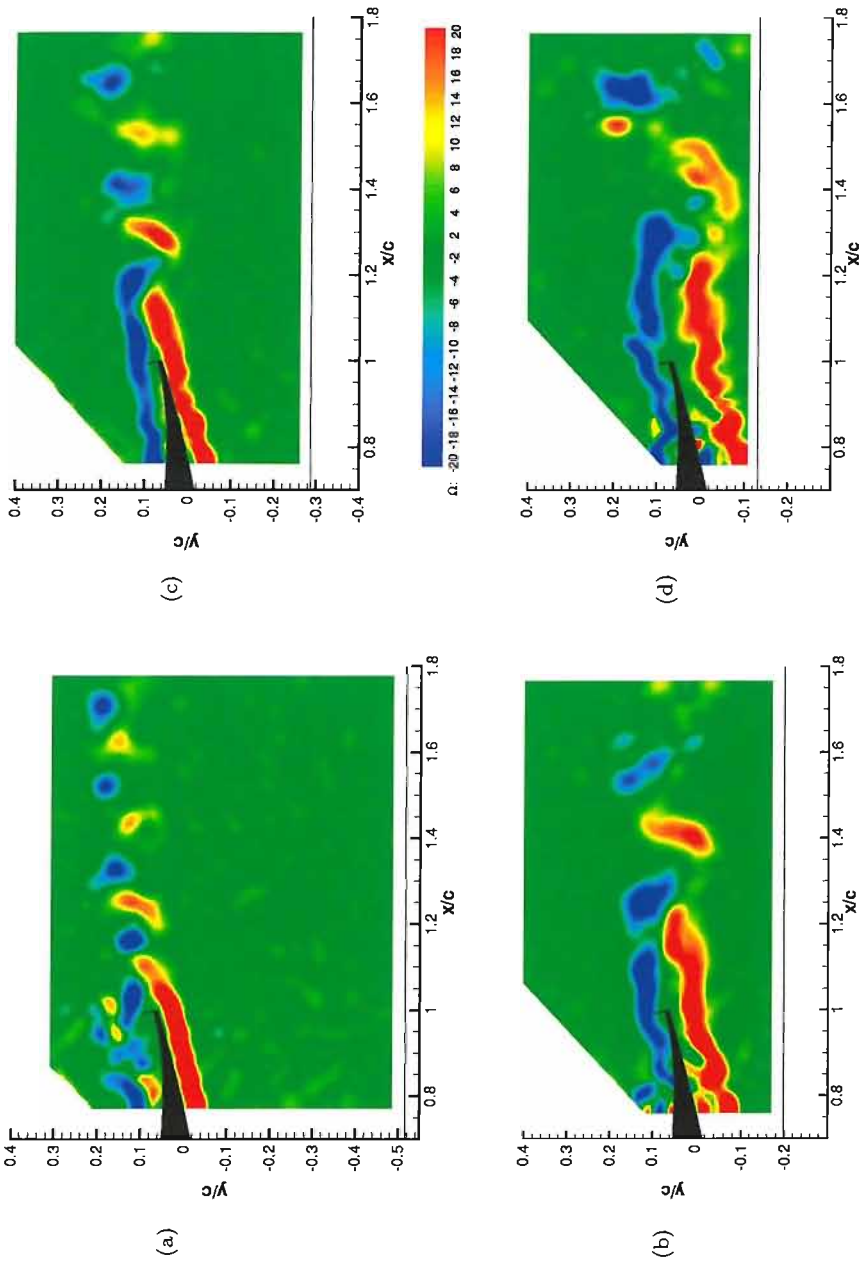

Figure 35: Instantaneous PIV vorticity contours at heights of $h/c = 0.448, 0.224, 0.134, 0.067$, transition fixed.

h/c	x/c	u_{min}/U_∞	y/c at u_{min}	y at δ_{top}	y at δ_{bottom}	δ_{99}/c	$\delta_{gurney} - \delta_{clean}$
0.448	1.5	0.82	0.13	0.20	0.04	0.16	0.09
	2.0	0.85	0.17	0.24	0.05	0.19	0.09
	3.0	0.88	0.22	0.33	0.06	0.26	0.13
0.224	1.5	0.80	0.14	0.22	0.01	0.20	0.11
	2.0	0.81	0.15	0.24	0.00	0.24	0.12
	3.0	0.86	0.19	0.33	0.01	0.32	0.15
0.134	1.5	0.72	0.07	0.20	-0.04	0.24	0.09
	2.0	0.77	0.09	0.22	-0.10	0.32	0.13
	3.0	0.82	0.13	0.33	-0.10	0.43	0.18

Table 12: Wake information including maximum velocity deficit and 99% wake thickness; 2.90% Gurney flap

Chapter 8

Double Element Wing

8.1 Introduction to Chapter

In this chapter, a presentation of the experimental results of the final series of tests is given, together with a discussion of the flow, around a multi-element wing in ground effect. The tests were all performed using free transition, for a range of heights from freestream to close to the ground, at a single incidence of $\alpha = 1°$ as measured by the inclinometer bed on the main element as described in Chapter 2. The true incidence for the datum deflection, from the leading edge of the main element to the trailing edge of the flap is $\alpha = 14.1°$. For the forces, three flap deflections were used; the datum, for which the coordinates are given in Table 4, and a deflection of $-8.5°$ and $+9.5°$. For all other results, i.e. surface pressures, PIV, LDA, and oil flow visualisation, results are presented for the lower two flap deflections. The point about which the flap was rotated was at a location of $x/c = 0.567$, $y/c = 0.076$, i.e. 2mm downstream from the leading edge of the flap.

8.2 Forces

The first series of tests performed were in order to find the flap location at which the optimum downforce was produced for a constant flap deflection. The gap and the overlap were varied in steps of 2mm (0.005c), using a selection of brackets and endplates. The overlap was defined as the horizontal distance between the trailing edge of the main element and the leading edge of the flap, with a positive overlap for the flap leading edge upstream of the main element trailing edge. The gap was defined as the vertical distance between the trailing edge of the main element and the lowest point on the flap suction surface, with a positive gap for the flap leading edge above the main element trailing edge. The flap location optimisation was performed for the datum flap deflection angle at an arbitrary height of $h/c = 0.263$.

Results of the optimisation can be seen in Figure 36a. The optimum location for the flap can

be seen to be an overlap of 0.024c, and a gap of 0.032c. These correspond to 9mm and 12mm respectively. This was used as the location of the flap for all further tests at the different heights and flap deflections.

Figure 36b gives the downforce generated as the height of the wing is varied for the three flap deflection angles. First, considering the results for the flap deflection of $-8.5°$, it can be seen that the basic characteristics of the downforce with height curve are broadly similar to the single element wing. The downforce increases as the height reduces, eventually a maximum downforce is obtained, after which the downforce reduces sharply. However, at a height of $h/c = 0.171$ a discontinuity can be seen as the trend of increasing downforce with height reduction abruptly stops; just above this height the gradient of the line is high, and just below this point the gradient is low. As the height is reduced further, the slope of the line increases again, in a similar manner to that at large heights, until it gradually reduces, and the downforce eventually reaches a maximum at a height of $h/c = 0.066$, corresponding to $C_L = 2.588$. To aid in describing the aerodynamic characteristics, heights greater than and equal to $h/c = 0.171$ for the $-8.5°$ flap angle will be referred to as region a, and heights less than $h/c = 0.171$ will be referred to as region b. Figure 37a shows the height range of the region a and b flows, together with additional annotations described later.

Results can also be seen in the same plot for the datum flap deflection. At nearly all heights, the wing generates significantly more downforce than for the lower flap deflection. At large heights, greater than $h/c = 0.237$, similar characteristics can again be seen as the downforce increases with a growing gradient as the height is reduced. However, a discontinuity again exists in the curve, at $h/c = 0.237$, and the downforce actually reduces suddenly just below this height. As the height is reduced further, the portion of the curve seems more linear. A peak in the downforce occurs at $h/c = 0.079$, corresponding to $C_L = 3.028$. Below this height, a sudden drop in the downforce is observed. In a similar manner to the $-8.5°$ flap deflection, heights above and including $h/c = 0.237$ will be referred to as region a, and heights below $h/c = 0.237$ will be referred to as region b in further discussions, and can be seen in Figure 37b.

At a third flap deflection of $+9.5°$, a lower level of downforce was obtained for practically all heights. Rudimentary flow visualisation during the tests showed the flow over the flap to have stalled at a large height.

The variation of drag with height is given in Figure 38a. The curves for the three flap deflections show a general trend of increasing drag as the height is reduced. At the $-8.5°$ flap deflection, the curve is relatively smooth, with the gradient of the line generally increasing as the ground height is reduced. However, just above $h/c = 0.171$, at the lower boundary of the type a flows at this flap deflection, the gradient is greater than just below this height, i.e. a similar characteristic to the downforce against height curve is observed. At the datum flap deflection, a significantly greater drag is obtained at all heights, than compared to the $-8.5°$ flap deflection. A broadly similar variation with height is observed. In the border between the type a/b flows, at $h/c = 0.237$, the general trend is for a sharper gradient at low type a heights, and a lower gradient at greater type

b heights. This is somewhat more pronounced than for the $-8.5°$ flap deflection. At the $+9.5°$ deflection, a significantly greater drag is obtained at all heights. The curve increases smoothly to a maximum, and then reduces slightly.

All remaining tests were performed at the lower two flap angles. Hereafter, the $-8.5°$ flap deflection will be referred to as the low flap angle, and the datum flap deflection will be referred to as the high flap angle.

8.3 Surface Pressures

The surface pressures were taken for the complete set of tappings; chordwise central and tip, and spanwise, for both the low and high flap deflection. The results at the centre are presented first, then three-dimensional effects are shown, using the spanwise tappings, and the chordwise tappings near to the tip.

8.3.1 Chordwise Pressures at Wing Centre

Figure 38b shows the pressure distributions for the double element wing for both flap deflections, in addition to that for the single element wing. The x/c coordinate for the single element wing has been non-dimensionalized using the combined chord for the double element wing. Adding the flap to the main element has the effect of introducing a finite pressure over the trailing edge of the main element. The pressures on the pressure surface are increased, and the suction generated on the suction surface also increases compared to the single element wing. The increments are greater for the high flap angle, than for the low flap angle. Over the mid and aft-portions of the wing, the increases are broadly constant for both flap angles. However, to $x/c \approx 0.15$, the shape of the distribution changes more significantly for the double element wing compared to the single element wing. On the pressure surface, the acceleration of the flow from stagnation at the leading edge is more smooth with the flap, in the region to $x/c \approx 0.1$. For the single element wing, the flow reaches a velocity approaching freestream at $x/c \approx 0.02$. On the suction surface, the suction peak for the single element wing at $x/c = 0.08$ remains at the same place. This will be known as the suction *peak* in future discussions. However, a suction spike near to the leading edge at $x/c = 0.01 - 0.02$ becomes apparent when the flap is added, which shall be referred to as the suction *spike*. The spike grows for the higher flap angle. The bump that is present in pressure on the single element suction surface at $x/c = 0.17$ representing the transition bubble is not as apparent for the double element wing.

Only approximately two-thirds of the flap is tapped, due to the aft portion being too thin to install tappings. The two flap angles yield different types of distributions. For the low flap angle, the flow is accelerated over the suction surface a little from the higher than freestream velocity near to the main element trailing edge. It remains at $C_P \approx -1$ until $x/c = 0.72$, then the recovery starts as the trailing edge is approached. For the high flap angle, the flow is accelerated rapidly

from the leading edge at $x/c = 0.564$ to a peak suction at $x/c = 0.570$. The flow then retards for all further tappings. The difference in suction between the high and low flap angles reduces along the chord of the flap, and is small for the final tap at $x/c = 0.880$. On the pressure surface, the flow is accelerated from stagnation at a greater rate for the low flap angle. The pressures remain broadly constant for each configuration, but are greater in magnitude for the high flap angle than for the low angle.

The chordwise distributions for the low flap angle are presented in Figure 39a for large heights, and Figure 39b for small heights. For the large heights (Figure 39a), when the height of the wing from the ground is reduced, the suctions increase on the lower surface of both the main element and the flap. The increase, however, appears greater on the main element when compared to the flap. The suction near to the trailing edge of the main element increases with increasing ground proximity, the magnitude of which is comparable to the increase in suction near to the flap leading edge. The fundamental shape of the distributions does not change, and the main suction peak, and the spike very close to the leading edge, are still present as the ground is approached, and remain at the same location within the spatial resolution of the tappings. The reduction in pressure from after the spike, to the main peak increases as the height is reduced. The distribution over the pressure surface varies very little from freestream to $h/c = 0.211$.

Closer to the ground (Figure 39b), the effect differs slightly. Results presented are for a variation in height of only $h/c = 0.026$ for the different datasets, compared to much larger height changes for the greater heights in Figure 39a. Even with these small height changes, the suction on the main element lower surface increases significantly as the height is reduced, especially in the chordwise region from $x/c = 0.08$ and downstream. The increment starts to reduce from $x/c \approx 0.25$, and is small at the trailing edge of the main element. For the lowest height, $h/c = 0.053$, a reduction in suction is found from $x/c = 0.25$ compared to $h/c = 0.079$. The tapping recording the suction peak moves from $x/c = 0.079$ to $x/c = 0.105$ as the height is reduced. The characteristics of the spike near to the leading edge also change. Although not overly clear, at heights lower than and including $h/c = 0.132$, the maximum suction over the entire surface is found in the suction peak at $x/c = 0.105$, compared to the leading edge spike at heights greater than this. The peak suction at the lowest height corresponds to $C_P = -8.7$, much greater than the maximum for the single element wing. Over the lower surface of the flap, the change in suction is very small compared to the main element. There is a tendency for the suction to increase near to the leading edge, with the lowest height case showing a slight reduction in suction from $x/c = 0.65$. The distributions over the pressure surface of both elements changes very little, but the slight effect of reducing pressure with height can be seen.

Results for the high flap angle (Figure 40), show a similar effect of the ground on the pressure distributions. At the large heights (Figure 40a), there is a large increase in suction on the main element lower surface as the height is reduced. Over the flap lower surface, the increase in suction is not as significant, and is very small for $h/c = 0.211$. Again, the suction spike very near to the

leading edge of the main element provides the greatest overall suction at these heights. The change in pressure on the the upper surface of both elements is very small as the height is reduced. At the lower heights (Figure 40b), for all heights apart from the lowest of $h/c = 0.053$, the lower surface pressures on the main element reduce, most significantly over the region from $x/c = 0.1$ to $x/c = 0.25$. The suction peak close to this chordwise position moves aft, from $x/c = 0.079$ to $x/c = 0.105$ with the reduction in height. Again, this suction peak contains the maximum suction over the entire wing for all heights lower than and including $h/c = 0.132$. At greater heights than this, the maximum overall suction is found in the suction spike at the leading edge. For the flow over the flap suction surface at all heights apart from the lowest, the suction changes very little as the height is reduced in this height range. There is a slight tendency for increasing suction in the peak upstream of $x/c = 0.63$ and reducing suction downstream of this, as the height is reduced. For the lowest height of $h/c = 0.053$, the suction over the main element lower surface reduces significantly over the entire surface. A constant pressure region is observed on the flap from $x/c = 0.7$, also with reduced suctions on the flap upstream of this. For both the main element and the flap, the pressure reduces very slightly over the upper surface with a reduction in height. An additional reduction is observed at the lowest height.

8.3.2 Spanwise Pressures

Figure 41 presents the spanwise pressures as measured by the quarter-chord tappings on the main element for the low flap angle. It can be seen from the graphs that the flow is highly three-dimensional. The suctions on the lower surface increase rapidly from the tip as the central portion of the wing is approached. As described from the chordwise pressures, the flow over the upper surface does not change significantly as the height is changed, but the suction surface results vary greatly with the height. Figure 42 shows the same results for the high flap angle. The results show a similar effect as the height is reduced, with a significant increase in lower surface suctions, and a very small change in upper surface pressures. The distribution of suction does not appear to be as smooth as the results at the low flap angle; at $\eta \approx 0.15$ and 0.75, bumps can be seen, especially at the large heights.

Due to the large increase in lower surface pressures as the height is changed, it is difficult to compare the spanwise distributions for different heights. In a similar manner to the single element wing, the spanwise pressures on the lower surface of the main element have been normalized by the integral of the pressures with respect to the spanwise position, and the distributions plotted in Figure 43, where the normalized pressure coefficient, C_{Pnorm}, would correspond to -1 for the case where the flow is entirely two-dimensional. For the low flap angle, it can be seen that from $\eta \approx 0.73$, a small region of flow that does not feature large spanwise pressure gradients is present at all heights. Outboard of this point, losses in the pressure coefficient are found over the entire region. The flow is highly three-dimensional over the outer two-thirds approximately. The (normalized) spanwise pressure gradients increase over the outer region as the height is reduced, as the flow

would appear to increase three-dimensionality.

For the high flap angle, Figure 43b, a broadly similar effect is seen. However, at the smaller heights, the region of flow at the centre of the element over which the pressures are approximately constant, reduces, and appears to have disappeared for the lowest height. Again, the three-dimensionality increases over the outboard region as the height is reduced, as can be seen by the increase in gradient. Slight irregularities exist, as described in the standard spanwise pressure distributions at the high flap angle, at $\eta \approx 0.15$ and nearer to the centre, at a few heights. It must be noted that the normalized spanwise pressure distributions have been calculated using a single streamwise pressure at the quarter-chord chord position, and are not equivalent to the spanwise variation of loading. The small bumps seen will be discussed later.

Referring to Figure 44a the spanwise pressure distribution along the flap can be seen, for the low flap angle. In freestream, there is some variation in the pressure over the semispan. Near to the centre, i.e. inboard of $\eta = 0.83$, there is a slight reduction in pressure on the lower surface. Near to the tip, outboard of $\eta \approx 0.2$, there is a gradual increase in suction, and at the tip, there is a finite suction, of magnitude similar to the suction over the mid semi-span portion of the flap. The upper surface flow has a relatively constant pressure, with a small dip at $\eta = 0.32$. As the height is reduced until $h/c = 0.211$, the suction increases over the central portion of the lower surface, from $\eta \approx 0.3$. Over the tip region, the suction also increases. However, for each height, the increment in suction near to the flap tip compared to the further inboard region increases. At $h/c = 0.211$, $C_P \approx -1.4$ over the inboard portion of the flap lower surface, i.e. ignoring the very centre. The increase near to the tip is large, at which $C_P \approx -2.3$. There is a very small reduction in upper surface pressure as the height is reduced. Figure 44b shows the variation for smaller heights. The trend as the height reduces is different. The suction over the inboard portion stays relatively constant, with a slight trend of reducing suction with increasing ground proximity, especially visible in the $h/c = 0.053$ case. However, the reduction in height has an adverse effect on the suction increase near to the tip. The magnitude of this reduces, and for the $h/c = 0.053$ case, this has reduced sufficiently that the suction in this region is less than that found further inboard. On the upper surface, a slight trend of decreasing pressure with decreasing height can be seen. The maximum suction near to the flap tip has been added to Figure 37 for heights near to the boundary of the type a/b flows, indicated by the $C_P =$ values.

The results for the high flap deflection are presented in Figure 45. In freestream, Figure 45a, the suction over the inboard portion (ignoring the centre) of the lower surface is greater than the low flap angle; $C_P \approx -1.2$ compared to $C_P \approx -0.8$ for the low flap angle. The characteristics near to the tip are qualitatively similar, however the magnitude of the increase in suction is bigger for the high flap angle. The suction near to the tip corresponds to $C_P \approx -1.7$ compared to $C_P \approx -1.1$ for the low flap angle. The increase in suction from the inboard portion to the tip is therefore greater for the high flap angle. As the height reduces to $h/c = 0.263$, the suctions over the inboard portion increase, but not as rapidly as those near to the tip. At this height, the suction near to

the tip is greatest, and corresponds to a C_P greater than -3. At smaller heights, Figures 45a &b, the suction over the inboard portion reduces. Moreover, the suction near to the tip reduces more significantly, such that at $h/c = 0.079$, the spanwise loading near to the tip is less than over the central portion. Again, the upper surface pressures reduce slightly with reducing height.

8.3.3 Chordwise Pressures near to Wing Tip

The chordwise pressure distributions at the centre and near to the tip will be discussed in this section, for three heights for each of the flap angles. Figure 46 presents the results at a height of $h/c = 0.395$, a typical type a height. For the low flap angle, Figure 46a, the lower surface suctions on the main element are reduced at the tip. There appears to be very little difference in the suction at the trailing edge of the main element, i.e. the boundary layer is dumped at the same velocity. For the centre tappings, the maximum overall suction on the element is found in the spike very close to the leading edge. Although the spike is still present for the tip tappings, it is not as prominent, and the magnitude of the suction is less than at the suction peak at $x/c = 0.08$. On the flap lower surface, the suction is slightly larger near to the tip than at the centre, for the entire chordwise range mapped. On the upper surface, the pressures are reduced by a broadly constant amount over both the main element and the flap. At the high flap angle (Figure 46b), a loss in suction is again present over the main element lower surface from the centre to the tip. On the flap, the suction generated is larger at the tip compared to the centre. The magnitude of the increase is greater than that for the low flap angle. The upper surface pressures reduce similarly from the centre to the tip.

Figure 47 shows the distributions at the lowest type a height for each flap angle. Figure 47a, for the low flap angle is at $h/c = 0.184$. Again, the main element lower surface suction is reduced at the tip. The maximum suction is in the spike at the centre and the main peak near to the tip. The reduction in suction from the centre to the tip is more significant than that at the larger height (Figure 46a). The suction on the flap lower surface is greater at the tip, the increment larger at the greater height. There is a small reduction in pressure from the centre to the tip, on the upper surface of both elements. The same trends can be seen in Figure 47b, for the high flap angle at $h/c = 0.263$. The main difference near to the tip is that it is not clear whether the maximum suction on the main element is at the spike or the main suction peak.

Similarly, Figure 48 shows the results at a height of $h/c = 0.105$, a typical height for type b flows. For the low flap angle (Figure 48a), the lower surface suctions on the main element are again significantly reduced from the centre to the tip. The loss in suction from centre to tip is greater than at the two previous heights (Figures 46a & 47a). The maximum suction is at the suction peak at $x/c = 0.10$ for the main element centre and the tip. On the flap lower surface, the suction generated at the tip is lower than the centre, for the region to $x/c \approx 0.65$. Downstream of this, the suction at the tip is a small amount greater than at the centre. On the upper surface, the pressure reduces from the centre tappings to the tip tappings. At the high flap angle (Figure 48b), results

follow the same trend as the low flap angle.

8.3.4 Integrated Pressures

In order to present the individual contributions from the main element and the flap to the overall downforce of the wing, the surface pressures both at the semispan and near to the tip have been integrated to form the sectional lift coefficients, C_{lcent} and C_{ltip}, for each of the elements. Although the portion of the flap near to the trailing edge is not tapped, the results have been calculated using a pressure at the trailing edge to be $C_P = 0$. Although errors are introduced here, the overall loading provided by this portion of the flap is small compared to other portions of the wing, and the entire process of integrating the pressures is only an estimation of the loading, due to the discrete locations of the tappings.

Figure 49a shows the results for the low flap angle. The integrated pressures at the centre, C_{lcent}, for the combined elements are as expected, greater than the overall downforce, C_L as measured by the overhead balance. The results at the centre, C_{lcent}, do not show any significant discontinuity at $h/c = 0.171$, the lowest type a height, as seen in the overall forces. A large proportion of C_{lcent} is generated by the main element. The variation of C_{lcent} for the main element is qualitatively similar to C_{lcent} for the overall wing. The downforce increases asymptotically as the height reduces. The gradient then starts to reduce, a maximum is found, and the downforce then falls. The flap accounts for only about 15-25% of the downforce generated at the centre. In addition to this, the trend is different. Although the downforce increases as the ground is approached, the maximum is only about 20% greater than that found far from the ground, i.e. the downforce generated at the centre of the flap is significantly less sensitive to a change in height, than the main element. Referring to the results at the tip, the loss in C_{ltip} for the combined elements compared to the overall downforce C_L is roughly the same as the deficit in the overall downforce compared to C_{lcent}. The discontinuity between the type a/b regions is quite prominent; at $h/c = 0.184$, a low type a height, C_{ltip} is greater than at $h/c = 0.158$, a large type b height. The variation of C_{ltip} for the main element is not as severe as at the centre near to the boundary of the type a/b flows. In addition to this, the downforce does not fall close to the ground. At the tip, the main element only produces approximately 60-70% of that produced at the centre, depending on the height. Although a reduction is not observed below $h/c = 0.184$, a bump can be seen here. The downforce produced by the flap near to the tip is similar but slightly less than that at the centre at larger heights. At $h/c = 0.184$, the downforce here is a maximum, and below this height, there is a steady decrease.

Figure 49b shows the variation for the high flap angle. For this case, the overall downforce features a sudden reduction just below $h/c = 0.237$, the lowest type a height. The total downforce at the centre of the wing increases asymptotically with a reduction in height. At $h/c = 0.079$, this downforce is a maximum, and below this a very sharp reduction follows, similar, but of a greater magnitude, than the overall downforce. Again, the main element produces the major portion of the downforce at the centre, approximately 70-80%, depending on height, and follows the same trend.

The downforce produced by the flap is roughly constant, but reduces suddenly below $h/c = 0.079$, similar to the main element. At the tip, the sectional downforce follows a similar trend to the overall downforce to $h/c = 0.263$. Below this, the curve features a plateau, then a reduction. In a similar manner to the low flap angle, the flap produces a similar level of downforce than that at the centre. Due to the reduced total downforce at the tip, the contribution from the flap is therefore of a greater relative magnitude than that at the centre. C_{ltip} for the flap increases slightly at the large heights, and reaches a maximum at $h/c = 0.263$. Below this height, steadily less downforce is produced.

8.4 Particle Image Velocimetry Surveys near to Wing Tip

The surface pressure results highlighted an area of the flow on which it was decided to perform further studies. The PIV system was used to map the tip vortex at different heights from the ground, to explain the surface pressure results, and in turn, the direct performance of the wing at different heights. Two different streamwise locations were examined for each of the flap angles. The first was at the quarter-chord position on the flap, i.e. at a location of $x/c = 0.672$, for exact comparison with the flap spanwise tappings. For this setup, a vertical slot was cut out of the metal endplate, from the lower edge, to the flap lower surface, 2mm upstream and downstream of the interrogation area. This was replaced by a microscope slide on the inside edge of the endplate, through which the light sheet was directed. The second streamwise location at which results were taken was at $x/c = 1.092$, i.e. behind, but close to the endplate. The camera was located downstream of the moving ground, perpendicular to the light sheet, aimed at a position slightly inboard of the endplate. The bottom edge of the image was lined up to be below the ground. Results were taken using 200 datasets, performing a cross-correlation with a 50% overlap on 32 × 32 pixels to give results on a 77 × 61 grid. In addition to this, the results were range validated.

Both the mean flow and instantaneous results are presented, for a selection of the configurations. Table 13 lists the maximum mean-flow vorticity found in the vortex core for all the tests. First, the mean flow results will be described, at each of the two locations, for different heights. Then the instantaneous results will be presented.

8.4.1 Mean Flow Results

Figure 50 shows vorticity contours at the two locations for heights of $h/c = 0.263$ and $h/c = 0.211$, for the low flap angle, both type *a* flows. In the figures, the black lines indicate the outline of the wing and the endplate. For the results at the flap quarter-chord position, an area has been blacked out, corresponding to the endplate, and the flap surface vertically above the flap quarter-chord, over which no flow exists. Although attempts were made to eliminate all the reflections during the testing, it was inevitable that some reflections remained. In particular, these originated from

the lower edge of the endplate, specifically the microscope slide. Some results behind the wing suffer spurious data in the region directly between the endplate and the ground, which was a more significant problem for the results at the flap quarter-chord. Most data in this region is erroneous directly between the endplate lower edge and the ground, especially for the low flap angle.

At a height of $h/c = 0.263$, the results at the flap quarter-chord show the vortex core to have a maximum vorticity of $\omega c/U_\infty = 104$ (see also Table 13). There is a shear layer on the outer edge of the endplate, that increases strength to the endplate lower edge. This then rolls up, feeding the vortex. The approximate location of the vortex core is at $z/c = 0.04$, $y/c = -0.04$; it is near to the lower edge of the main element, and close to the inner edge of the endplate. There is evidence of a secondary shear layer on the inner edge of the endplate, of negative vorticity, at the same height as the core. This is due to the induced velocity from the vortex, and the shear on the endplate surface. There is also a region of negative vorticity on the ground, below the vortex, due to the induced cross flow velocity from the vortex, and the shear due to the ground. Behind the endplate, the vortex is of comparable strength, $\omega c/U_\infty = 105$. The shear layer feeding the vortex is well resolved, and arises from the lower portion of the outer edge of the endplate. Although the maximum vorticity is similar to that at the quarter-chord, the region of positive vorticity defining the overall vortex size has grown. An effect of this is that the core has moved away from the endplate surface, and is now at $z \approx 0.1$. The height of it has increased by a small amount. The induced areas of secondary shear are still present, behind the endplate, and on the ground.

At $h/c = 0.211$ at the quarter-chord position (Figure 50), the vorticity is a little greater, at $\omega c/U_\infty = 111$. The location of the vortex is approximately the same. The higher strength vortex has induced greater velocities on the ground and possibly on the endplate inner edge, and these areas of negative vorticity appear stronger than for the greater height. This effect is again seen at the results behind the endplate. The maximum vorticity is similar to that at the quarter-chord, $\omega c/U_\infty = 112$. The negative vorticity regions are stronger than at the greater height. It appears that the vortex core may have traversed inboard a little compared to the greater height; the core position is approximately $z = 0.13$, $y = -0.04$.

Figure 51 gives the results at two more heights, $h/c = 0.158$ and $h/c = 0.105$ for the two locations, both type b heights. At $h/c = 0.158$ at the quarter-chord, the vortex is stronger than the results in the previous figures; $\omega c/U_\infty = 119$. It also appears a little larger. (It has, however, reduced strength slightly from the maximum at $h/c = 0.184$ of $\omega c/U_\infty = 128$, Table 13.) The higher strength vortex has induced yet greater velocities, and the inner surface of the endplate and the ground have stronger negative vorticities in these regions. In difference to the previous trend, the results behind the endplate do not show the presence of a strong vortex core. The vortex is significantly larger than at the greater heights, but is a significantly reduced strength. It appears to have diffused drastically. The maximum vorticity measured corresponds to $\omega c/U_\infty = 20$. The roll up of the shear layer from the endplate outer edge is still present. It seems that the region of shear on the endplate inner edge is of a slightly reduced strength than at the greater heights.

However, the negative vorticity on the ground appears to be stronger than the greater heights.

At the lower height of $h/c = 0.105$, the results at the quarter-chord now show a weak, diffused vortex. The maximum strength was found to be $\omega c/U_\infty = 30$. The shear layer on the endplate has reduced in strength significantly. However, the negative vorticity on the ground appears stronger than at the previous heights. Behind the endplate at this height, a conventional vortex does not exist. The results show a large spanwise region of small positive vorticity, maximum magnitude $\omega c/U_\infty = 14$, above a shear layer of comparable magnitude but opposite direction just above the ground.

The contours are now given for the high flap angle. At a height of $h/c = 0.263$ (type a) (Figure 52), the maximum vorticity in the core was measured as $\omega c/U_\infty = 153$. This is approximately 50% stronger than that for the low flap angle at this height and streamwise location. The core seems to be in a similar location compared to the low flap angle. Behind the endplate, a comparable strength of the vortex is again obtained, at $\omega c/U_\infty = 147$. In a similar manner to the results at the low flap angle, the rollup has been mapped quite well. The core has moved inboard, and is at approximately $z/c = 0.12$, $y/c = -0.03$. Again, it is difficult to be entirely certain, but it appears that the core is a little further inboard, and a little higher, than compared to the low flap angle. The outer edge of the vortex, furthest away from the wing tip lies further inboard than that at the low flap angle. Also, the strength of the negative vorticity shear on the ground and that arising from the inner surface of the endplate are stronger than further upstream, and also than at the low flap angle.

At $h/c = 0.211$ (type b), the vortex is regular and concentrated, at the quarter-chord. The maximum vorticity, however, has reduced slightly compared to that $h/c = 0.263$, and corresponds to $\omega c/U_\infty = 126$, about 20% lower. Behind the endplate, the strength has reduced suddenly, and diffused over a large area, and give a maximum vorticity of $\omega c/U_\infty = 21$.

At $h/c = 0.158$ (type b), the results at the quarter-chord (Figure 53), show that the vortex has now deteriorated here at this height. A moderate strength of $\omega c/U_\infty = 53$ was measured. There is however, still a strong region of negative vorticity close to the ground, which can also be seen behind the endplate. Lower still, at $h/c = 0.105$, similar results to the low flap angle are again seen, with a weak area of positive vorticity for the results at the quarter-chord, which form a layer behind the endplate.

For heights near to the type a/b flow boundary, the maximum vorticity found in the core has been added to Figure 37 for both of the locations, at each flap angle.

8.4.2 Instantaneous Results

For a selection of the cases described in the mean flow results, the instantaneous state of the tip vortex is presented. For the low flap angle, at a height of $h/c = 0.263$ (type a), the mean flow results at the quarter-chord position can be seen in the top left of Figure 54, together with three instantaneous snapshots that are representative of the flow. The mean flow results show a

concentrated vortex, which is fed by the shear layer, rolling up over the bottom edge of the endplate. The three snapshots are all similar. The images all feature some noise in the results. This may either be due to a real flow phenomenon, such as turbulence, or the experimental conditions, such as a lack of seeding, a reflection, or a light intensity reduction due to the microscope slide. For all three snapshots, the vortex seems to be of the same size and location, and the strengths are also comparable.

The same can generally be described of the results at $h/c = 0.211$ (type *a*), Figure 55. The strong vortex core remains in the same location for the three images. There is a little change in the shape of the core, however, for the three images. At this height, the mean flow results show a stronger shear layer on the ground. This can also be seen in the instantaneous results, although there is a little noise or unsteadiness present. Again, broadly similar results are to be found at a height of $h/c = 0.158$, Figure 56 (type *b*).

At $h/c = 0.105$ (type *b*), the mean flow results exhibit the sudden reduction in vortex strength, and the vortex is diffused over a large region, Figure 57. For the mean flow results, a maximum vorticity of $\omega c/U_\infty = 30$ was measured, at a location of $z/c = 0.08$, $y/c = -0.09$. The flow exhibited a large amount of unsteadiness with different images showing differing flows. The three snapshots presented, however, are typical of the flowfield. The first image, in the bottom left of the figure, shows a region of positive vorticity that does not appear to be regular, in terms of the shape and vorticity distribution. The core of the vortex is not readily apparent, however, the peak vorticity is measured as $\omega c/U_\infty = 52$, at $z/c = 0.07$, $y/c = -0.10$. For the second image, top right, the vortex is still irregular in terms of the shape and the distribution. The peak vorticity is stronger, at $\omega c/U_\infty = 71$, at $z/c = 0.08$, $y/c = -0.07$. There is a second peak of vorticity, of a weaker strength, slightly inboard and to the right of the main core. In the final image, the peak is stronger again, at $\omega c/U_\infty = 86$, and has moved again, at $z/c = 0.09$, $y/c = -0.04$. All three images exhibit a strong shear layer presence on the ground due to the induced velocity from the vortex.

For the high flap angle at a height of $h/c = 0.263$ (type *a*), Figure 58, the characteristics of a regular vortex with the strong core for the mean flow results are replicated in each of the instantaneous images. At $h/c = 0.211$ (type *b*), Figure 59, the maximum vorticity from the mean flow results is $\omega c/U_\infty = 126$, less than that at $h/c = 0.263$ which is $\omega c/U_\infty = 153$. The first two images are typical of 90-95% of the 200 samples taken. Image 3 is typical of about 5-10% of all of the snapshots. The first image, bottom left, shows a regular core, of maximum vorticity $\omega c/U_\infty = 138$ at $z/c = 0.05$, $y/c = -0.06$. Similar results are found for the second image, $\omega c/U_\infty = 135$, again at $z/c = 0.05$, $y/c = -0.06$. However, for the third image, there is a significant reduction in strength, to $\omega c/U_\infty = 78$, but it is at the same location. No images with a significantly reduced strength were found at $h/c = 0.263$.

At a height of $h/c = 0.158$ (type *b*), the flow was found to be highly unsteady, and fluctuating between different states (Figure 60). The mean flow features a vortex of maximum strength

$\omega c/U_\infty = 53$, significantly reduced from that at greater heights, at $z/c = 0.05$, $y/c = -0.06$. The three snapshots reflect an approximately equal distribution of flow types of the entire sample. The image at the bottom left shows a weak vortex, of maximum vorticity $\omega c/U_\infty = 63$, at $z/c = 0.11$, $y/c = -0.09$. The second image, top right, shows a regular, high strength vortex of $\omega c/U_\infty = 128$ at $z/c = 0.07$, $y/c = -0.06$. The third features an irregular vortex of $\omega c/U_\infty = 114$ at $z/c = 0.05$, $y/c = -0.04$. There is also a second peak, of reduced magnitude, to the right and lower than the main core. The three images have a maximum vortex strength greater than the average due to the variation in location of the core. An inspection of the other samples indicates this trend to be present in nearly all instantaneous images.

Figure 61 gives the results at $h/c = 0.105$. Mean flow results do not show the presence of a discrete core; the vortex is weak and distributed. The instantaneous images all show a highly unsteady flowfield. However, unlike the case at $h/c = 0.158$ where the vortex is unsteady, but fluctuating between strong regular core, strong irregular core, and weak irregular core, all the results at $h/c = 0.105$ show a irregular tip vortex.

Only a small sample of the instantaneous results taken behind the wing are also presented. Figure 62 shows the images at $h/c = 0.263$ for the high flap angle (type a). The mean flow results show a strong vortex rolling up, from the shear layer originating from the outer edge of the endplate. All three images show a similar flowfield; the vortex core is in the same location and of comparable strength for all cases.

At $h/c = 0.211$ (type b), the mean flow results show a weak, distributed vortex, compared to a strong vortex core for the results at the quarter-chord (Figure 63). At this height, for the high flap angle, most images at the quarter-chord show a regular strong vortex, with about 5-10% of images showing an irregular core, with significantly reduced strength (Figure 59). Behind the endplate, however, all snapshots are similar. The vortex is distributed over a large area and does not feature a strong core. The distribution of vorticity within the vortex is not regular, and does not increase near to the centre. Regions of small negative vorticity are found interspersed within the vortex.

At reduced heights for the high flap angle, similar results were found, with a large, distributed vortex, with no strong core. They are not presented here as the quality of the instantaneous is not as high. This was also found to be the case for the low flap angle, at which the instantaneous images are comparable to similar mean flow results. Figure 37 also contains an annotation as to whether the flow is generally steady, or as to the proportion of the instantaneous images that feature a burst vortex.

8.5 Oil Flow visualisation

Oil flow visualisation was performed at heights of $h/c = 0.395$, 0.263, 0.211, 0.158, and 0.105. It was not possible to test at lower heights than this due to the excessive heat generated when applying greater belt suctions for the extended periods required for the mixture to dry. The results

are discussed with reference to two features of interest in the flowfield; transition location, and the three-dimensionality of the flow.

8.5.1 Transition

The suction surfaces of the main element and the flap are shown for the low flap angle at a height of $h/c = 0.395$ in Figure 64a, with the leading edge lowermost. On the main element, the separation bubble indicating transition is clear over most of the span of the wing. The separation point in the bubble was measured at $x/c = 0.11 - 0.13$, with turbulent reattachment at $x/c = 0.16$. However, near to the centre of the wing, a small region can be seen where the bubble is breaking up just to the left of the semispan, and where the bubble is not present slightly to the right of the semispan. Close inspection of the patterns on the wing, difficult to see in the figure, reveal a small bubble very close to the leading edge, $x/c = 0.01 - 0.02$, where there is no main transition bubble. (This phenomenon is discussed further below.) Hence, on the main element, transition is observed at two chordwise locations at this height for the low flap angle; $x/c = 0.01 - 0.02$ for a small region at the centre of the wing, and $x/c = 0.11 - 0.16$ elsewhere. On the flap, a reasonably large transition bubble is again seen. It is broken up at three spanwise locations where the brackets secure the flap in place. The separation point was measured at $x/c = 0.69 - 0.72$, with turbulent reattachment at $x/c = 0.75$.

Similar results (not presented here) were found at $h/c = 0.263$ for the low flap angle, where transition occurs close to the leading edge of the main element for a very small region near to the semispan, and at $x/c \approx 0.1 - 0.15$ for the rest of the span. The leading edge transition was not seen at $h/c = 0.211$, and heights below this, for the low flap angle. Results at $h/c = 0.158$ for the low flap angle can be seen in Figure 64b. On the main element, the detachment point in the bubble was measured at $x/c = 0.12 - 0.14$, with reattachment at $x/c = 0.17$, i.e. at approximately the same location within the measurement uncertainty. The bubble on the flap was measured at the same position as that at $h/c = 0.395$.

For the high flap angle, there is a significant difference. Figure 65a shows the suction surfaces at $h/c = 0.211$. On the main element, transition at the leading edge accounts for a significant portion of the span of the wing. There is a close up of this in Figure 65b. In the left portion of the image, the leading edge bubble can be seen, and on the right, the bubble is further back, at $x/c = 0.11 - 0.18$. As at the low flap angle, this portion of the wing with leading edge transition reduces as the ground height is reduced. At this height, it is approximately 36% of the span. This reduces from 57% at $h/c = 0.395$ to 46% at $h/c = 0.263$, 36% at $h/c = 0.211$, 20% at $h/c = 0.158$ to virtually zero at $h/c = 0.105$. Referring back to the main image (Figure 65a), the transition location for the flap is now very close to the leading edge, at $x/c \approx 0.58$. This was found to be the case for all heights tested at for the high flap angle.

8.5.2 Flow Three-dimensionality

Results showing the flow over the semispan, including the tip region are presented in Figure 66 at heights of $h/c = 0.395, 0.211$ and 0.105 for the low flap angle. On inspection of the region on the main element from the transition to the trailing edge, at $h/c = 0.395$, there is a moderate cross-flow directed to the centre of the wing over most of the surface, but very close to the tip, a slight cross-flow directed outwards marks the formation of the main vortex. At the flap tip, patterns exist showing presence of a secondary corner vortex, as can be seen in the region between the transition bubble and the endplate. At $h/c = 0.211$, the cross-flow on the main element is more extreme, both directed towards the centre, and in the vortex region. The secondary corner vortex on the flap tip is stronger. The flow lines at the trailing edge of the flap show a greater cross-flow, as flow is entrained into the main vortex. At $h/c = 0.105$, there is a greater three-dimensionality to the flow on the main element and the cross-flow pulling the flow to the centre of the wing, from outside the vortex is stronger. Near to the trailing edge of the flap, the cross-flow appears similar or possibly slightly less than that at $h/c = 0.211$. For all the results, the flow patterns on the surface of the flap do not show the direct presence of the main wing tip vortex that originates from the main element, only the effect of it.

Figure 67 shows the results near to the tip at heights of $h/c = 0.211$ and 0.105 for the high flap angle. Comparing the patterns on the main element, it can be seen that the cross-flow directed to the wing centre is greater for the lower height case. Again, there is a secondary corner vortex that exists on the flap, very close to the tip. Near to the trailing edge of the flap, there is a greater deviation from the streamwise direction for the flow at $h/c = 0.211$, highlighting the effect of the main wing tip vortex that originates from the main element being stronger for this height.

8.6 Laser Doppler Anemometry

LDA testing was performed near to the beginning of the test schedule for the double element wing. Despite the high flow three-dimensionality, and due to the limited amount of time available, the tests were performed at the centre of the wing, investigating the wake, in a similar manner to the previous studies involving the single element wing. Attempts were made to map the flow from the main element onto the flap, using mirror boxes mounted on the laser heads, with the beams shining through a perspex endplate. However, it was not possible to gain useful data with this setup. The results presented here were performed using the LDA system in the standard setup without mirror boxes, taking wake surveys at four streamwise locations of 30,75,150 and 300mm behind the trailing edge of the flap, corresponding to $x/c = 1.066, 1.184, 1.381$ and 1.776. Boundary layer surveys were taken along a line perpendicular to the suction surface, at the trailing edge of the flap. Results were acquired at heights of $h/c = 0.395, 0.211$ and 0.105 for the low and the high flap angles. The results will be discussed with respect to the contour plots (Figures 68 & 69), wake surveys, and boundary layer profiles (Figures 70- 72).

At the low flap angle at an arbitrary height, e.g. $h/c = 0.211$ (Figure 68), shows a wake from the wing that rises from the trailing edge, as the flow is deflected through a relatively high angle, due to the flap. Near to the trailing edge, two minima for the u/U_∞ velocity exist; the more significant in terms of velocity deficit and thickness appears to be due to the main element, and the smaller from the flap, see also Figure 70a. As the wake develops downstream, turbulent mixing increases the thickness of the wake, as was found for the single element wing, and the maximum velocity deficit reduces. The wake directly due to the portion from the flap seems to disappear from the contours, and the wake surveys confirm that the flap wake has mixed with the wake from the main element, such that at $x/c = 1.776$ for $h/c = 0.211$, no sharp discontinuity in the profile exists, indicating that the wakes are fully merged. At $x/c = 1.066$, the flow velocity increases from the wake to the ground. This vertical pressure gradient is as would be expected from vertical traverses not perpendicular to the curved surface of the flap. Close to the trailing edge, the flow is at a higher velocity than freestream in the region between the wing and the ground. In the region from the wake to the ground, the adverse pressure gradient can be seen to reduce the velocities in the streamwise direction. The final point, at $x/c = 1.776$ shows a relatively constant velocity profile in this region. The boundary layer very close to the ground can be seen, and is more prominent than the single element wing. For $h/c = 0.211$ at the low flap angle, the velocity deficit appears similar as the flow moves downstream, with a minimum velocity of $u/U_\infty \approx 0.95$. The layer does, however, appear to have grown in thickness.

As the height of the wing is reduced (Figures 68 & 70b), the wake from the wing increases as was found for the single element wing. However, the portion of the wake from the flap does not change significantly, in terms of the velocity, and the thickness. The portion from the main element is the cause of the increase; the wake thickens and the velocities reduce as the height is reduced. In a similar manner to the single element wing, it is the portion from the suction surface (of the main element) that changes, and the pressure surface contribution does not vary significantly. Similar values for the velocity are found in the region of accelerated fluid between the wake and the ground. The retarded flow very close to the ground becomes more significant as the height is reduced, as the layer becomes thicker, and possibly becomes more extreme in terms of the velocity deficit.

The most obvious effect of increasing the flap angle, is to increase both the wake size, and the deflection to the wake (Figures 69 & 71a). Both the velocity deficit, and the wake thickness are greater for the high flap angle, not only due to the main element, but also from the flap. From the wake surveys, it can be seen that, for the high flap angle, the wakes are further from merging than for the low flap angle. The fluid between the wing and the ground is accelerated to a greater extent for the high flap angle for the results near to the wing. For $h/c = 0.105$, the contours show that the velocity deficit very close to the ground is greater for the high flap angle, both in terms of the velocity, and the thickness. At the greater heights, it is clear that the layer thickens as it moves downstream, but it is difficult to compare the velocities directly. The general effect of changing the height on the flowfield, and the development of the wake downstream is similar to those found

for the low flap angle.

Boundary layer profiles of the local velocity u_n/U_∞ (Figure 71b) confirm that at the trailing edge of the flap, the wake from the main element is separate from the boundary layer of the flap, and that the merging of the layers, if any has happened, is small at this streamwise location. As the height is varied for the low flap angle, the boundary layer directly due the flap changes little, and the results are within the positional accuracy of the equipment used. The velocity at the confluence between the layers is $u_n/U_\infty \approx 1.06$ for the three heights for the low flap angle. The minimum velocity due to the wake from the main element reduces as the height reduces, and the location of this moves further away from the surface, as the wake thickness increases. The effect of the overall boundary layer thickness increasing as the ground is approached is due to the contribution from the main element. For the high flap angle at $h/c = 0.395$, the boundary layer directly due to the flap is thicker. In addition, the merging of the wake from the main element with the flap boundary layer is less developed than for the results at the low flap angle. The main element boundary layer is both thicker and more significant in terms of the velocities, compared to the low flap angle.

The $u'u'/U_\infty^2$ perturbation velocities are presented in Figure 72a for the boundary layer profiles. For the low flap angle results, concentrations in $u'u'/U_\infty^2$ are found in the region close to the flap surface. The greatest results for the turbulent stress are found at values of ζ less than 0.002 from the surface, and this decreases to minima at $\zeta \approx 0.015c$, a height near to the merging of the main element wake and the flap boundary layer. In the region of the main element wake, $u'u'/U_\infty^2$ increases to a maximum. For all three heights, this maximum is at a location further away than the centre of the main element wake, and the magnitude increases as the height is reduced. Some evidence of a second peak of perturbations exists at a location closer than the centre of the boundary layer, but this is not well defined. The curve then drops as the edge of the boundary layer is approached. For the high flap angle, the peak within the flap boundary layer is of a greater magnitude than the low flap angle, at $h/c = 0.395$. The perturbations then drop sharply to practically zero, confirming that this is out of, or very close to the edge of the main element wake. The curve increases to a first small peak, on the inner side of the centre of the wake, drops slightly, and increases again to a second peak, further out from the centre of the wake, then falling off to the edge of the boundary layer.

Wake profiles showing the development of the wake in terms of $u'u'/U_\infty^2$ (Figure 72b), show two distinct peaks at $x/c = 1.066$, representing the wakes from the flap and the main element. Here, the contribution from the flap is more significant than that of the main element. At the next point, $x/c = 1.184$, the perturbations from main element have reduced only slightly in the portion of the wake from the main element, but very significantly in the portion from the flap. At $x/c = 1.381$, the flap contribution falls again, and is more like a plateau, until at $x/c = 1.776$ the results show advanced merging, with only a small bump. High levels of the perturbation velocity can be seen in the boundary layer close to the ground, which decrease significantly with distance downstream.

8.7 Discussion

8.7.1 Downforce Generation

Adding the flap to the main element induces a greater circulation around the main element, as can be seen by the greater suctions on the lower surface, and the increased pressures on the upper surface (Figure 38b). The fact that there is a finite suction at the trailing edge of the main element implies that the pressure recovery from the suction peak on the main element to the trailing edge is not as severe. Large regions of separated flow were observed for the single element wing, but for the double element wing separation is not as widespread. The two effects, the *circulation effect* and the *dumping effect* were described by Smith [60] as contributory factors to the benefit of a multi-element configuration.

For the single element wing, the downforce generated at different heights from the ground increases asymptotically, following a smooth curve, which then falls off gradually below the maximum downforce. For the double element wing, two flow regions have been identified. Region a heights, at and above $h/c = 0.171$ for the low flap angle and at and above $h/c = 0.237$ for the high flap angle feature an increasing downforce with an increasing proximity to the ground. The slope increases as the height reduces. Below this, at region b heights, the curve also increases with reducing ground height until the maximum downforce is obtained. For the low flap angle, there is an asymptotic increase, then a smooth reduction in the gradient to the maximum downforce, followed by a reduction in downforce. For the high flap angle, the curve is more linear, and there is a sharp reduction below the maximum downforce. At the boundary between the type a/b flows, there is a discontinuity in the downforce curve. For the low flap angle, this is manifested as a plateau region at the large type b heights. For the high flap angle, there is a sudden reduction in downforce, compared to the lowest type a heights.

The integrated pressures at the centre of the wing show that the sectional downforce from the centre of the main element follows a smooth curve; there is no effect on the downforce at the boundary of the type a/b flows. For the low flap angle, the points follow a smooth curve, qualitatively similar to the single element wing results, featuring an asymptotic increase, reduction in gradient, maximum downforce, and reduction in downforce. The high flap angle results are similar, but feature a sudden reduction at heights below the maximum downforce. Surface pressures show a sudden increase in pressure over the suction surface for the lowest height tested.

At the centre of the wing, the contribution from the flap at the low flap angle increases by about 30% as the height is reduced from $h/c = 0.592$, until a maximum at $h/c = 0.105$, and then reduces a little below this. Similar results are found for the high flap angle, where the height at the maximum sectional downforce is $h/c = 0.158$. The pressure distributions suggest that the small reductions in downforce are due to reductions in pressure on the pressure surface, and small reductions in suction in the region $x/c = 0.65 - 0.8$ on the flap suction surface. The general increase in downforce as the ground is approached for the flap is significantly smaller than that

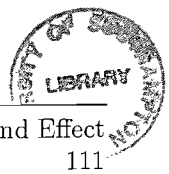

for main element. As the height of the wing is changed, the flap is further from the ground, and therefore less sensitive to changes in ground height than the main element. There is a more significant reduction in downforce at the lowest height for the high flap angle, which is due to the boundary layer separating over the flap. The lower circulation imparted by the flap on the main element can be seen represented by the lower suctions on the main element suction surface for the lowest height. Two hypotheses are presented. First, the boundary layer may separate from the main element suction surface for the lowest height with the high flap angle, preventing the wake from flowing over the flap, leading to the flap boundary layer separating, and a lower flap loading. However, the flap flow may separate itself, causing a loss in flap circulation, reducing the main element circulation.

The cause of the discontinuity in the downforce with height curve is due to three-dimensional effects. For region *a* flows, the sectional downforce at the tip is lower than the overall downforce by a broadly constant value. For region *b* flows, the difference increases significantly. The contribution of the downforce at the tip due the main element generally increases steadily as the height is reduced. There is a small bump at the boundary of type *a/b* flows. For the flap, the downforce at the tip increases steadily in region *a*, then falls steadily in region *b*. The small bump in the downforce from the main element at the region *a/b* boundary is due to the direct influence in the loading from the flap reducing at the particular height.

8.7.2 Tip Effects

Spanwise pressures suggest that on the main element at the quarter-chord, the flow increases three-dimensionality for all heights, as the height is reduced. On the flap, there is an increase in suction near to the tip. In region *a* heights, the suction near to the tip of the flap increases as the height is reduced. The maximum suction near to the flap tip is at the lowest type *a* height, for both flap angles. The suction near to the flap tip then reduces as the ground is approached, through the type *b* heights. This is found to be the case for the low and high deflection angles, Figure 37.

Mean PIV results on the wing tip vortex at the flap quarter-chord position shows us that the strongest vortex here occurs at the lowest type *a* height, for both flap angles, correlating with the surface pressures at the same location. In type *b* heights, the vortex strength at this location reduces a little, then more significantly. The results taken behind the trailing edge are a little different. The vortex strength increases as the height is reduced for the type *a* heights. However, there is a rapid reduction in strength for all type *b* heights, for both the flap angles. Hence, at the largest type *b* height for both flap angles, the vortex at the flap quarter-chord is still relatively strong, but less than its maximum, and when it has reached the measurement point behind the trailing edge, the strength has reduced significantly, and a weak, diffuse vortex exists. For the remainder of type *b* heights, a weak vortex exists at both locations (Figure 37).

The instantaneous PIV images allow us to describe the time varying state of the tip vortex. For all type *a* heights, the vortex is steady, regular, and strong in all images, at both locations. As the

height reduces throughout the type a region, the strength increases, such that at the smallest type a height, the vortex is stronger than at all other heights, for each of the locations. At the largest type b height for the low flap angle, $h/c = 0.158$, the instantaneous images at the quarter-chord still appear to show a regular, strong vortex for all the images. For the high flap angle at the largest type b height, $h/c = 0.211$, approximately 5-10% of the images show a vortex of significantly reduced strength, that has *burst* intermittently, at the quarter-chord. For each of these heights, i.e. $h/c = 0.158$ for the low flap angle, and $h/c = 0.211$ for the high flap angle, the vortex bursts by the time that it is at the second measurement point behind the trailing edge for all images, if it has not already done so. At a lower height in the type b region, $h/c = 0.105$ for the low flap angle, at the quarter-chord position, the instantaneous images show a weaker vortex, which is of uneven distribution and which changes location according to time. The vortex has burst for all samples. For a similar region b height for the high flap angle, $h/c = 0.158$, some of the images show a strong, regular vortex, and some show a vortex that has burst (Figure 37).

It is assumed that a strong regular vortex, as found for a type a height, will have a high speed vortex core. This will induce greater velocities in the region near to the tip of the flap. As the strength increases as the height is reduced in the type a regions, the suction imparted near to the flap tip will increase. As the vortex bursts in the type b flows, the suction near to the flap tip reduces, causing the loading near to the tip to reduce.

One reason for the vortex bursting may be due to the direct influence of the ground. Figure 59 shows a flowfield that generally features a strong vortex, but for which the vortex occasionally bursts, at $h/c = 0.211$ for the high flap angle at the quarter-chord. It can be seen that, from the mean flow results, there is a finite distance between the shear feeding the vortex rollup, and the induced shear on the ground, which is of opposite direction. The reason for the vortex bursting, therefore, is not due to a merging between the main vortex and the ground, (or the induced shear above the ground). For the same height, behind the trailing edge (Figure 63), the mean and the unsteady results again show that there is a finite distance between the (already burst) vortex and the shear above the ground. It is possible that further downstream, there may be direct interaction between the vortex and the shear above the ground, given the growth of the vortex. However, it is unlikely that this is the *cause* for the vortex to burst. The location at which the vortex bursts is upstream of $x/c = 1.092$, and generally downstream of $h/c = 0.672$ for the largest type b height, although the burst occasionally moves upstream of this.

It is believed that the vortex bursts due to vortex breakdown. This phenomenon has been observed in many aeronautical studies, for example for vortices over delta wings [74], and also for rectangular wings [74, 75]. The phenomenon occurs when a vortex is under an adverse pressure gradient, as would be expected for the current study. For a fixed ground height, it is clear that the adverse pressure gradient for the high flap angle would be greater than for the low flap angle. This would explain why the breakdown occurs at a greater height for the high flap angle than for the low flap angle. The location of the breakdown has been frequently observed to oscillate about

position, as can be seen in the current results (Figures 59 & 60), where some instantaneous images show a burst vortex, and some show a regular, strong, vortex. When vortex breakdown occurs, this results in a rapid deceleration in the axial velocity of the vortex. Near to the flap tip, for type b heights, surface pressures indicate a reduction in the suction, due to the reduction in vortex strength, and lower induced velocities.

For a strong vortex, the high axial velocity induces a large suction on the lower surface near to the tip of the flap. When the vortex breakdown occurs, there is a reduction in the suction near to the flap tip. Before breakdown, the vortex strength for the high flap angle is greater than that for the low flap angle. The suction that it induces is also greater for the high flap angle. When breakdown occurs, there is a reduction in local loading for the low flap angle, resulting in a plateau in the downforce level. For the high flap angle there is a greater effect, and there is a sharp reduction in overall downforce for the wing.

The oil flow tests also show greater cross-flows near to the trailing edge of the flap in presence of a strong tip vortex. However, it is difficult to visualise the vortex flow, in particular the breakdown, on the surface of the wing.

8.7.3 Transition

The oil flow visualisation tests yield interesting results regarding the transition location. For the low flap angle, transition was observed over the majority of the main element at $x/c \approx 0.10 - 0.15$, for $h/c = 0.395$ and 0.263. At the very centre of the wing, transition was observed very close to the leading edge of the main element. At all other heights close to the ground, transition occurred at $x/c \approx 0.10 - 0.15$ for the entire span of the main element. For the high flap angle, similar, but more extreme results were found. At $h/c = 0.395$, transition at the leading edge was observed for nearly 60% of the span. This reduced steadily to virtually zero at $h/c = 0.105$. The chordwise surface pressures for the centre and the tip are useful in explaining this phenomenon. Adding the flap promotes a spike in the suction on the main element, very close to the leading edge. This effect is similar to the previous configurations when the incidence of the wing is increased, or the Gurney flap was added, to the single element wing. The suction spike is greater for the larger flap angle, than for the smaller flap angle (Figure 38b). It seems that near to the tip, the suction spike is significantly reduced than compared to the centre (Figure 46). Other researchers [89] have shown that for a two-dimensional wing with a leading edge suction peak, the peak is virtually eliminated for a low aspect ratio three-dimensional case. Hence it is likely that the reduction in the spike near to the tip is directly due to the tip effects. As the height of the wing is reduced, the suction at the lowest point on the surface near to the suction peak increases significantly. The suction at the spike however, changes very little. In this manner, a large height may give the maximum suction on the main element at the centre in the spike, and near to the tip in the peak. As the height is reduced, the suction at the peak increases, and that at the spike remains relatively constant, such that closer to the ground, the maximum suction at the centre changes to the peak from the spike,

and at the tip remains at the peak. Hence, the transition, occurring after the peak suction, tends to occur in the centre of the wing at large heights, with this region reducing as the height reduces. The larger spike with the higher flap angle promotes the leading edge transition at the suction spike for a greater range of heights.

8.7.4 Wake

Regarding the wake flow measurements at the centre of the wing, as taken with the LDA system, the general trend is similar to the single element. The wake becomes thicker and the velocities in the wake increase as it moves downstream, due to turbulent mixing. As the height is reduced, the wake thickens, and the velocities reduce. Inspection of the results shows that the increase in the thickness of the wake as the height is reduced is due to that from the main element. The portion of the wake from the flap remains relatively unaffected by a change in height. This can be explained by the surface pressures. As the height is reduced, the pressures on the lower surface of the main element change significantly, and the pressure recovery increases. There is a little change in the pressures found over the lower surface of the flap. However, this is very small compared to that found on the main element. As described previously, the flap is less sensitive than the main element to changes in ground height since it it further away from the ground. For a reduction in height, therefore, the adverse pressure gradient on the main element increases, causing the boundary layer to be closer to separation, resulting in a larger contribution to the wake.

The boundary layer surveys at the trailing edge show that for the high flap angle, the flap boundary layer and the main element wake are not close to confluence. At the low flap angle, however, it seems that the shear layers are about to, or have just started to merge. Results further downstream for the low flap angle show that the wakes from the flap and the main element only seem to have fully merged when they reach $x/c = 1.776$, a large distance downstream. Other researchers have found that for optimised aerofoils for an aeronautical type application, boundary layer merging occurs at a location along the element [67] or at the trailing edge of the element [60]. The flap gap and overlap was only optimised for the high flap angle, due to time constraints, at which the wakes are further from merging than for the low flap angle. The current results are therefore contradictory to other researchers, and it would seem that the flap gap may be too large for an optimised aerofoil. It is believed that the difference may be due to three-dimensional effects. The influence of the tip vortex near to the tip of the flap is significant in the production of downforce. The effect of this may be that near to the tip, an optimised wing could require a larger gap than at the centre of the wing, for this particular configuration.

The turbulence levels of $u'u'/U_\infty^2$ found in the boundary layer profiles at the flap trailing edge show a high level of fluctuating velocity in the flap boundary layer. This then reduces as the edge of the boundary layer/main element wake confluence is approached. Concerning the wake from the main element, two peaks in the fluctuating velocity are present. The peaks are located either side of the minimum u/U_∞ velocity, with the peak further from the centre of the wake having the

larger magnitude. These peaks refer to the shedding from the main element finite trailing edge, as discussed in the single element study. It would appear that, at the flap trailing edge, the vortices shed from the main element suction surface are stronger than those shed from the main element pressure surface, due to the larger size of the respective peaks. The peaks also increase thickness and velocity as the height is reduced; the boundary layer thickens and the shedding becomes less regular, and the vortices are of greater magnitude. From the results in the wake, two peaks are now evident. These are attributed to the main element wake, and the flap wake. Results close to the flap trailing edge show that the peak due to the flap is significantly greater than that from the main element. Although $u'u'/U_\infty^2$ from the main element reduces a little as the wake moves downstream, that due to flap reduces suddenly, and for the last two profiles, the wakes are in the advanced stage of merging. The spatial resolution, and the fact that the results nearest to the trailing edge are at $x/c = 1.066$ mean that it is not clear whether there is shedding just behind the trailing edge of the flap.

8.8 Summary

The flow around a double element wing has been investigated experimentally. At large heights, region *a*, the downforce increases asymptotically with a reduction in height. Then there is either a plateau, in the case of the low flap angle, or a reduction in downforce, in the case of the large flap angle. The downforce then increases again, region *b*, until it reaches a maximum, and then reduces. In the case of the low flap angle, the maximum downforce is dictated by gains in downforce from lower surface suction increases and losses in downforce due to upper surface pressure losses and flap lower surface suction losses, with a reduction in height. For the high flap angle, there is a sharp reduction just beyond the maximum, due to the boundary layer separating, and a resultant loss of circulation on the main element.

The main element produces most of the downforce. The flow on the main element is highly three-dimensional. At the tip of the wing, the downforce from the main element is significantly reduced compared to that at the centre. The tip vortex from the main element induces a region of high suction near to the tip of the flap. When the vortex is strong, the flap produces more downforce at the tip than at the centre. In type *b* flows, the tip vortex breaks down, resulting in a loss of downforce near to the tip of the flap.

As with the single element wing, the wake increases as the height is reduced. This is attributed to the portion from the main element.

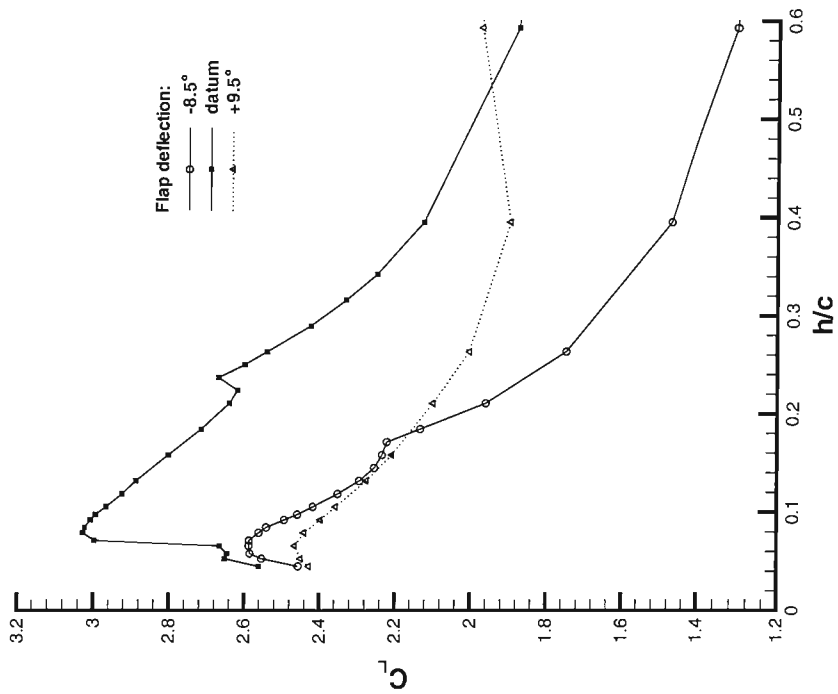

(b)

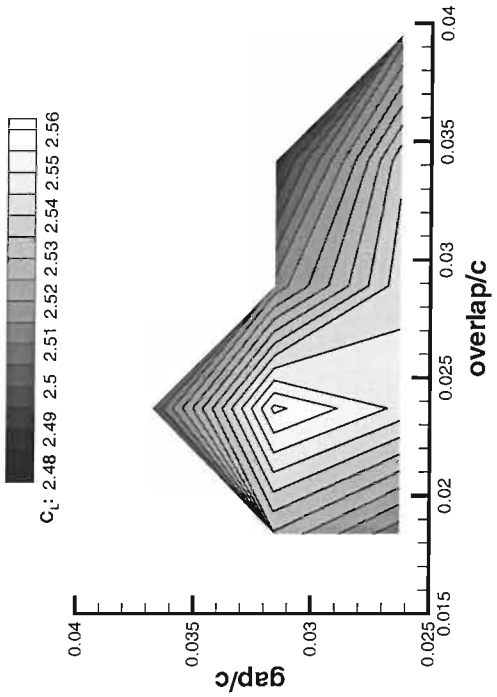

(a)

Figure 36: Forces in ground effect; (a) Effect of varying flap overlap and gap at a height of $h/c = 0.263$ at the datum flap angle. (b) Downforce with ground height.

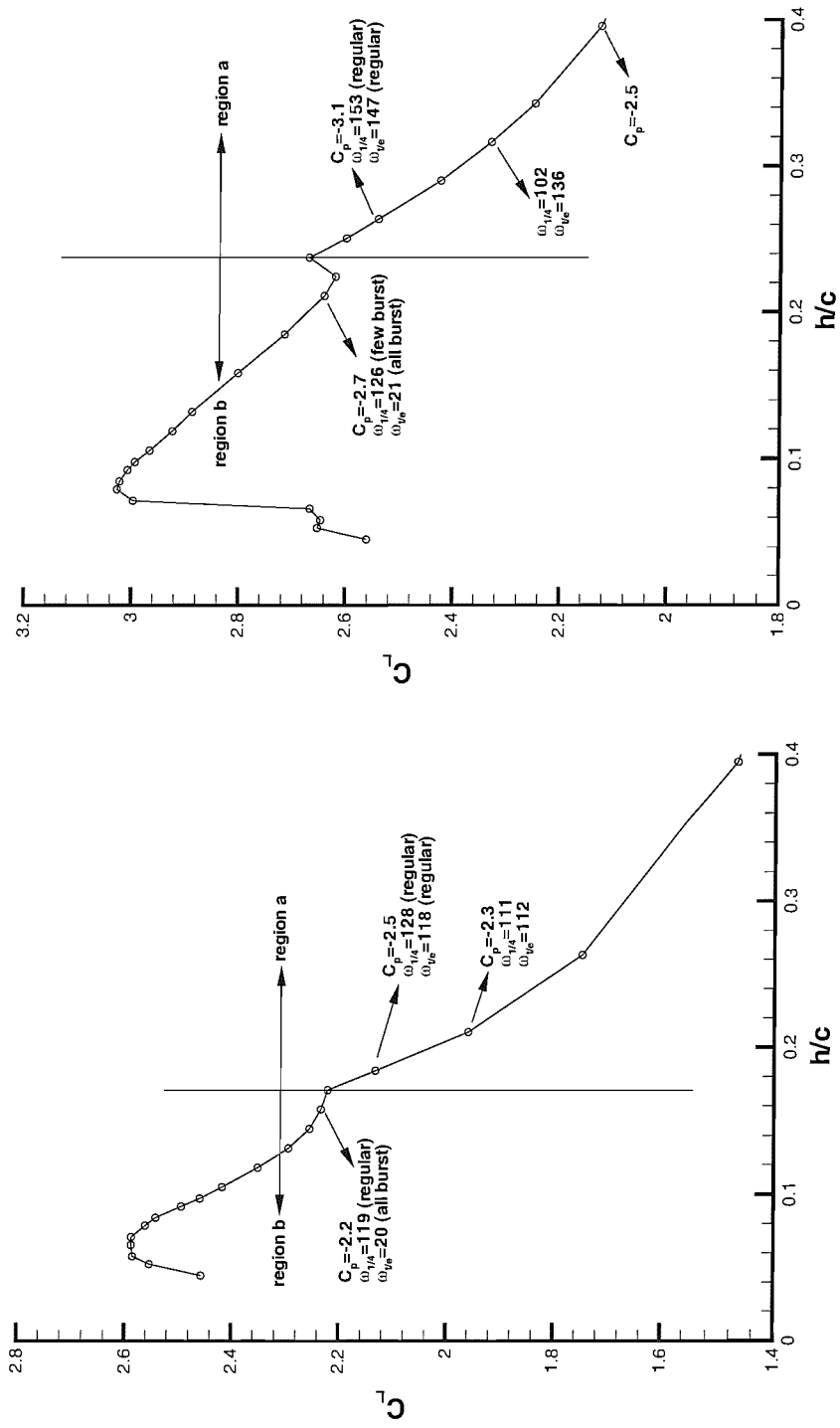

Figure 37: Downforce with ground height, including flow regions and features, (a) Low flap angle. (b) High flap angle.

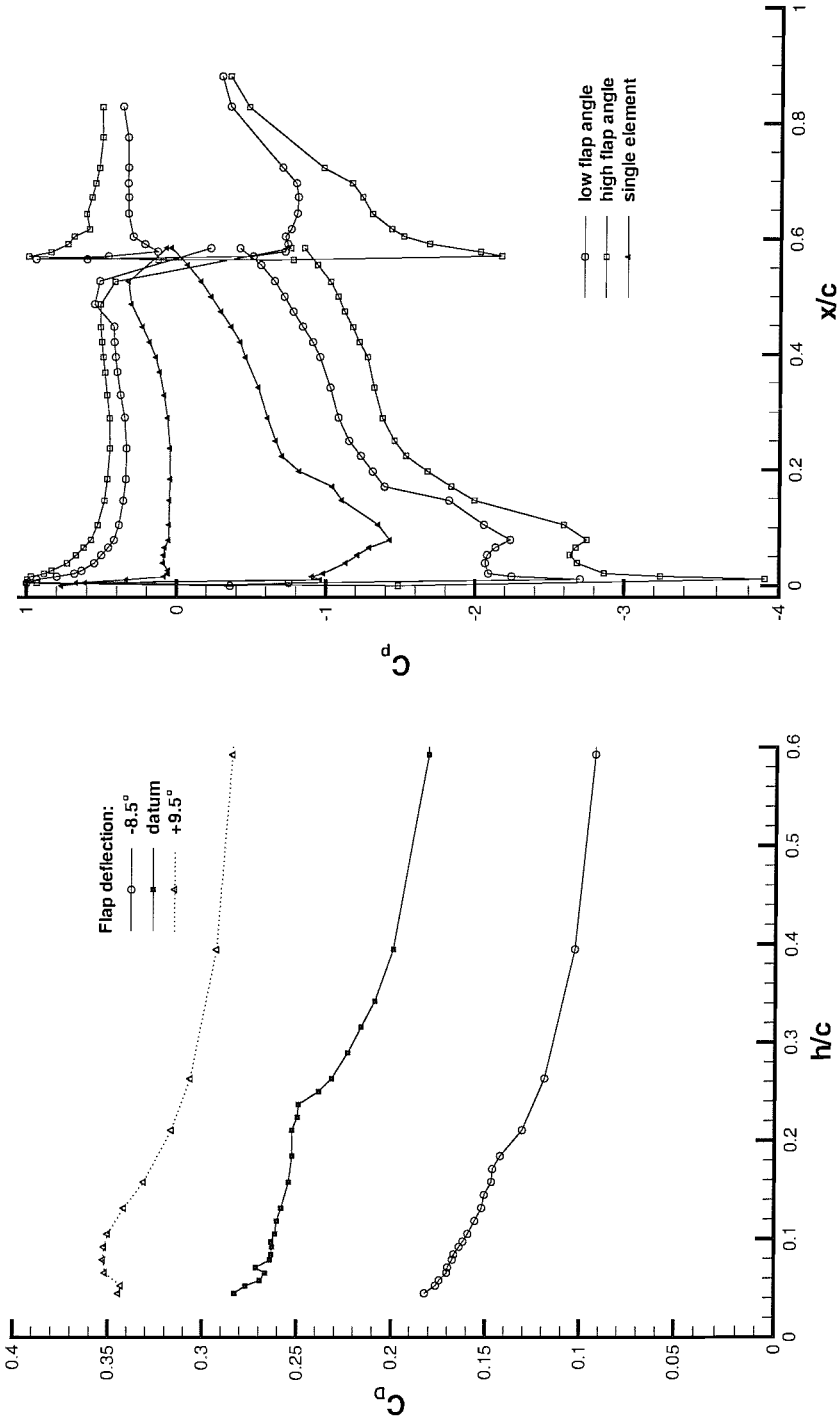

Figure 38: (a) Drag with ground height. (b) Chordwise surface pressures at wing centre in freestream, for double and single element wings

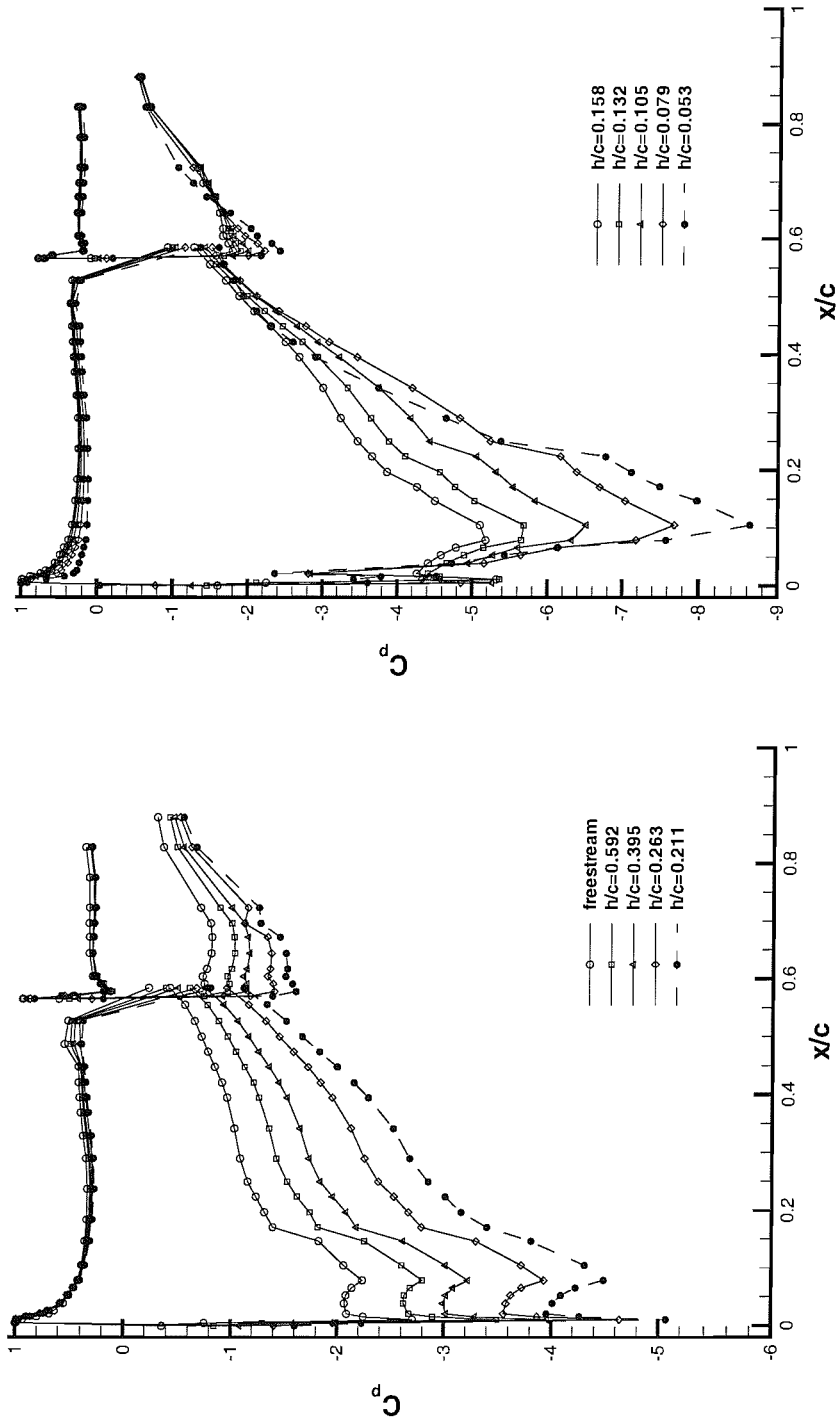

Figure 39: Chordwise surface pressures at wing centre in ground effect for −8.5° flap deflection (a) Large heights. (b) Small heights.

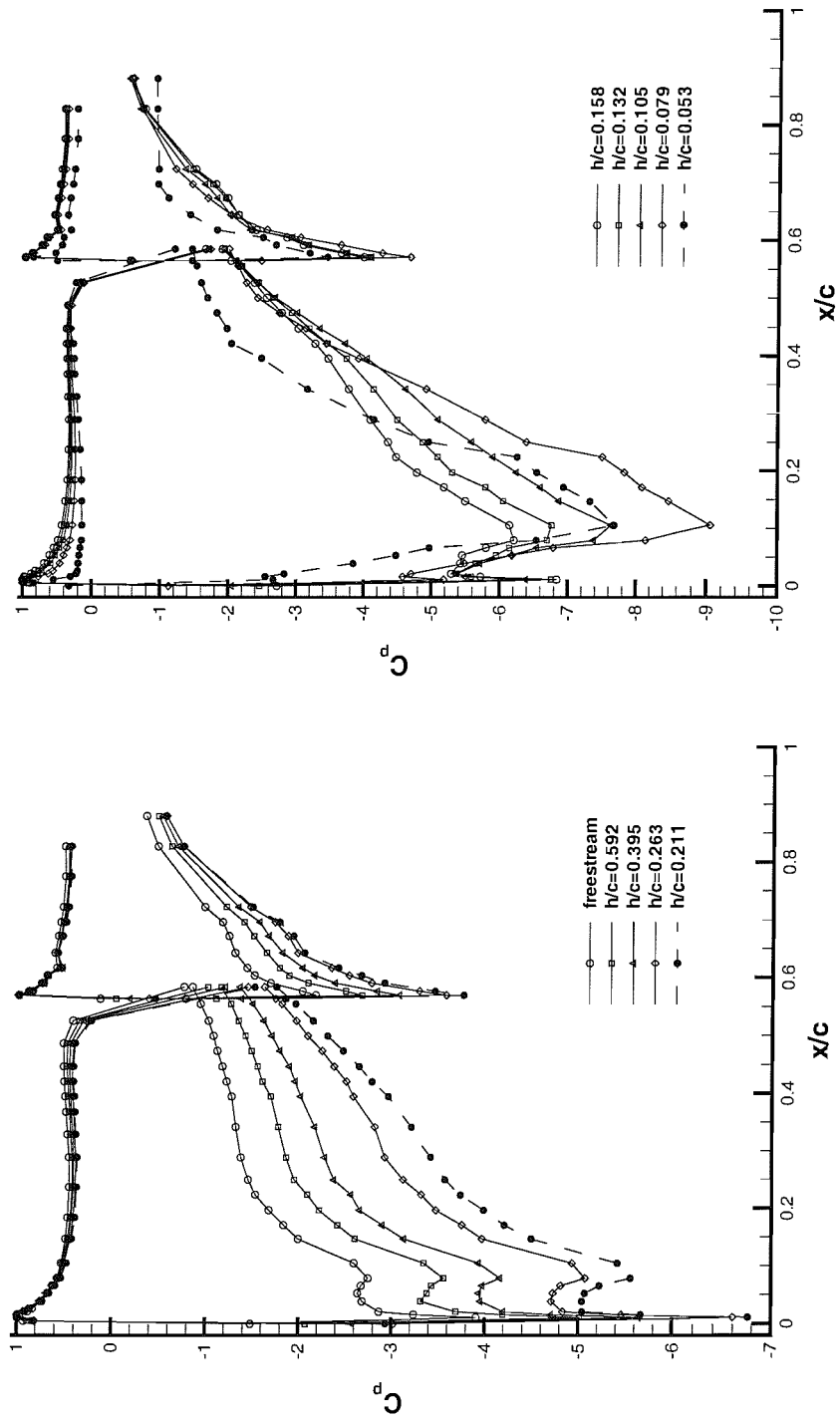

Figure 40: Chordwise surface pressures at wing centre in ground effect for datum flap deflection (a) Large heights. (b) Small heights.

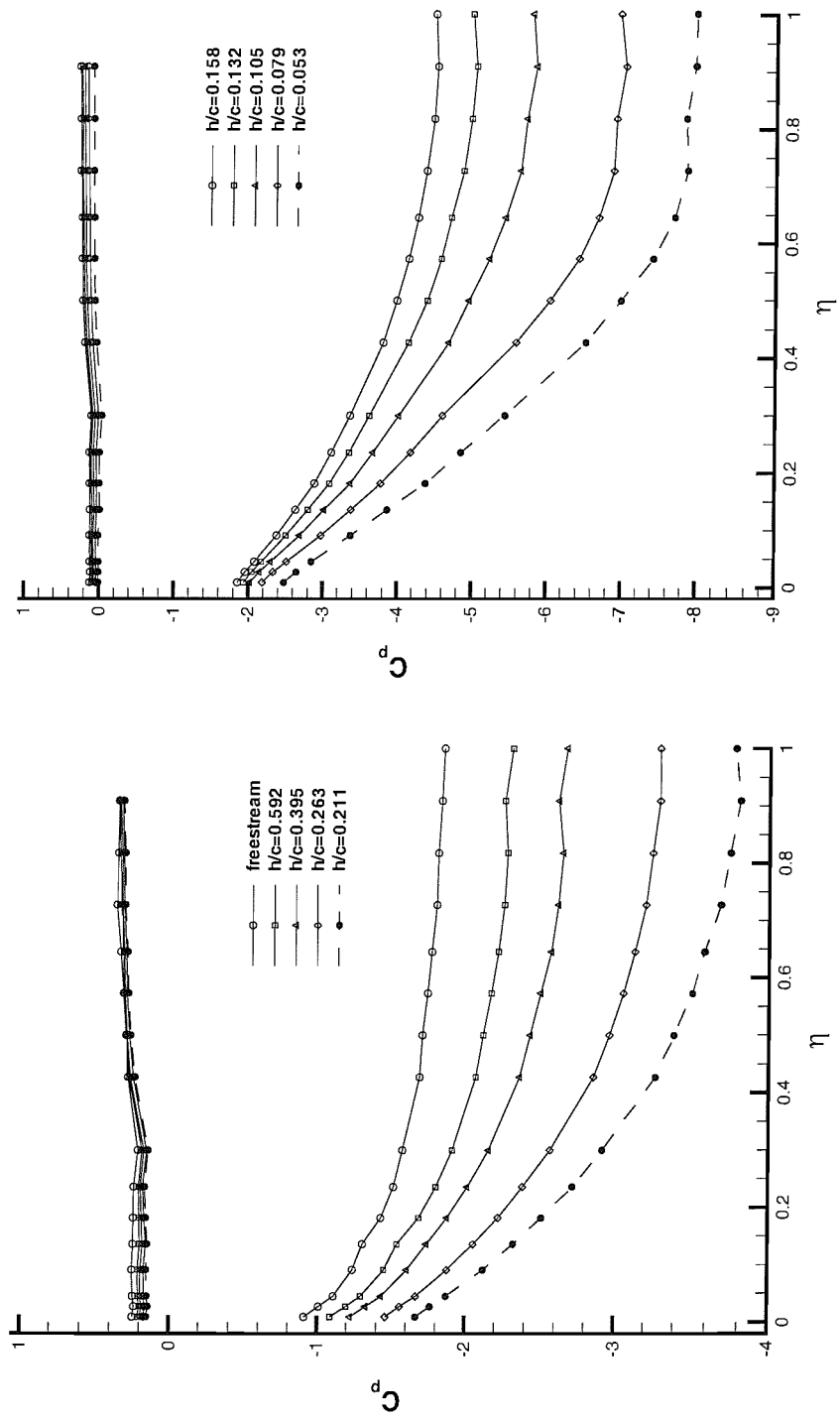

Figure 41: Spanwise surface pressures on main element at quarter-chord position for −8.5° flap deflection (a) Large heights. (b) Small heights.

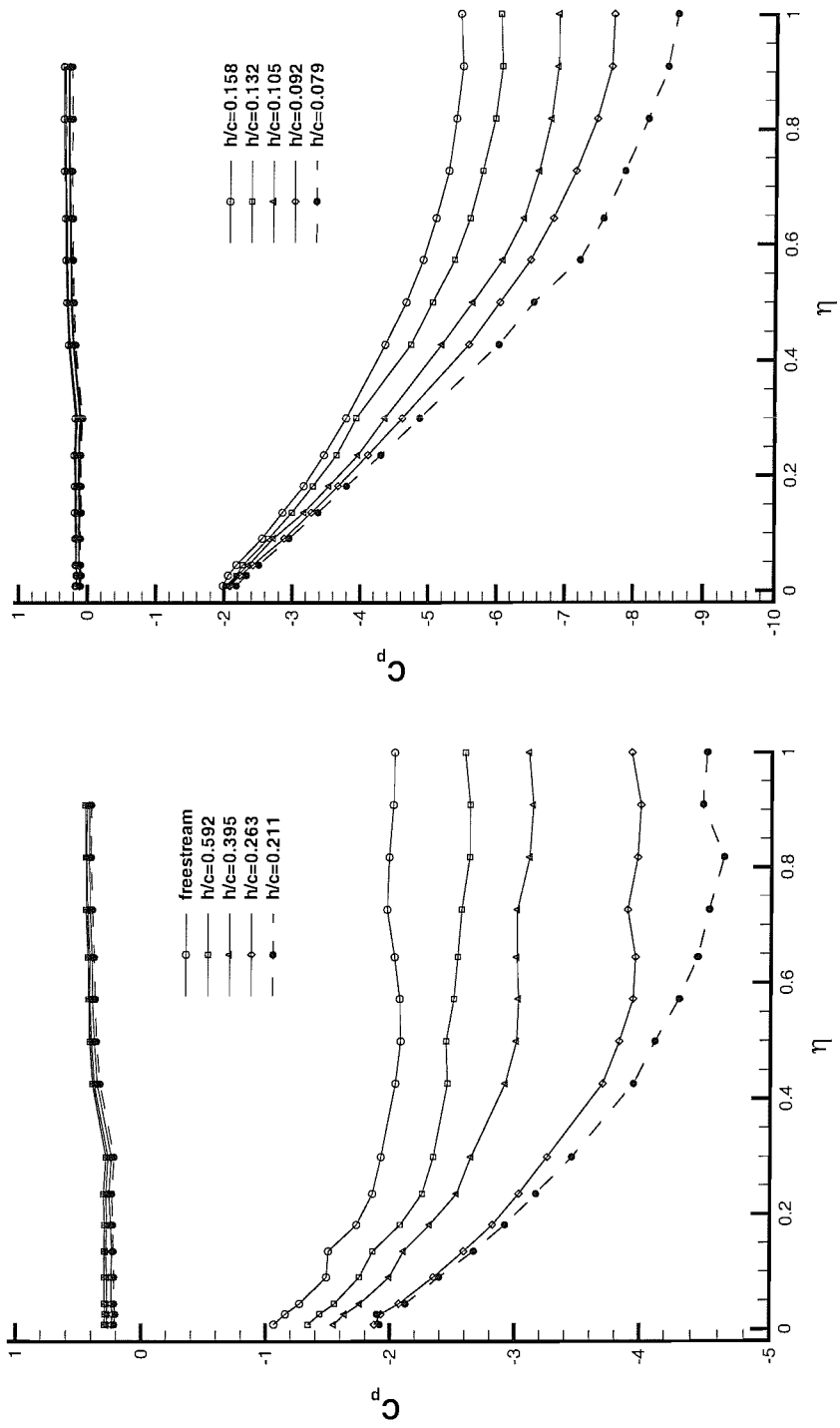

Figure 42: Spanwise surface pressures on main element at quarter-chord position for datum flap deflection (a) Large heights. (b) Small heights.

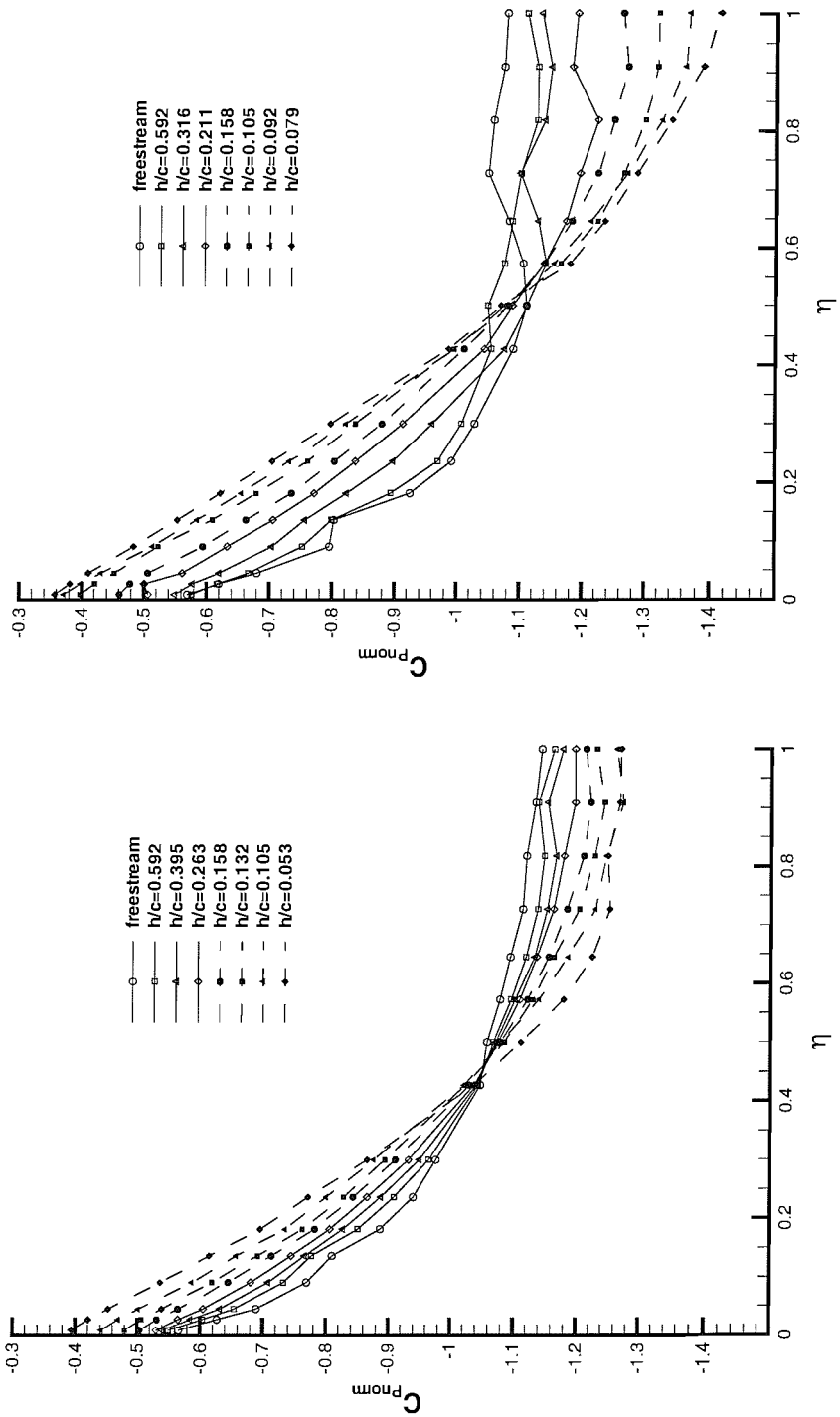

Figure 43: Normalised spanwise surface pressures on main element (a) Low flap deflection. (b) High flap deflection.

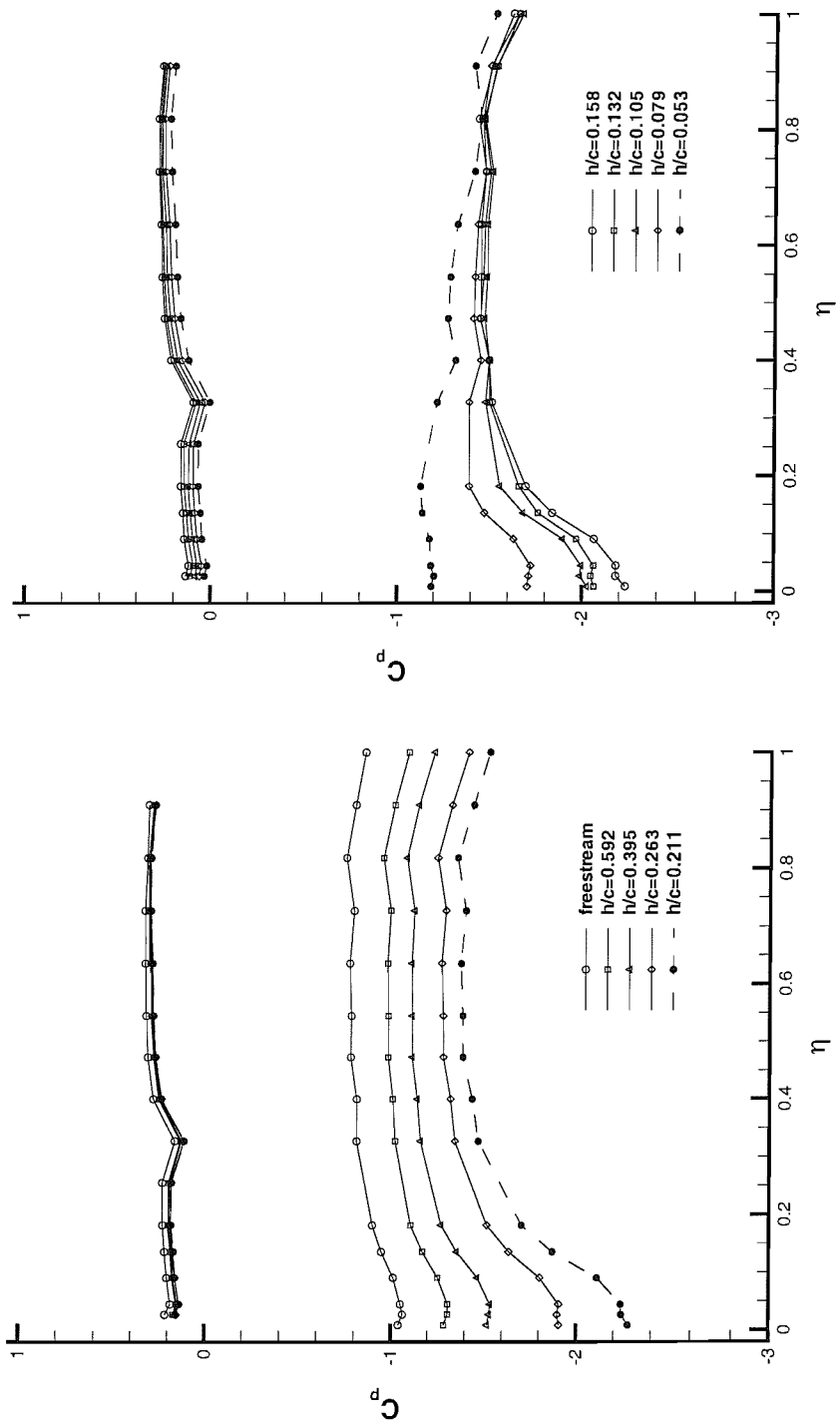

Figure 44: Spanwise surface pressures on flap at quarter-chord position for −8.5° flap deflection (a) Large heights. (b) Small heights.

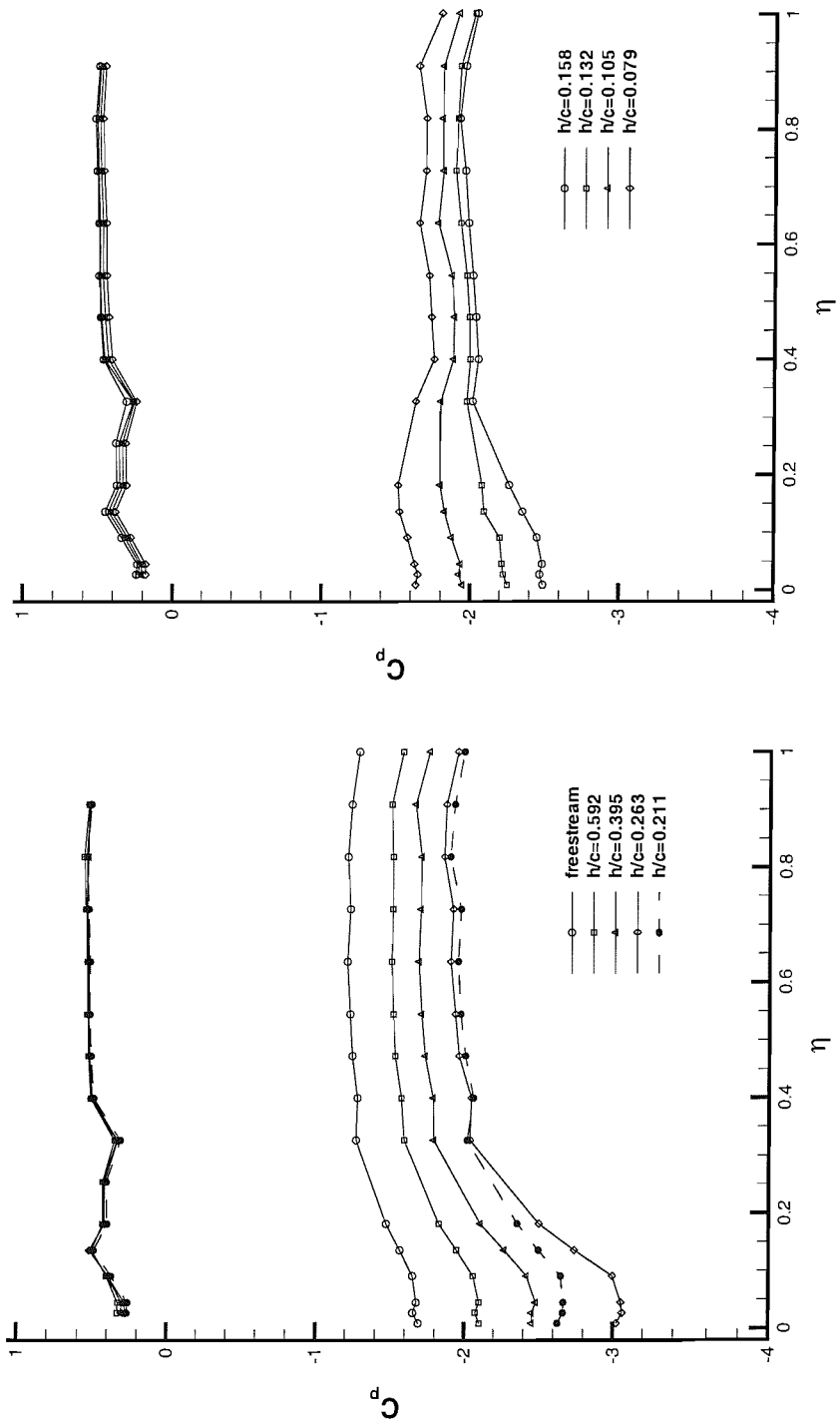

Figure 45: Spanwise surface pressures on flap at quarter-chord position for datum flap deflection (a) Large heights. (b) Small heights.

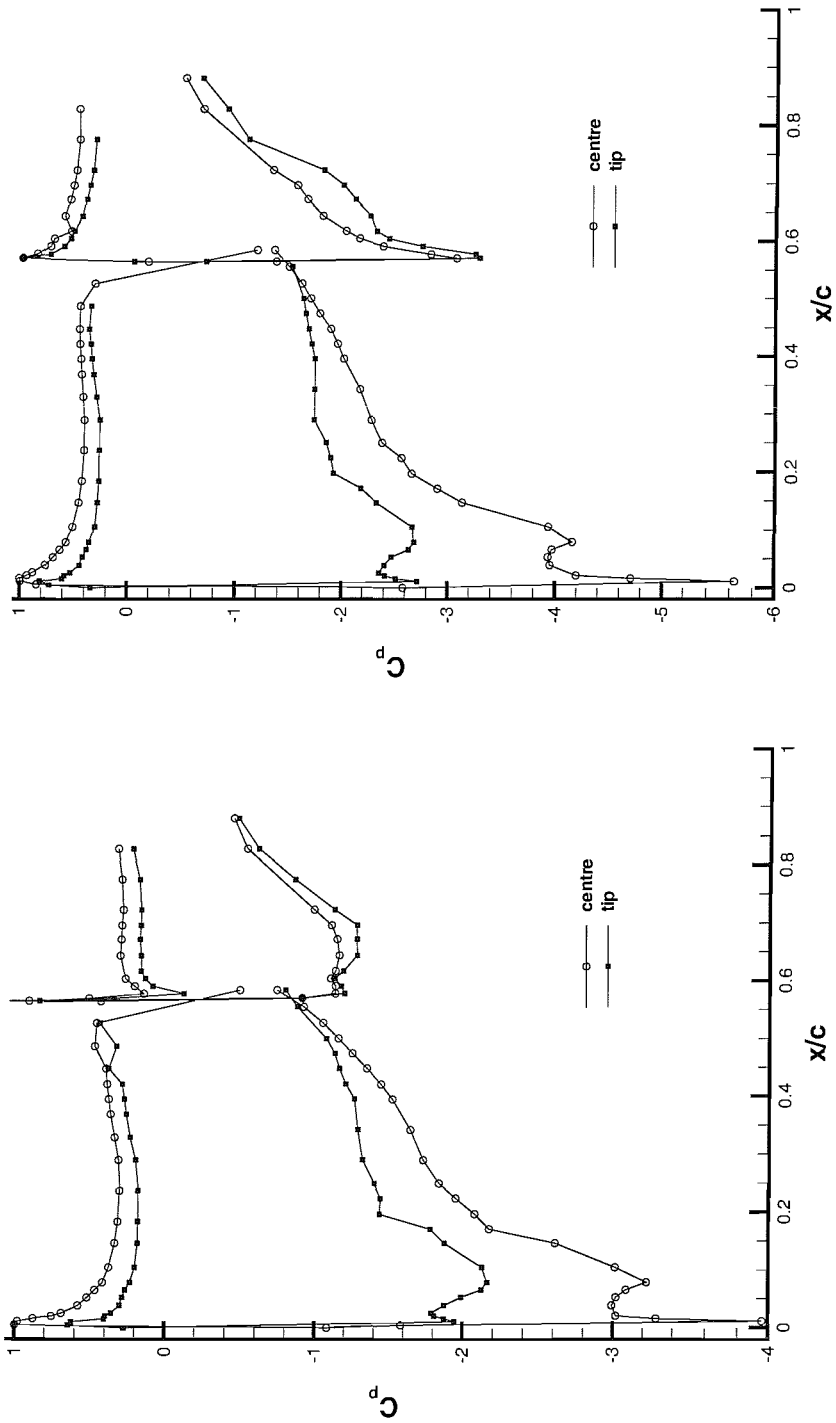

Figure 46: Chordwise surface pressures at centre and near to wing tip at $h/c = 0.395$, a typical type a height (a) Low flap angle. (b) High flap angle.

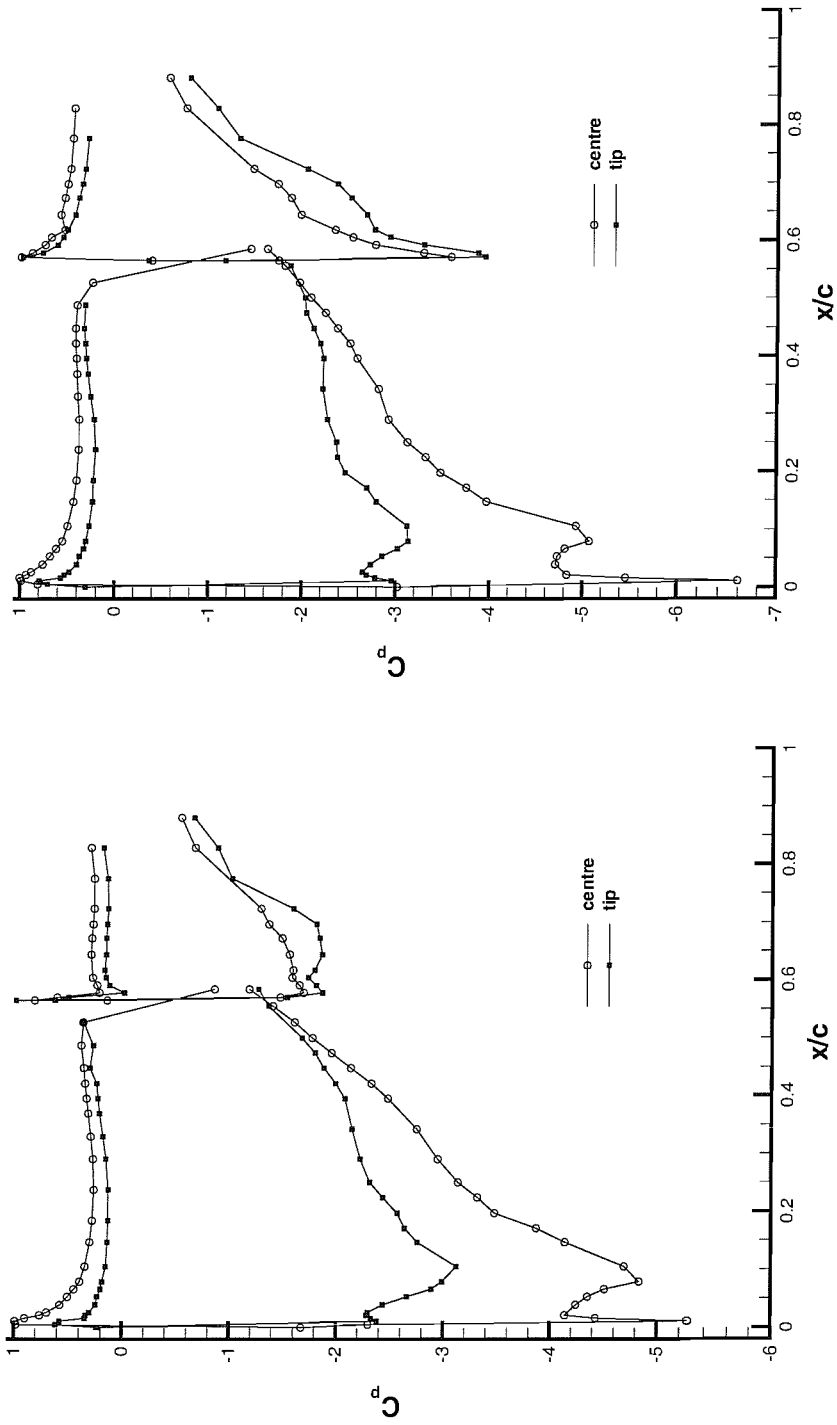

Figure 47: Chordwise surface pressures at centre and near to wing tip at a height on type a/b boundary (a) Low flap angle at $h/c = 0.184$. (b) High flap angle at $h/c = 0.263$.

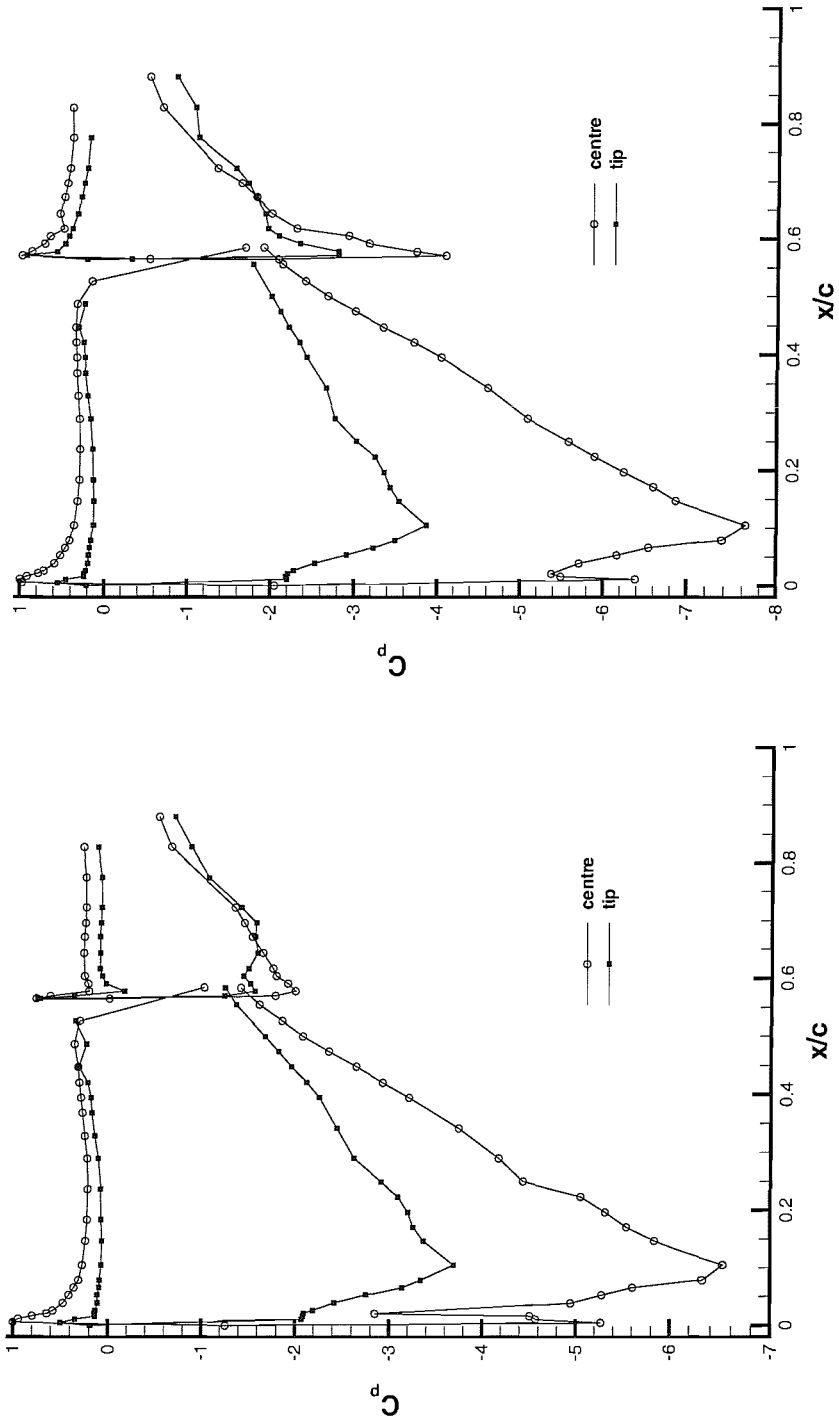

Figure 48: Chordwise surface pressures at centre and near to wing tip at $h/c = 0.105$, a typical type b height (a) Low flap angle. (b) High flap angle.

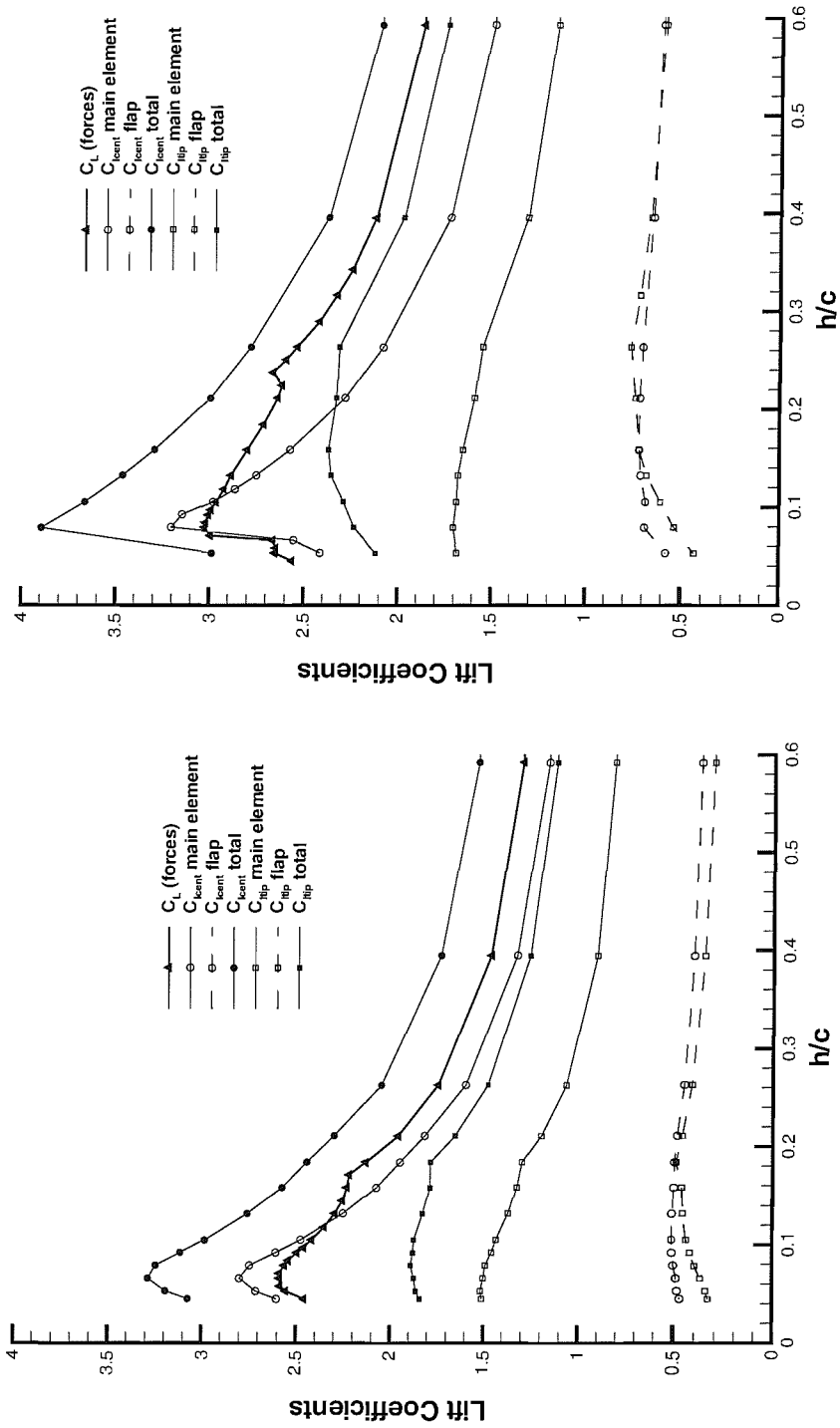

Figure 49: Integrated surface pressures on main element and flap with ground height (a) Low flap angle. (b) High flap angle.

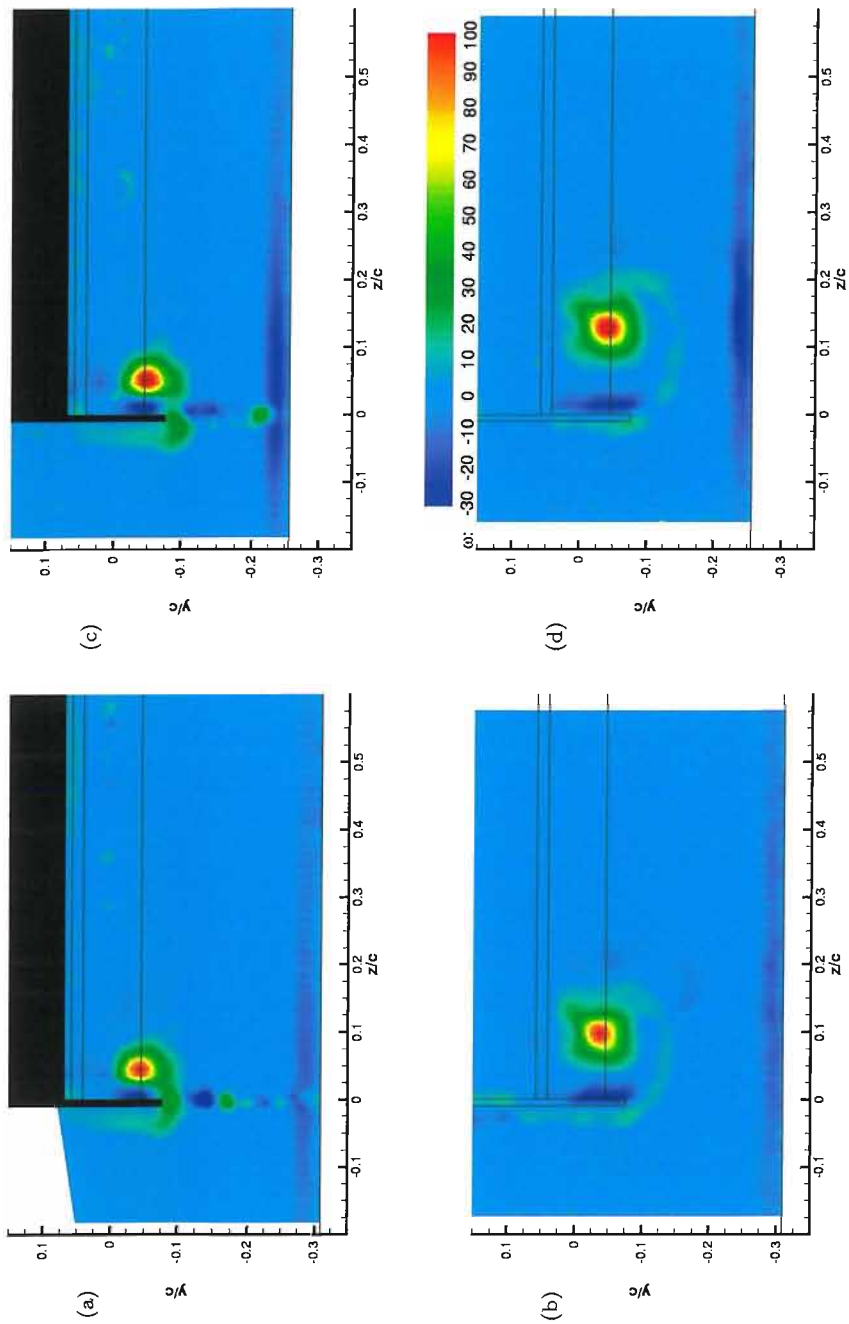

Figure 50: Vorticity contours showing mean flow results for wing tip vortex at low flap angle. (a) $h/c = 0.263$ at $x/c = 0.672$, (b) $h/c = 0.263$ at $x/c = 1.092$, (c) $h/c = 0.211$ at $x/c = 0.672$, (d) $h/c = 0.211$ at $x/c = 1.092$

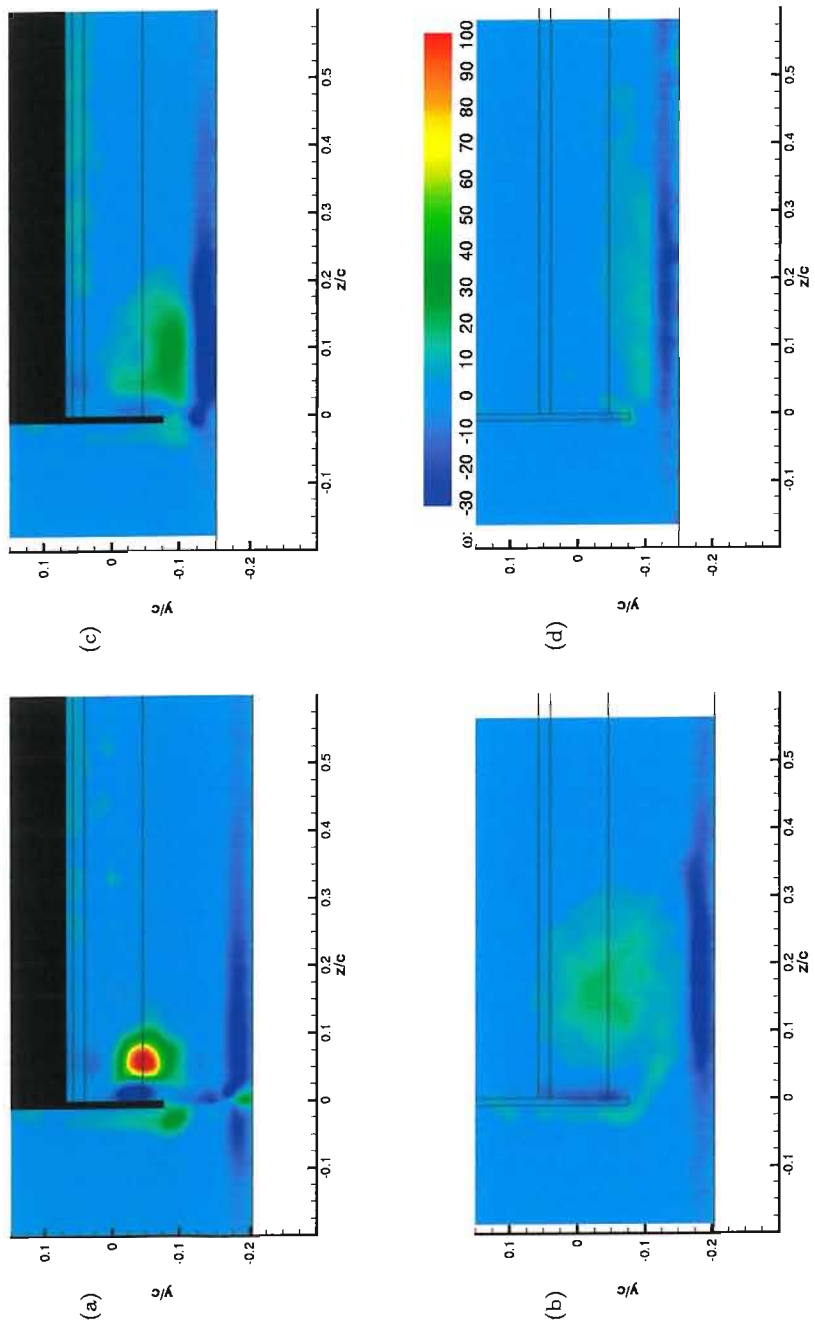

Figure 51: Vorticity contours showing mean flow results for wing tip vortex at low flap angle. (a) $h/c = 0.158$ at $x/c = 0.672$, (b) $h/c = 0.158$ at $x/c = 1.092$, (c) $h/c = 0.105$ at $x/c = 0.672$, (d) $h/c = 0.105$ at $x/c = 1.092$

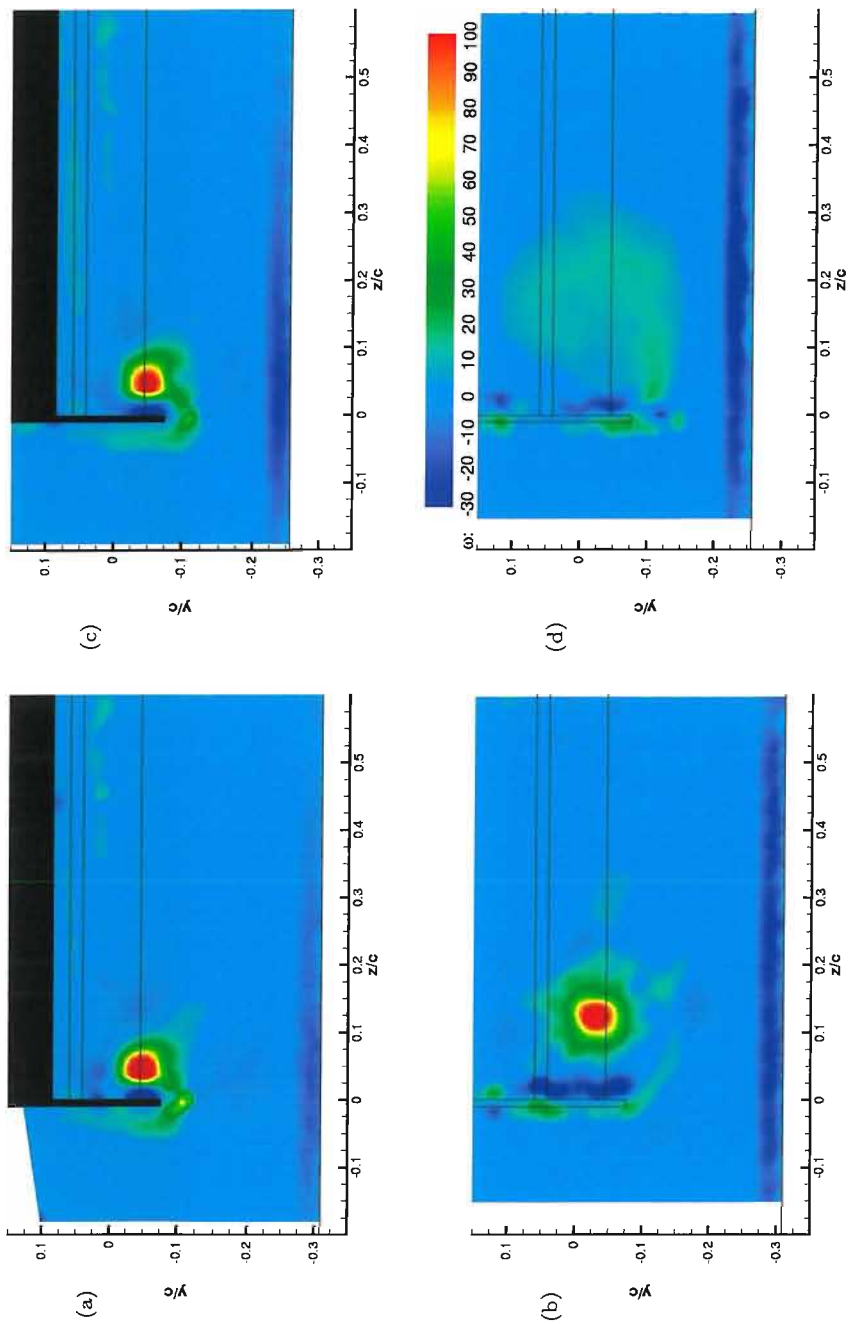

Figure 52: Vorticity contours showing mean flow results for wing tip vortex at high flap angle. (a) $h/c = 0.263$ at $x/c = 0.672$, (b) $h/c = 0.263$ at $x/c = 1.092$, (c) $h/c = 0.211$ at $x/c = 0.672$, (d) $h/c = 0.211$ at $x/c = 1.092$

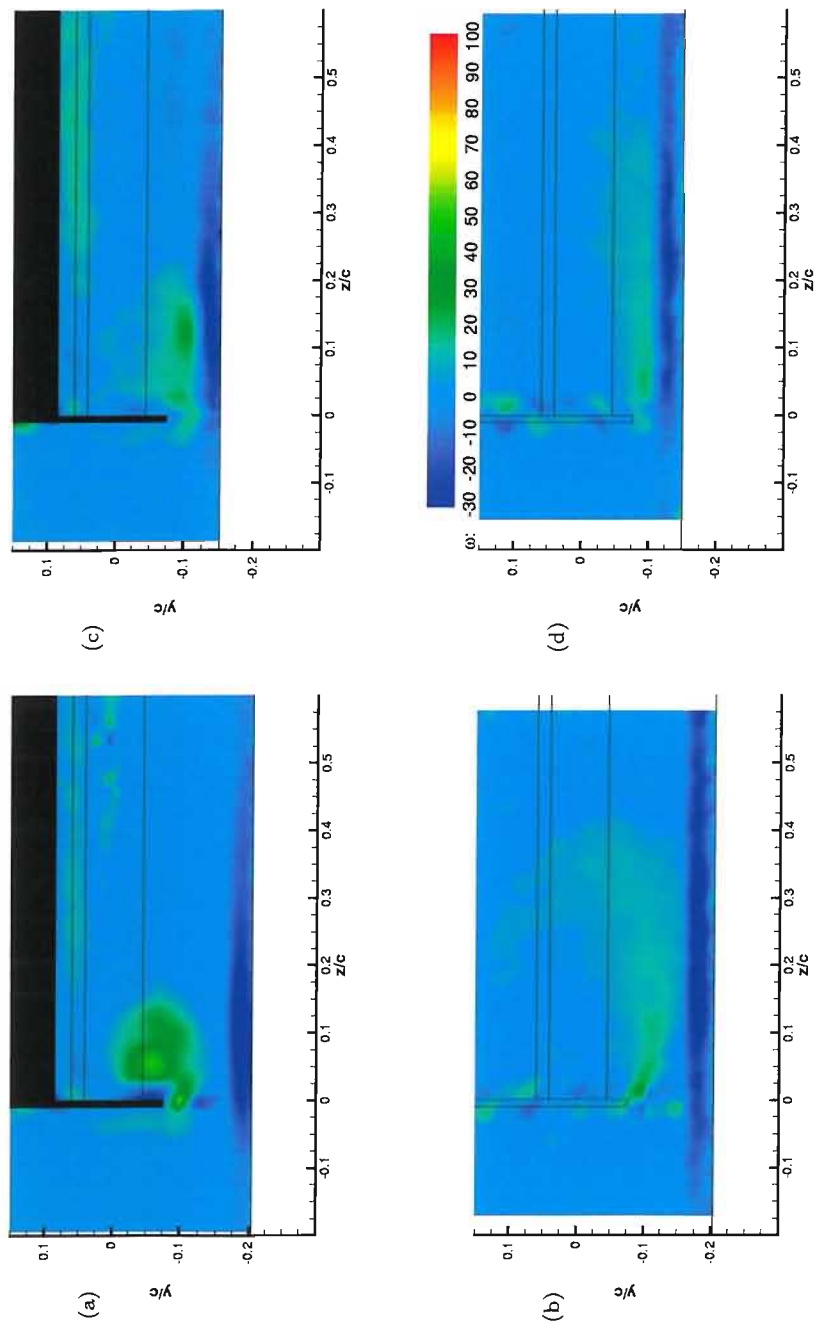

Figure 53: Vorticity contours showing mean flow results for wing tip vortex at high flap angle. (a) $h/c = 0.158$ at $x/c = 0.672$, (b) $h/c = 0.158$ at $x/c = 1.092$, (c) $h/c = 0.105$ at $x/c = 0.672$, (d) $h/c = 0.105$ at $x/c = 1.092$

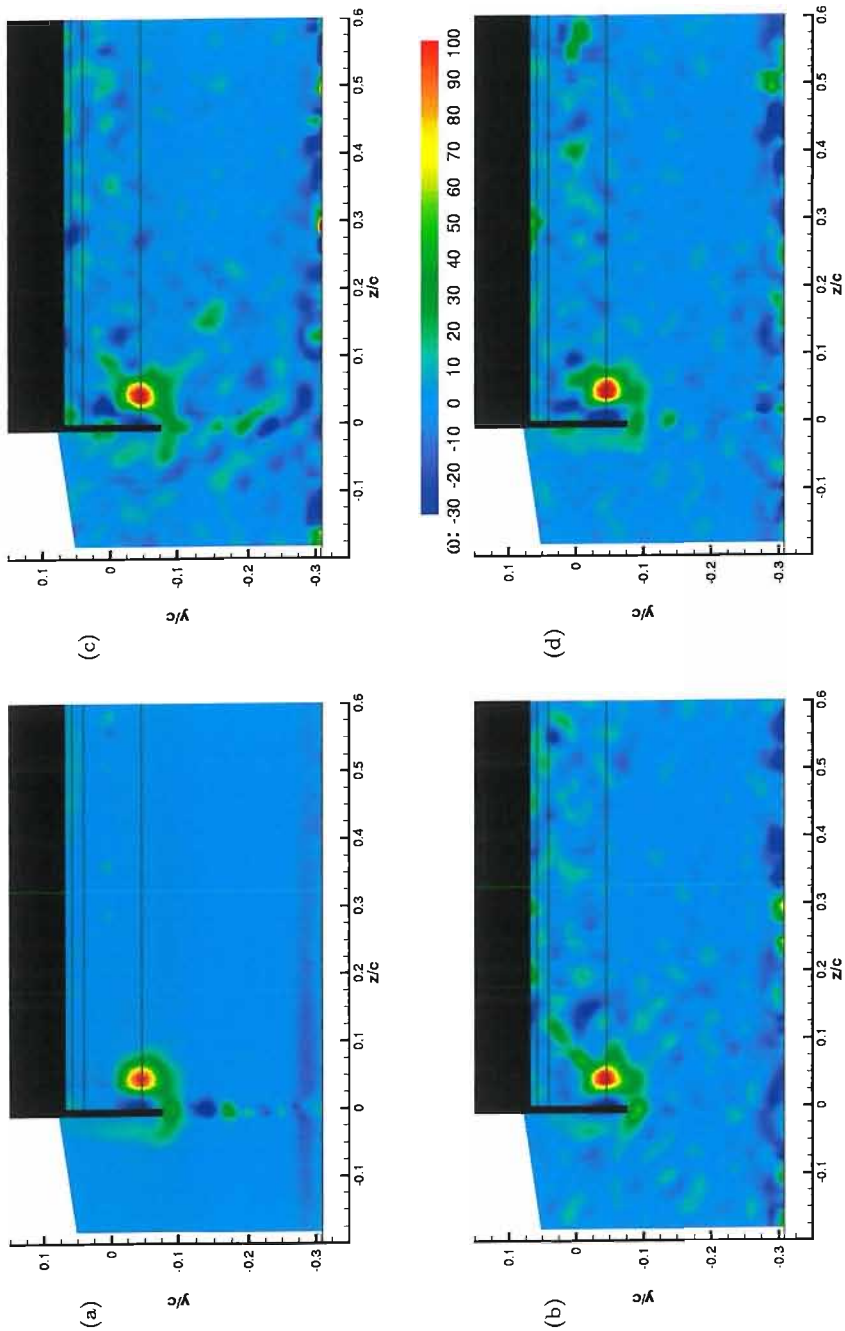

Figure 54: Wing tip vortex at a height of $h/c = 0.263$, at quarter-chord position on flap, low flap angle, a type a flow. Vorticity contours showing (a) mean flow results and (b,c,d) three instantaneous snapshots representative of the flow.

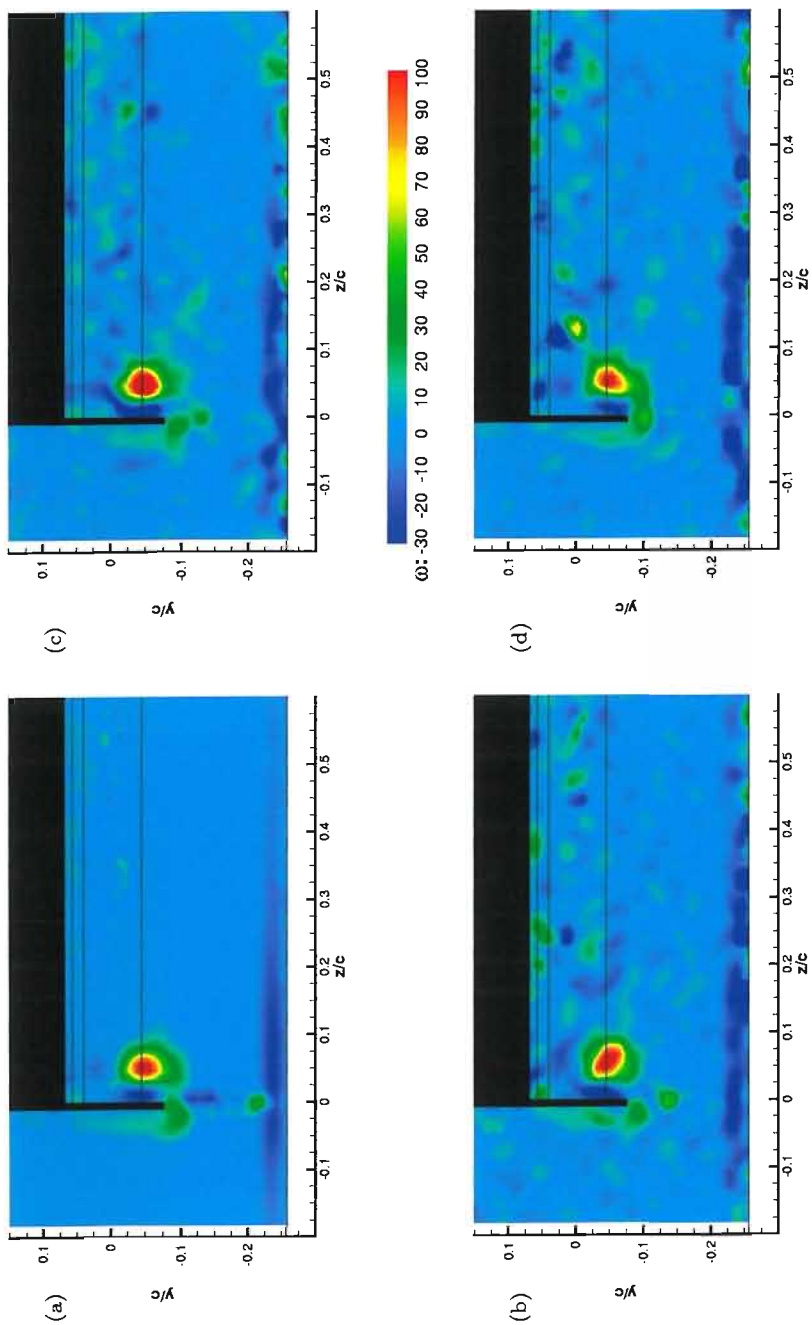

Figure 55: Wing tip vortex at a height of $h/c = 0.211$, at quarter-chord position on flap, low flap angle, a type a flow. Vorticity contours showing (a) mean flow results and (b,c,d) three instantaneous snapshots representative of the flow.

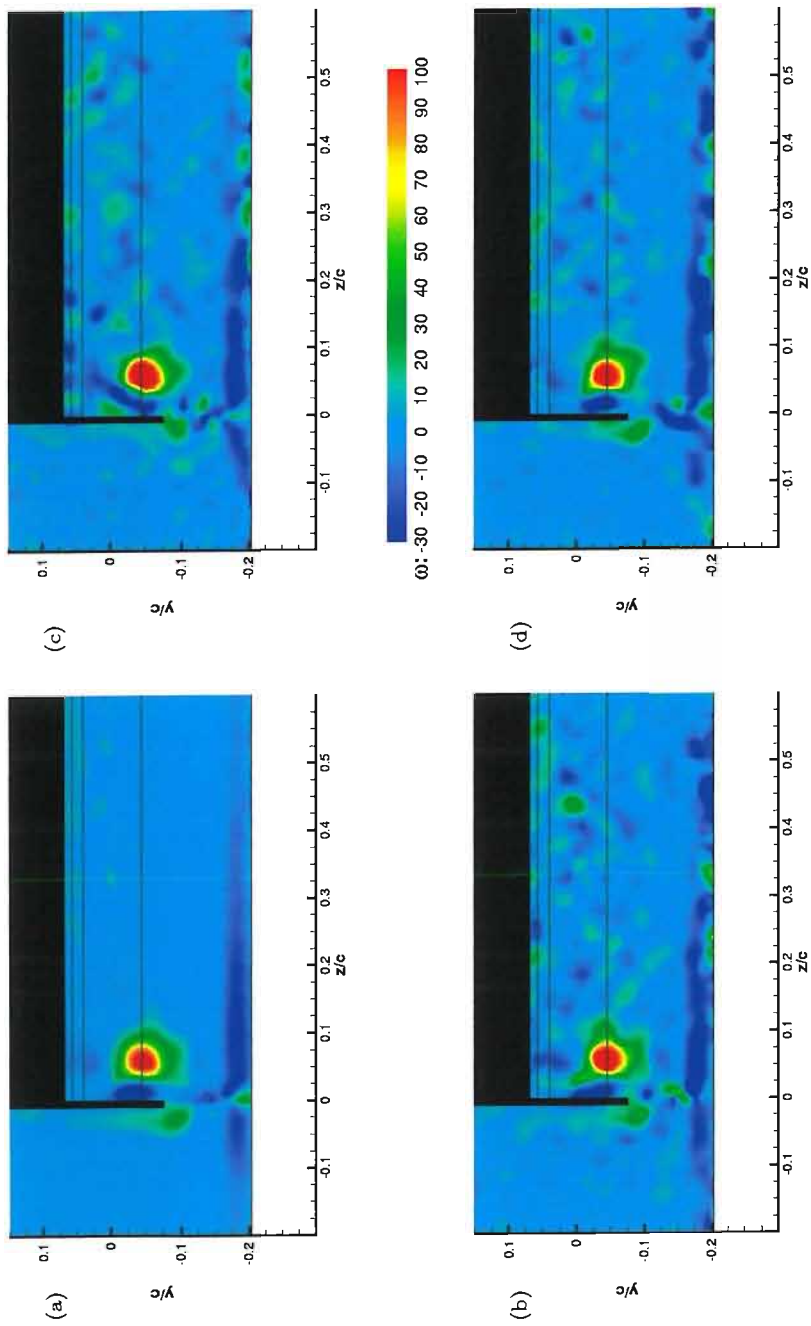

Figure 56: Wing tip vortex at a height of $h/c = 0.158$, at quarter-chord position on flap, low flap angle, a type b flow. Vorticity contours showing (a) mean flow results and (b,c,d) three instantaneous snapshots representative of the flow.

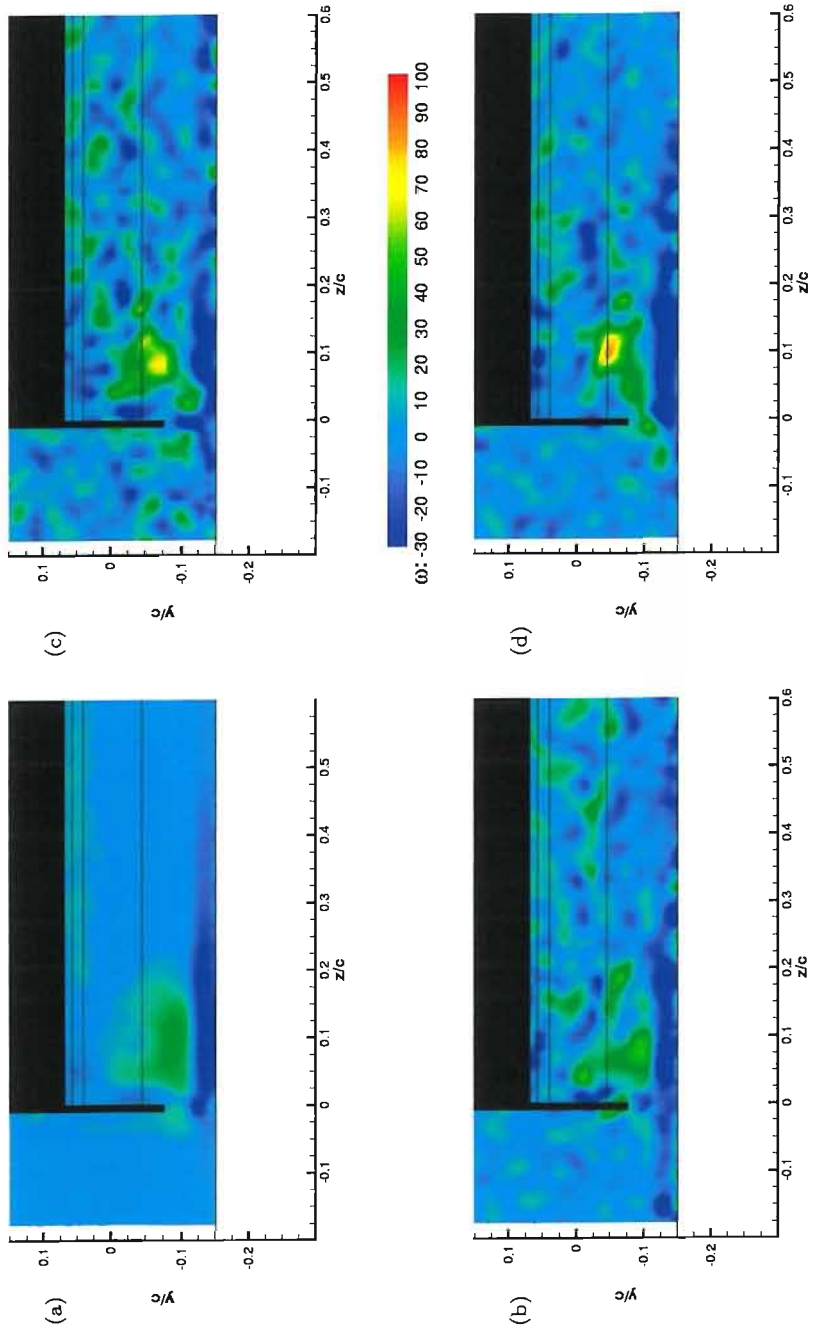

Figure 57: Wing tip vortex at a height of $h/c = 0.105$, at quarter-chord position on flap, low flap angle, a type b flow. Vorticity contours showing (a) mean flow results and (b,c,d) three instantaneous snapshots representative of the flow.

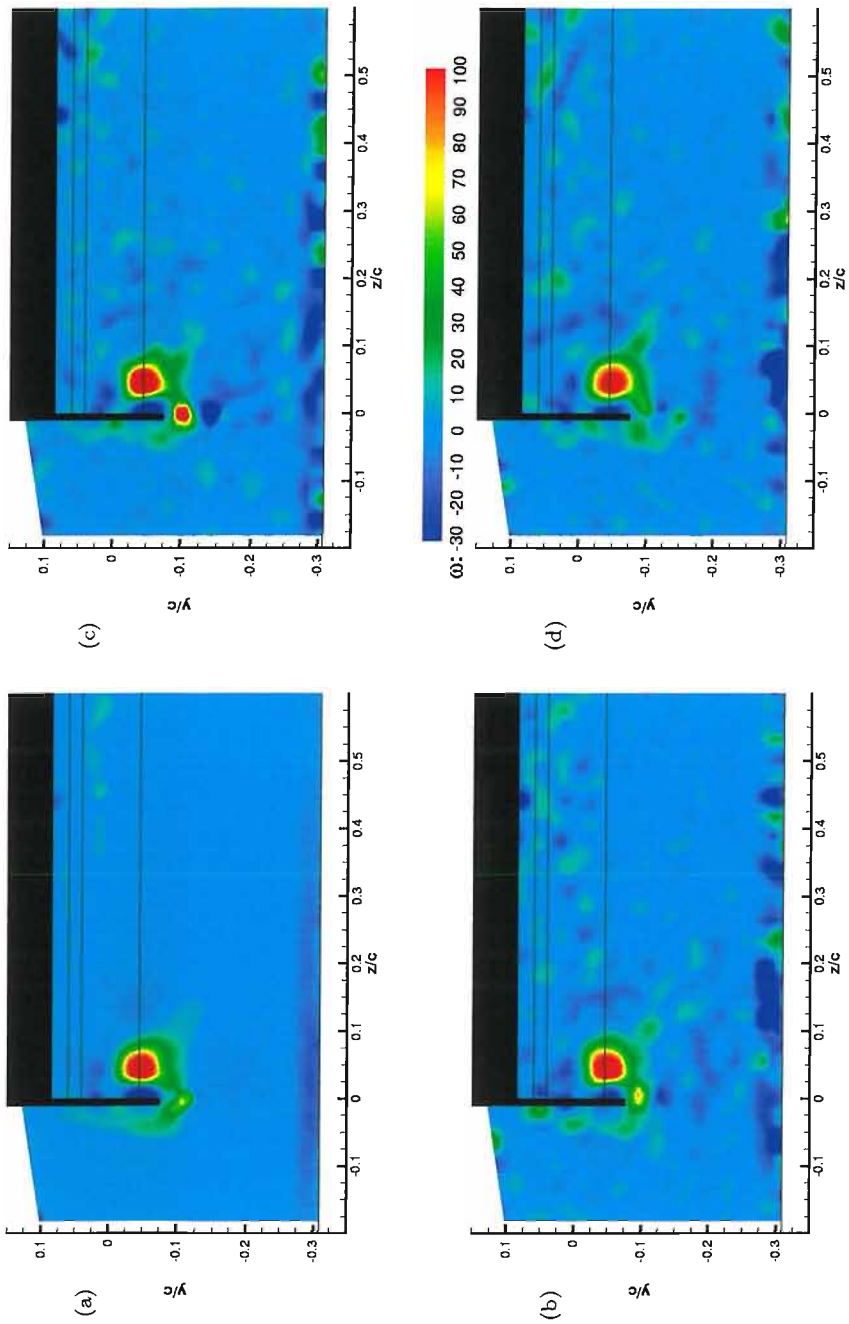

Figure 58: Wing tip vortex at a height of $h/c = 0.263$, at quarter-chord position on flap, high flap angle, a type *a* flow. Vorticity contours showing (a) mean flow results and (b,c,d) three instantaneous snapshots representative of the flow.

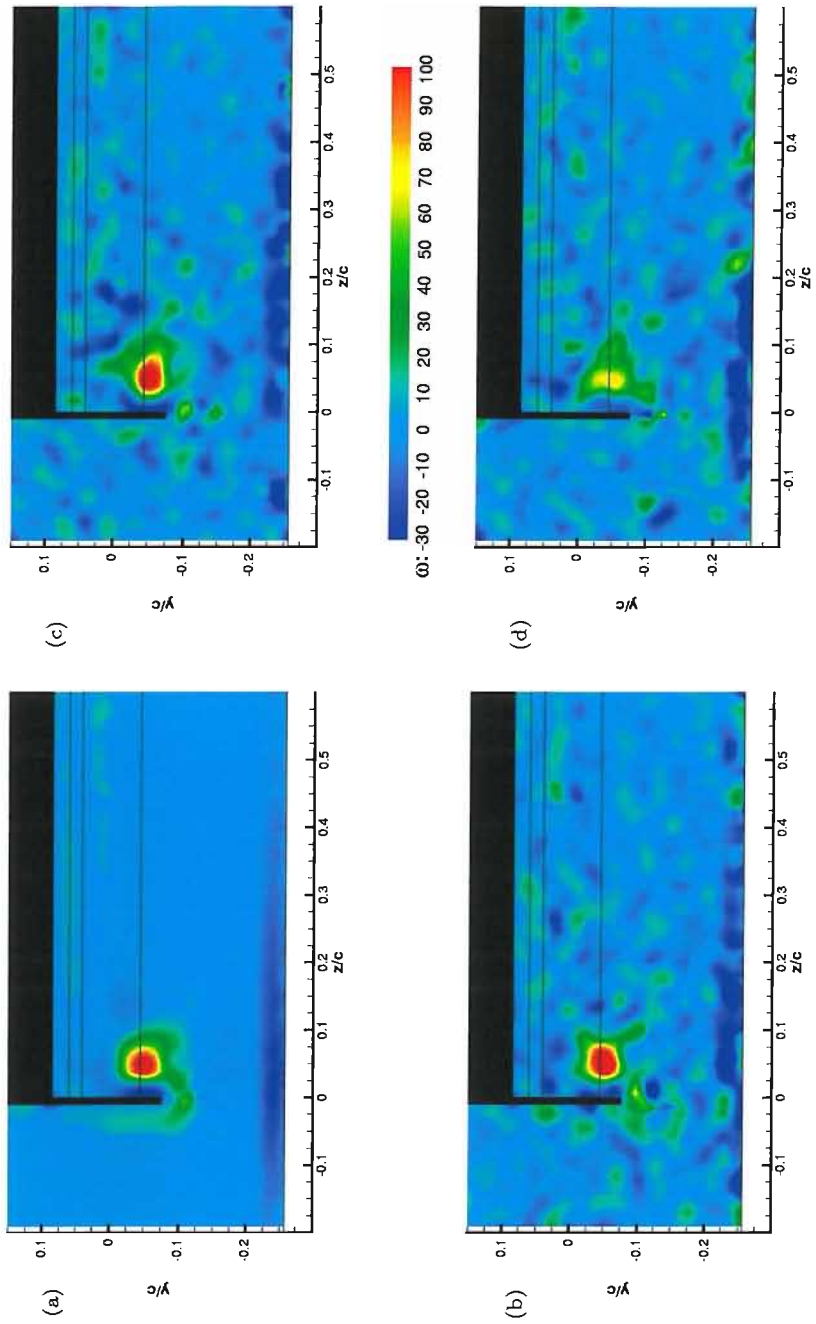

Figure 59: Wing tip vortex at a height of $h/c = 0.211$, at quarter-chord position on flap, high flap angle, a type b flow. Vorticity contours showing (a) mean flow results and (b,c,d) three instantaneous snapshots representative of the flow.

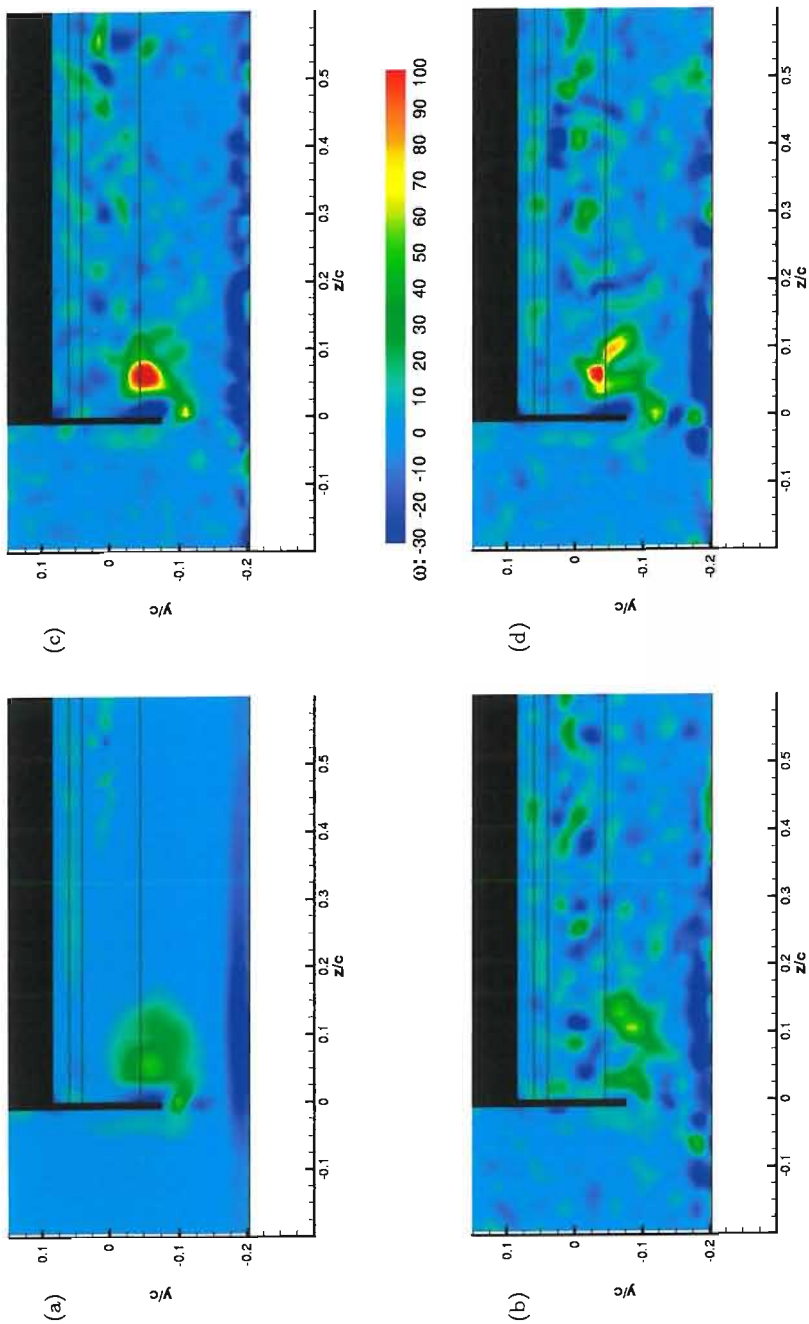

Figure 60: Wing tip vortex at a height of $h/c = 0.158$, at quarter-chord position on flap, high flap angle, a type b flow. Vorticity contours showing (a) mean flow results and (b,c,d) three instantaneous snapshots representative of the flow.

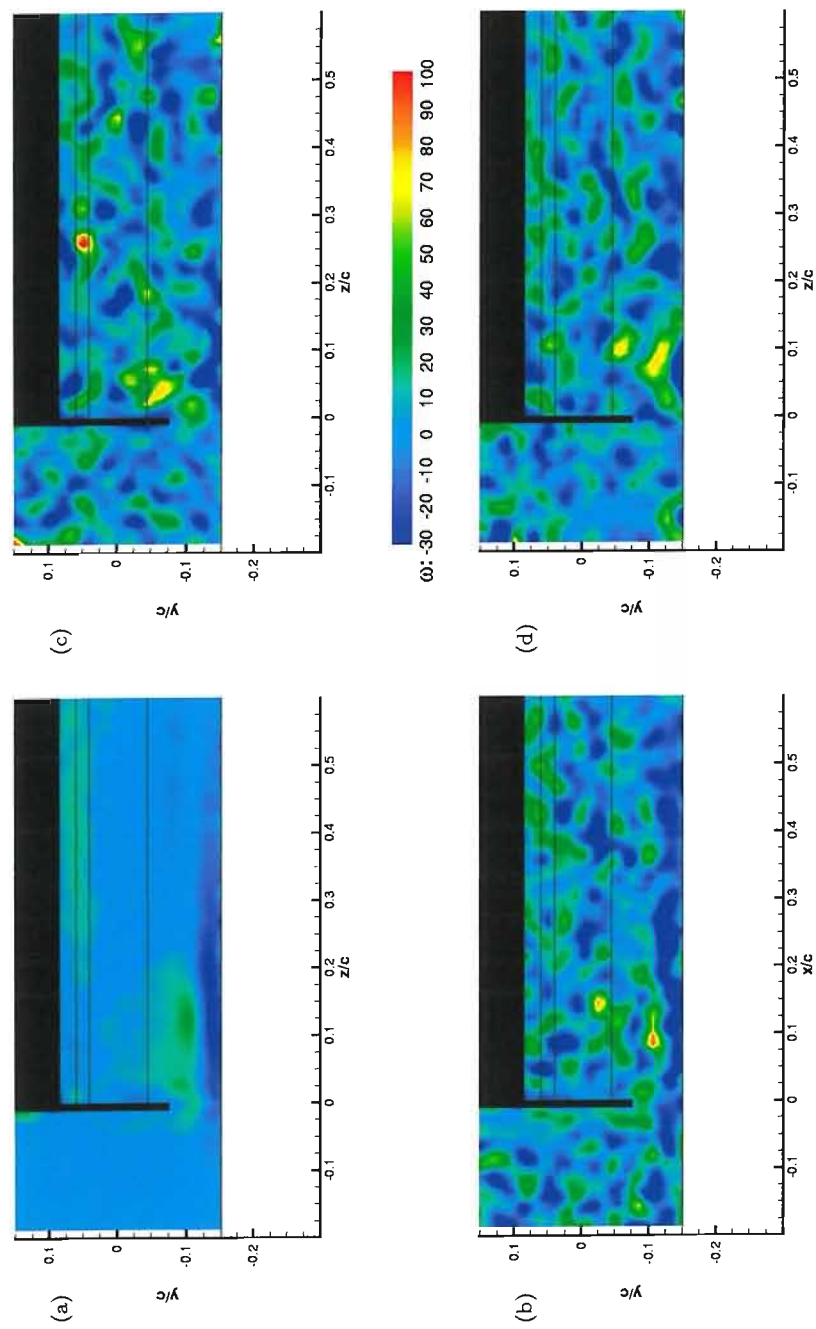

Figure 61: Wing tip vortex at a height of $h/c = 0.105$, at quarter-chord position on flap, high flap angle, a type b flow. Vorticity contours showing (a) mean flow results and (b,c,d) three instantaneous snapshots representative of the flow.

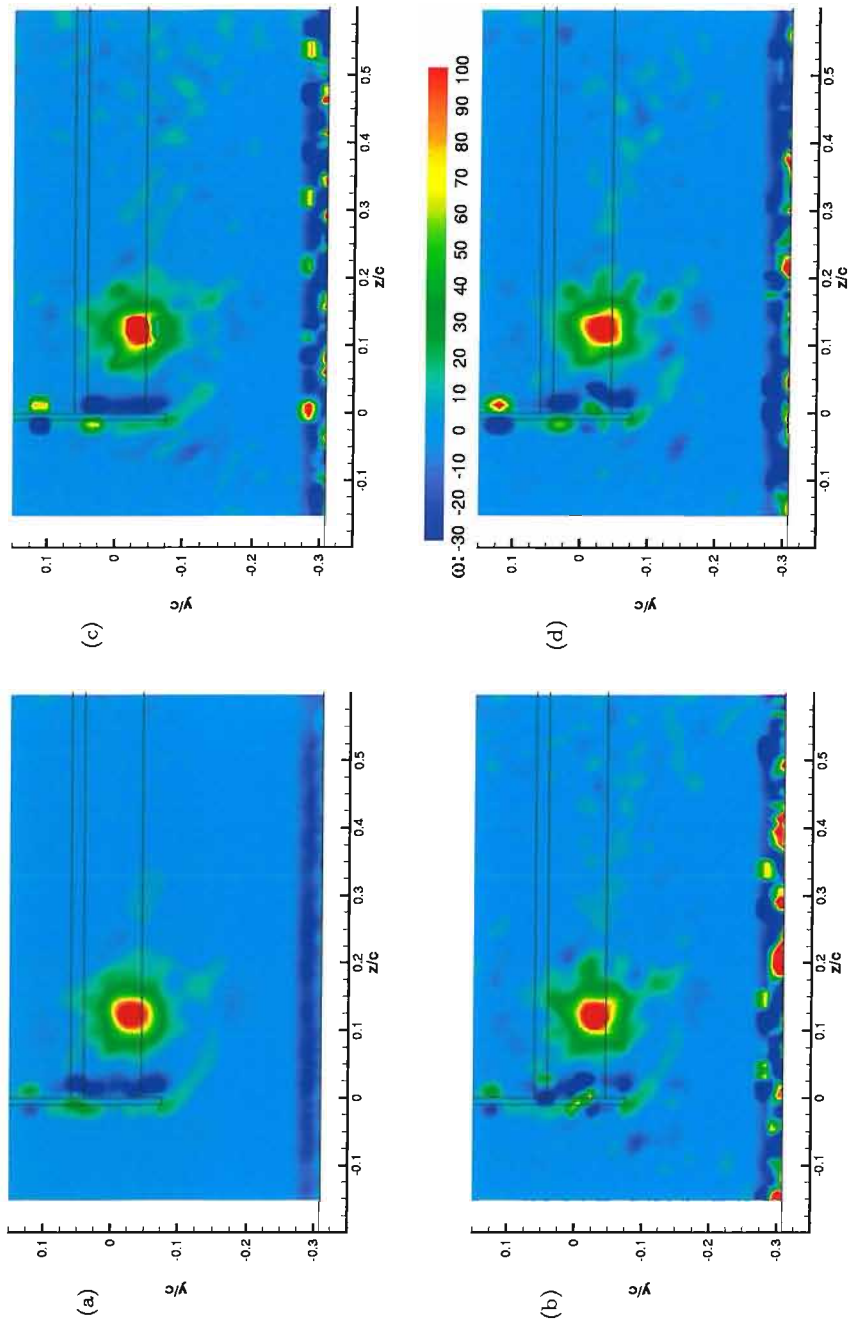

Figure 62: Wing tip vortex at a height of $h/c = 0.263$, at $x/c = 1.092$, high flap angle, a type a flow. Vorticity contours showing (a) mean flow results and (b,c,d) three instantaneous snapshots representative of the flow.

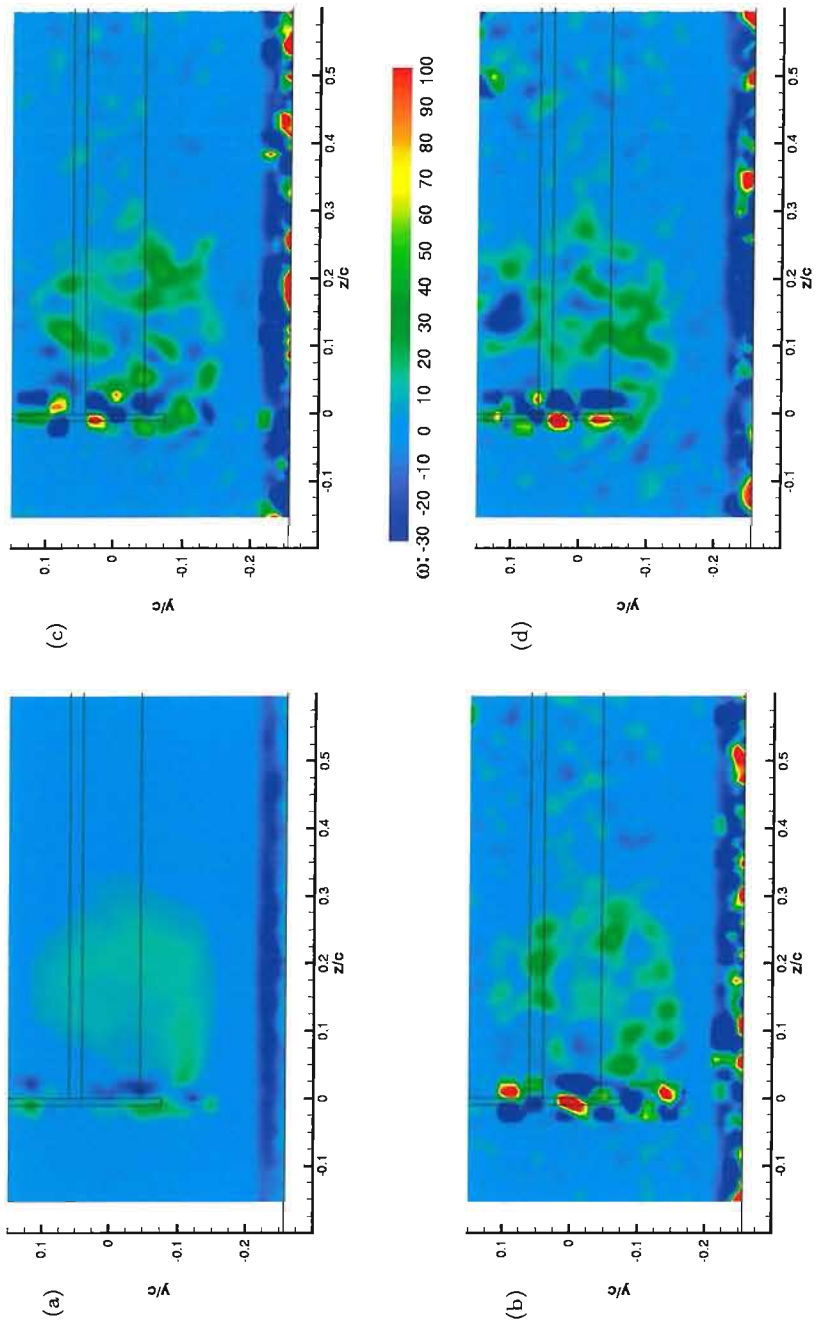

Figure 63: Wing tip vortex at a height of $h/c = 0.211$, at $x/c = 1.092$, high flap angle, a type b flow. Vorticity contours showing (a) mean flow results and (b,c,d) three instantaneous snapshots representative of the flow.

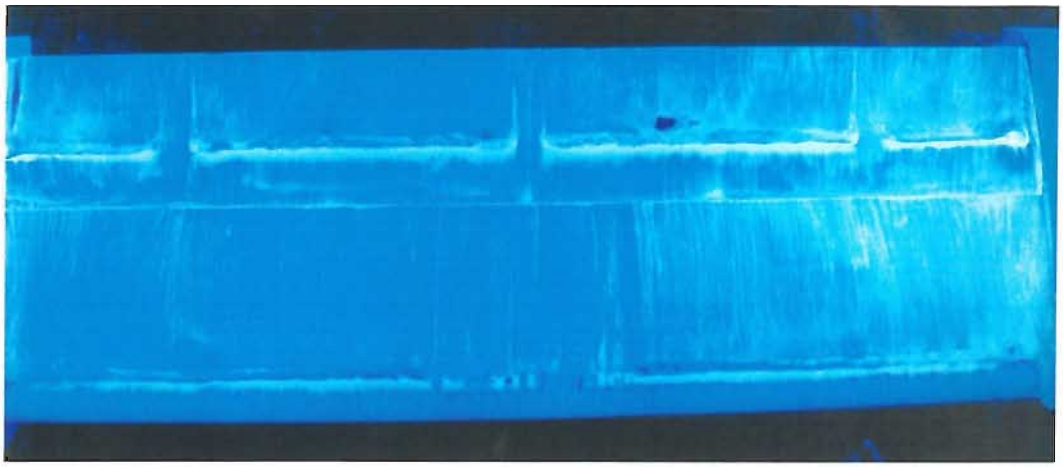

(a)

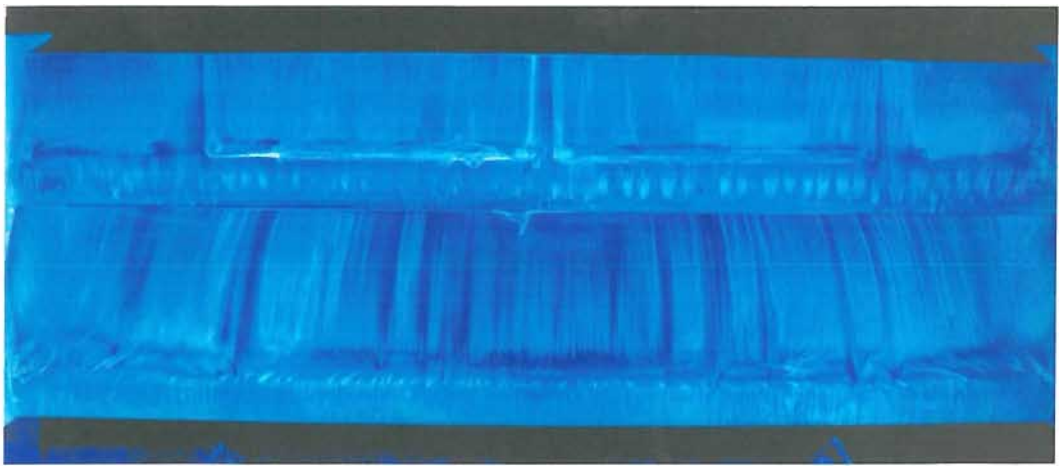

(b)

Figure 64: Oil flow visualisation on suction surface showing leading edge lowermost; transition location for low flap angle, (a) $h/c = 0.395$ (b) $h/c = 0.158$.

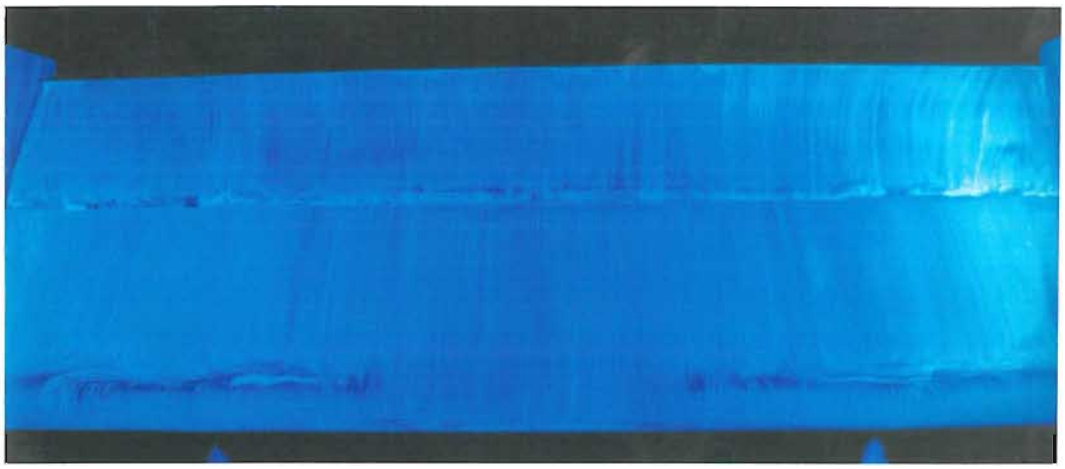

(a)

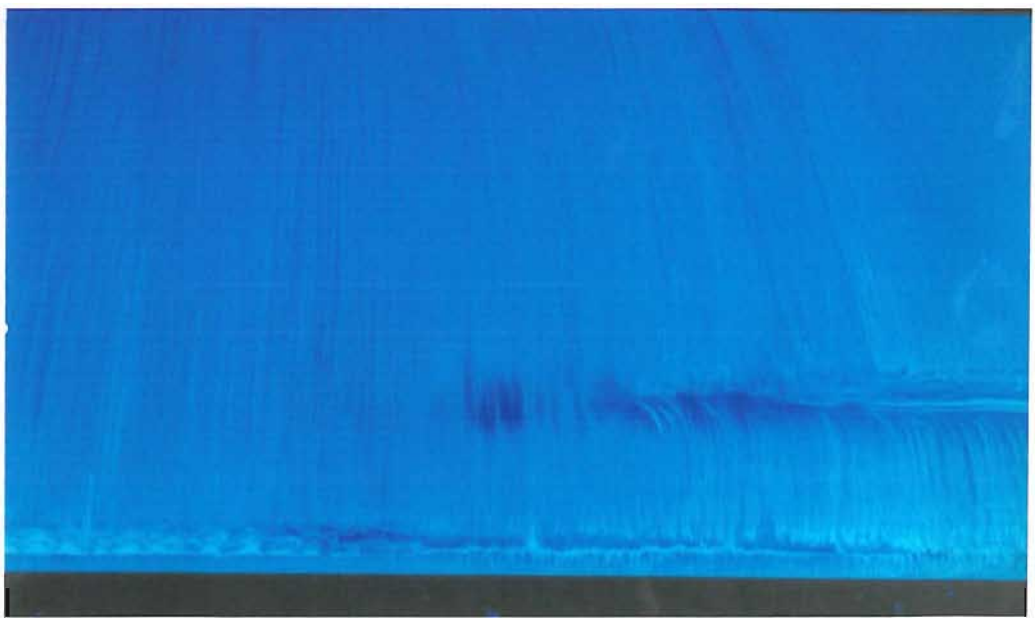

(b)

Figure 65: Oil flow visualisation on suction surface showing leading edge lowermost; transition location for high flap angle at $h/c = 0.211$, (a) entire wing (b) close up near to wing centre.

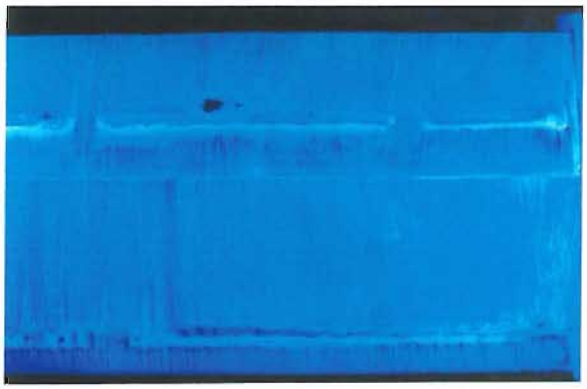

(a)

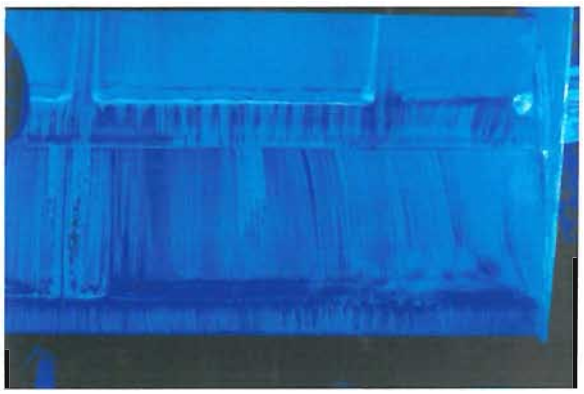

(b)

(c)

Figure 66: Oil flow visualisation on suction surface showing leading edge lowermost; tip flow for low flap angle, (a) $h/c = 0.395$ (b) $h/c = 0.211$ (c) $h/c = 105$.

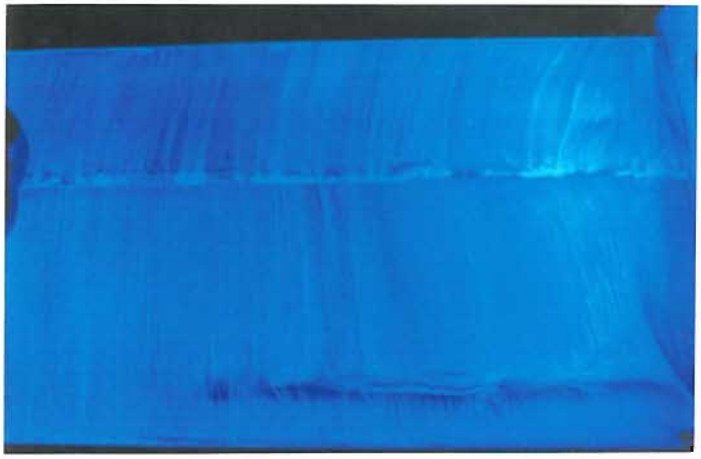

(a)

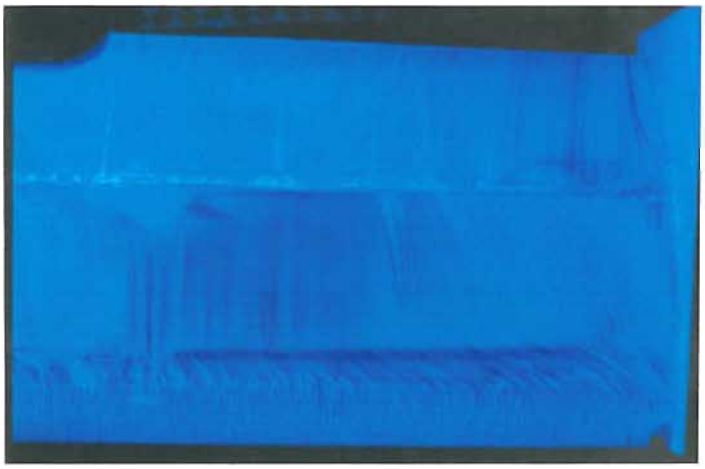

(b)

Figure 67: Oil flow visualisation on suction surface showing leading edge lowermost; tip flow for high flap angle, (a) $h/c = 0.211$ (b) $h/c = 0.105$.

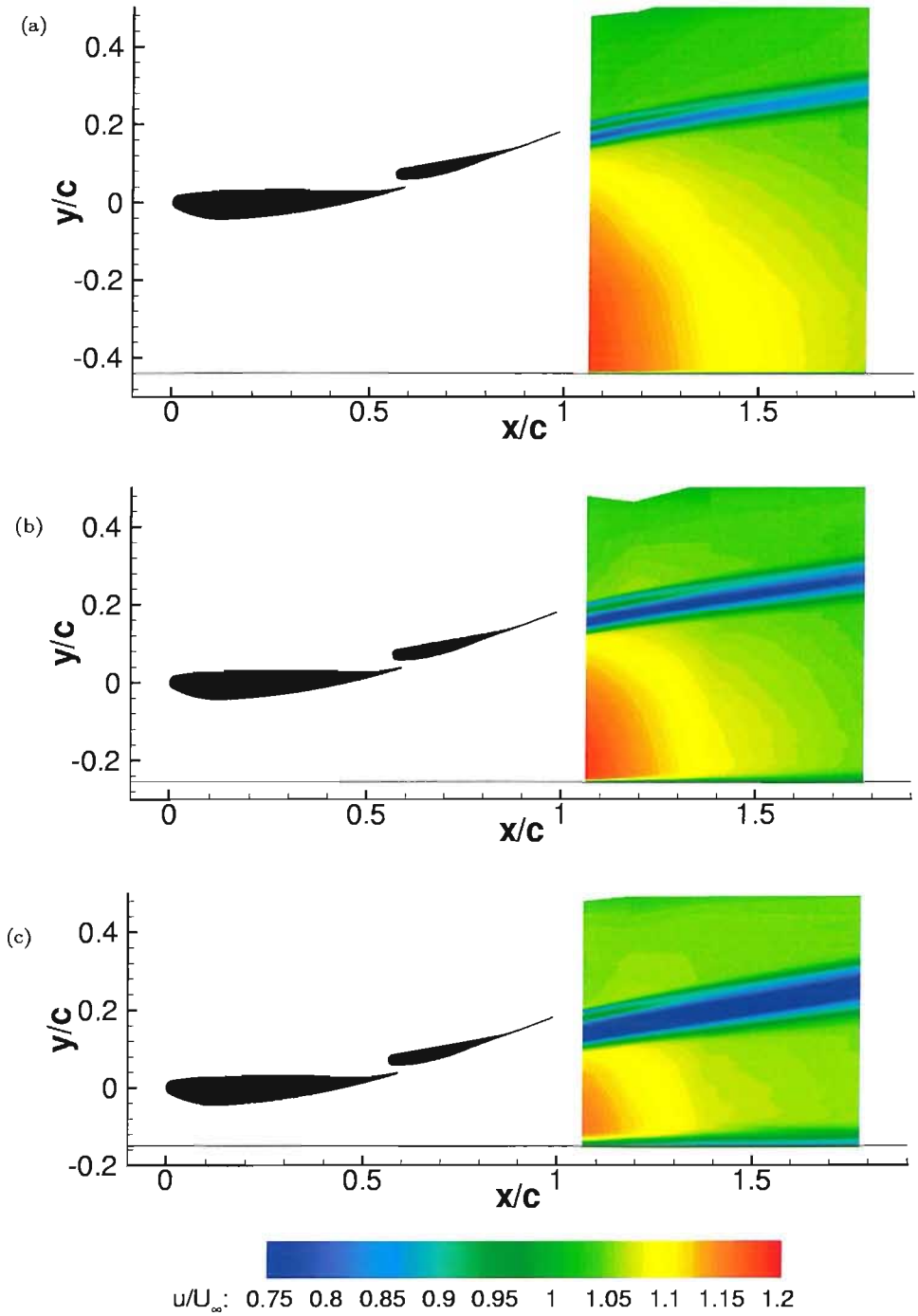

Figure 68: LDA u/U_∞ velocity contours at heights of $h/c = 0.395, 0.211, 0.105$ for low flap angle

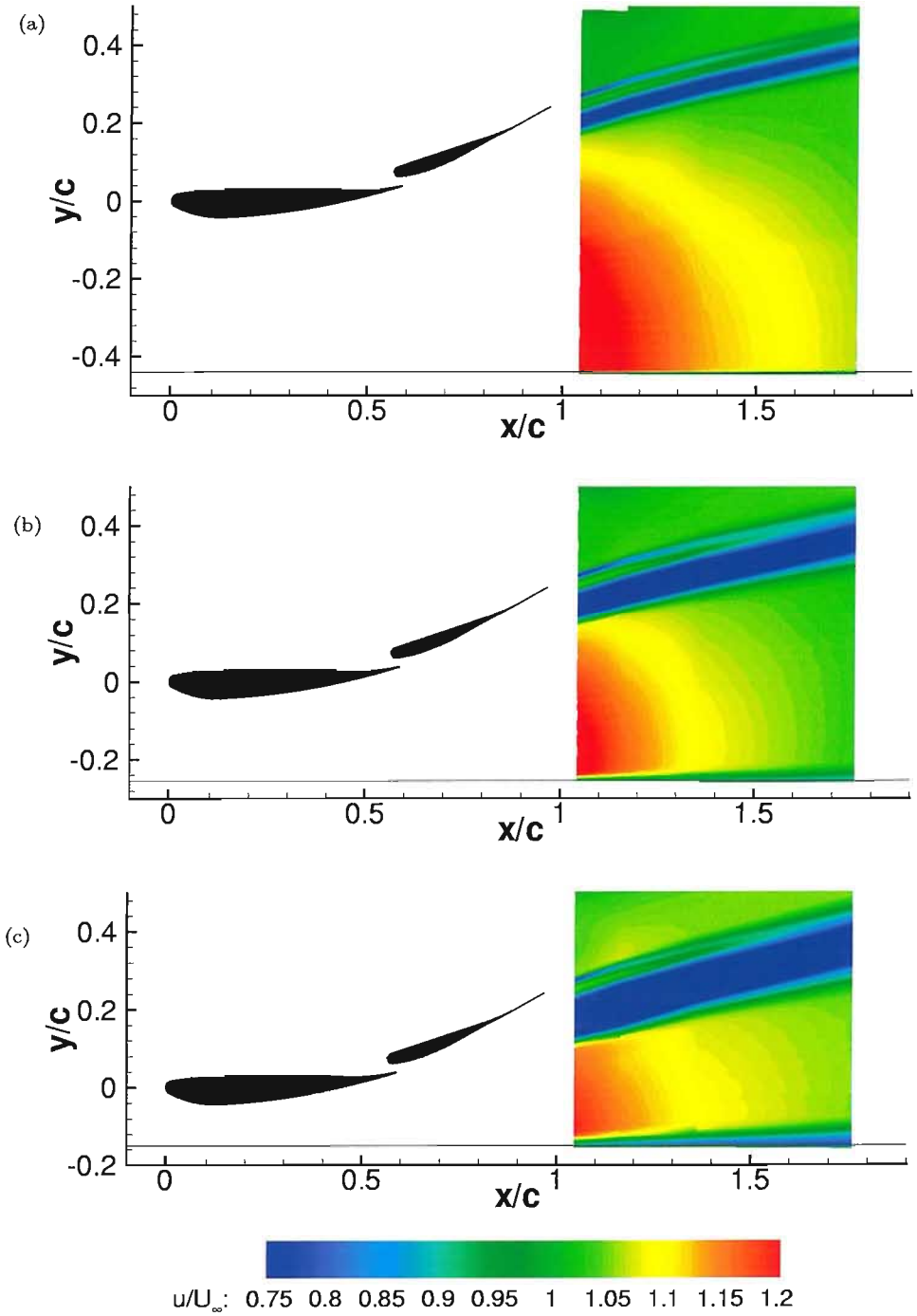

Figure 69: LDA u/U_∞ velocity contours at heights of $h/c = 0.395, 0.211, 0.105$ for high flap angle

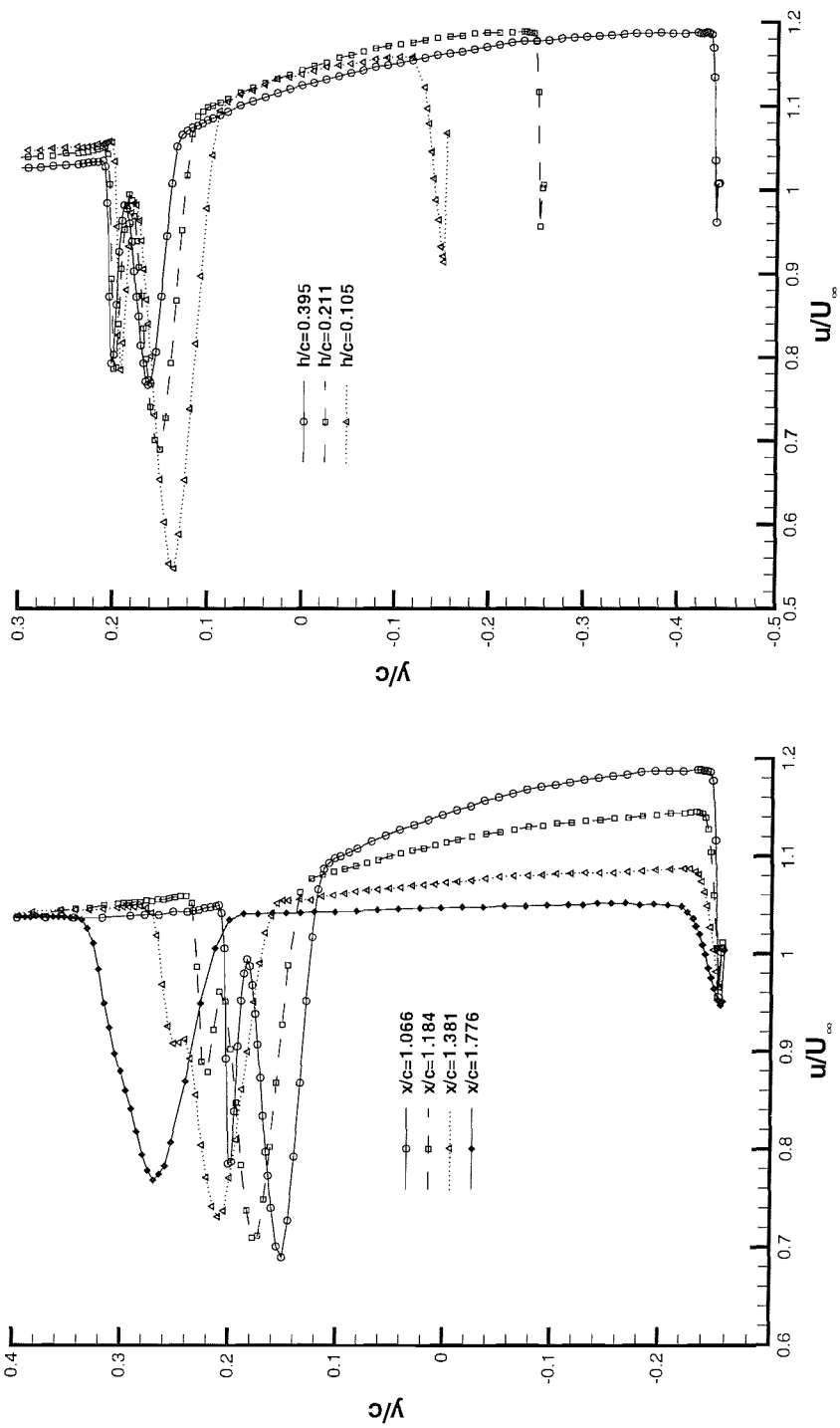

Figure 70: LDA u/U_∞ wake surveys for low flap angle; (a) Streamwise surveys at $h/c = 0.211$. (b) Surveys at $x/c = 1.066$ for different heights.

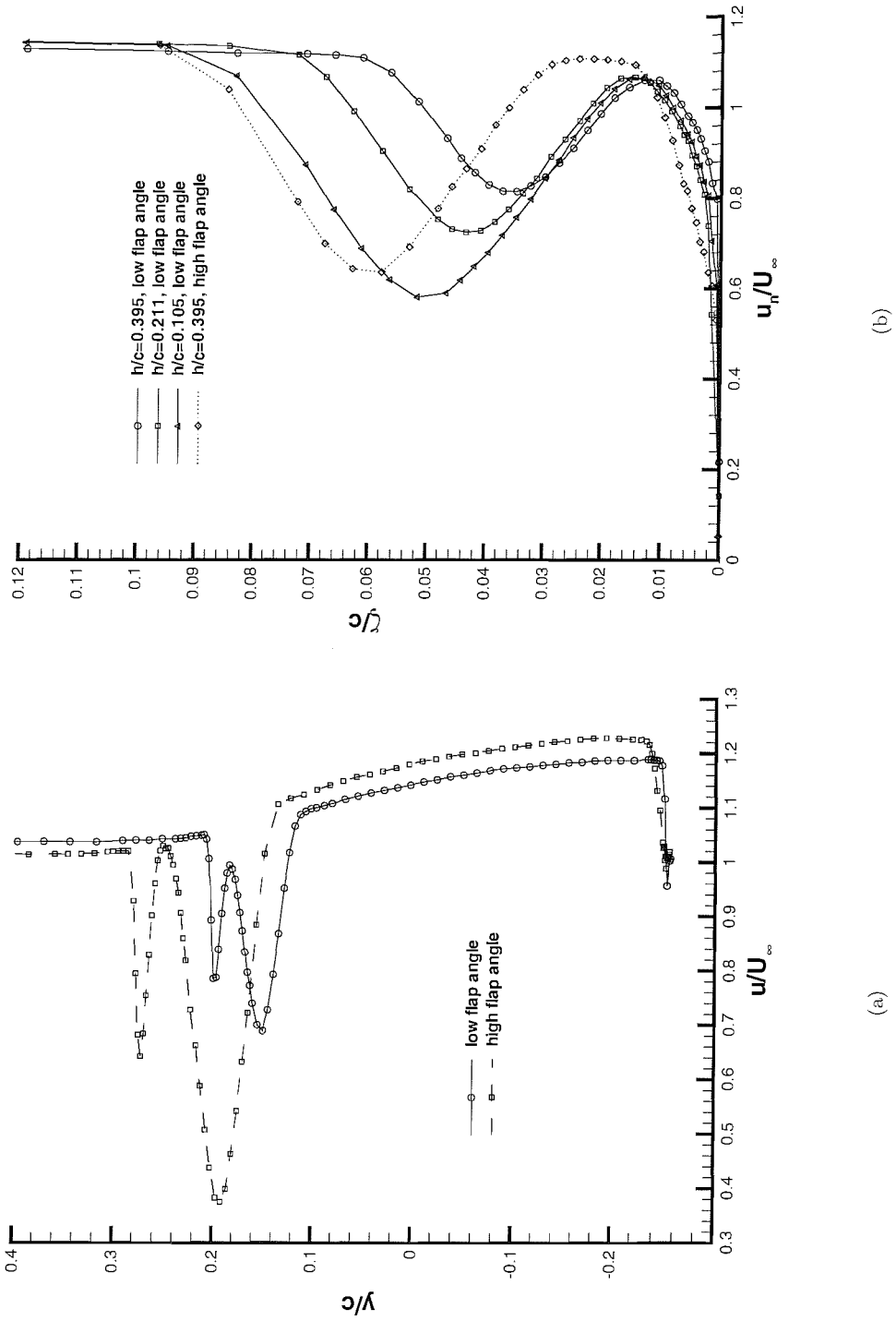

Figure 71: LDA u/U_∞ results; (a) Wake surveys at $x/c = 1.066$ for low and high flap angles. (b) Boundary layer surveys at flap trailing edge.

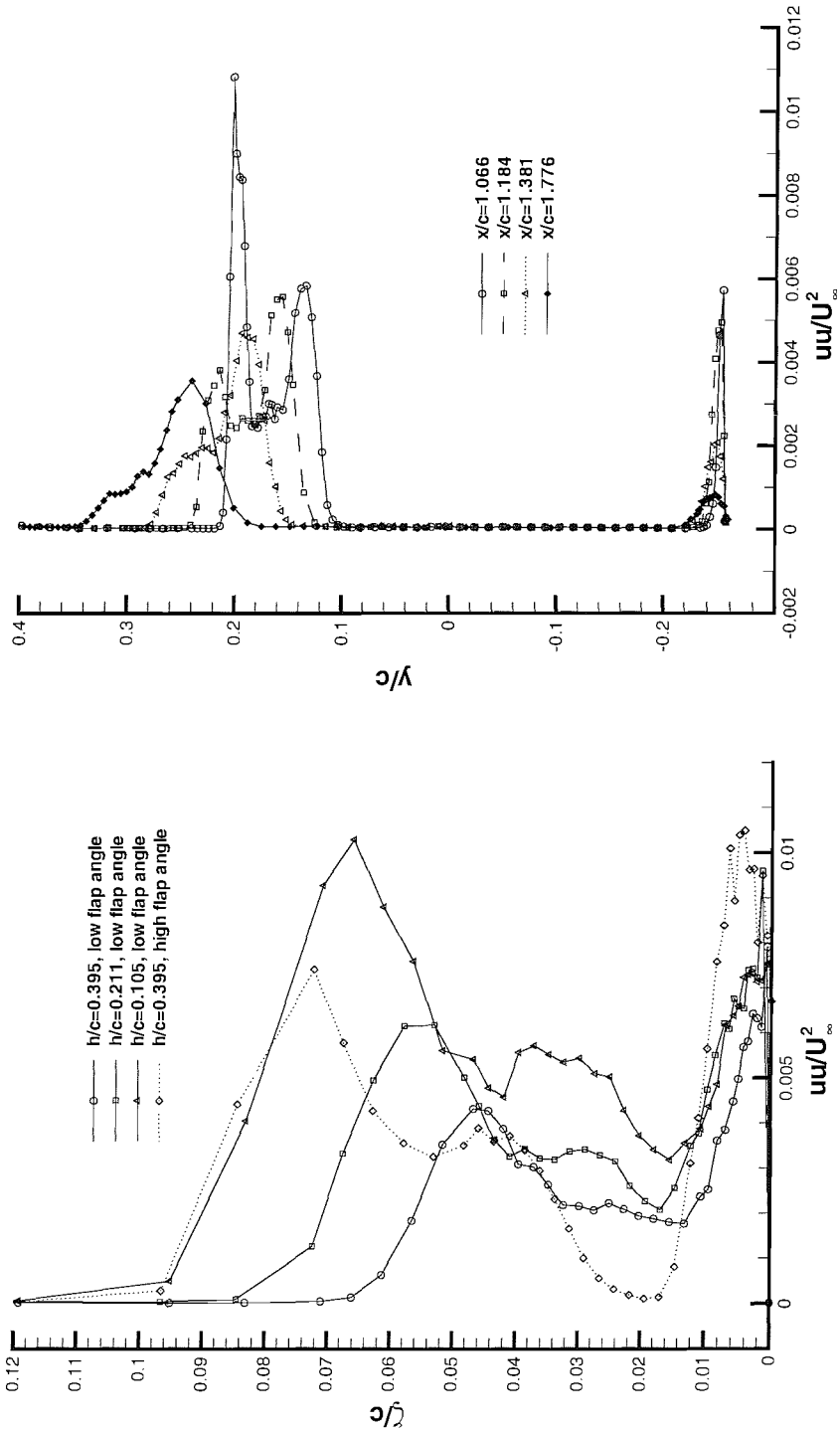

Figure 72: LDA $u'u'/U_\infty^2$ perturbation velocities; (a) Boundary layer surveys at flap trailing edge. (b) Streamwise surveys at $h/c = 0.211$ for low flap angle.

	Low flap deflection		High flap deflection	
h/c	$\omega_{1/4}c/U_\infty$	$\omega_{t/e}c/U_\infty$	$\omega_{1/4}c/U_\infty$	$\omega_{t/e}c/U_\infty$
0.395	80	71		128
0.316	102		102	136
0.263	104	105	153	147
0.211	111	112	126	21
0.184	128	118		
0.158	119	20	53	21
0.105	30	14	30	19
0.053	n/a	n/a	n/a	n/a

Table 13: Maximum vorticity in wing tip vortex; double element wing. $\omega_{1/4}$ for results at flap quarter-chord position, i.e. $x/c = 0.672$. $\omega_{t/e}$ behind trailing edge, at $x/c = 1.092$

Chapter 9

A Computational Fluid Dynamics Model of an Aerofoil in Ground Effect

9.1 Introduction

As an attempt to examine the application of CFD to model a wing in ground effect, two-dimensional studies have been performed using a single element configuration. Because a quasi two-dimensional region of flow exists near to the centre of the wing, it is a valid approximation for comparison with experimental results. In specific, the surface pressure distributions and the LDA results are to be compared.

The code that was available for use was CFL3D [82], an implicit upwind code, that solves the three-dimensional thin layer compressible Reynolds-averaged Navier-Stokes equations in a time dependent manner. A full description is given in [90].

9.2 Computational Model

9.2.1 Governing Equations

From [82], the compressible three-dimensional Navier-Stokes equations, in Cartesian coordinates are:

$$\frac{\partial Q}{\partial t} + \frac{\partial f}{\partial x} + \frac{\partial g}{\partial y} + \frac{\partial h}{\partial z} = 0$$

where:

$$Q = \begin{bmatrix} \rho \\ \rho u \\ \rho v \\ \rho w \\ e \end{bmatrix}$$

$$f = \begin{bmatrix} \rho u \\ \rho u^2 + p - \tau_{xx} \\ \rho uv - \tau_{xy} \\ \rho w - \tau_{xz} \\ (e+p)u - u\tau_{xx} - v\tau_{xy} - w\tau_{xz} + q_x \end{bmatrix}$$

$$g = \begin{bmatrix} \rho v \\ \rho uv - \tau_{xy} \\ \rho v^2 + p - \tau_{yy} \\ \rho vw - \tau_{yz} \\ (e+p)v - u\tau_{xy} - v\tau_{yy} - w\tau_{yz} + q_y \end{bmatrix}$$

$$h = \begin{bmatrix} \rho w \\ \rho uw - \tau_{xz} \\ \rho vw - \tau_{yz} \\ \rho w^2 + p - \tau_{zz} \\ (e+p)w - u\tau_{xz} - v\tau_{yz} - w\tau_{zz} + q_z \end{bmatrix}$$

and:

$$\tau_{xx} = \frac{2}{3}\mu\left(2\frac{\partial u}{\partial x} - \frac{\partial v}{\partial y} - \frac{\partial w}{\partial z}\right)$$

$$\tau_{yy} = \frac{2}{3}\mu\left(2\frac{\partial v}{\partial y} - \frac{\partial u}{\partial x} - \frac{\partial w}{\partial z}\right)$$

$$\tau_{zz} = \frac{2}{3}\mu\left(2\frac{\partial w}{\partial z} - \frac{\partial u}{\partial x} - \frac{\partial v}{\partial y}\right)$$

$$\tau_{xy} = \tau_{yx} = \mu\left(\frac{\partial u}{\partial y} + \frac{\partial v}{\partial x}\right)$$

$$\tau_{xz} = \tau_{zx} = \mu\left(\frac{\partial w}{\partial x} + \frac{\partial u}{\partial z}\right)$$

$$\tau_{yz} = \tau_{zy} = \mu\left(\frac{\partial v}{\partial z} + \frac{\partial w}{\partial y}\right)$$

The pressure is defined by the equation of state for an ideal gas:

$$p = (\gamma - 1)\left[e - \frac{\rho}{2}\left(u^2 + v^2 + w^2\right)\right]$$

9.2.2 Turbulence Modelling

Initial tests at a single height and in freestream were performed using two turbulence models; the Spalart-Allmaras (S-A) one equation model [91], and the Menter $k-\omega$ model [92], with a view to establish the difference in the performance and the flowfield of the models. Previous studies have found the S-A model to predict attached flows and two-dimensional separated flows well using CFL3D [93]. The $k-\omega$ model has been shown to be very capable compared with the S-A model for separated flows [94].

The comparison of results at a single height in ground effect were inconclusive as to which model performed better, and due to the significant differences found, it was decided to use both models for each height.

9.2.3 Numerical Algorithm

For a full treatment, see [90]. Briefly, CFL3D uses second order accurate upwind biased spacial differencing. The generalised fluxes representing the pressure and convection terms are split into forwards and backwards contributions and differenced accordingly. Central differencing is used for the shear stress terms. Time advancement is implicit, and steady or unsteady flows can be solved. Both mesh sequencing and multigrid are available for convergence acceleration.

9.2.4 Boundary Conditions

Figure 73 shows a schematic of the computational domain, with the boundary conditions that were used. The upstream and downstream boundaries are modelled with the inflow/outflow boundary condition. The top boundary uses an extrapolation simulation. The no-slip condition is applied to the surface of the aerofoil, using the viscous surface condition.

Preliminary test cases performed before experimental flowfield data had been collected attempted to model the ground plane using a variety of boundary conditions. The inviscid surface was used in order to check that a solution could be obtained, even though this is not the correct way to model the ground. No boundary condition in the original version of the code was ideal. As attempts had been started to modify an existing boundary condition, an updated version of CFL3D became available, with a boundary condition where the velocities and the turbulence quantities are prescribed. Investigations were performed on defining the turbulence quantities as having high and low values. The solution was found to be insensitive to this, and values of zero were used.

Freestream was defined as a Mach number of 0.0874, with the Reynolds number based on the chord as $R = 462000$, with a temperature for the flow of $T = 527°$ Rankine.

9.2.5 Grid Strategy

In order to generate the two-dimensional structured grids at different heights from the ground, Gridgen [95] was used. Substantial grid refinement tests were performed to identify the resolution required in various regions of the mesh. First, the effect of grid density and the spacing of the first point from the ground was investigated on the flowfield around the wing. It was found that the entire solution was extremely dependant on the grid in this region. The spacing was reduced, and number of grid points between the wing and the ground increased, until the surface pressure distribution around the wing was seen to converge. A $y^+ \approx 1$ was required. Similar tests were performed on the circumferential spacing around the aerofoil on the upper and lower surfaces, and the distribution of the points over each surface. It was found that a fine grid was required, especially over the suction surface, as is described below.

After preliminary tests on the gridding strategy were performed, it was decided to use a solution that required neither grid patching nor grid overlaying. Although not all the features of the grid are ideal, this was felt as the best compromise. The grid, for a height of $h/c = 0.179$ can be seen in Figure 74. This is shown in more detail for the region near to the aerofoil leading and trailing edges in the same figure, together with an example of another grid at $h/c = 0.313$. The upstream and downstream boundaries are located at $8c$ from the aerofoil. The boundary above the wing is at $y = 7c$, which corresponds to the approximate location of the wind tunnel roof. The computational domain contains about 25000 to 30000 grid points, depending on ground height.

The grid contains five blocks in total. The first block is a square C-type grid, around the aerofoil. The grid cells at the corners of the grid are not ideal, but this grid approach was the best compromise. A $y^+ \approx 1$ was used for the first grid point normal to the aerofoil surface. The grid is clustered near to the aerofoil leading and trailing edges. It was found that more grid points were required on the suction surface compared to the pressure surface. Effort was made to force a perpendicular grid near to the trailing edge region of the suction surface. The aerofoil features a finite trailing edge, corresponding to 0.007c. Block 2 is a H-type grid covering the region from the trailing edge to the downstream boundary; a closed wake type grid. Block 3 is an H-type grid, extending from block 1 vertically to the top of the computational domain. Block 4 grids the upstream area from block 1 to the upstream boundary, and is H-type. Block 5 is H-type, and covers the entire ground plane from the upstream to the downstream boundaries. The reason that block 5 is required is for the fine grid spacing necessary on the ground plane; a $y^+ \approx 1$ is also required for the first grid point from the ground. The grid points per block, and the total number of cells is given in Table 14 for all heights.

In order to simulate the flow around an aircraft wing at varying angles of attack, the same grid is generally used, specifying a different incidence in the CFD input datafile. For the configuration of a wing at different heights in ground effect, a new grid has to be generated for each height from the ground, which is a tedious process. The geometry in the database file was modified, and blocks 1, 3, 4 and 5 had to be regenerated. For a reduction in ground height, it was required to reduce

the circumferential size of the C-type grid around the aerofoil, in addition to moving the ground grid vertically up relative to the aerofoil.

9.2.6 Solution Process

It was found to be extremely difficult to obtain a solution. When a steady solution was performed, this yielded results with unsteady periodic characteristics. However, an unsteady solution would generally converge on a single steady result.

The solution process used started with a steady run. Mesh sequencing was employed, performing the analysis on three grid levels, for convergence acceleration. Multigrid was then used for the remainder of the steady and unsteady solutions. The output from the steady solution was used as a restart for the next stage, the unsteady solution. It was not possible to start with an unsteady solution; the semi-converged steady results were required to avoid the solution from blowing up. The S-A model was found to be more robust than the $k-\omega$ model, although this depended on the exact characteristics of the grid and the flowfield. For the $k-\omega$ model, it was necessary to perform two unsteady analyses consecutively; the first with a small time step, and the second with a larger time step. The S-A model only needed the run with the larger time step.

Convergence problems using compressible solvers at low Mach numbers are well documented [96]. The combination of this, and the fact that a time-accurate solution method is required leads to long solution times, generally 3-4 days in total on a single node of an Origin 2000.

9.3 Results

The results of the computations are compared in terms of the aerodynamic performance, and the flowfield results.

9.3.1 Aerodynamic Performance

Freestream

Both turbulence models give very similar results in freestream, as can be seen by the pressure distributions in Figure 76a.

The first point to make is that the computational results show a large spike near to the leading edge of the suction surface. The experimental results for this case do not show this spike. This may either be due to the spacing between the tappings, or because it is not present for this particular experimental configuration. Note that many other experimental results do show the presence of this spike, for example the single element wing at other incidences, the Gurney flap results, and more prominently in the double element results. The magnitude of the spike is sufficiently large that it is slightly greater than the main suction peak, near to $x/c = 0.16$. The suction peak is overpredicted a little by the computation. In the pressure recovery region, however, from $x/c \approx 0.25$ to the

trailing edge of the suction surface, the pressures compare extremely well with the experimental values.

Near to the leading edge of the pressure surface, stagnation is predicted well. The flow is then accelerated rapidly. At $x/c = 0.03$, the experimental results show the flow to have reached a velocity, which remains approximately constant for a large portion of the surface, before a gradual retardation starting at $x/c = 0.5$. But, the computational results show a small, but significant deceleration at $x/c = 0.03$ to $C_P = 0.25$. The pressures are then overpredicted by the computation, with the difference decreasing in the streamwise direction. From $x/c \approx 0.6$, the difference is small, and the remainder of the computational results compare well with the experimental values.

The C_l for the aerofoil was found to be 0.885 for the S-A model and 0.872 for the $k-\omega$ model. An estimation of the sectional downforce C_l from the experiments can be obtained by integrating the surface pressures. However, it is stressed that this is only an estimate, and will be used to compare the qualitative trends between the experimental and computational results, not as a quantitative comparison. The experimental results give $C_l = 0.766$. This is a difference of approximately 16% between the computational and the experimental results for the S-A model, and 14% the $k-\omega$ model. In addition to the difference in the surface pressures at discrete points, this approximately 15% difference is also due to the leading edge suction spike, and the linear interpolation of the results using a large number of points, computationally about 200, with the relatively coarse spacing of the 45 experimental results.

Ground Effect

The downforce predicted by the CFD, together with C_l from the integrated pressures can be seen in Figure 75a for all heights. Tabulated results are given in Table 15. The comparisons are only to highlight the trends, not the outright values. In addition, C_d is given for the computational results, Figure 75b. Each of the surface pressure distributions will be discussed below.

The distributions at $h/c = 0.671$ show the results for the largest height in ground effect, Figure 76b. The ground effect has increased the lower surface suctions, in addition to a slight reduction in the upper surface pressures, which overall leads to an increase in downforce. Again, the leading edge suction spike is of a similar magnitude to the main suction peak. The main peak is overpredicted by the computations, as in freestream. However, the suctions throughout the pressure recovery are also overpredicted by the computation, unlike the freestream results. Again on the pressure surface, the pressures are too great from the spike at $x/c = 0.03$ to about the mid-chord. Further downstream, they compare better. The computations predict $C_l = 1.052$ (S-A) and 1.030 ($k-\omega$), compared to the experimental value of 0.902, which is a similar difference that in freestream, of 17% and 14%. The very slightly greater downforce from the S-A model compared to the $k-\omega$ model can be seen to be due to increments in the loading predicted on each surface.

The same general trends can be observed at $h/c = 0.448$ (Figure 77a). The overprediction of the lower surface suctions has increased slightly, over the whole of the surface. Although the

suction at the leading edge spike has increased, that at the main peak increases at a greater rate such that it can be seen that the largest suction is that at the mean peak. The slight increase in the lower surface suction prediction is offset by a small reduction in the overprediction in the pressure surface results, resulting in computational results for C_l are 16% and 13% greater than the experimental value.

At $h/c = 0.313$, a small difference starts to appear in the overall results from the two different turbulence models. As can be seen in the pressure distribution (Figure 77b), the overprediction of the S-A results on the suction surface are very slightly greater than at the previous height, and that of the $k-\omega$ results has decreased slightly. There is little change on the pressure surface. This yields predictions of C_l that are 15% greater (S-A) 9% greater ($k-\omega$) than the experimental results. As it can be seen in Figure 75a and Table 15, it appears that the S-A results are predicting the trends for the downforce at the large heights better than the $k-\omega$ model.

Similarly for $h/c = 0.224$ (Figure 78a), the overprediction in lower surface suctions remains approximately constant for the S-A model, compared with the previous height. However, this reduces for the $k-\omega$ model, such that most of the suction surface results are mapped very well for this example. For both models, nearly all pressure surface results are mapped well, too. The effect is that the S-A model gives $C_l = 1.475$, again 15% greater than the experimental prediction of $C_l = 1.286$. The $k-\omega$ model gives a closer result of $C_l = 1.352$, just 5% greater than the experimental value. The same trend can be seen in Figure 78b, for a height of $h/c = 0.179$, where C_l for the two turbulence models are 15% (S-A) and 2% ($k-\omega$) greater than the experimental values.

At $h/c = 0.134$, the greatest experimental C_l was found. Again, the S-A model overpredicts the lower surface suctions (Figure 79a) by a similar amount to the previous height. The $k-\omega$ model starts to underpredict the suctions very slightly, especially in the region of the suction peak. On the pressure surface, the flow is mapped well by both models, the S-A model giving a slightly higher pressure near to the leading edge region. The S-A model gives $C_l = 1.604$, 16% greater than the experimental value of $C_l = 1.385$, whereas the $k-\omega$ model predicts $C_l = 1.386$. Results at the lowest height of $h/c = 0.090$ show the same trend, but more extreme in nature; there is a similar overprediction of the lower surface suctions from the S-A model, but the $k-\omega$ model is underpredicting the suctions more severely. This gives a 12% overprediction and a 5% underprediction in C_l from the S-A and the $k-\omega$ models respectively.

9.3.2 Flowfield

Results from the computational database were extracted in order to compare with the experimental wake and boundary layer surveys performed with the LDA system.

Boundary layer

As described previously, the finite size of the measurement volume coupled with flare from the surface implied that it was impossible to obtain results very close to the surface of the wing. For simplicity, the surface, at which $\eta = 0$, was defined as the last point at which zero data was obtained. In this manner, the LDA results are a finite distance below their true location. It is believed that the first 1mm approximately from the wall was void of any data. This is a rough estimate. Hence, the LDA profiles should be raised by, very approximately, 0.005c. This has not been performed, due to the uncertainty in the size of the correction required.

Figure 80a shows the computational results with the LDA results, for u/U_∞ at $h/c = 0.224$. The two turbulence models give different results within the boundary layer. It can be seen that, very close to the surface, the S-A model has a negative velocity, as the flow separated. Although this is not clear from the profile for the $k-\omega$ case, examination of the skin friction on the wall gives a negative value also for the $k-\omega$ case, as the flow has also separated. Through the boundary layer, for a particular distance from the surface, the velocity is consistently lower for the S-A model, until it reaches the edge. Although within the boundary layer, the experimental results lie closer to those for the $k-\omega$ model, given the problem with obtaining experimental results near to the surface, and the shape of the profile, it is difficult to say which model gives a better match. Outside the edge of the boundary layer, u/U_∞ is approximately 0.03 greater for the experimental results than for the computation.

At $h/c = 0.134$ (Figure 80b), both computational results clearly show a separated boundary layer. In a similar manner to the results at $h/c = 0.224$, the S-A model gives a thicker boundary layer than the $k-\omega$ model. Again, it would appear that, although the experimental points lie closer to the $k-\omega$ results, it is difficult to say which model gives the best results. Both models fail to predict the magnitude of the velocity in the recirculation region. Again, beyond the edge of the boundary layer, both turbulence models give results that are less than the experimental results, by $u/U_\infty \approx 0.05$.

Nearfield wake

To investigate the wake results, comparisons are made at two streamwise locations. At $x/c = 1.2$, the results are compared with velocities extracted from the LDA grid results mapping the trailing edge region. At $x/c = 1.5$, the results are compared with the LDA wake surveys. Note that the dedicated wake surveys included a finer distribution of points in the direct wake from the wing, and also additional points very close to the ground, to map the ground boundary layer. Tabulated results for the wake thickness from the computations and experiment are presented in Table 16 for $x/c = 1.5$. Information on the ground boundary layer is also given, in Table 17 at the same streamwise location.

At a height of $h/c = 0.448$, the wake surveys at $x/c = 1.2$ are compared in Figure 81a. Outside

of the edge of the wake, the computations point to velocities that are $u/U_\infty \approx 0.025$ lower than the experimental values. The results within the wake are difficult to compare to a high degree of accuracy due to the coarse spacing of the experimental points. The S-A model gives a slightly greater minimum velocity at the centre of the wake. The wake thickness appears similar, for the computations and the experiment. It is difficult to be more precise, due to the coarse spacing of the experimental results, and the increased velocity outside of the wake for the experimental results. The main difference between the two models appears in their ability to model the ground boundary layer. Although few experimental points are available at this streamwise location, it is clear that the $k-\omega$ model gives a ground boundary layer significantly thicker than the S-A model and the experiments.

Results are similar at $x/c = 1.5$ for the same height (Figure 81b). Outside of the wake, the velocities according to CFD are $u/U_\infty \approx 0.03$ lower than the experimental results. The wake thickness is modelled well by the computations (Table 16). There is a difference in the maximum velocity deficits of $u/U_\infty \approx 0.06$, which implies a little overprediction by the CFD in addition to the difference found out of the wake. The results for the $k-\omega$ model show the ground boundary layer to have grown compared to the previous streamwise location, also Table 17. The thickness of this from the S-A model is significantly closer to the experimental values.

For the results at $h/c = 0.224$ (Figure 82) there is a small overprediction of the wake thickness and the maximum velocity deficit at $x/c = 1.2$. At $x/c = 1.5$, the wake velocities are underpredicted more significantly, see also Table 16. The differences between the two turbulence models used are relatively small compared to the difference between the computations and the experiments in general. The ground boundary layer for the $k-\omega$ model is much thicker than at the previous height, whilst the S-A model would appear to give better results here regarding the thickness of the layer (Table 17). The minimum velocity, however, is underpredicted a little, however this may partly be due to the underprediction in the edge velocity.

For results at $h/c = 0.134$, which is at the maximum downforce experimentally, and for the S-A model, but below the maximum downforce for the $k-\omega$ model, the results are again similar, but more severe (Figure 83). The main wake is now a little thicker than the experimental results at $x/c = 1.2$. The velocity at the wake centre is closer with the S-A model, but both models show an incorrect upward shift in the wake, compared to the LDA results. At $x/c = 1.5$, the velocities in the wake are significantly underpredicted. The wake thickness is slightly underpredicted by both models (Table 16). For both streamwise locations, $k-\omega$ shows an increased ground boundary layer. From the results at $x/c = 1.5$, it is apparent that the S-A model gives a boundary layer that is a little too thin but which is massively overpredicts the velocity deficits.

Farfield wake

A further comparison of the wake results is given in Figure 84, in which the u/U_∞ velocity contours are plotted for $u/U_\infty < 0.99$, to highlight the results within the wake and the ground boundary

layer. Results are for the S-A turbulence model at the same heights of $h/c = 0.448, 0.224, 0.134$. In addition, results at $h/c = 0.134$ are also given for the $k-\omega$ model, and for the experimental LDA results. As the flow moves downstream, it can be seen that, for a given height, the wake thickens, and the velocities in the wake reduce. A reduction in the height thickens the wake, especially on the lower edge, where this is due to the increase of the suction surface boundary layer thickness. The effect of using the $k-\omega$ model is to massively overpredict the thickness of the ground boundary layer. Both computational models give relatively similar results within the wake, however. Far from the trailing edge, at $x/c = 3.0$, it can be seen that there is now a significant difference in the velocities for the computational results compared with the experimental results. Generally, the velocities within the wake are too low for the computational results, and the thickness of the wake is too large.

Flow between wing and ground

The u/U_∞ velocity contours are also presented in Figure 85 for the flow between the wing and the ground, for the same heights of $h/c = 0.448, 0.224, 0.134$ for the S-A model, and $h/c = 0.134$ for the $k-\omega$ model. The reduction in the height of the wing from the ground results in the flow being accelerated to a greater extent, as can be seen in the figure, and also from the surface pressures presented earlier. Studying the results close to the ground near to the peak in suction, it can be seen that the ground boundary layer originates as the flow starts to retard after the peak suction. Further analysis of the results (not presented here) confirms this. The overprediction of the ground boundary layer thickness with the $k-\omega$ model is evident from near to its formation, e.g. at $x/c = 0.4$. There is also a small difference in using the $k-\omega$ and S-A models in the velocity contours, which can be seen more clearly in the surface pressure distributions. Using the $k-\omega$ model gives velocities which are lower than for the S-A model.

9.4 Discussion

Examining the performance of the wing in freestream shows that the pressure distributions are modelled well, and the difference between the S-A and the $k-\omega$ models is insignificant. On the suction surface, the peak suction is overpredicted a little, but the pressure recoveries compare extremely well. A spike is prominent in the computational results, but is not as apparent in the experimental results. On the upper surface, the pressures are overpredicted a little by the computations. Integrating the surface pressures gives an experimental result of about 15% less than the computations. Although this is partly due to the small overpredictions in the pressures and suctions over some portions of the upper and lower surfaces respectively, a significant contributory factor is the coarser distribution of discrete points experimentally over which interpolation is applied, especially considering the spikes that are present in the computations.

In ground effect, the lower surface suctions are constantly overpredicted a little by the S-A

model. At large heights, this is also the case for the $k-\omega$ model. However, the overprediction reduces as the height is reduced, and at $h/c = 0.179$, the predicted lower surface suctions are too low. The underprediction of suction increases still as the height is reduced. Generally, little difference is found on the pressure surface, and results compare well. The effect of this is that the S-A model predicts the qualitative trend of the ground effect very well, and results for C_l are constantly 15% too great. However, the $k-\omega$ model does not show the correct trends, and at the closest height to the ground, the overall loading is lower than the experiment.

The surface pressure distributions along with the contour plots show that the difference using the two models arises from the suction surface, and increases as the height is reduced. The $k-\omega$ model starts to give reduced suctions compared to the S-A model, but still greater than the experimental values, which are clear from about $h/c = 0.313$. This effect is amplified such that at small heights, the $k-\omega$ results have reduced suctions than the experimental results. This gives the S-A results a greater adverse pressure gradient for the pressure recovery region. The boundary layer profiles seem to confirm this, with a thicker boundary layer for the S-A results. It is difficult to confirm which model generates the more realistic boundary layer profiles, due to the problem in obtaining LDA results close to the surface.

The major flaw with the $k-\omega$ model is an overprediction of the ground boundary layer thickness. The computational results confirm that this originates due to the adverse pressure gradient after the peak suction from the wing. At a constant height close to the ground, the $k-\omega$ model gives a thick boundary layer, and lower velocities in the region between the wing and the ground. It would appear that the lower velocities are a direct effect of the thicker boundary layer. It is believed that this causes the difference in the predictive capabilities of the models.

9.5 Summary

Good qualitative results predicting the correct trends have been obtained, in an attempt to model a two-dimensional slice of a single element wing in ground effect, using the S-A turbulence model. Comparing the results to integrated pressures from the experimental study gives a constant difference of about 15% in C_l. However, the pressure distributions appear more accurate than this, the differences partly due to the discrete spacing of experimental points. There are deficiencies in modelling the wake flow, and CFD predicts a larger wake, in terms of thickness and velocity deficit as the streamwise distance is increased. The $k-\omega$ model was shown not to model the ground boundary layer correctly, resulting in bad performance at low ground heights.

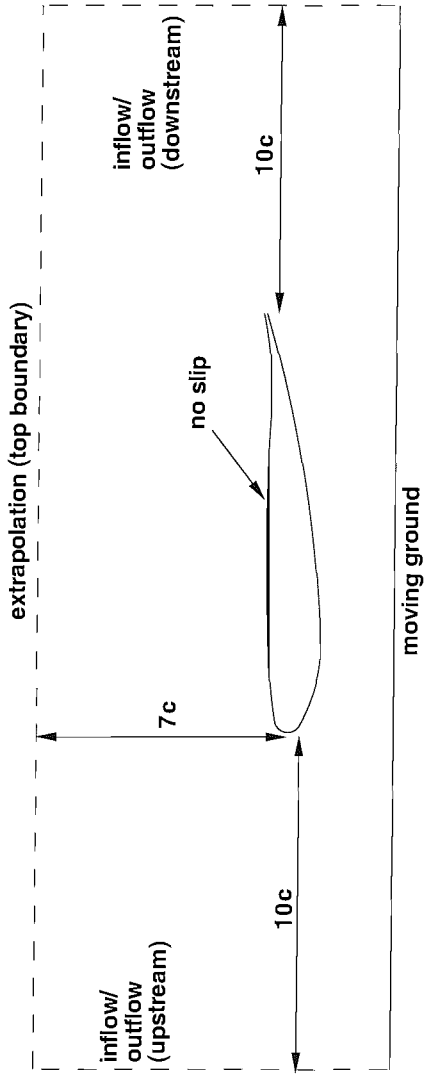

Figure 73: Schematic of computational grid including boundary conditions

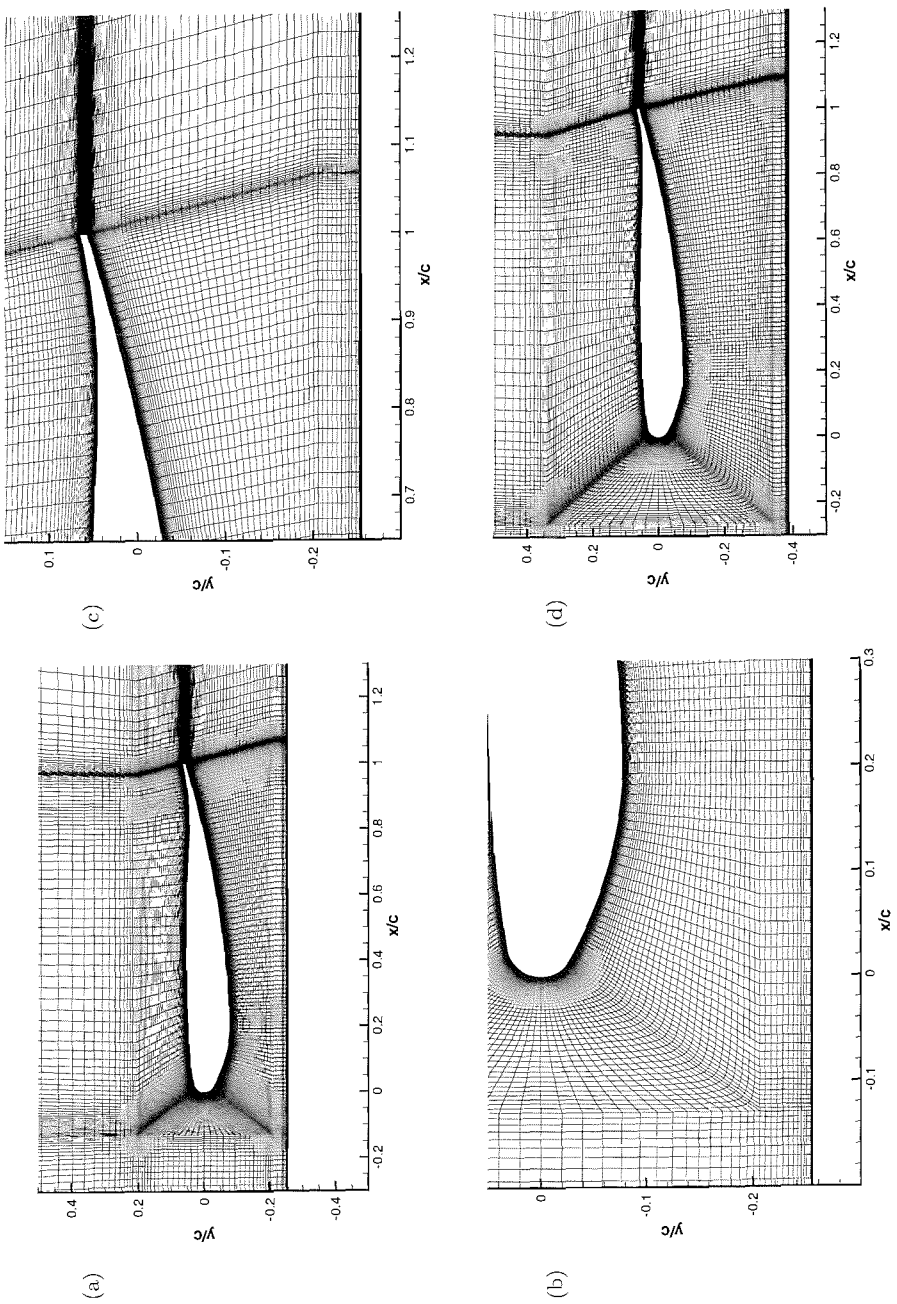

Figure 74: Computational mesh; (a) $h/c = 0.179$. (b) Leading edge region. (c) Trailing edge region. (d) $h/c = 0.313$.

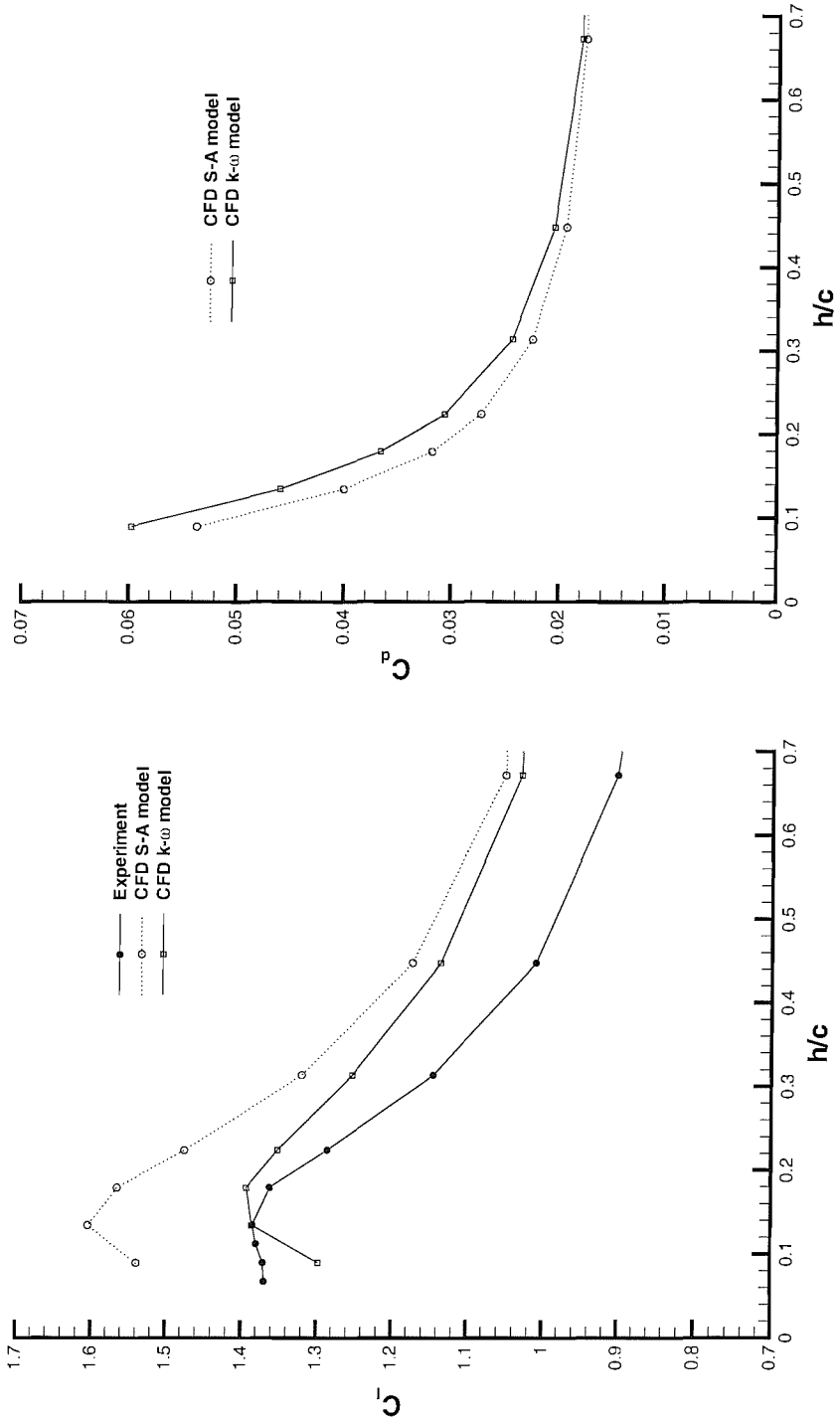

Figure 75: Forces in ground effect; (a) Downforce. (b) Drag.

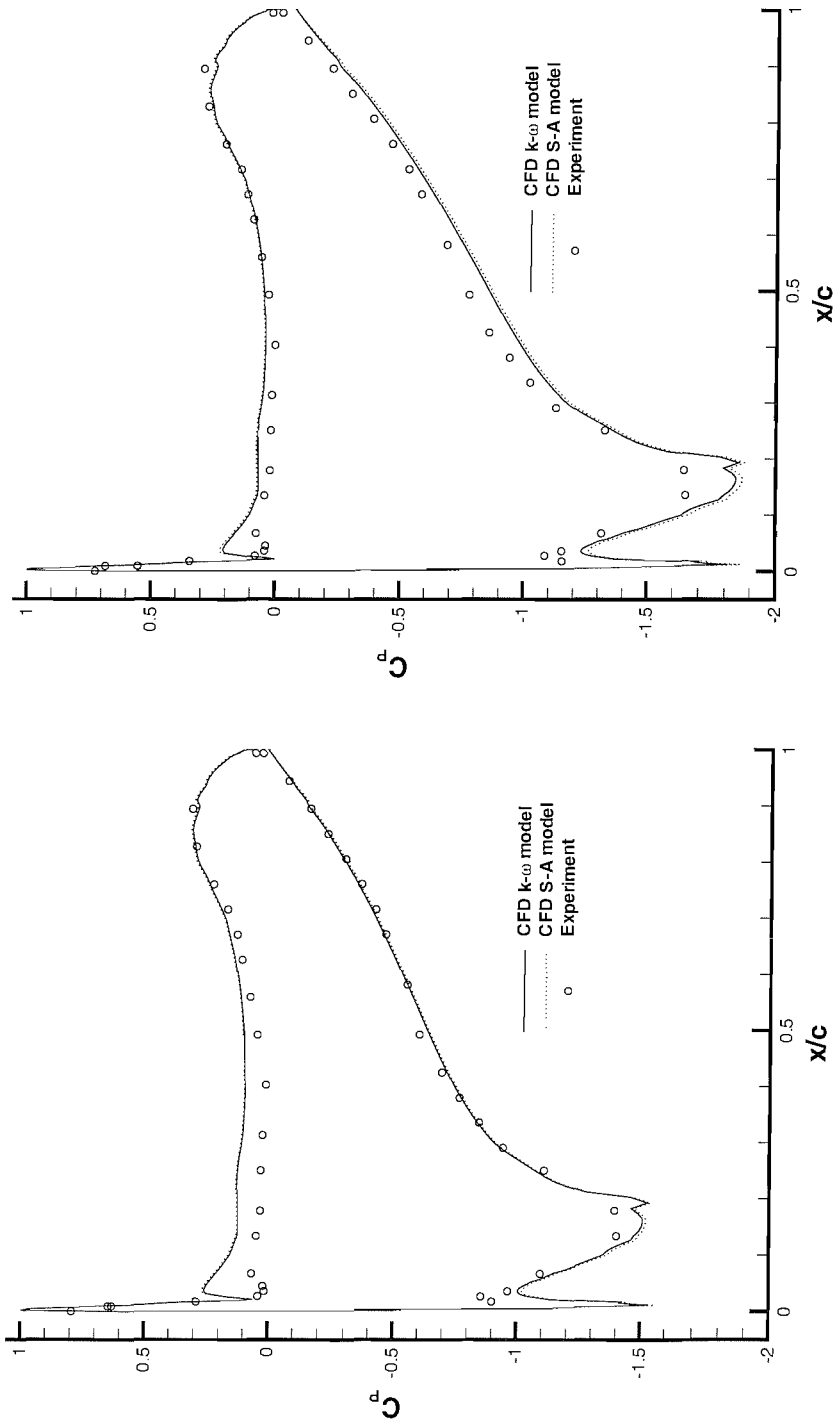

(a) (b)

Figure 76: Comparison of computational and experimental surface pressures; (a) freestream. (b) $h/c = 0.671$.

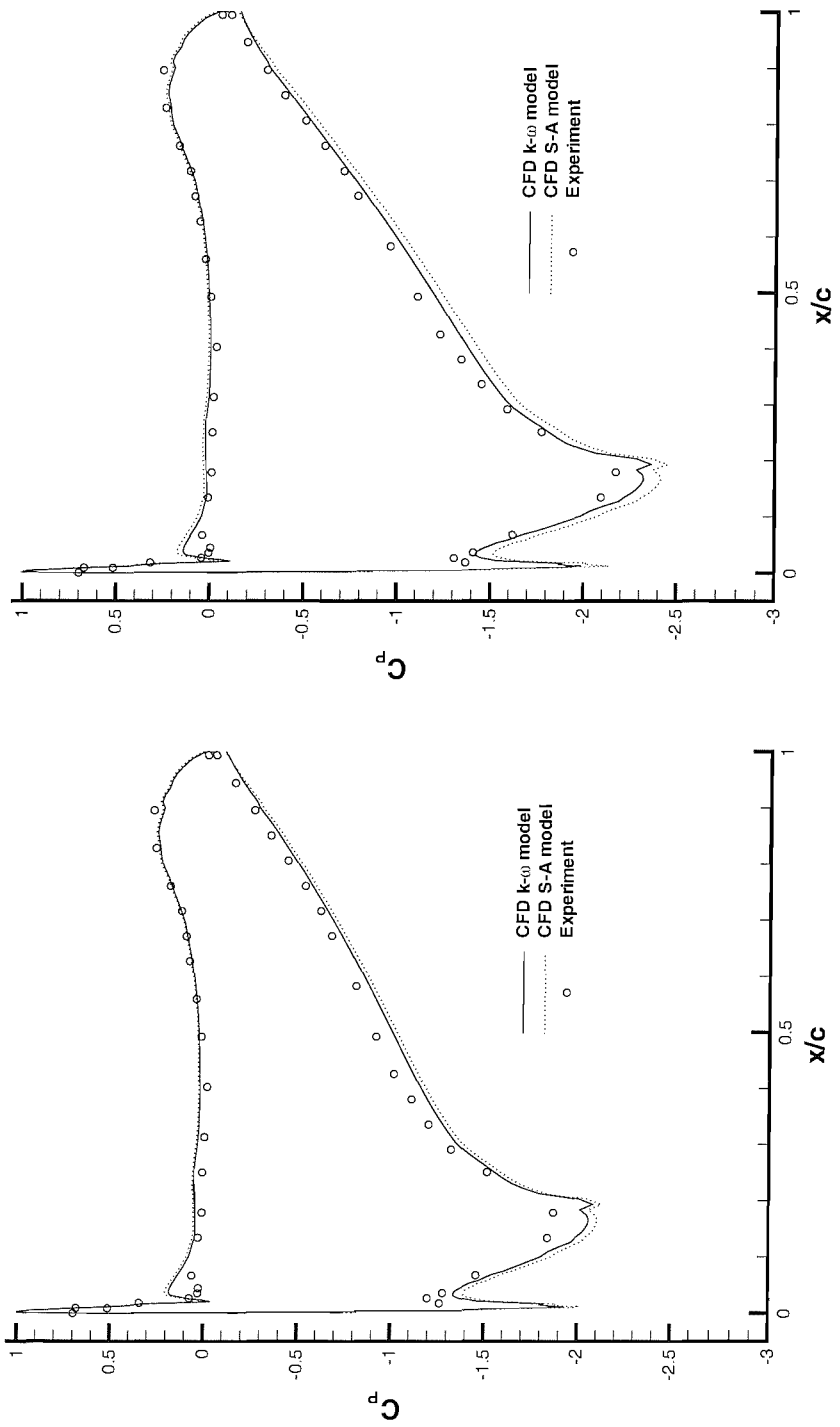

Figure 77: Comparison of computational and experimental surface pressures; (a) $h/c = 0.448$. (b) $h/c = 0.313$.

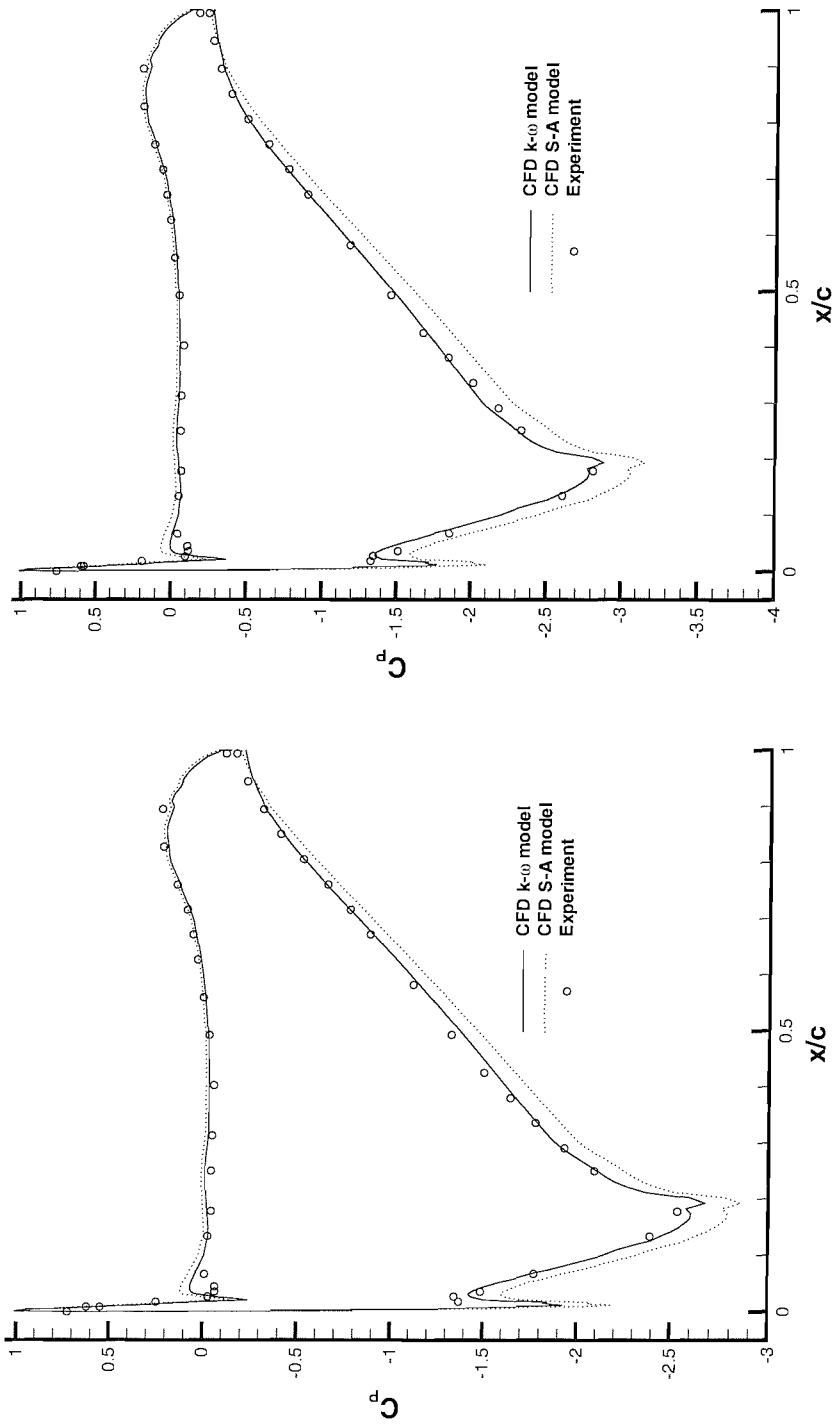

Figure 78: Comparison of computational and experimental surface pressures; (a) $h/c = 0.224$. (b) $h/c = 0.179$.

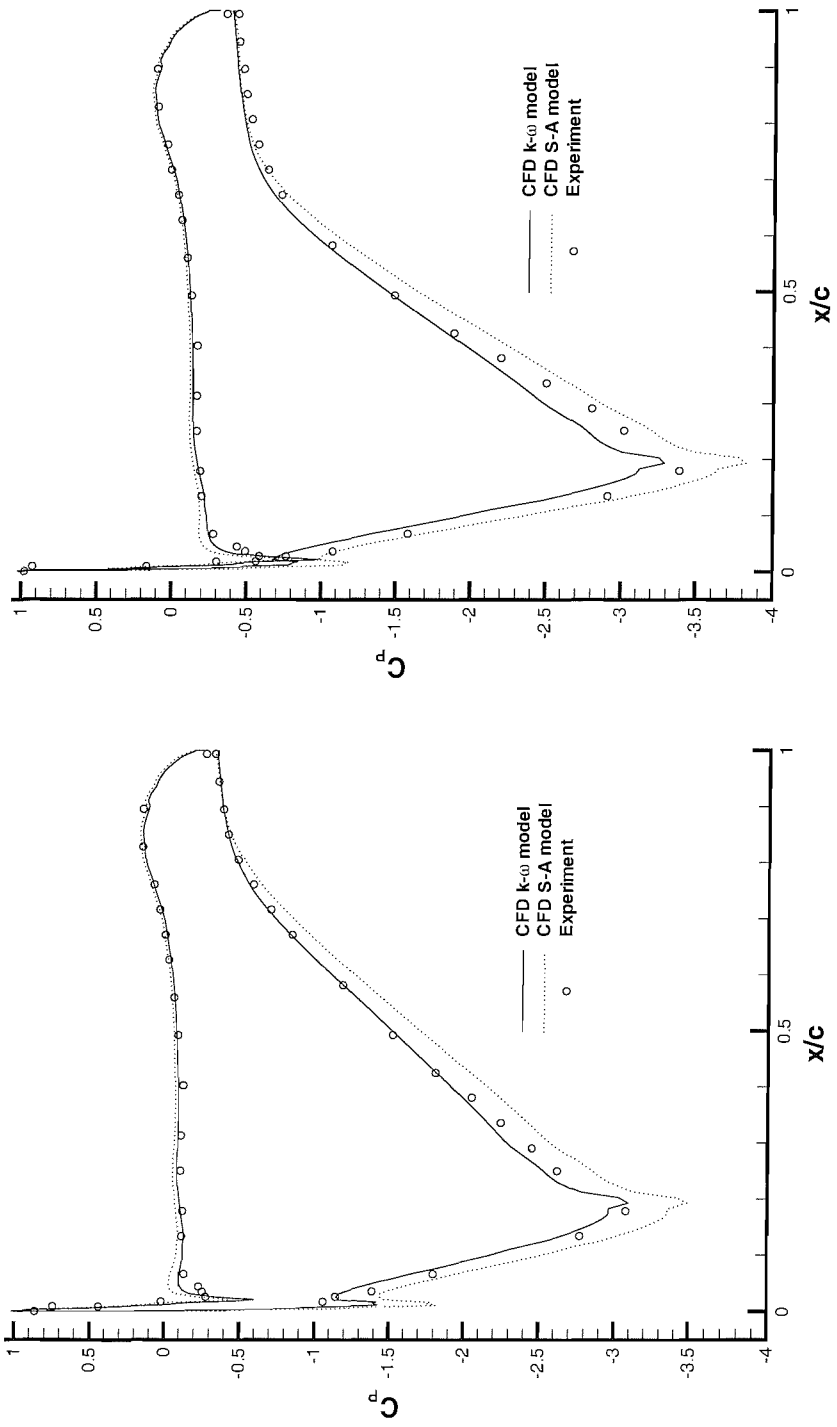

Figure 79: Comparison of computational and experimental surface pressures; (a) $h/c = 0.134$. (b) $h/c = 0.090$.

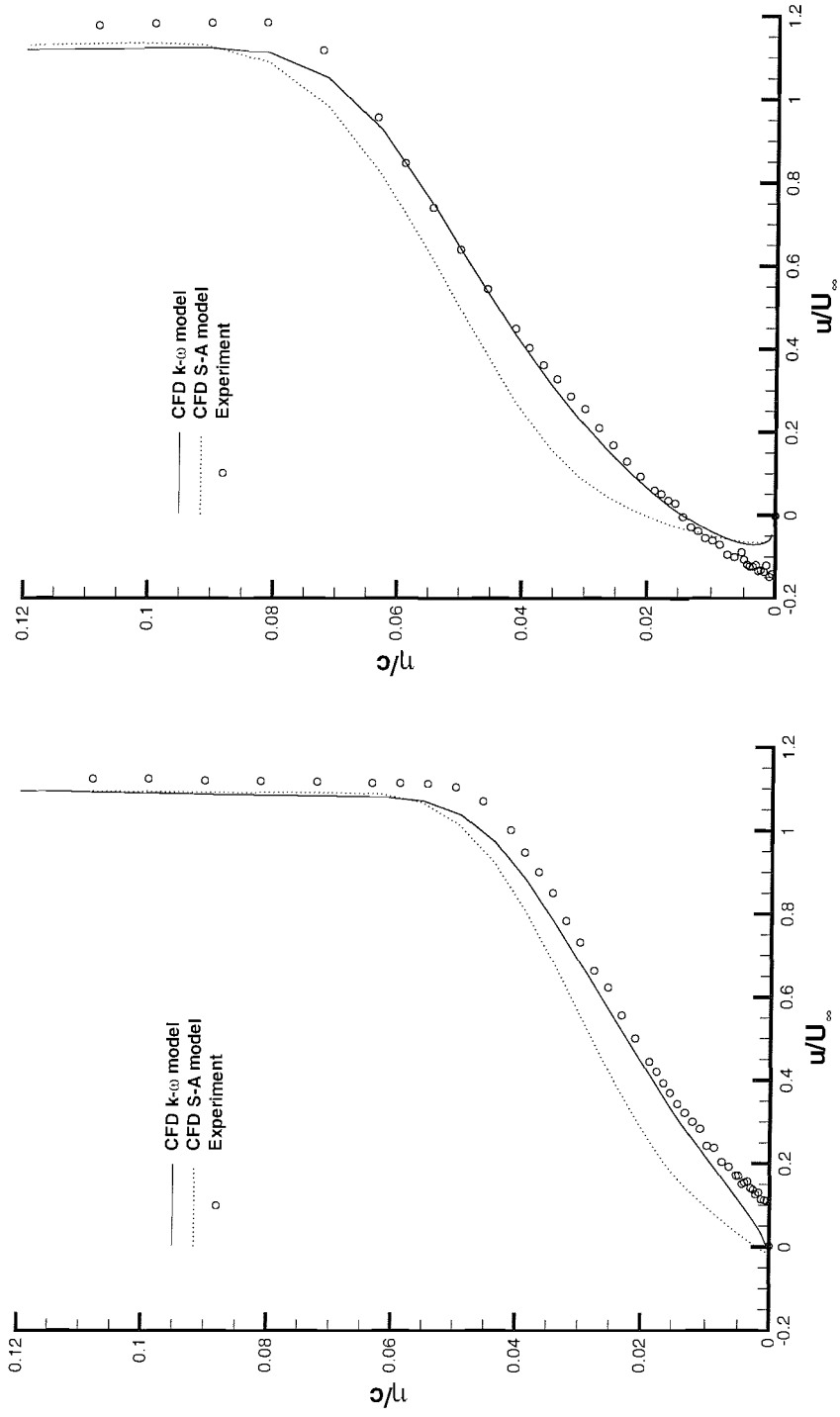

Figure 80: Comparison of computational and experimental boundary layer surveys at suction surface trailing edge; (a) $h/c = 0.224$. (b) $h/c = 0.134$.

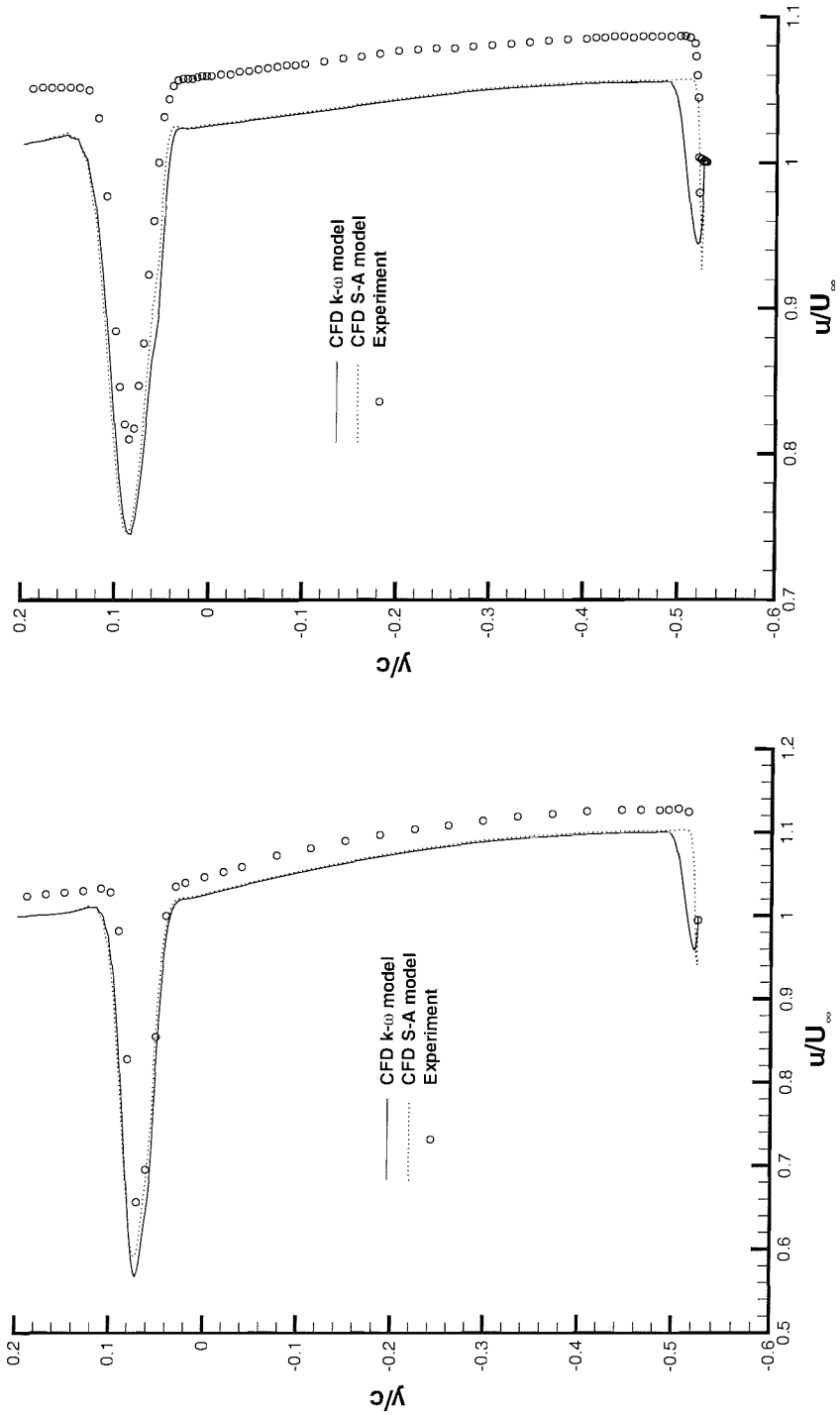

Figure 81: Comparison of computational and experimental wake surveys at $h/c = 0.448$; (a) $x/c = 1.2$. (b) $x/c = 1.5$.

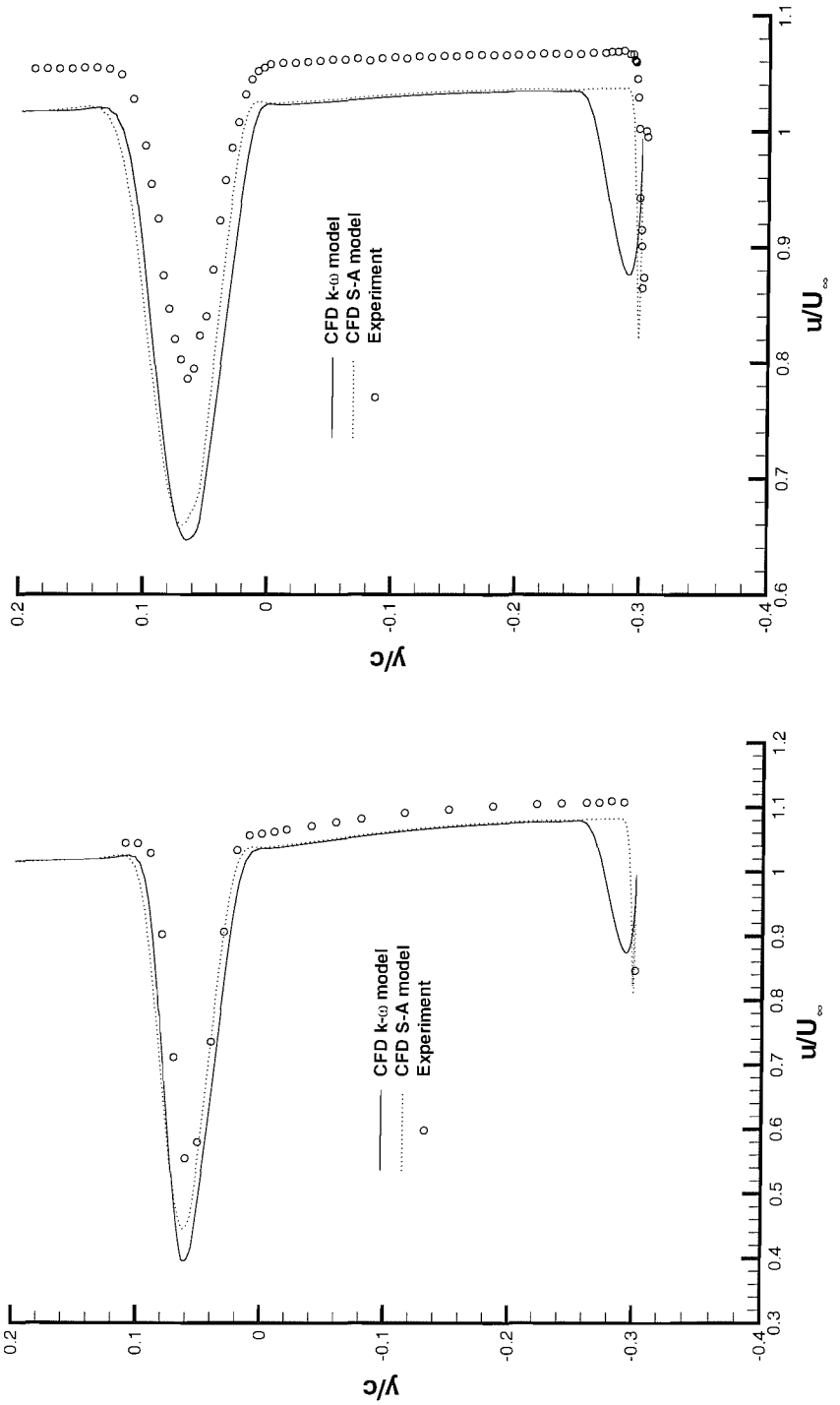

Figure 82: Comparison of computational and experimental wake surveys at $h/c = 0.224$; (a) $x/c = 1.2$. (b) $x/c = 1.5$.

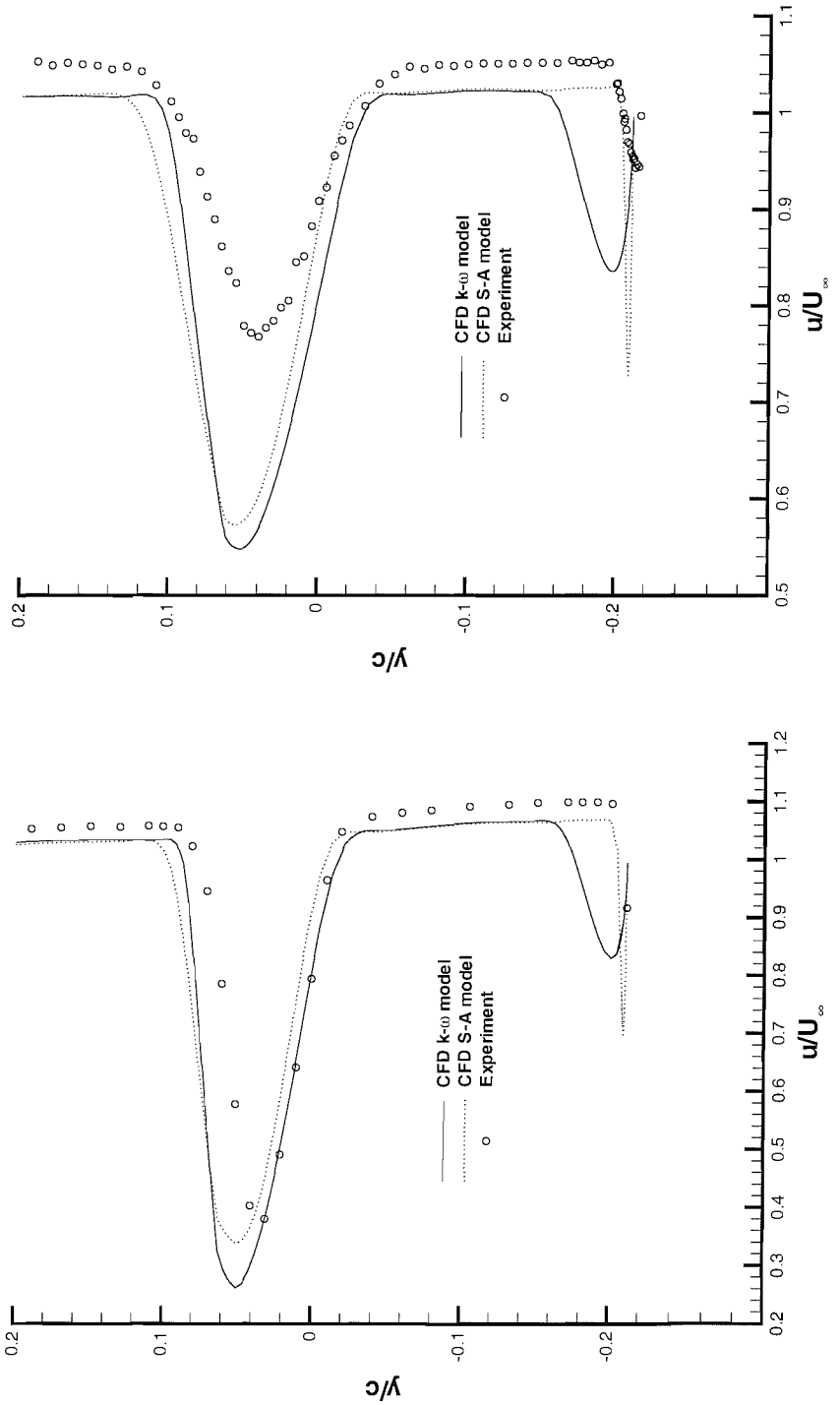

Figure 83: Comparison of computational and experimental wake surveys at $h/c = 0.134$; (a) $x/c = 1.2$. (b) $x/c = 1.5$.

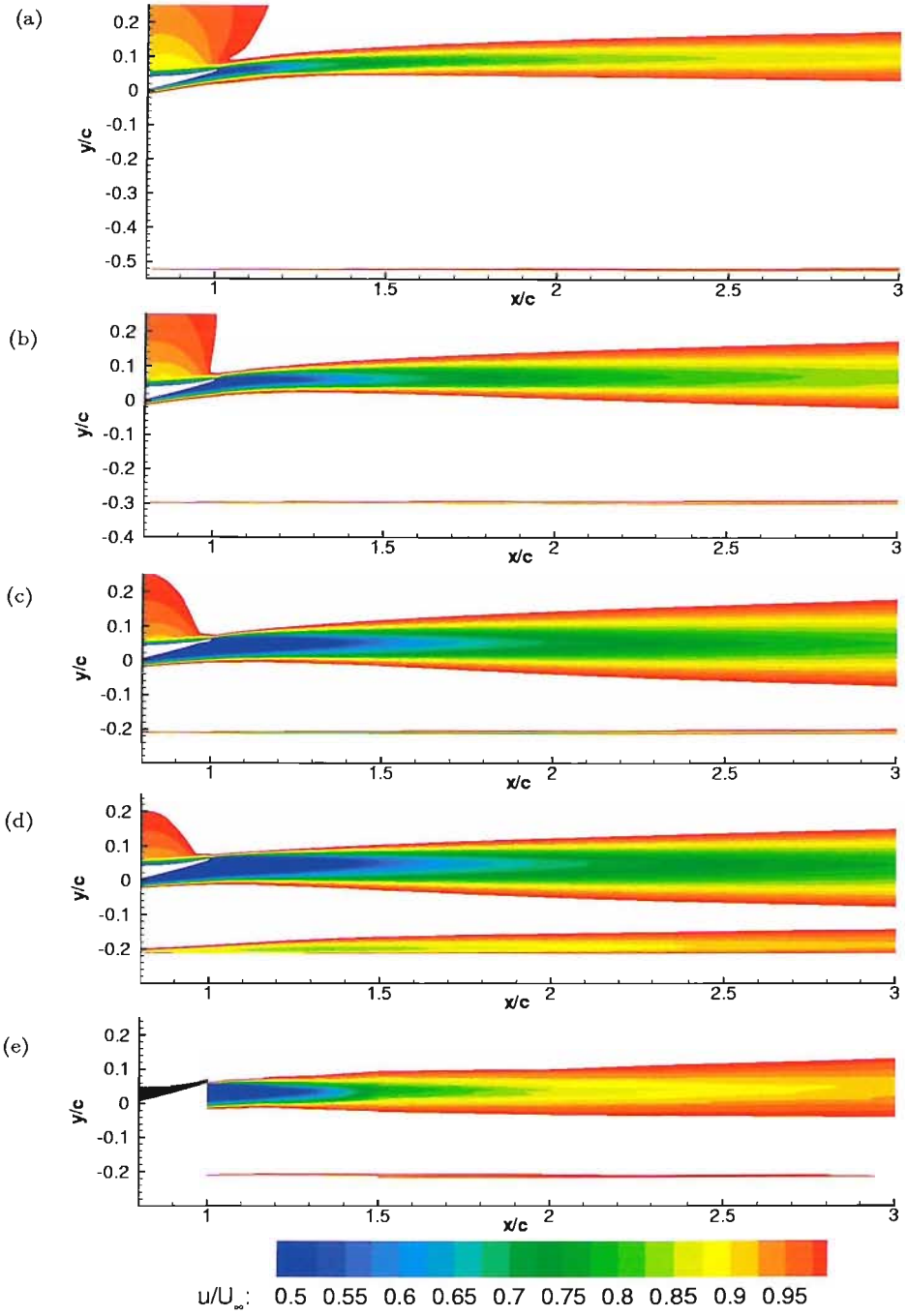

Figure 84: u/U_∞ velocity contours within wake and ground boundary layer; (a) $h/c = 0.448$, S-A. (b) $h/c = 0.224$, S-A. (c) $h/c = 0.134$, S-A. (d) $h/c = 0.134$, $k - \omega$. (e) $h/c = 0.134$ LDA results

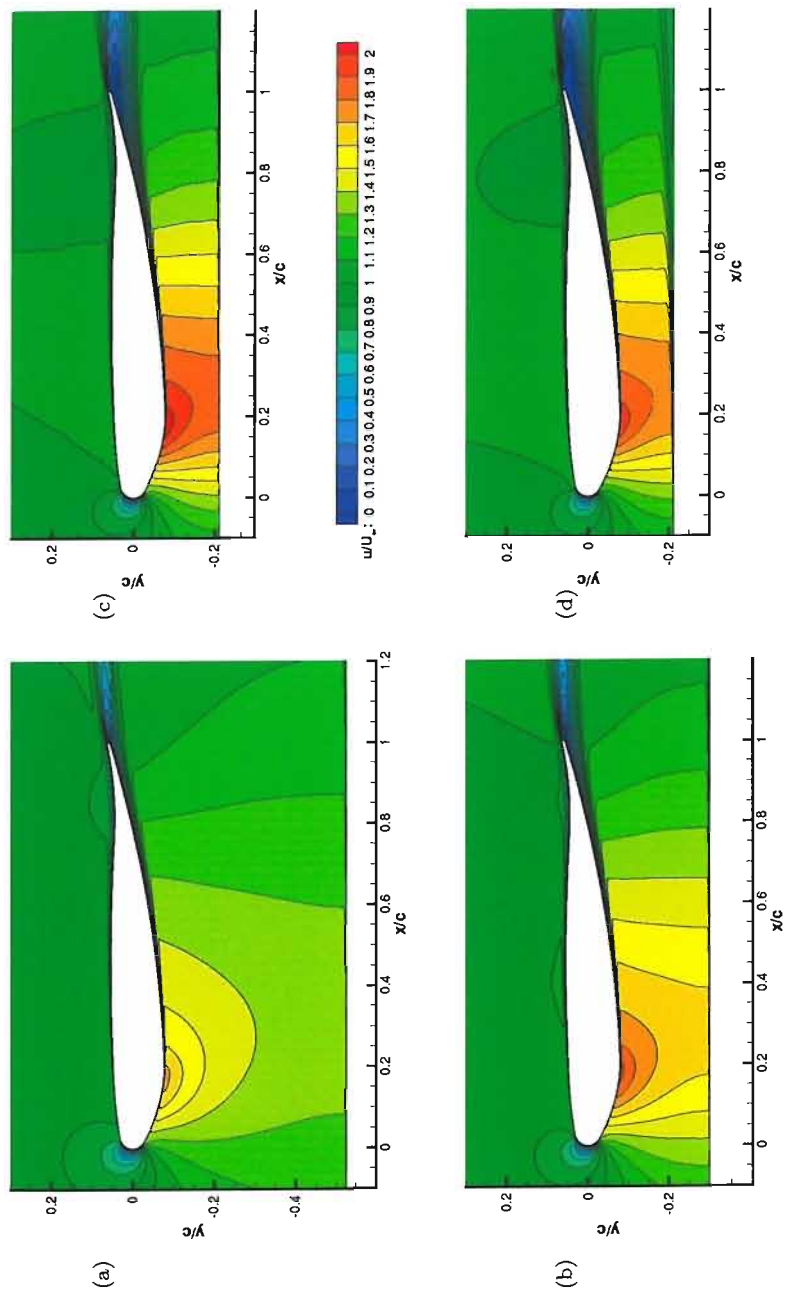

Figure 85: u/U_∞ velocity contours within wake and ground boundary layer; (a) $h/c = 0.448$, S-A. (b) $h/c = 0.224$, S-A. (c) $h/c = 0.134$, S-A. (d) $h/c = 0.134$, $k - \omega$.

	Block 1	Block 2	Block 3	Block 4	Block 5	Total
freestream	289×65	41×41		17×33		20544
$h/c = 0.448$	289×65	41×41	153×33	41×33	185×25	30592
$h/c = 0.313$	289×65	41×41	153×33	41×33	185×25	30592
$h/c = 0.224$	289×65	41×41	153×33	41×33	185×25	30592
$h/c = 0.179$	289×65	41×41	153×33	41×33	185×25	30592
$h/c = 0.134$	289×65	41×41	153×33	41×33	185×25	30592
$h/c = 0.090$	289×49	41×41	153×33	41×33	185×25	25984
$h/c = 0.067$	289×41	41×41	153×33	41×33	185×33	25152

Table 14: Grid dimensions and total number of cells

h/c	C_l expt	C_l S-A	C_l $k-\omega$	$\%C_{l_{S-A}} \vert C_{l_{expt}}$	$\%C_{l_{k-\omega}} \vert C_{l_{expt}}$
freestream	0.766	0.885	0.872	16	14
0.671	0.902	1.052	1.030	17	14
0.448	1.009	1.174	1.136	16	13
0.313	1.145	1.320	1.253	15	9
0.224	1.286	1.475	1.352	15	5
0.179	1.362	1.565	1.393	15	2
0.134	1.385	1.604	1.386	16	0
0.090	1.371	1.539	1.297	12	-5

Table 15: Computational and experimental C_l

h/c	expt/CFD	u_{min}/U_∞	y/c at u_{min}	y at δ_{top}	y at δ_{bottom}	δ_{99}/c
0.448	expt	0.81	0.08	0.13	0.04	0.09
	S-A	0.75	0.09	0.14	0.05	0.09
	$k-\omega$	0.75	0.08	0.14	0.04	0.10
0.313	expt	0.81	0.08	0.13	0.04	0.09
	S-A	0.71	0.08	0.13	0.03	0.10
	$k-\omega$	0.71	0.08	0.13	0.03	0.10
0.224	expt	0.79	0.07	0.13	0.01	0.11
	S-A	0.66	0.07	0.13	0.02	0.11
	$k-\omega$	0.65	0.06	0.13	0.01	0.12
0.179	expt	0.78	0.05	0.12	-0.02	0.14
	S-A	0.61	0.06	0.13	0.00	0.13
	$k-\omega$	0.59	0.06	0.12	-0.01	0.12
0.134	expt	0.77	0.04	0.12	-0.05	0.17
	S-A	0.57	0.05	0.13	-0.02	0.15
	$k-\omega$	0.55	0.05	0.11	-0.03	0.14
0.090	expt	0.72	0.02	0.12	-0.10	0.22
	S-A	0.51	0.03	0.13	-0.06	0.19
	$k-\omega$	0.47	0.03	0.10	-0.07	0.17

Table 16: Wake information including minimum velocity and 99% wake thickness for experimental and computational results at $x/c = 1.5$.

h/c	expt/CFD	u_{min}/U_∞	u_e/U_∞	δ_{99}/c
0.448	expt	0.98	1.09	0.006
	S-A	0.93	1.06	0.007
	$k-\omega$	0.94	1.06	0.028
0.313	expt	0.90	1.07	0.007
	S-A	0.88	1.05	0.008
	$k-\omega$	0.91	1.04	0.036
0.224	expt	0.86	1.07	0.009
	S-A	0.82	1.04	0.009
	$k-\omega$	0.88	1.04	0.044
0.179	expt	0.91	1.06	0.014
	S-A	0.78	1.03	0.009
	$k-\omega$	0.85	1.03	0.048
0.134	expt	0.94	1.05	0.019
	S-A	0.93	1.03	0.009
	$k-\omega$	0.84	1.02	0.054
0.090	expt	0.91	1.03	0.022
	S-A	0.68	1.02	0.010
	$k-\omega$	0.81	1.02	0.061

Table 17: Ground boundary layer information including minimum velocity, edge velocity, and 99% boundary layer thickness for experimental and computational results at $x/c = 1.5$.

Chapter 10

Further Discussions

10.1 Introduction

In this chapter, further discussions of the ground effect are presented. Reducing the height of a wing in ground effect is compared to increasing the incidence of a wing in freestream, and the effect of transition fixing is expanded.

10.2 Single Element, Transition Free

10.2.1 Freestream

Chapter 3 presents the aerodynamic performance results for the single element wing in freestream, for free transition. A linear region exists in the liftcurve, for fully attached flow, a fundamental result for a single element wing in freestream. Similarly, the manner in which a greater lift is produced at a higher incidence is conventional. Figure 5a shows that as the incidence is increased until $\alpha = 9°$, more loading is generated by both surfaces. On the suction surface, most of the increment is obtained from the leading edge to $x/c \approx 0.2$. This then decreases throughout the pressure recovery, and is insignificant by $x/c \approx 0.8$. The existence of the leading edge suction spike also becomes apparent at the higher incidences. On the pressure surface, similar general trends are observed; the maximum increment in loading comes near to the leading edge, and reduces steadily along the chord of the wing. As the incidence is increased of a generic wing in freestream, the local curvature and the deflection caused to the flow result in changes to the pressure distribution as discussed. At an incidence of $\alpha = 13°$, a sudden loss in loading is encountered over the suction surface, as the boundary layer separates due to the high adverse pressure gradient. Highly three-dimensional flow was observed as the wing stalls. At $\alpha = 9°$, a broadly constant region of two-dimensional flow exists over the central half of the wing. However, at $\alpha = 13°$, when the boundary layer separates, a sharp loss of loading occurs from $\eta \approx 0.6$. Oil flow visualisation

(not presented here due to the poor quality of the recorded results) shows that at this incidence, separated flow occurs in a large bubble confined to the central portion of the wing, which moves forwards rapidly and outwards a little as the incidence is increased. Similar flow patterns were observed as in reference [97]. For the three-dimensional wing, this results in a liftcurve with a linear region for fully attached flow, a plateau after a small peak when separation occurs and is moving forwards, and a sudden drop when the boundary layer separates from the entire suction surface.

10.2.2 Ground Effect

In ground effect, different features were observed. The downforce generated reaches a maximum at a small height, and then stalls (Figure 7a). Maximum downforce in ground effect is $C_L = 1.72$, significantly greater than that measured in freestream of $C_L = 1.35$. The surface pressures at the wing centre, Figure 8 shows that as the ground height is reduced, the main effect is to increase loading over the entire suction surface. At very small heights, a little loading is lost near to the leading edge and the trailing edge on the suction surface. On the pressure surface, small reductions in loading are observed as the height is reduced.

10.2.3 Comparisons

Comparisons of the surface pressures at the centre of the wing, for increasing incidence in freestream, and reducing height in ground effect are given in Figure 86a. The main difference in the characteristics of the flow can be seen on the suction surface. Whereas in freestream, greater suctions are generally found near to the leading edge, it is the portion of the wing closest to the ground, i.e. $x/c \approx 0.1 - 0.4$ that experiences the greatest increments in loading in ground effect. In addition to this, the magnitude of the suction is significantly more in ground effect than in freestream. At a high incidence in freestream ($\alpha = 9°$), the localised suction spike at the leading edge has a maximum suction approaching $C_P = -4$. Apart from this, a suction of $C_P = -2.5$ is obtained until $x/c \approx 0.15$. At a small height in ground effect ($h/c = 0.067$), a suction peak greater than $C_P = -4.5$ occurs, and although this falls throughout the pressure recovery, a suction of $C_P = -2.5$ is still obtained at $x/c = 0.4$.

For the wing in freestream, boundary layer separation from the suction surface trailing edge results in a rapid loss in loading, as the separation point moves forwards rapidly. Figure 86b shows integrated pressures at the wing centre, together with the overall forces, in freestream. There is a sudden decrease in C_l at the wing centre above $\alpha = 11°$, when the boundary layer separates. As discussed previously, loading is first lost at the centre of the wing, and the overall effect is for a plateau in the three-dimensional forces. In ground effect, very small amounts of separated flow were first observed at $h/c = 0.224$. As the height is reduced, the separation point moves forwards steadily. There is no sudden decrease in downforce, either sectional at the centre or overall, when

separation occurs.

In ground effect, because of the accelerated flowfield due to the ground, regions of flow separation can be sustained. For a wing at a high incidence in freestream, as the boundary layer starts to separate at the trailing edge, this results in an instability as the separation point moves forwards. It is the direct effect of the ground constraining the flow, that drives the flow around the suction surface, preventing the separated flow from suddenly moving forwards. In general for an aeronautical configuration, flow separation is generally the limiting factor. But, for a wing with the suction surface nearest to a moving ground, the separation of the boundary layer is not the sole factor governing the maximum downforce that can be attained.

10.3 Transition Fixing

Results presented in Figures 20a & 21a show the effect of fixing transition on the forces achieved in freestream and in ground effect. As described in Chapter 6, significant differences were found when different grit sizes were used, for the configuration in ground effect. From the figures, it can be seen that in ground effect the downforce is reduced for the transition fixed case more significantly than in freestream. In freestream, the boundary layer separates at a lower incidence. The stall reduces suddenly from $\alpha = 11°$ to $9°$, directly due to the boundary layer separating at a lower incidence. In ground effect, the boundary layer separates at a greater height. This results in lower loadings relative to the transition free condition, for the large range of heights close to the ground at which flow has separated, but at which the downforce still increases for a reduction in height.

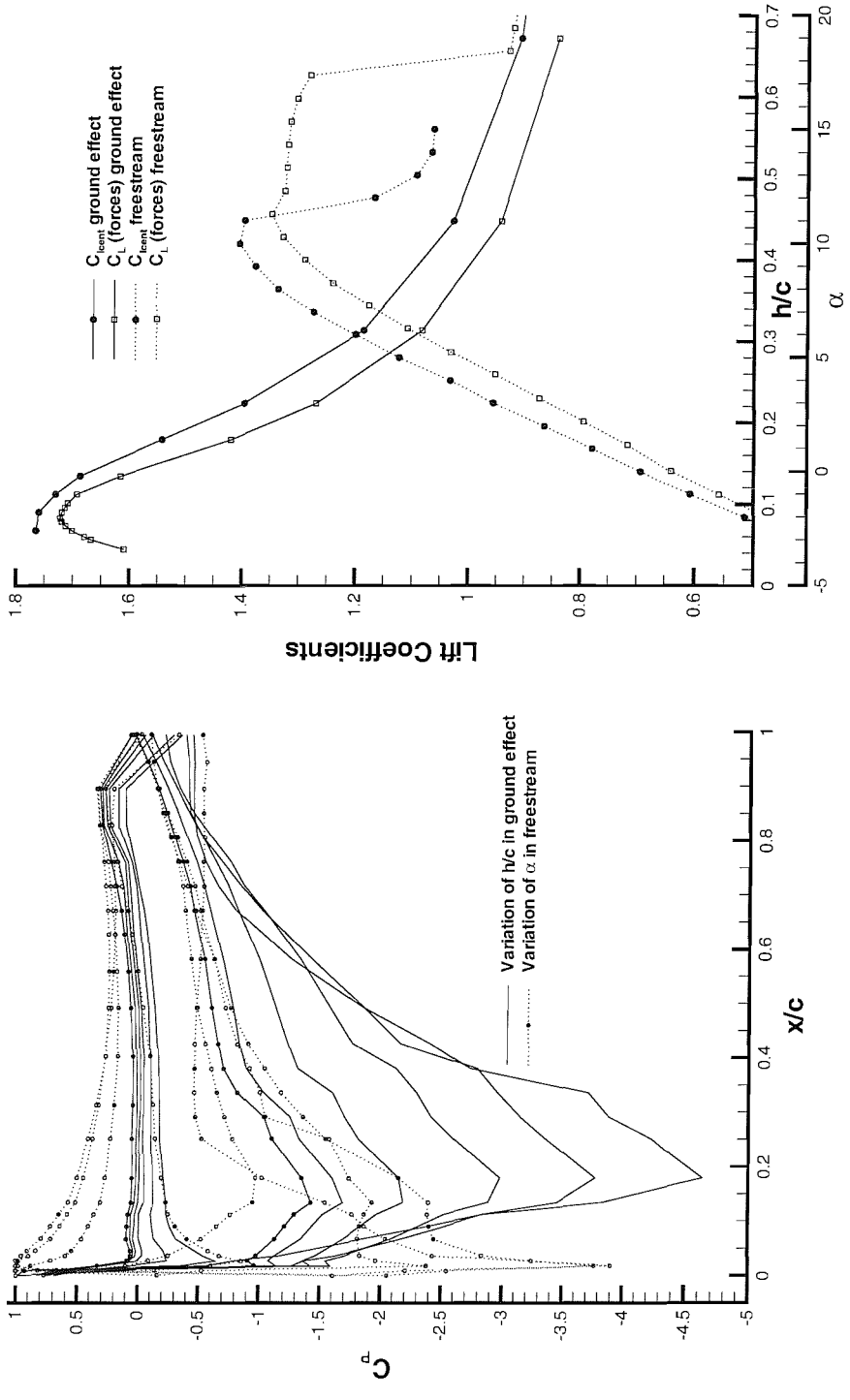

Figure 86: (a) Pressure distributions (b) Integrated pressures and overall forces, in freestream and ground effect, for single element wing, transition free.

Chapter 11

Conclusions and Recommendations for Future Work

11.1 Conclusions

The ground effect has been investigated experimentally and computationally for a variety of configurations. For a single element wing, it was found from experiments that:

- Downforce increases asymptotically as the height is reduced, for large and medium heights. Then the gradient reduces, and a maximum downforce is obtained. The downforce then falls sharply below this height.
- The effect of reducing the ground height on the pressure distribution is generally to increase the loading over the entire suction surface. A small loss in loading over the pressure surface is seen.
- In close proximity to the ground, small losses in loading were found near to the suction surface leading edge and trailing edge. The maximum downforce is at a height where a reduction in height causes balances in the reduction in loading in these regions and over the pressure surface, and an increase in loading over the portion of the wing closest to the ground.
- Maximum downforce in ground effect is greater than in freestream. The ground effect causes greater suctions to be sustained than in freestream. The downforce generated also increases for some heights in ground effect, even though separation exists.
- Transition fixing is more significant in terms of reduction in downforce for the configuration in ground effect than in freestream.

- LDA measurements at the centre of the wing show that the thickness of the wake increases as the height is reduced. This is attributed to the portion from the suction surface increasing thickness as the adverse pressure gradient increases.
- PIV results on the transition fixed configuration show the existence of vortex shedding from the finite trailing edge of the wing. The shedding is relatively irregular, and becomes more chaotic as the height is reduced.

An investigation into the application of Gurney flaps on a wing in ground effect shows that:

- Gurney flaps are more effective in ground effect than in freestream, in terms of the downforce produced. This is due to a coupling of the ground effect and the increase in suction at the lower surface trailing edge, and the force enhancement of the Gurney.
- From PIV results, the instantaneous flow behind a Gurney flap consists of discrete alternately shedding vortices. The shedding becomes more irregular as the height is reduced, with the appearance of separated flow.

For the double element wing, experiments yielded the results that:

- Although the downforce increases as the height is reduced until the maximum is obtained, a discontinuity exists in the curve which is either a plateau, as found for the low flap angle, or a reduction in downforce, as for the high flap angle.
- The maximum overall downforce is attributed to gains in loading over most of the suction surface, and losses over the pressure surface, for the low flap angle configuration, or for separation over the flap, for the high angle configuration.
- The main element features highly three-dimensional flow. The vortex that forms at the tip of the main element induces a high suction as it flows over the tip of the flap.
- The discontinuity in the downforce level is due to the breakdown of the tip vortex, and the associated loss in suction near to the tip of the flap.

Computational studies on a two-dimensional section at the centre of the single element wing using a RANS solver produced good qualitative results in terms of aerodynamic performance, and wake flow.

11.2 Recommendations for Future Work

11.2.1 Computational Modelling

As the research progressed, a greater priority was placed on obtaining experimental results of more configurations (e.g. the double element study) than extending the computational work. The direct

continuation of the current research would involve performing computational studies on a three-dimensional model, and then investigating other configurations such as that with the Gurney flap, for which unsteady flow features are of interest, or the double element wing.

11.2.2 Aeronautical Field

Experimentally, the range of results acquired details fully the general aerodynamics of generic wings in ground effect. The results feature a wide range of flow physics, such as multi-element flows, three-dimensional vortical flows including vortex breakdown, and bluff body flows including vortex shedding, that the study should be of interest to the general aeronautical field. The research serves as a stand alone database for computational validation of fundamental multi-element wing flows with challenging fluid mechanics, and also for ground effect configurations.

11.2.3 Practical Applications

Current Front Wing Configurations

The aerodynamics of modern racing cars involves complicated interactions between the constituent elements of the car, such that an optimised car will have no individual element working in its best individual configuration. The front wing is critical as the wake that it generates effects the rest of the car. The downstream devices are therefore *tuned* for the front wing configuration, to create the best entire car. As an example, on the current industrial partner's car, it is possible to generate more downforce from the front wing, however this destroys the flow over the remainder of the car. In terms of practical applications, it is therefore important to investigate the flow features at the height ranges used on contemporary vehicles. This may not include the heights extremely close to the ground where the greatest downforce is obtained, which may, conversely be of a more fundamental interest.

At the time of the start of the research, late 1997, the main element of the front wing on the partners car featured a constant profile along the entire span. The flap used a large chord over the outboard section, a smaller chord over the central section (the latter used for the current research), which were joined by a small spanwise length of reducing chord section. Contemporary year 2001 cars feature main elements that are significantly lower at the centre than at the tips (to overcome a loophole in the regulations), but which also may feature a variable height and twist along the span of the wing. Complex endplates are now used, with fences and diveplanes. For a fundamental study, future work will need to model either a simple configuration, as in the current study, or a more modern configuration for greater practical interest. If it is chosen to continue with the current type of configuration, the wing profile should be modified to eliminate the discontinuity in curvature near to the leading edge of the main element.

Frequently, strakes are added to the wing. These comprise of a single vertical fence, attached to the suction surface of both elements, near to the tip of the wing. The effect of these on the

tip vortex should be identified. In addition to the elements of the wing assembly, items in close proximity to the wing could be added to identify their effect on the flow features. The wheels generate a large disturbance to the flow, and their effect on the structure of the tip vortex should be identified, with particular reference to their breakdown. The effect of the nose on the wake flow near to the wing centre and on the subsequent performance could be modelled with moderate ease.

Although the effect of Gurney flaps was investigated for the single element configuration, this ignored any three-dimensional effects. Gurney flaps are frequently used on the flap of the front wing, generally at the tips. The interaction of the fluid flow from the Gurney with the tip vortex needs to be examined, as this may alter the characteristics of the breakdown.

Testing Methodology

In order to change the height of the model at which to obtain results, the wind tunnel was stopped, and adjustments made to the length of the telescopic struts. Hence, any hysteresis as the height is varied cannot be modelled. The first modification to this area of testing must be to implement a motorised system, which are commercially available in a form similar to that required, to change the height of the model during the run. As an extension to this, the effect of a dynamic change in height, for example a step response, or an oscillatory motion could be added, to simulate a bump, or suspension movements.

A contemporary problem for racing cars is the difficulty to overtake when following a car closely. It is believed that the turbulence that a leading car generates reduces the ability of the following car to produce downforce, particularly the front wing. This could be simulated easily in a wind tunnel using increased levels of freestream turbulence, for example with extra turbulence grids.

The effect of yaw and roll should be included, and steer of the wheels if present, to further enhance the simulation of a racing car front wing.

Further Developments

Once further tests have been performed, of an investigatory nature, it may be possible to implement flow control devices to enhance the performance of the wing. This may range, for example, from simple devices (holes in endplates or solid vortex generators), to more complex items such as airjet vortex generators and porous surfaces.

Alternatively, the wing profile could be varied to control the flow, for example using a computational based design tool, such as an optimiser or an inverse design program. A three-element wing could also be investigated, computationally, or experimentally.

Bibliography

[1] Agathangelou, B. and Gascoyne, M. Aerodynamic considerations of a Formula 1 racing car, 1998. SAE Publication 980399.

[2] Jeffrey, D. and Alperin, M. Aspects of the Aerodynamics of Year 2000 Formula One Racing Cars. 3rd Mira International Vehicle Aerodynamics Conference, 18–19 October 2000, Rugby.

[3] Knowles, K., Donahue, D.T. and Finnis, M.V. A study of wings in ground effect, 1994. Loughborough University Conference on Vehicle Aerodynamics, pp.22.1-22.13.

[4] Ranzenbach, R. and Barlow, J.B. Two-dimensional airfoil in ground effect, an experimental and computational study, 1994. SAE Publication 942509.

[5] Ranzenbach, R. and Barlow, J.B. Cambered airfoil in ground effect - an experimental and computational study, 1996. SAE Publication 960909.

[6] Ranzenbach, R., Barlow, J.B. and Diaz, R.H. Multi-element airfoil in ground effect - an experimental and computational study, 1997. AIAA Paper 97–2238.

[7] Jasinski, W.J. and Selig, M.S. Experimental study of open-wheel race-car front wings, 1998. SAE Publication 983042.

[8] Ranzenbach, R. and Barlow, J.B. Cambered airfoil in ground effect - wind tunnel and road conditions, 1995. AIAA Paper 95–1909.

[9] Zahm, A.F. and Bear, R.M. Ground-plane influence on airplane wings. *Journal of the Franklin Institute*, pages 687–693, May 1921.

[10] Recant, I.G. Wind-tunnel investigation of ground effect on wings with flaps. Technical Report NASA-TN-705, NACA, May 1939.

[11] Kirkpatrick, D.L.I. Experimental investigation of the ground effect on the subsonic longitudinal characteristics of a delta wing of aspect ratio 1.616. Technical Report 66179, Royal Aircraft Establishment, June 1966.

[12] East, L.F. The measurement of ground effect using a fixed ground board in a wind tunnel. Technical Report 70123, Royal Aircraft Establishment, July 1970.

[13] Barlow, J.B., Rae, W.H. and Pope, A. Low-Speed Wind Tunnel Testing, 1999.

[14] Tani, I., Taima, M. and Simidu, S. The effect of ground on the aerodynamic characteristics of a monoplane wing. *Aeronautical Research Institute, Tokyo Imperial University*, 156(13):23–76, September 1937.

[15] Tani, I., Itokawa, H. and Taima, M. Further studies of the ground effect on the aerodynamic characteristics of an aeroplane, with special reference to tail moment. *Aeronautical Research Institute, Tokyo Imperial University*, 158(13):117–145, November 1937.

[16] Serebrinsky, Y.M. and Biachuev, S.A. Wind-tunnel investigation of the horizontal motion of a wing near the ground. Technical Report NASA-TM-1095, NACA, September 1946.

[17] Fink, M.P. and Lastinger, J.L. Aerodynamic characteristics of low-aspect-ratio wings close to the ground. Technical Report NASA-TN-D-926, NASA, July 1961.

[18] Klemin, A. A belt method of representing the ground. *Journal of the Aeronautical Sciences*, 1:198–199, 1934.

[19] Burgin, K., Adey, P.C. and Beatham, J.P. Wind tunnel tests on road vehicle models using a moving belt simulation of ground effect. *Journal of Wind Engineering and Industrial Aerodynamics*, 22:227–236, 1986.

[20] Garry, K.P. Some effects of ground clearance and ground plane boundary layer thickness on the mean base pressure of a bluff vehicle type body. *Journal of Wind Engineering and Industrial Aerodynamics*, 62:1–10, 1996.

[21] Kim, M.S. and Geropp, D. Experimental investigation of the ground effect on the flow around some two-dimensional bluff bodies with moving-belt technique. *Journal of Wind Engineering and Industrial Aerodynamics*, 74-76:511–519, 1998.

[22] Werlè, H. Simulation de l'effet de sol au tunnel hydrodynamique. *La Recherche Aèrospatiale*, (95):7–15, July-August 1963.

[23] Werlè, H. Le tunnel hydrodynamique au service de l'industrie. *Sciences et techniques*, (17):35–42, 1969.

[24] Raymond, A.E. Ground influence on aerofoils. Technical Report NACA-TN-67, NACA, December 1921.

[25] Weiselsberger, C. Wing resistance near the ground. Technical Report NACA-TM-77, NACA, 1922.

[26] Steinbach, D. and Jacob, K. Aerodynamic aspects of wings near ground. *Transactions of the Japan Society for Aeronautical and Space Sciences*, 34(104):56–70, August 1991.

[27] Saunders, G.H., F/O. Aerodynamic characteristics of wings in ground proximity. *Canadian Aeronautics and Space Journal*, 11(16):185–192, June 1965.

[28] Coulliette, C. and Plotkin, A. Aerofoil ground effect revisited. *Aeronautical Journal*, pages 65–74, February 1996.

[29] Hsiun, C. and Chen, C. Improved procedure for the inverse design of two-dimensional airfoils in ground effect. *Journal of Aircraft*, 6(33):1094–1100, November–December 1996.

[30] Nuhait, A.O. and Mook, D.T. Numerical Simulation of wings in steady and unsteady ground effects. *Journal of Aircraft*, 12(26):1081–1089, December 1989.

[31] Hsiun, C. and Chen, C. Aerodynamic characteristics of a two-dimensional airfoil with ground effect. *Journal of Aircraft*, 2(33):386–392, March–April 1996.

[32] Steinbach, D. Comments on "Aerodynamic Characteristics of a two-dimensional airfoil with ground effect". *Journal of Aircraft*, 34(3):455–456, May–June 1997.

[33] Barber, T.J., Leonardi, E. and Archer, R.D. A Technical Note on the appropriate CFD boundary conditions for the prediction of ground effect aerodynamics. *The Aeronautical Journal*, pages 545–547, November 1999.

[34] Im, Y. and Chang, K. Unsteady aerodynamics of a WIG airfoil flying over a wavy wall, 2000. AIAA Paper 2000–0657.

[35] Dominy, R.G. Aerodynamics of Grand Prix cars. *Proceedings of the Institution of Mechanical Engineers, Part D: Journal of Automobile Engineering*, 206:267–274, 1992.

[36] Katz, J. Aerodynamic model for wing-generated down force on open-wheel-racing-car configurations, 1986. SAE Publication 860218.

[37] Katz, J., Luo, H., Mestreau, E., Baum, J. and Lōhner, R. Viscous-flow simulation of an open-wheel race car, 1998. SAE Publication 983041.

[38] Katz, J. Calculation of the aerodynamic forces on automotive lifting surfaces. *Transactions of the ASME: Journal of Fluids Engineering*, 107:438–443, December 1985.

[39] Katz, J. Considerations pertinent to race-car wing design, 1994. Loughborough University Conference on Vehicle Aerodynamics, pp.23.1-23.7.

[40] Katz, J. High-lift wing design for race-car applications, 1995. SAE Publication 951976.

[41] Pailhas, G., Sauvage, P., Touvet, Y. and Coustols, E. Flowfield in the vicinity of a thick cambered trailing edge, July 13-16 1998. 9th International Symposium on Applications of Laser Techniques to Fluid Mechanics, Lisbon, Portugal.

[42] Vassilopoulos, K. and Gai, S. Unsteady pressures on a blunt trailing edge - end plate and boundary layer effects, 1998. AIAA Paper 98–0418.

[43] Khorrami, M., Berkman, M., Choudhari, M., Singer, B., Lokhard, D. and Brentner, K. Unsteady flow computations of a slat with a blunt trailing edge, 1999. AIAA Paper 99–1805.

[44] Allison, D.O. and Sewall, W.G. Airfoils modifications effects on subsonic and transonic pressure distributions and performance for the EA-6B airplane. Technical Report NASA-TP-3516, NASA, May 1995.

[45] Koss, D., Bauminger, S., Shepshelovich, M., Seifert, A. and Wygnanski, I. Pilot test of a low Reynolds number DTE airfoil, 1993. AIAA Paper 93–0643.

[46] Liebeck, R.H. Design of subsonic airfoils for high lift. *Journal of Aircraft*, 15(9):547–561, September 1978.

[47] Giguère, P., Lemay, J. and Dumas, G. Gurney flap effects and scaling for low-speed airfoils, 1995. AIAA Paper 95–1881.

[48] Myose, R., Papadakis, M. and Heron, I. Gurney flap experiments on airfoils, wings and reflection plane model. *Journal of Aircraft*, 35(2):206–211, March–April 1998.

[49] Jeffrey, D. *An investigation into the aerodynamics of Gurney flaps.* PhD thesis, University of Southampton, Southampton, U.K., July 1998.

[50] Jeffrey, D., Zhang, X. and Hurst, D. Aerodynamics of Gurney flaps on a single-element high-lift wing. *Journal of Aircraft*, 37(2):295–302, March–April 2000.

[51] Katz, J., Largman, R. Effect of 90 degree flap on the aerodynamics of a two-element airfoil. *Journal Fluids Engineering*, 111:93–94, March 1989.

[52] Olson, L.E. and Orloff, K.L. On the structure of turbulent wakes and merging shear layers of multi-element airfoils, 1998. AIAA Paper 81–1248.

[53] Adair, D. and Clifton, H.W. Turbulent separated flow in the vicinity of a single-slotted airfoil flap, 1988. AIAA Paper 88–0613.

[54] Nakayama, A., Kreplin, H.-P. and Morgan, H.L. Experimental Investigation of flowfield about a multielement airfoil. *AIAA Journal*, 28(1):14–21, January 1990.

[55] Biber, K. and Zumwalt, G.W. Flowfield measurements of a two-element airfoil with large separation. *AIAA Journal*, 31(3):459–464, March 1993.

[56] Nelson, T.E., Zingg, D.W. and Johnston, G.W. Compressible Navier-Stokes computations of multielement airfoil flows using multiblock grids. *AIAA Journal*, 32(3):506–511, March 1994.

[57] Rogers, S.E. Progress in high-lift aerodynamic calculations. *Journal of Aircraft*, 31(6):1244–1251, November–December 1994.

[58] Anderson, W.K., Bonhaus, D.L., McGhee, R.J. and Walker, B. Navier-Stokes computations and experimental comparisons for multielement airfoil configurations. *Journal of Aircraft*, 32(6):1246–1253, November–December 1995.

[59] Valarezo, W.O. and Mavriplis, D.J. Navier-Stokes applications to high-lift airfoil analysis. *Journal of Aircraft*, 32(3):618–624, May–June 1995.

[60] Liebeck, A.M.O. High-lift aerodynamics. *Journal of Aircraft*, 12(6):501–530, June 1975.

[61] Wentz, W.H. and Seetharam, H.C. Development of a Fowler flap system for a high performance general aviation aerofoil. Technical Report NASA-CR-2443, NASA, 1974.

[62] Woodward, D.S. and Lean, D.E. Where is high lift today? — A review of past UK research programmes, September 1993. AGARD Conference Paper CP-575.

[63] Lin, J.C. and Dominik, C.J. Parametric investigation of a high-lift airfoil at high Reynolds numbers. *Journal of Aircraft*, 34(4):485–491, July–August 1997.

[64] Brune, G.W. and Sikavi, D.A. Experimental investigation of the confluent boundary layer of a low speed aerofoil, 1983. AIAA Paper 83–0566.

[65] Squire, L.C. Interactions between wakes and boundary-layers. *Progress in Aerospace Science*, 26:261–288, 1989.

[66] Yeung, C.P. and Squire, L.C. A study of the three-dimensional interaction of wakes and boundary layers. *Aeronautical Journal*, pages 343–351, October 1995.

[67] Seetharam, H.C. and Wentz, W.H. A low speed two-dimensional study of flow separation on the GA(W)-1 aerofoil with 30 % chord Fowler Flap. Technical Report NASA-CR-2844, NASA, 1977.

[68] Baker, G.R., Barker, S.J., Bofha, K.K. and Saffman, P.G. Laser anemometer measurements of trailing vortices in water. *Journal of Fluid Mechanics*, 65(2):325–336, 1974.

[69] Green, S.I. and Acosta, A.J. Unsteady flow in trailing vortices. *Journal of Fluid Mechanics*, 227:107–134, 1991.

[70] Devenport, W.J., Rife, M.C., Liapis, S.I. and Follin, G.J. The structure and development of a wing-tip vortex. *Journal of Fluid Mechanics*, 312:67–106, 1996.

[71] Ramaprian, B.R. and Zhang, Y. Measurements in rollup region of the tip vortex from a rectangular wing. *AIAA Journal*, 35(12):1837–1843, December 1997.

[72] Khorrami, M.R., Singer, B.A. and Radeztsky, R.H. Jr. Reynolds-Averaged Navier-Stokes computations of a flap-side-edge flowfield. *AIAA Journal*, 37(1):14–22, January 1999.

[73] Snyder, D.O. and Spall, R.E. Numerical investigation into multiple vortex structures formed over flat end-cap wings. *AIAA Journal*, 38(8):1486–1489, August 2000.

[74] Payne, F.M, Ng, T.T., Nelson, R.C. and Schiff, L.B. Visualisation and wake surveys of vortical flow over a delta wing. *AIAA Journal*, 26(2):137–143, February 1988.

[75] Delery, J.M. Aspects of vortex breakdown. *Progress in Aerospace Science*, 30:1–59, 1994.

[76] Gursul, I. and Xie, W. Origin of vortex wandering over delta wings. *Journal of Aircraft*, 37(2):348–350, March–April 2000.

[77] Harvey, J.K. and Perry, F.J. Flowfield produced by trailing vortices in the vicinity of the ground. *AIAA Journal*, 9(8):1659–1660, August 1971.

[78] Storms, B.L., Takahashi, T.T. and Ross, J.C. Aerodynamic influence of a finite-span flap on a simple wing, 1995. SAE Publication 951977.

[79] Radeztsky, R.H. Jr., Singer, B.A. and Khorrami, M.R. Detailed measurements of a flap side-edge flow field, 1998. AIAA Paper 98–0700.

[80] Takallu, M.A. and Laflin, K.R. Reynolds-averaged Navier-Stokes of two partial-span flap wing experiments, 1998. AIAA Paper 98–0701.

[81] Mathias, D.L., Roth, K.R., Ross, J.C., Rogers, S.E. and Cummings, R.M. Navier-Stokes analysis of the flow about a flap edge. *Journal of Aircraft*, 35(6):833–838, November–December 1998.

[82] Krist, S.L., Biedron, R.T. and Rumsey, C.L. *CFL3D user's manual version 5.0.* NASA Langley Research Center, November 1996.

[83] Carr, G.W. and Atkin, P.D. Influence of moving-belt dimensions on vehicle aerodynamic forces, April 14-16 1997. Wind tunnels and wind tunnel test techniques, Royal Aeronautical Society, Cambridge, U.K.

[84] Wood, B. Notes on aerodynamic development of Tyrrell 026 front wing, 1999. Personal Communication, formerly at Tyrrell Racing Organisation.

[85] Baldwin, G. 11×8 wind tunnel boundary layer test results 14th March 1999 and 7×5 wind tunnel boundary layer tests 16 July 1996. Internal report, Southampton University Wind Tunnels.

[86] Yeung, A.F. and Lee, B.H. Particle image velocimetry study of wing-tip vortices. *Journal of Aircraft*, 36(2):482–484, March–April 1999.

[87] Dantec Measurement Technology. *FlowManager user manual version 3.11.*

[88] Braslow, A.L. and Knox, E.C. Simplified method for determination of critical height of distributed roughness particles for boundary-layer transition at Mach numbers from 0 to 5. Technical Report NACA-TN-4363, NACA, September 1958.

[89] Katz, J. Aerodynamics of high-lift low aspesct-ratio unswept wings. *AIAA Journal*, 27(8):1123–1124, August 1989.

[90] Thomas, J., Krist, S. and Anderson, W. Navier-Stokes computations of vortical flows over low-aspect-ratio wings. *AIAA Journal*, 28(2):205–212, February 1990.

[91] Spalart, P. and Allmaras, S. A one-equation turbulence model for aerodynamic flows, 1992. AIAA Paper 92–0439.

[92] Menter, F. Zonal two equation $k-\omega$ turbulence models for aerodynamic flows, 1993. AIAA Paper 93–2906.

[93] Rumsey, C.L. and Vatsa, V.N. Comparison of the predictive capabilities of several turbulence models. *Journal of Aircraft*, 32(3):510–514, May–June 1995.

[94] Godin, P., Zingg, D.W. and Nelson, T.E. Highlift aerodynamic computations with one- and two-equation turbulence models. *AIAA Journal*, 35(2):237–243, February 1997.

[95] Pointwise, Inc. *Gridgen user manual version 13.*

[96] Milholen, W.E. II, Chokani, N. and Al-Saadi, J. Performance of three-dimensional compressible Navier-Stokes codes at low Mach numbers. *AIAA Journal*, 34(7):1356–1362, July 1996.

[97] Winkelmann, A.E. and Barlow, J.B. Flowfield model for a rectangular planform wing beyond stall. *AIAA Journal*, 18(8):1006–1008, August 1980.

[98] Bragg, M.B. and Gregorek, G.M. Experimental study of airfoil performance with vortex generators. *Journal of Aircraft*, 24(5):305–309, May 1987.

[99] Storms, B.L. and Jang, C.S. Lift enhancement of an airfoil using a Gurney flap and vortex generators. *Journal of Aircraft*, 31(3):542–547, May–June 1994.

[100] Moffat, R.J. Contributions to the theory of single-sample uncertainty analysis. *Transactions of the ASME: Journal of Fluids Engineering*, 104:250–260, June 1982.

[101] Zhang, X. An inclined rectangular jet in a turbulent boundary layer-vortex flow. *Experiments in Fluids*, 28:344–354, 2000.

[102] Benedict, L.H. and Gould, R.D. Towards better uncertainty estimates for turbulence statistics. *Experiments in Fluids*, 22(2):129–136, 1996.

Appendix A

Fixed Ground Case

A.1 Introduction

As described in Chapter 1, only a single experimental study is reported for a downforce producing wing in ground effect close to a moving ground [3], offering force and surface pressure data for a limited range of heights for a two-dimensional configuration. More studies have been reported using a fixed ground [4, 5, 6, 7, 8]. Some studies have compared the ground effect for aeronautical type wings, both experimentally [23] and computationally [32, 33], in which the overall lift produced, and frequently the flow physics are severely affected by the ground boundary conditions. Due to the lack of overlap in work investigating downforce producing wings close to a fixed and a moving ground, there have been no comparisons made. It is therefore important to quantify the ground effect for the wing, for a fixed ground, in addition to the moving ground case.

Forces and chordwise surface pressures at the wing centre were taken at a range of heights, at an incidence of 1°, for the single element wing with free transition. In order to minimise the short-term uncertainties, force results were taken with a moving ground, then a fixed ground. Fixed ground results were taken with belt and boundary layer section applied.

A.2 Results

A.2.1 Forces

Forces from the overhead balance can be seen in Figure 87a, for the fixed ground and moving ground results. In terms of the general effect of height on downforce, the fixed ground results show similar features; an asymptotic increase at large and moderate heights, followed by a maximum downforce, and then a reduction in downforce closer to the ground. For heights greater than $h/c \approx 0.2$, the difference in the downforce produced is relatively small, but grows as the ground is approached, to about 15%. Below this height, the moving ground results feature the greatest

gradient, the slope of the fixed ground results is severely reduced. This results in a rapid change in the levels of downforce produced for the two cases. The curve reduces gradient, and the maximum downforce for the fixed ground case is at $h/c = 0.112$, corresponding to $C_L = 1.31$. This is at a greater height than for the moving ground, at $h/c = 0.090$, and the downforce is significantly reduced, compared to $C_L = 1.73$. The reduction in downforce below the maximum is then follows the same trend as for the moving ground case.

A.2.2 Surface Pressures

The surface pressures at the wing centre are shown in Figure 88a for the fixed ground case. At large and moderate heights, there are increases in suction over the entire suction surface, and small reductions in pressure over the pressure surface, in a similar manner to the moving ground results (Figure 8a). Comparing the fixed and moving results directly shows that the general difference is for a slightly reduced lower surface suction. For example, at $h/c = 0.224$, the peak suction on the lower surface is $C_P = -2.6$ for the moving ground results, but is $C_P = -2.3$ for the fixed ground results.

For reduced ground clearances (Figure 88b) the fixed ground results again show increases in peak suction on the lower surface as the height is reduced. Below $h/c = 0.134$, however, the increases are small. Comparing with the moving ground results (Figure 8b) shows significant differences with the flow over the suction surface. For heights less than $h/c = 0.134$ for the moving ground, where large suction gains, especially near to the peak suction in the range $x/c = 0.15$ to $x/c = 0.40$, are found. For example, at $h/c = 0.067$, the suction peak is C_P=-4.6 for the moving ground compared to the fixed ground. For the lowest height for the fixed ground results, there is a reduction in the suction in the region from $x/c = 0.40$ to $x/c = 0.90$, compared to at greater heights.

A.2.3 Canonical Pressures

The canonicals pressure distributions are are given in Figure 87b. The ground has a similar effect of increasing the canonical pressure as pressure recovery progresses, for a reduction in height. The results however, point to reduced canonical pressures when compared to the moving ground results (Figure 9b) near to the trailing edge for small ground heights. It would appear that, for the smallest height of $h/c = 0.067$, the canonical pressure is such that separated flow may be present from $s/s_{T/E} \approx 0.9$, i.e. $x/c \approx 0.85$. The size, therefore, of the separated flow region, is greatly reduced from the moving ground case, at which separation was observed at $s/s_{T/E} = 0.66$.

A.2.4 Discussion

At large and moderate heights, the downforce produced for the fixed ground case is a small amount less than that produced by the moving ground case, which has been shown to be due to slightly

reduced lower surface suctions for the fixed ground results. At heights near to the maximum downforce, the fixed ground results show relatively small increases in suction at the suction peak for a reduction in height, whereas for the moving ground case, significant increases are found near to the portion of the suction surface closest to the ground. It would appear that, for the fixed ground case at small ground heights, there may be a viscous phenomenon causing the very small increases suction near to the peak suction for a reduction in ground height. The boundary layer thickness for the transition fixed configuration at the wing trailing edge is approximately 0.05c for an arbitrary height. Although no data is available for the ground boundary layer thickness without the boundary layer suction, given the model location at over 2m downstream of the boundary layer suction, it is possible that a boundary layer of significant thickness may have developed at the location of the wing. Considering a turbulent boundary layer developing from the start of the boundary layer suction location, and using the equation $\delta = 0.383\frac{x}{(Re_x)^{1/5}}$ for an estimate of the boundary layer thickness, the ground boundary layer thickness over the ground at the location of the wing is very approximately $0.15 - 0.20c$ thick. It may be possible, therefore, to conclude that the wing and ground boundary layers have merged, as reported in other studies [4, 8, 5, 6].

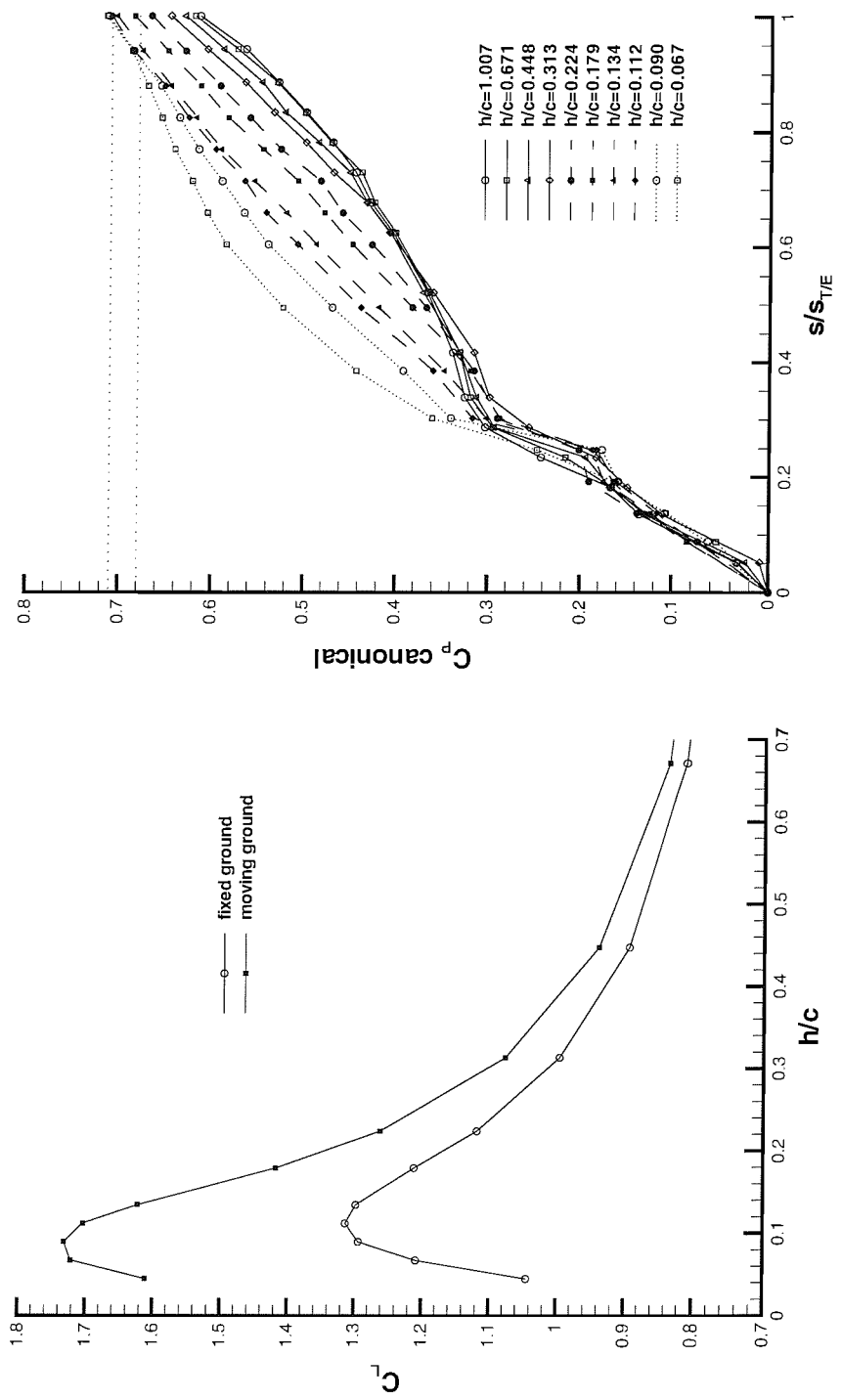

Figure 87: (a) Downforce in ground effect for fixed ground and moving ground, (b) Canonical pressure distributions for fixed ground, for single element wing, transition free, at $\alpha = 1°$.

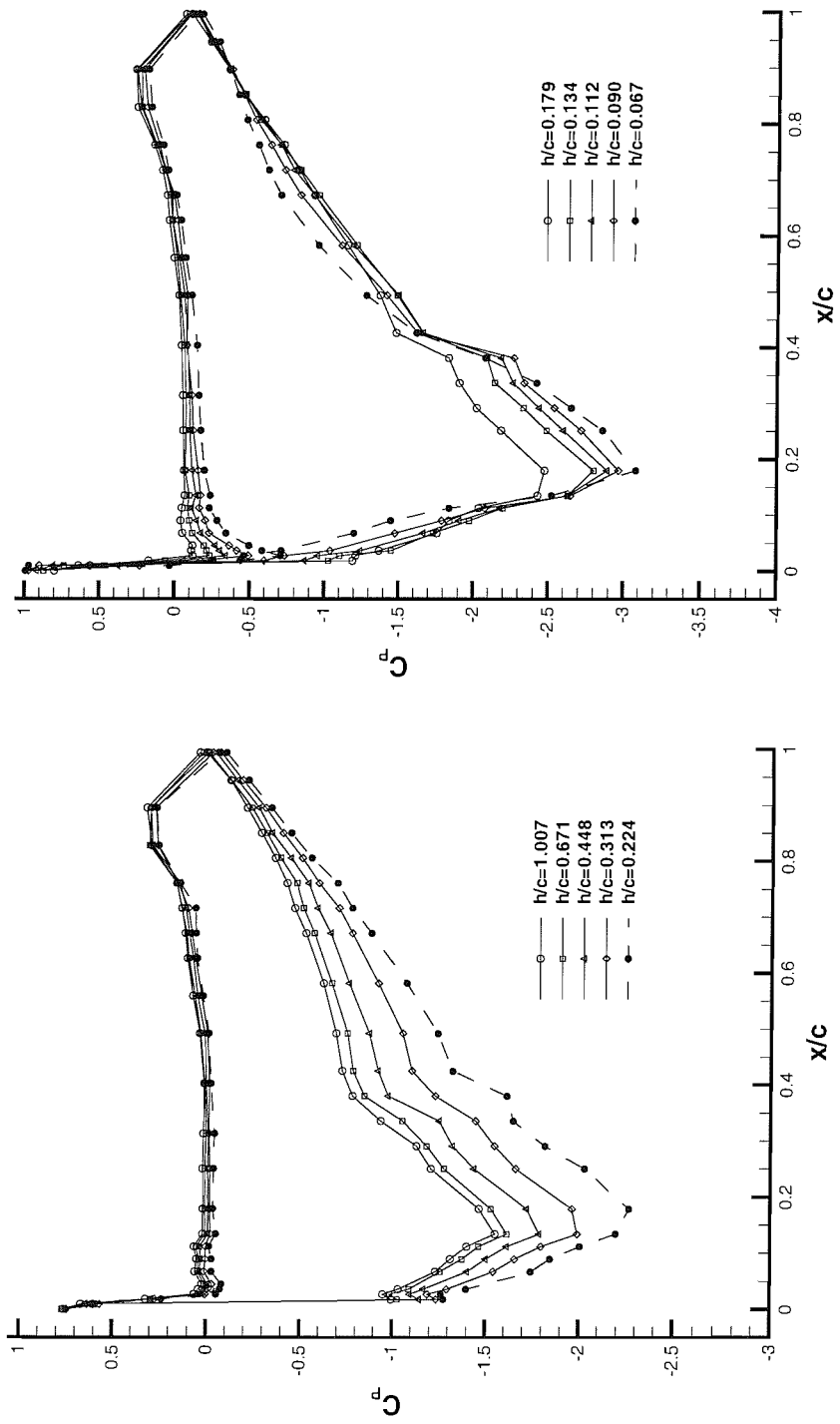

Figure 88: Chordwise pressure distributions at wing centre for fixed ground (a) large and moderate heights (b) small heights, for single element wing, transition free, at $\alpha = 1°$.

Appendix B

Vortex Generators

B.1 Introduction

Vortex generators are commonly used on aircraft to improve wing performance in situations where the wing has been effected by adverse atmospheric conditions, for example reference [98]. Although the wing may function as desired in ideal conditions, ice or rain can cause early transition, and effect the flow downstream, causing premature separation. This is not dislike the simulated transition fixed case of the wing in the current investigation, where debris picked up by the wing by the end of a race may reduce its performance.

A short series of tests was performed using vortex generators in an attempt to increase the overall level of downforce for the single element wing. The intention of the tests was to alleviate the reduction in downforce for the transition fixed case compared to the transition free case. In this manner, the practical performance of the wing at a certain height would be more constant for the flow states that may occur at the start and the end of a race. This is similar to their use on aircraft wings.

It must be stressed that the tests were purely investigative in nature to explore the possibility of their implementation. A thorough study into the flow physics was not performed. Because of this, only the results for the optimal configuration of vortex generators is presented.

B.2 Description of Tests

Standard delta planform vortex generators were manufactured in two different sizes corresponding to heights of 3mm and 5mm. The vortex generators were made individually on small aluminium squares, approximately 10mm$\times$10mm, to facilitate investigating contra- and co-rotating vortex generators and changing the space between them. A single corner of each square was bent so as to be perpendicular to the remainder of the surface, with the fold along a line 22.5° to the edge, for

the desired vortex generator height. Each vortex generator was applied individually using adhesive. Applying the vortex generators and removing the residue from the glue was found to be extremely time consuming.

Tests were performed transition fixed with the 60 grit, at a height of $h/c = 0.179$ from the ground, at an incidence of $\alpha = 1°$. The testing was performed before it was diagnosed that the 60 grit was adversely affecting the boundary layer. This height was chosen because, a significant difference in the downforce was seen between the transition free and fixed cases. A very small region of flow separation was present for the transition free case, but significant flow separation and loss of downforce existed for the transition fixed case.

The tests were generally performed with the vortex generator trailing edges at 70%c. The spacing between the vortex generators was varied, and contra- and co-rotating pairs were investigated. For each configuration, a force run was performed using the overhead balance. Then, oil flow visualisation was used to trace the flow patterns behind the vortex generators. The configuration of the vortex generators for the next run was determined according to the success of the previous run in terms of the downforce obtained and the effect on the separated flow behind the generators.

B.3 Results

Baseline results for the clean wing were taken in the same test session. The downforce obtained was a C_L of 1.15 and 1.40 for the transition fixed and free cases respectively. The drag was recorded as a C_D of 0.054 and 0.063 respectively. For the transition free case, the boundary layer separates at $x/c = 0.96$. For the transition fixed with 60 grit, separation was observed from the oil flow tests at $x/c = 0.80$.

The optimum configuration that was found during the test session was for contra-rotating pairs of vortex generators, using the 5mm tall generators, with 20mm between the centres of each set of generators. This configuration yielded a downforce of C_L of 1.29, for a drag of C_D of 0.064. This represents a recovery of 54% of the downforce lost under the fixed transition case, for a negligible drag penalty.

Figure 89 shows the surface visualisation. Between the pairs of generators, separation has been practically eliminated. Note that the trailing edge of the vortex generators are located at $x/c = 0.70$, and without the vortex generators, flow separates at $x/c = 0.80$. As described in much literature, for example [99], a pressure difference is generated, creating a streamwise vortex that entrains high speed fluid nearer to the surface, where the boundary layer would otherwise be close to separation. The boundary layer is re-energised, and remains attached until the trailing edge. Behind the pairs of generators, some separated flow is still present, as can be seen.

B.4 Conclusion

It has been shown that the application of vortex generators, in order to recuperate some of the lost downforce for the transition fixed case compared to the transition free case, is possible. Greater than 50% of the downforce lost can be regained, for the best configuration tested. Given more time to investigate the problem thoroughly, it is believed that greater gains could be obtained.

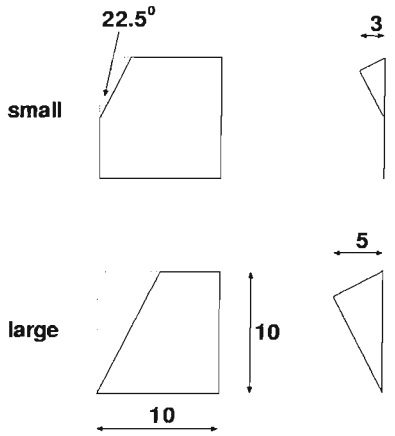

(a)

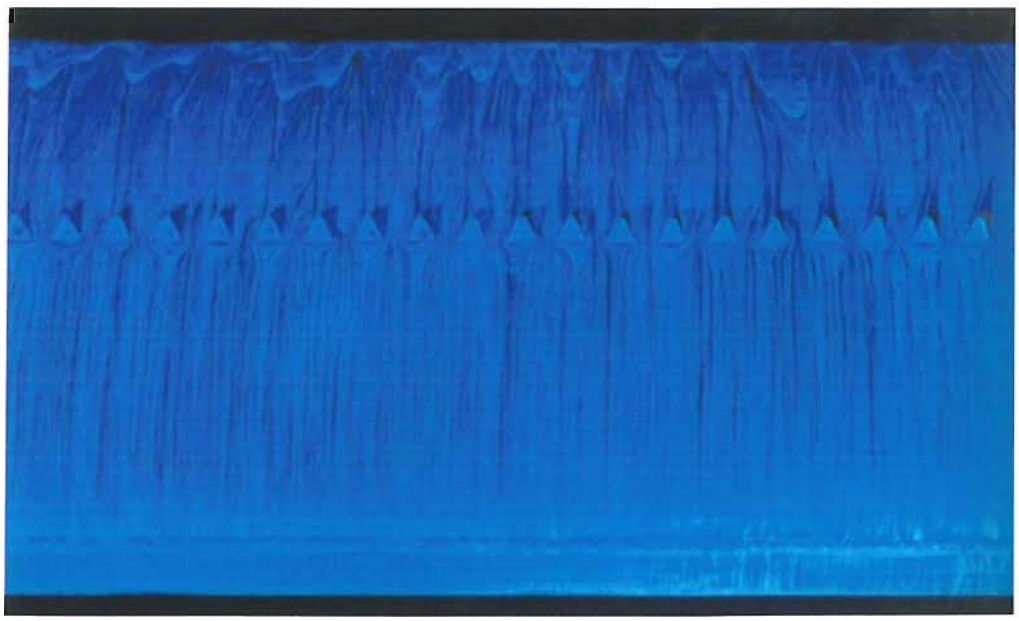

(b)

Figure 89: (a) Schematic showing vortex generator (b) Oil flow visualisation on suction surface with leading edge lowermost showing effect of vortex generators.

Appendix C

Uncertainty and Repeatability

C.1 Introduction

This chapter discusses the quality of the experimental results, with particular reference to the uncertainty and the repeatability of the data. For each type of test performed, i.e. forces, surface pressures, PIV and LDA, the overall uncertainty is assessed according to the contributions due to the uncertainty in different experimental parameters, for example the wind speed or the angle of incidence. The repeatability of the tests has been categorised into short term, medium term, and long term repeatability. Short term repeatability measurements are taken during a single wind tunnel run, without turning the wind off. They typically highlight the effects of the change of the flow during a run. Medium term repeatability is used to describe the similarity of results when the installation of the model has changed, for example resetting the angle of incidence, or the height of the wing. These were typically taken during the same testing slots, or during successive schedules. The long term repeatability has been investigated, by repeating the first tests performed approximately 18 months later. This can be used to show any long term degradation of the model, for example changes in the surface finish due to application and removal of transition strips.

C.2 Uncertainty of Force Measurements

The computer program for which all standard data is recorded from the overhead balance records a mean based on 75 samples, for the lift and the drag acting on the single element wing with free transition. The frequency of sampling data was 5Hz. In order to investigate the uncertainty of this sample, the program was modified to output all 75 samples. Statistical analysis of the sample data at an arbitrary height of $h/c = 0.090$ was performed. The mean was found to be $C_L = 1.71855$, with a standard deviation of 0.00058. The 95% confidence level for the uncertainty, using 2 standard deviations, gives an uncertainty based on the sample of $C_L \pm 0.00115$. At this

height, the flow is separated, this is believed to be a conservative estimate for all heights.

It is estimated that the height was set to ± 0.2mm, using the metal shims and spacers on which the wing was rested. Assuming a linear variation in the slope of the downforce against height curve, the uncertainty due to the height was calculated for each height. This was ± 0.00462 for the worst height of $h/c = 0.045$.

The incidence of the wing was set to $\pm 0.005°$ using the digital inclinometer. Using the liftslope found for different heights, an estimate in the uncertainty due to the incidence was calculated for all heights. The worst contribution was for $h/c = 0.112$ and below, with $C_L \pm 0.00100$.

The wind tunnel was run at a constant dynamic pressure of 56.25mm water ± 0.05mm water. The downforce at each height was scaled directly in proportion to the variation in dynamic pressure. The greatest contribution to the uncertainty in downforce is at maximum downforce, at a height of $h/c = 0.082$ corresponding to $C_L \pm 0.00153$.

Although testing was performed at a constant dynamic pressure, the Reynolds number throughout testing changed according to the ambient pressure, and the temperature in the wind tunnel. Using records of the temperature and the pressure, the range of Reynolds numbers tested at was found to be $Re = 0.430 - 0.462 \times 10^6$. The effect of Reynolds number variation was estimated at each height, considering the range of Reynolds numbers tested at, and a linear variation using the results at the lower dynamic pressure of 25mm water. It was found that the greatest contribution is at $h/c = 0.0895$ and corresponds to $C_L \pm 0.00118$.

The system acquires the data in terms of steps, where 59.903 steps is equal to 1N, for the lift component of the balance. The output of the data is accurate to one step. In addition to this, the readings from the overhead balance were examined after the end of the run. A control of a maximum of 20 steps for reading for the lift component after the run was applied. Any runs that failed this criteria (maybe 5-10 in all tests performed) pointed to a problem with the system, for example contact between the strut and the tunnel structure. The uncertainty contribution due to these factors was estimated as $C_L \pm 0.00130$, and was applied to all heights.

An overall estimate of the uncertainty was calculated using Moffat's method [100], from the root of the sum of the squares from all the individual components. The worst case was found to be at $h/c = 0.045$, corresponding to $C_L \pm 0.00523$. The average uncertainty was found to be $C_L \pm 0.00284$. The results can be seen in Figure 90a for the downforce against height curve for the single element wing, with free transition.

C.3 Repeatability of Force Measurements

In order to measure the short term repeatability, 20 repeat runs were performed for the single element wing at a height of $h/c = 1.343$ at $\alpha = 1°$, transition free. Between each run, the model was not moved. Statistical analysis gives a mean downforce of $C_L = 0.7695$, with a standard deviation of ± 0.0006. Using twice the standard deviation as a 95% confidence level, the repeatability is

± 0.0012.

Using runs that were repeated during a wind tunnel test, but after the model had been moved, the medium term repeatability was found to be ± 0.004, using a 95% confidence level, and a selection of heights, for the single element wing, transition free.

The long term repeatability was investigated in the final slot for single element testing. The complete set of forces at $\alpha = 1^\circ$ with free transition was taken for different ground heights, to compare with the results that had been taken approximately 18 months earlier. The results can be seen in Figure 90b. The long term repeatability can be seen to be excellent. For the repeated case, at large heights there is a very slightly smaller downforce generated, and at small heights, a very slightly larger downforce is generated. The mean of the differences for all heights is $C_L = 0.006$.

C.4 Uncertainty of Surface Pressures

The results for the surface pressure measurements were taken using the ZOC pressure transducer. Zeros for the system were taken with the wind off, with the wing at the required incidence. The tunnel was then run up to speed, and three sets of readings were acquired at that incidence. Each set of results was taken from the mean of 280 samples, over 7s in time, which is a wind tunnel standard, and is used for other research and customers. (Unfortunately, the software did not allow the output of all the samples.) The wind and road were then turned off, and the residual readings in each of the pressure tappings were examined. The characteristics of the pressure transducer are such that it is highly dependent on the temperature. For fair number of runs, approximately 10-25%, the initial run was ignored, if the residual was deemed to be too large. A *large* offset was taken to be 1mm water, or approximately 2% of the reading. The most frequent times at which runs had to be repeated were after a short break of wind, about 10 minutes, for example after a height change. The temperature in the working section of the tunnel varied when compared with the air in the rest of the wind tunnel. In this manner, the temperature of the transducers when the tunnel was run was different to the temperature during the run. Because of this, unsatisfactory results were found when performing runs at more than one incidence. Surface pressure testing also proved problematic during the mid-morning and late afternoon of hot days, as the temperatures in the working section and return leg varied. Problems were also observed close to the ground, when the platten would be cool before the run, due to the cooling water being passed through it, and warmer during the run, from the friction generated from the belt suction applied to counteract the belt lifting due to the model induced suction. The process of repeating the runs according to the offset, due to the problems of testing in ground effect configuration, was used in research for this thesis only and has not been applied to other research in the wind tunnel.

Since the transducers were connected to the same pressure tappings for each configuration tested, and the characteristics of each transducer was found to vary due to its temperature sensitivity, in addition to the results from each tapping varying due to the flow characteristics, the

uncertainty analysis has been performed according to each tapping, for the single element wing with free transition.

The residual for each transducer has been found, using an average of 10 randomly selected runs. The worst found was for the tapping at $x/c = 0.716$ on the suction surface, with an uncertainty in $C_P = 0.0144$. The average was $C_P = 0.0055$.

It is estimated that the height of the wing was set to ± 0.2mm. The sensitivity of the pressure to the height was found to be worst at the smallest heights. Using the results for the individual tappings, the uncertainty in C_P due to a 0.2mm error in height was estimated, using a linear variation between $h/c = 0.067$ and $h/c = 0.045$ as a worst case. The worst uncertainty in pressure was found to be at $x/c = 0.336$ on the suction surface, i.e. near to the peak suction, corresponding to $C_P = 0.0306$. The average for all tappings was $C_P = 0.0083$.

The incidence of the wing was set to $\pm 0.005°$. The uncertainty in pressure due to the incidence was estimated using linear interpolation between results at $h/c = 0.671$ for $\alpha = -3°$ to $1°$, at $h/c = 0.179$ for $\alpha = 1°$ to $5°$, and for $h/c = 0.090$ for $\alpha = 5°$ to $9°$, which seemed to be reasonably sensitive configurations, on inspection. The worst of the three height and incidence configurations was found for each tapping. The worst was found to be $C_P = 0.0034$ at $x/c = 0.0179$ on the suction surface, i.e. at the leading edge suction spike, with average uncertainty for all tappings of $C_P = 0.0012$.

The tunnel was run at a constant dynamic pressure of 56.25mm water. This was kept constant to ± 0.05mm water. This was applied to the height found at which the greatest suctions were observed as a worst case; $h/c = 0.045$. The variation in dynamic pressure caused the greatest uncertainty at $x/c = 0.179$, i.e. at the peak suction, of $C_P = 0.0049$. The average for all the tappings was found to be $C_P = 0.0013$.

The quoted accuracy of the transducer is ± 0.8mm water. This corresponds to $C_P = 0.0142$ for all tappings. The equipment outputs the values to three decimal places, corresponding to an uncertainty in $C_P = 0.0005$.

Using the uncertainty in C_P from all contributions from each tapping, the overall uncertainty was calculated using the sum of the root of the squares, as described by Moffat [100]. The worst uncertainty was found to be at $x/c = 0.336$ on the suction surface, corresponding to $C_P = 0.0347$. The average was found to be $C_P = 0.0190$. The results for all the tappings are shown in Figure 91a, for the wing at an arbitrary height of $h/c = 0.224$ at an incidence of $1°$.

C.5 Repeatability of Surface Pressures

In a similar manner to the forces, the short term repeatability of the surface pressure measurements was investigated using 20 runs at $h/c = 1.343$, $\alpha = 1°$, with free transition for the single element wing. A statistical analysis of the results was performed to estimate the repeatability using a 95% confidence level, based on twice the standard deviation. The results can be seen in Figure 91b,

where the error bars indicate the repeatability from the averaged results. The worst repeatability is found in the tapping at $x/c = 0.134$ at the peak suction, where the pressure is $C_P = -1.522 \pm 0.0375$. The repeatability at $x/c = 0.336$ on the suction surface also shows relatively low levels of repeatability. This is just behind the transition bubble, and the flow is likely to be unsteady here. The average repeatability has been calculated as ± 0.0178.

Using repeat runs performed after the angle and the height of the wing was changed, the medium term repeatability was estimated, using a selection of single element wing results with free transition, at a range of heights. The average repeatability using 95% confidence levels for all tappings was ± 0.0150.

The long term repeatability is illustrated in Figure 91a, where surface pressures for the single element wing, transition free, are shown for $h/c = 0.224$ at $\alpha = 1°$ for two different tests. The first set of results is from the initial investigation, the second results are from the tests performed at the same time as the fixed ground results, approximately 6 months after the original tests. The mean of the differences between the two tests is ± 0.018. The greatest differences occur near to the peak suction and the transition bubble, where the greatest uncertainties were found. The long term repeatability of the tests is generally within the bounds estimated by the uncertainty analysis.

C.6 Uncertainty of PIV Results

It is difficult to perform a thorough uncertainty analysis of the PIV results. The quality of the mean flow results depends directly on the quality of the individual snapshots of the flow. In all PIV testing, it was found that some images in a run contained good data with little noise, and some of the images contained more noise. The major contribution to this is believed to be the quantity and the distribution of the seeding. During the runs, it was noticed that the seeding in the working section varied according to time. On waiting for the seeding distribution to become more homogeneous, it died too quickly, and too little seeding resulted. The quality of cross-correlation of the results was highly dependent on the seeding level. Either too little or too much seeding gave bad cross-correlations. Once the desired amount of seeding was achieved with the tunnel running, results were acquired for 50 instantaneous datasets, over about 30s. Unsatisfactory results were found when performing longer run times. PIV testing was performed during three wind tunnel slots. The first was to investigate the flow at the centre of the wing, for the transition fixed case with and without the Gurney flap, predominantly for the instantaneous flow features. Results for 50 flow snapshots were taken. The tip vortex from the single element wing was then investigated. The mean flow results were found using 100 instantaneous samples, from two runs of 50. For the double element testing, 200 samples of the flow in the tip vortex region were taken from four runs of 50.

In addition to the acquisition of the data, the processing methodology was found to be critical. For example, for investigation of the shedding from the finite trailing edge in the single element

transition fixed results, it was necessary to perform a cross-correlation with a 75% overlap on 32×32 pixels to give results on a 157×125 grid, which is a very fine resolution. When results were processed using the next coarser grid level, either by reducing the overlap to 50% or by increasing the interrogation area to 64×64 pixels, to give either 77×61 or 79×63 vectors, the shedding completely disappeared from the results. It is generally recommended to filter the results, or to use a moving average technique. Again, these were found to have the same effect of smoothing or blurring the results too much, so all PIV results were only processed using a range validation. Results in Figure 92a show a wake profile extracted from the mean flow PIV results at $x/c = 1.5$ for the single element wing, transition fixed. These compare excellently with the LDA results. Although a little noise exists, the u/U_∞ velocity is generally within about $\pm 1\%$ of the LDA results. The effect of using a coarser grid to process the results on, with a 64×64 interrogation area, can be seen to reduce the velocity outside the wake by about 2%. There is a greater effect in the wake, where the maximum velocity deficit is nearly 5% too large, due to the blurring effect of using a coarser grid spacing for the cross-correlation. Filtering or performing a moving average (not shown here) blurs the wake more significantly. Hence although it is difficult to estimate the uncertainty of the PIV results, excellent comparisons can be made with the LDA results.

C.7 Repeatability of PIV Results

In addition to the quality of the individual flow snapshots, the flow unsteadiness is an issue specifically for mean flow PIV results. For the final PIV tests on the tip vortex of the double element wing, 200 samples were taken in total for each run, to find the time-averaged results. Typically, this fills approximately 300MB of hard disk space. For each run of 50 samples, the mean results were found, and exported from FlowManager. A fortran program was written to find the mean of the four output files. For a height of $h/c = 0.211$ for the low flap angle, a peak vorticity of $\omega c/U_\infty = 111$, was found at the flap quarter-chord. The runs of 50 samples give peak vorticities of $\omega c/U_\infty = 115.8, 113.9, 109.3$ and 109.0. There is little variation in the results from each run of 50 samples, and although the mean flow results were generated from the entire set of 200 samples, the short term repeatability of the mean flow results using each run of 50 is good. No medium or long term repeatability was investigated for the PIV results.

C.8 Uncertainty of LDA Results

An estimation of the uncertainty is first given for the mean velocity components, and then for the turbulent stress measurements. The accuracy of the traverse is 0.01mm, but there is a gear backlash of 0.5mm. Attempts were made to reduce the effect of this, by always approaching a boundary layer or wake profile from the same direction. Following an analysis by Zhang [101], an estimate of the uncertainty in the velocity measurement gives $u/U_\infty \pm 0.005$ and $v/U_\infty \pm 0.005$.

During testing, problems were frequently experienced with the LDA system, which directly effected the quality and quantity of data obtained. For the single element wing tests, transition free, typically 400-500 bursts (coincident) were taken. Poor data rates were experienced whilst testing for the transition fixed case at most heights, and with the Gurney flap, for the downstream wake surveys at $x/c = 1.5, 2.0$ and 3.0, and only approximately 200-300 coincident bursts were acquired. The problem had been resolved by the next test, such that for these configurations, for the trailing edge region to $x/c = 1.2$, including the boundary layer surveys, and for all the results at $h/c = 0.448$, 400-500 coincident bursts were typically taken. For the final tests, all double element results, an improved seeder was available, and 800-1000 bursts were typically acquired at each data point.

An estimate of the 95% confidence level has been performed following procedures detailed for the specific analysis of such data [102]. For the results at which 400-500 bursts were taken, the analysis was performed on the results for the single element wing, transition fixed, at $h/c = 0.448$ for the wake surveys at $x/c = 1.5$. For $u'u'$, the maximum uncertainty was found in the direct wake, as can be seen in Figure 92b. The worst uncertainty is 0.006 for $u'u'/U_\infty^2 = 0.007$, or less than 10% of the value. For the u velocity, the worst uncertainty found from the analysis is less than 0.1%, found in the wake.

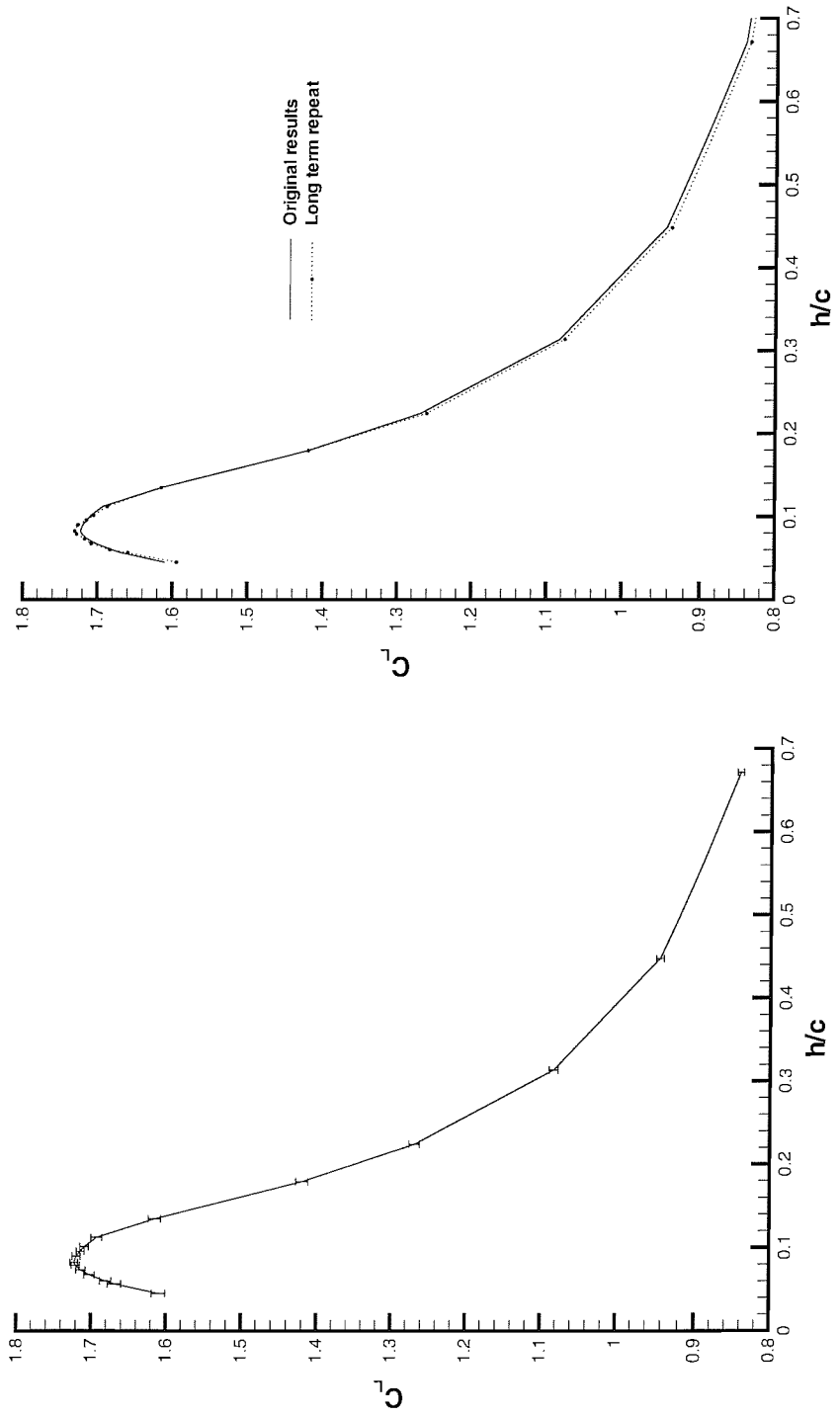

(a) (b)

Figure 90: (a) Uncertainty, (b) Long term repeatability, for single element wing, transition free, at $\alpha = 1°$.

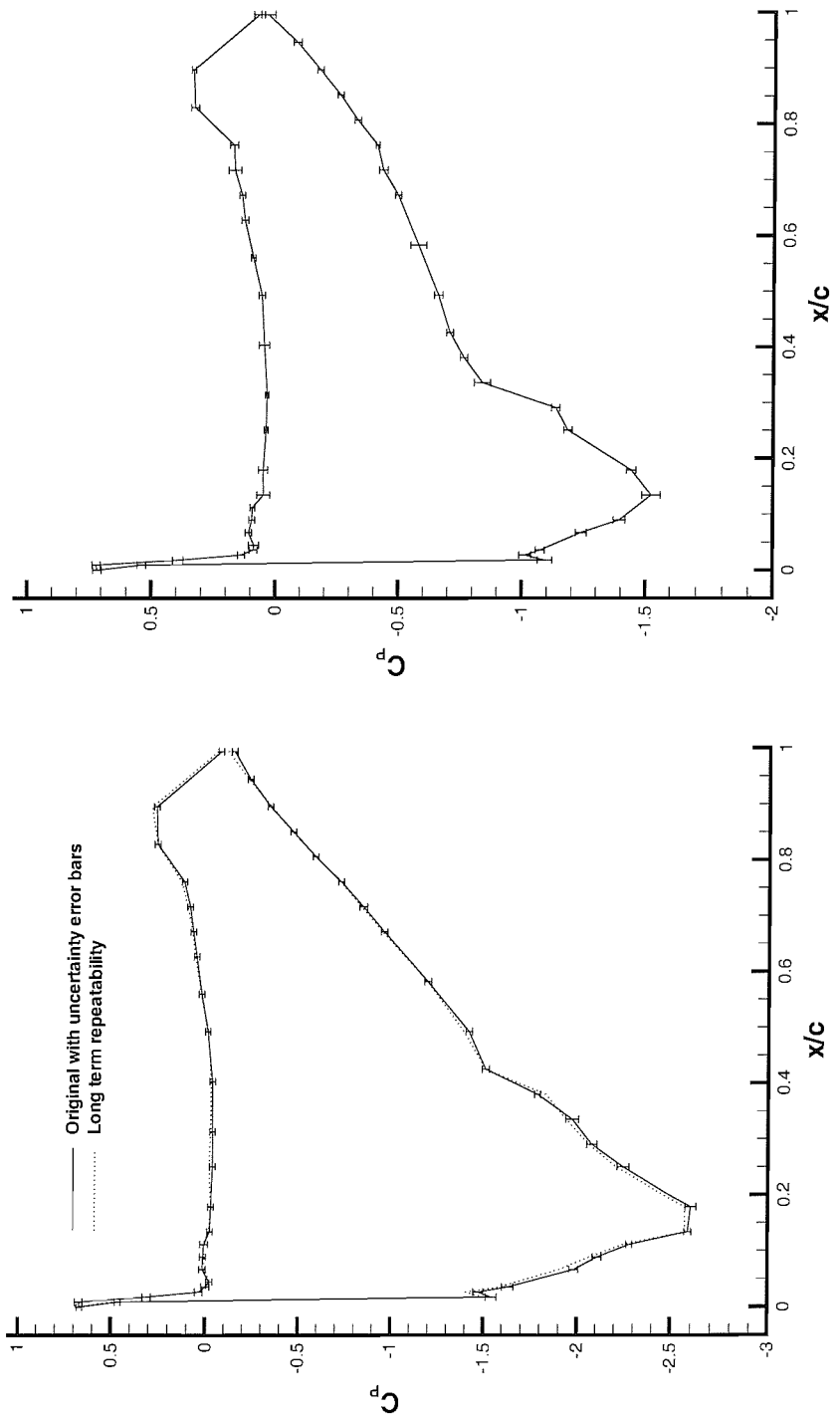

Figure 91: (a) Uncertainty and long term repeatability at $h/c = 0.224$, (b) Short term repeatability at $h/c = 1.343$, for single element wing, transition free, at $\alpha = 1°$.

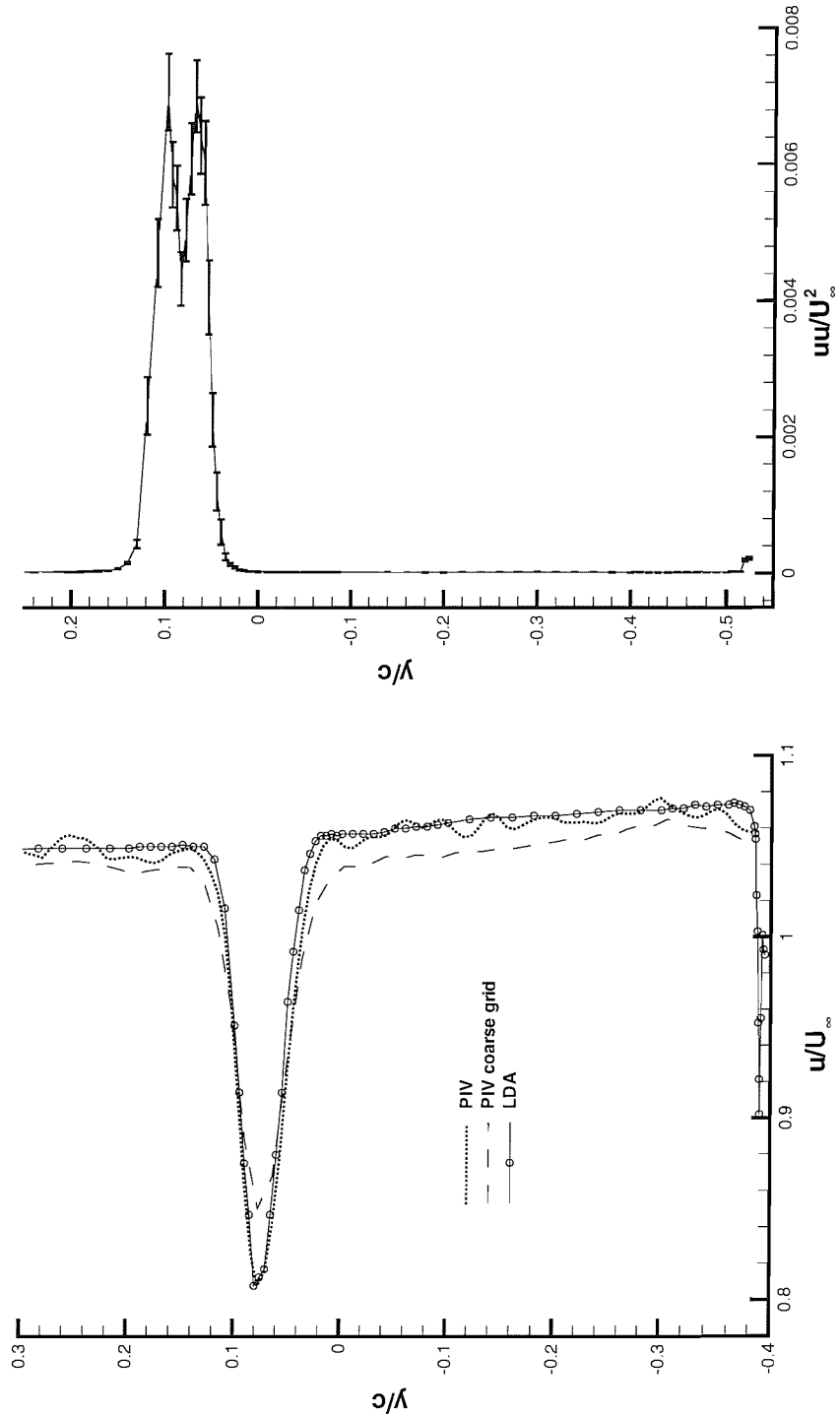

(a) (b)

Figure 92: (a) Comparison of wake profiles at $x/c = 1.5$ extracted from PIV results with LDA survey for single element wing, transition fixed, $h/c = 0.313$ at $\alpha = 1°$. (b) Estimation of 95% confidence level of $u'u'/U_\infty^2$ for single element wing, transition fixed, $h/c = 0.448$ at $x/c = 1.5$.

Appendix D

Miscellaneous

D.1 Effect of Pressure Tappings

After all surface pressure tests had been performed, the influence of the tappings was investigated using oil flow visualisation. A single run was performed for the double element wing with the high flap angle, at a height of $h/c = 0.263$. Results showing the suction surface can be seen in Figure 93a for the tapped wing, together with Figure 93b for the untapped wing. The dark area near to the leading edge of the tapped wing is an experimental anomaly where the solution was not applied. For the untapped wing, the laminar separation bubble occurs at $x/c = 0.15$ from the tip to $z/c = 1.0$ on the main element. Transition then occurs at the leading edge suction spike over the central portion of the wing. For the tapped wing, it can be seen that the separation bubble has been broken up on the main element. This is visible near to the tip, where there is a group of chordwise tappings at $z/c = 0.25$, and also at other spanwise locations, due to single tappings at the quarter-chord. On the flap, transition occurs near to the leading edge. Near to the centre of the wing, a region of separated flow exists near to the trailing edge. It is believed that this is either due to the direct influence of the flap tappings near to the centre of the suction surface, or that the tappings on the main element have disturbed the flow to a greater extent, sufficient to cause this.

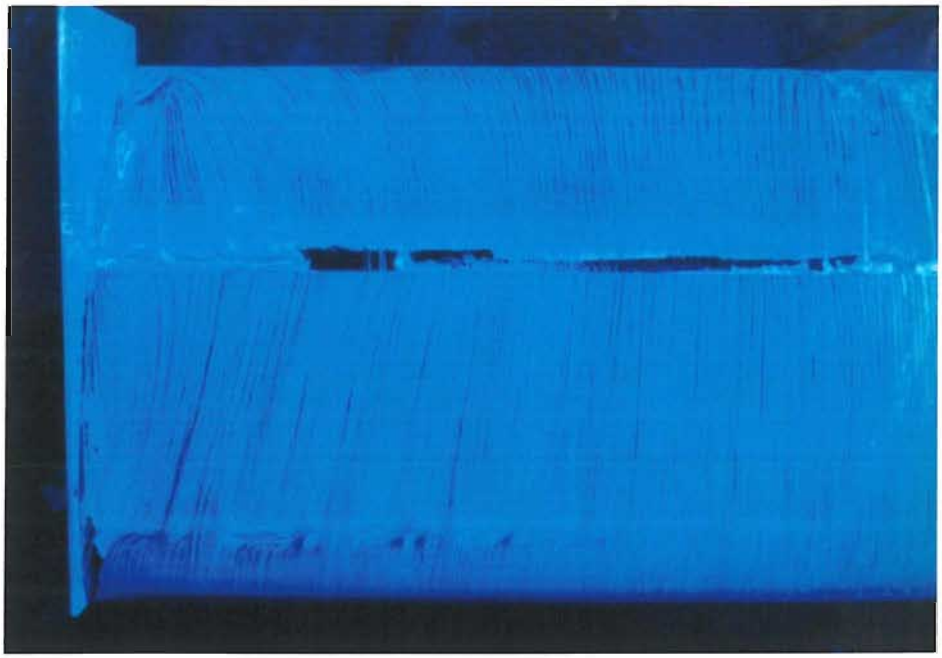

(a)

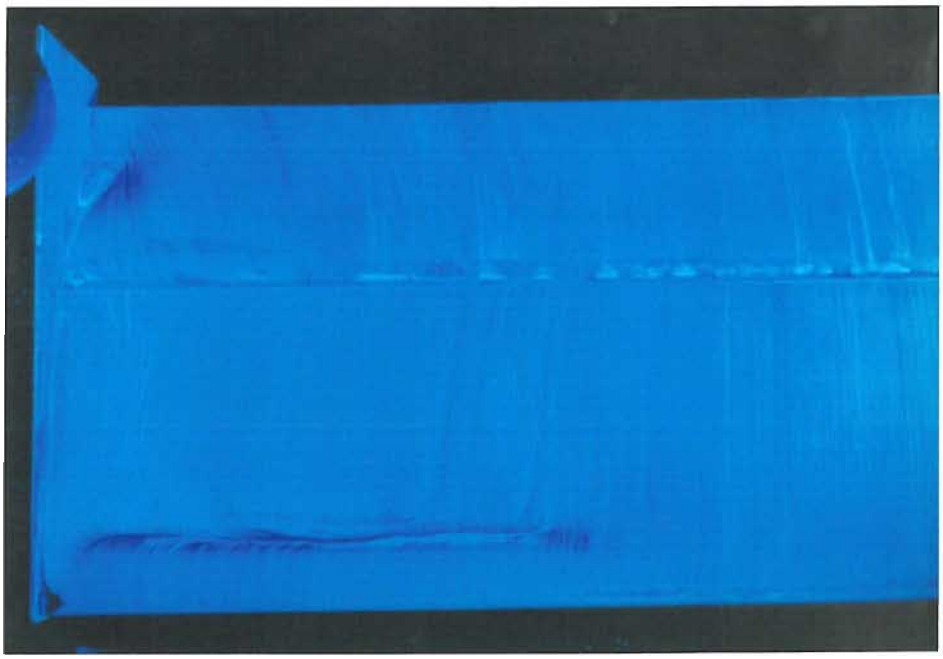

(b)

Figure 93: Oil flow visualisation on suction surface showing leading edge lowermost; (a) Pressure tapped wing (b) Untapped wing.